SOME INVESTIGATIONS IN FRICTION STIR WELDING OF CARBON STEEL

THESIS
SUBMITTED TO DELHI TECHNOLOGICAL UNIVERSITY
FOR THE AWARD OF THE DEGREE OF

DOCTOR OF PHILOSOPHY

IN

MECHANICAL ENGINEERING

By

ANMOL BHATIA

(2K16/Ph.D./ME/36)

Under the supervision of

Dr. REETA WATTAL
Professor
Department of Mechanical Engineering

DEPARTMENT OF MECHANICAL ENGINEERING
DELHI TECHNOLOGICAL UNIVERSITY
DELHI-110042 (INDIA)

OCTOBER, 2023

DELHI TECHNOLOGICAL UNIVERSITY
BAWANA ROAD
DELHI-110042 (INDIA)

DECLARATION OF ORIGINALITY

I hereby declare that the research work presented in this thesis titled, **"Some investigations in friction stir welding of carbon steel"** is an original and authentic work carried out by me under the supervision of Dr. Reeta Wattal, Professor, Department of Mechanical Engineering, Delhi Technological University, Delhi. This thesis has been prepared in conformity with the rules and regulations of the Delhi Technological University, Delhi. The research work reported and the results presented in the thesis have not been submitted either in part or full to any other university or institute for the award of any other degree or diploma. As per my understanding, this thesis is free from any plagiarized content.

<div align="right">

Anmol Bhatia
2K16/Ph.D./ME/36
Research Scholar
Department of Mechanical Engineering
Delhi Technological University

</div>

Date:

Place: Delhi

DELHI TECHNOLOGICAL UNIVERSITY
BAWANA ROAD
DELHI-110042 (INDIA)

SUPERVISOR'S CERTIFICATE

This is to certify that the Ph.D. thesis entitled *"***Some investigations in friction stir welding of carbon steel***"* being submitted by Mr. Anmol Bhatia, Roll No. 2K16/Ph.D./ME/36 for the award of the degree of Doctor of Philosophy in Mechanical Engineering, to Delhi Technological University, Delhi, India, is a bonafide record of the original research work carried out by him under my guidance and supervision. The work presented in this thesis has not been submitted to any other university or institution for the award of any degree or diploma.

Prof. Reeta Wattal

Department of Mechanical Engineering

Delhi Technological University

ACKNOWLEDGEMENTS

ABSTRACT

Friction stir welding (FSW) is the most promising welding technique that represents a significant advancement in the field of metal joining. While extensive research has been conducted in this area, initial investigations primarily focused on low-temperature softening materials such as aluminum alloys. However, as industries involved in steel welding seek more efficient and environment-friendly alternatives, there is a growing interest in exploring the application of FSW for steel joining. Welding steel poses unique challenges due to its high-temperature softening and high-strength properties. Although aluminum alloys were initially preferred for research purposes due to their inherent difficulty in conventional welding processes, the numerous advantages offered by FSW have prompted the need to develop this innovative technique for welding steels as well. Considering the increasing concerns over environmental pollution and health hazards associated with conventional welding processes, the development of a greener welding process holds great significance for various welding applications.

In this investigation, FSW was performed on AISI 1018 carbon steel plates, 3 mm thick. The welding process resulted in the successful creation of a butt joint extending along a length of 200 mm. FSW machine equipped with a high-powered spindle motor capable of generating the necessary torque was carefully selected for the study. Through experimentation, a specific grade of tungsten carbide was chosen, considering its ability to provide a longer tool life.

A series of extensive trial runs were conducted to establish an optimal welding procedure that would yield defect-free joints. Through these trials, the process parameters that have an impact on the weld quality were identified. The range of variation for these parameters was also determined. To examine the impact of input variables on the mechanical properties of the welds, experimentations were done using Taguchi's L9 orthogonal array (OA), with three repetitions for each experiment.

All 27 welds underwent thorough mechanical and metallurgical testing, requiring the extraction of samples from the welded plates. The samples underwent the transverse tensile test, reduced section tensile test, and impact test. Additionally, the fatigue test was conducted to evaluate the response of the welds and the base metal to cyclic loading.

To obtain the best possible machine settings for the welding process, both the single-response and multi-response optimization techniques were employed. Through the combined use of single-response and multi-response optimization techniques, the study aimed to find the optimal machine settings that would yield welds with improved mechanical properties and superior performance compared to the base metal. Metallurgical testing was carried out using microhardness testing, microstructural examination, and spectroscopic analysis of the welds.

The strength, impact energy absorbed, and fatigue properties of the weld were all found to have improved over the parent material properties. The process parameter, particularly welding speed, was found to have a significant effect on response parameters. Based on the experimental values, statistical models have been developed to find the effect of input variables on output variables. Microhardness values in the weld nugget and the HAZ were found to be more than the base metal.

TABLE OF CONTENTS

LIST OF FIGURES

xiii

LIST OF TABLES

LIST OF ABBREVIATIONS

S. No.	Abbreviation	Full form
1	ANN	Artificial neural network
2	ANOVA	Analysis of variance
3	AS	Advancing side
4	ASTM	American Society for Testing and Materials
5	BBD	Box-Behnken design
6	BM	Base metal
7	C(T)	Compact tension
8	CCD	Central composite design
9	DDRX	Discontinuous dynamic recrystallization
10	DOE	Design of experiment
11	EDAX	Energy dispersive analysis X-ray
12	FESEM	Field emission scanning electron microscopy
13	FSP	Friction stir processing
14	FSSW	Friction stir spot welding
15	FSW	Friction stir welding
16	FSWed	Friction stir welded
17	GA	Genetic algorithm
18	GMAW	Gas metal arc welding
19	GRA	Grey relational analysis
20	GRC	Grey relational coefficient
21	GRG	Grey relational grade
22	GTAW	Gas tungsten arc welding
23	HAZ	Heat-affected zone
24	ISO	International Organisation for Standardisation

25	MTM	Materials testing machine
26	NDT	Non-destructive testing
27	OA	Orthogonal array
28	PC	Principal component
29	PCBN	Polycrystalline cubic boron nitride
30	PWHT	Post-weld heat treatment
31	rpm	Revolutions per minute
32	RS	Retreating side
33	RSM	Response surface methodology
34	SAIL	Steel Authority of India Limited
35	SEM	Scanning electron microscope
36	SMAW	Shielded metal arc welding
37	SZ	Stir zone
38	TMAZ	Thermo-mechanically affected zone
39	TWI	The Welding Institute
40	UTS	Ultimate tensile strength

LIST OF SYMBOLS

S. No.	Symbol	Meaning
1	a	Crack length(mm)
2	B	The thickness of the specimen (mm)
3	C, C_1, C_2	Constants
4	Cov	Co-variance of sequences
5	D	Shoulder diameter(mm)
6	DF	Degree of freedom
7	i	Experiment number
8	K_1	Constant
9	m	Constant
10	MS	Mean squares
11	n	Constant
12	N	Tool rotational speed (rpm)
13	N	Number of cycles of load applied during fatigue testing
14	$n_{tr,i}$	Number of trials of the experiment i^{th}
15	P	Load (KN)
16	Q	Activation energy (kJ/mol)
17	R	Ideal gas constant (J mol^{-1} K^{-1})
18	R	Stress ratio
19	R_E	Square root of the coefficient of determination
20	R_E^2	Coefficient of determination
21	$R_E^2(adj)$	Adjusted coefficient of determination
22	SS	Sum of squares
23	T	Temperature (K)
24	T'	Peak temperature generated during friction stir welding (^{O}C)

25	T_m	Melting point of the alloy (°C)
26	u	Order of trials
27	V	Welding speed (mm/min)
28	V_{pk}	Eigen vectors
29	w	Width of the specimen (mm)
30	$y_i(k)$	Value of the kth response of ith experiment
31	$y_i'(k)$	Normalized experimental data based on the grey relational generation for response k^{th} of experiment i^{th}
32	y_u	Value of the measured performance characteristic for a given trial
33	Z	Zener-Hollomon parameter
34	α	Constant
35	β	The ratio of crack length to the specimen width
36	γ_i	Grey relational grade of all responses at the ith experiment
37	ΔK	Stress intensity factor (MPa $\sqrt{m}$)
38	Δ_{max}	Maximum values of $y_i(k)$
39	Δ_{min}	Minimum values of $y_i(k)$
40	$\dot{\epsilon}$	Strain rate (s^{-1})
41	θ	Tilt angle
42	λ_k	Eigen values
43	$\xi_i(k)$	Grey relational coefficient
44	σ_f	Flow stress (N/mm^2)
45	Ψ	Distinguishing coefficient
46	$\omega(k)$	Weighting factor of each response k^{th}

CHAPTER 1   INTRODUCTION

1.1 INTRODUCTION

Steel is widely used in industry due to its toughness, adaptability, and affordability. It is an alloy of iron and carbon, containing small quantities of other elements like silicon, manganese, and phosphorus. As reported by the world steel association, global crude steel production was approximately 1.9 billion metric tonnes in the year 2021, reflecting a 6.6% growth compared to the previous year. China retained its position as the largest steel producer globally, with a share of 58.9%, followed by India (6.7%) and Japan (5.2%).

It is crucial to note that the steel industry has a significant impact on the global economy by supplying raw materials for various sectors such as infrastructure, manufacturing, and others. Therefore, keeping track of worldwide steel production is critical to understanding economic trends and predicting future demand for steel products. Steel finds extensive use in various industries such as construction, transportation, and the energy sector, owing to its diverse range of applications. The remarkable strength and resilience of steel make it an excellent material for constructing infrastructure like buildings and bridges, as well as providing frameworks for pre-fabricated structures and reinforcing concrete. In transportation, steel is a critical component as it is utilized to produce engine components, axles, wheels, and bearings for automobiles, trucks, trains, and ships. The energy industry also relies on steel for pipelines, storage tanks, turbines, and other power generation components. Moreover, steel is an essential material in manufacturing, used in machinery, appliances, tools, and consumer goods, as well as electrical components and packaging, such as cans and containers.

Steels with high strength and low ductility have been successfully friction stir welded (FSWed), overcoming the challenges associated with conventional fusion welding methods. The process of FSW entails utilizing a rotating tool that enters the workpiece and produces heat through friction. As a result of the generated heat, the material undergoes softening, facilitating plastic deformation. The softened workpiece is then thoroughly mixed as the tool progresses along the joint's edge to produce a uniform joint. When welding steel, FSW offers various advantages over standard fusion welding processes, including increased weld strength, improved fatigue characteristics, and less distortion. Furthermore, FSW is more environmentally friendly than traditional welding procedures, producing far fewer emissions and trash.

1.2 OVERVIEW OF FRICTION STIR WELDING TECHNIQUE

This technique has gained significant traction due to its unique characteristics. It was developed by Wayne M. Thomas (Thomas et al., 1991) at The Welding Institute. It has numerous applications in different sectors such as automotive, aerospace, etc.

According to Figure 1.1, a cylindrical rotating tool equipped with a protruding pin is inserted between the adjacent surfaces of two workpieces, and it is then allowed to traverse along the joint line. This motion generates heat between the tool and the workpieces because of friction. As a result of this heat, the material becomes softer, enabling the tool to mix and stir the softened material. Ultimately, a solid-state joint is formed between the two workpieces without any melting.
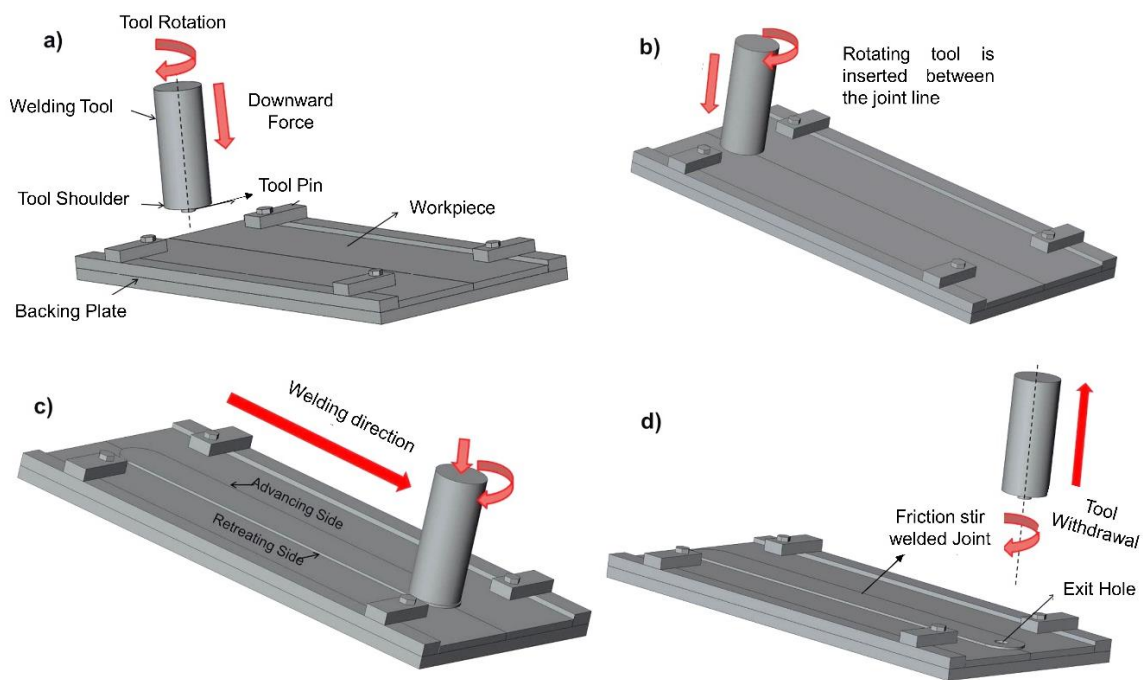
Figure 1.1: Operational concept of FSW

This technique encompasses various essential factors that can be fine-tuned to attain the desired level of weld excellence. The weld quality is influenced by a range of process parameters that necessitate optimization based on the specific application. Several essential factors significantly contribute to determining the quality of joints. These factors include:

- **Tool rotational speed:** The generation of heat is directly influenced by the rotational speed, and this would affect the weld integrity. Higher rotational speeds generate more

heat, leading to improved weld quality. Nevertheless, this also raises the likelihood of defects such as voids, cavities, and tunneling.

- **Traverse speed:** The tool's motion along the joint line is indicated by the traverse speed. A reduced speed provides additional time for the material to undergo softening and blending, leading to enhanced weld quality.

- **Tool geometry:** The configuration and dimensions of the tool impact both the quantity of material stirred and the heat generated. A well-designed tool can lead to a superior weld of excellent quality, minimizing any potential flaws.

- **Tool tilt angle:** It influences the flow and blending of the materials. Finding the ideal tilt angle for the tool can result in enhanced mixing and a more uniform weld.

- **Welding force:** The welding force influences the interaction of the tool with the workpiece. An increased welding force may result in better material flow and mixing, but it can also increase the risk of tool wear and damage.

- **Material properties:** The properties of the materials being welded affect the weld quality. Materials with high strength, high melting point, or high thermal conductivity can be more challenging to weld using FSW.

- **Process environment:** The conditions in which FSW takes place, including temperature, humidity, and pressure, can impact the weld's quality. Maintaining appropriate environmental control is essential to achieve a weld of high quality.

FSW enables the joining of diverse materials, including metallic and non-metallic substances. Some of the most common materials that can be welded using FSW include:

- **Aluminum and its alloys:** This includes alloys such as 6061, 7075, 2024, etc. FSW finds widespread application in the aerospace sector for the welding of aluminum components.

- **Copper alloys:** Copper alloys such as brass and bronze can also be welded using FSW. The utilization of the FSW process in joining copper alloys is extremely beneficial, as it efficiently hinders the creation of fragile intermetallic compounds that have the potential to undermine the weld's strength and reliability.

- **Magnesium:** Magnesium and its alloys are lightweight materials that can be difficult to weld using traditional welding processes. FSW has been successfully used to weld magnesium alloys, resulting in strong, high-quality welds.

- **Titanium:** The aerospace industry extensively utilizes titanium and its alloys due to their remarkable ratio of strength to weight. FSW can be used to weld titanium alloys, resulting in strong, high-quality welds that maintain the material's unique properties.
- **Steel:** While steel is not typically associated with FSW, recent advances have enabled the welding of certain types of steel. This includes high-strength steel used in the automotive and construction industries.

In addition to these materials, FSW has also been used to weld non-metals such as polymers and composites. FSW is particularly effective for welding thermoplastic materials, resulting in strong, high-quality welds without the need for adhesives or other bonding agents.

1.2.1 Variants of friction stir welding process

FSW can effectively weld difficult materials in comparison to the fusion welding process. Over time, researchers have developed various modifications to enhance its efficiency and versatility. Its numerous forms are listed below:

Friction stir spot welding (FSSW): This method employs spot welding in its configuration. It involves plunging the rotating tool into the workpiece and then moving it laterally to create a weld. FSSW has been used successfully to join aluminum, magnesium, and steel alloys. (Linert et al., 2012)

Friction stir processing (FSP): This process alters the characteristics of materials. The process entails the movement of a rotating tool along the surface of the material, without the need to join separate pieces. This technique is employed to enhance grain size, boost hardness, and improve fatigue performance (Mishra et al., 2005).

Friction stir spot welding with tool oscillation: The tool undergoes oscillations while performing the welding operation. This oscillatory movement aids in achieving a more consistent weld and FSSW-T exhibits the ability to decrease heat generation while welding, and it has proven to be effective in joining aluminum, copper, and magnesium alloys (Hu et al., 2011).

Friction stir blind riveting: It is a variation of FSW that is used to join dissimilar materials. It involves inserting a pre-formed rivet into a hole in one of the materials and then using FSW to join the two materials together. This process can be used to join aluminum to steel, magnesium to aluminum, and other dissimilar material combinations. (Mishra et al., 2003)

Orbital friction stir welding: This variant of FSW employs a rotating tool that incorporates an orbital movement. This orbital movement of the tool is specifically designed to create a circular weld characterized by consistent thickness and exceptional mechanical properties. OFSW has proven effective in welding materials that demand high strength, particularly aerospace alloys. It has exhibited the capability to generate welds of excellent quality while minimizing distortion.

Bobbin tool friction stir welding : BFSW is an alternative form of FSW that utilizes a bobbin-shaped tool instead of the typical pin tool. The bobbin tool has a unique shape that allows it to weld materials with varying thicknesses. This variant of FSW has been used to weld materials with a thickness range of 1-50 mm. The bobbin tool has been shown to reduce tool wear and increase welding speed, resulting in a more productive welding process. A study conducted by Chen et al. (2016) demonstrated that increasing the rpm, and tool tilt lead to the development of a more consistent grain structure.

Stationary shoulder friction stir welding: This process uses a stationary shoulder, which is a tool part that is not rotated. This technique can be used to weld materials that require low heat input, such as aluminum alloys. The stationary shoulder helps reduce the heat input by reducing friction and heat produced during the process. This variant has proved to enhance weld quality and reduce tool wear. Researchers have studied the influence of process variables on weld quality. In a study conducted by Wang et al. (2019), it was demonstrated that enhancing the rotational speed improved the quality of the weld while increasing the tool tilt angle led to a more consistent grain structure.

1.2.2 Advantages of friction stir welding

FSW offers numerous benefits in contrast to conventional fusion welding techniques. This section provides a detailed description of the benefits associated with FSW.

Improved joint strength

FSW offers a significant advantage by producing exceptionally strong joints in comparison to conventional welding methods. It creates defect-free joints without the typical issues encountered in fusion welding, such as porosity, solidification cracks, and solid-state weld defects. The solid-state characteristic of FSW guarantees defect-free joints, consequently leading to enhanced joint strength.

Lower distortion

FSW produces less distortion than traditional welding methods. In fusion welding, the material is heated to a molten state, which causes it to expand and contract. This expansion and contraction result in distortion, which can be difficult to control. In contrast, FSW, being a solid-state technique, induces minimal distortion.

Better quality welds

FSW produces high-quality welds that are free of defects. The process ensures the absence of porosity or solidification cracking. This leads to a high-quality weld that is free from defects and has excellent mechanical properties.

Improved efficiency

FSW is a highly efficient process that reduces welding time and eliminates the need for additional consumables such as filler wire, shielding gas, and flux. By utilizing a rotating tool, the process generates heat through friction, resulting in material softening and facilitating the joining process. As a result, the heat input necessary for weld formation is minimized, leading to a reduction in welding duration.

Better material properties

FSW produces a weld that has excellent material properties. Due to its solid-state characteristic, the process guarantees a refined microstructure in the weld, leading to exceptional mechanical properties. Additionally, FSW produces a weld that has a low level of distortion, which results in improved fatigue properties.

Environment friendly

FSW is an environment-friendly process that produces no fumes, gases, or radiation. Unlike traditional welding methods, FSW does not require shielding gas, which reduces the amount of gas used and eliminates the need for ventilation systems.

1.2.3 Limitations of friction stir welding process

FSW got popularised in recent times because of its distinct advantages over traditional processes. The utilization of this technique has been observed in the joining diverse range of metals across multiple industries, including aerospace, automotive, and shipbuilding.

Nevertheless, similar to other welding techniques, FSW possesses certain limitations that should be considered when determining the most suitable welding method.

FSW encounters a significant limitation in its inability to join materials with low melting points, such as plastics or polymers. The process, being a solid-state welding technique, depends on the frictional heat to soften and render the metal plastic, rendering it appropriate for welding materials characterized by high melting points. However, this heat can cause low melting point materials to melt and burn, making them unsuitable for welding. Welding materials with low melting points can also result in defect formation.

Another limitation of FSW is its difficulty in welding materials with complex geometries or contours. To carry out FSW, a specifically designed rotating tool featuring a unique pin and shoulder configuration is utilized, which penetrates the metal and generates heat through friction. However, the tool cannot access narrow or deep grooves or corners, making it difficult to weld materials with complex geometries. As a consequence, defects like cracks, voids, or incomplete welds may arise.

Furthermore, FSW may produce residual stresses in the welded parts, which can affect their mechanical properties and performance. Residual stresses occur when the metal cools down after welding, resulting in uneven cooling rates and temperature gradients. These stresses can cause distortion, warping, or even cracking, particularly when welding materials with different thicknesses or properties.

FSW also requires specialized equipment and tooling, which can be expensive and may not be readily available. The equipment and tools must be designed to withstand high temperatures and pressures and must be capable of rotating at high speeds. The tooling must also be designed specifically for each application, which can be time-consuming and costly. This can make FSW a less attractive option for small-scale operations or for welding low-volume production runs.

Moreover, FSW may not be suitable for welding certain materials, such as reactive metals or materials that are prone to corrosion. Reactive metals, such as titanium or magnesium, can react with the atmosphere or the surrounding environment during welding, resulting in the formation of oxides or other compounds that can weaken the weld. Similarly, metals prone to corrosion, such as aluminum or copper alloys, may experience the formation of oxides or other compounds during welding, which can diminish the weld's strength.

1.2.4 Applications of friction stir welding process

FSW has gained curiosity in recent years as a relatively new technology, primarily due to its unique benefits over traditional processes. The primary areas where it finds application are as follows:

Aerospace industry

One of the most significant applications of FSW is in the aerospace industry, where it is used to join large aluminum structures, such as the wings and fuselage of an aircraft. FSW proves to be highly advantageous in the welding of aluminum panels, presenting challenges when employing traditional welding techniques. The process has been used in the manufacturing of various aircraft, including the Boeing 787 and the Airbus A380 (Sinka, 2014).

Weight reduction is a crucial consideration in the aerospace sector due to its impact on aircraft fuel consumption. FSW offers a means of joining lightweight materials, effectively reducing the overall weight of an aircraft. The aerospace industry has experienced increased adoption of aluminum alloys, due to their outstanding ratio of strength to weight. Nonetheless, the high strength of these alloys poses challenges for traditional welding techniques. FSW presents a solution for welding these materials while preserving their strength. FSW has also been used in the repair of aerospace structures. The repair of damaged aircraft structures is a significant concern for the aerospace industry. Traditional welding methods can result in distortion, which can affect the structural integrity of the aircraft. FSW provides a method for repairing damaged aircraft structures without causing any distortion. FSW offers the capability to effectively join dissimilar materials, fulfilling a crucial demand of the aerospace sector.

Automotive industry

FSW finds another significant application in the automotive sector, where it is employed to weld materials with reduced weight such as aluminum and magnesium alloys. These materials are progressively employed to reduce the vehicle's weight and improve fuel efficiency. FSW has been utilized to join aluminum and magnesium parts in diverse automotive applications, including engine blocks, transmission housings, and suspension components (Kayode et al., 2019).

The automotive sector has witnessed growing adoption of aluminum and magnesium alloys owing to their excellent strength-to-weight ratio. FSW joins these materials while preserving

their strength. Implementing FSW in the automotive industry can lead to substantial weight reduction, thereby enhancing fuel efficiency and decreasing emissions.

FSW has also been used in the repair of automotive structures. The repair of damaged automotive structures is a significant concern for the automotive industry. Traditional welding methods can result in distortion, which can affect the structural integrity of the vehicle. FSW provides a method for repairing damaged automotive structures without causing any distortion.

Marine industry

FSW has also been used in the marine industry to join large structures, such as ship panels and hulls. FSW proves especially valuable in the welding of thick aluminum plates, a task that poses challenges when employing traditional welding techniques. FSW has been used in the construction of various marine vessels, including the fast ferry, Alakai, and the US Navy's Littoral Combat Ships (LCS) (Wahid et al., 2020).

The marine sector is progressively adopting lightweight materials like aluminum and titanium alloys to decrease ship weight and enhance fuel efficiency. FSW provides a method for joining these materials without affecting their strength. The use of FSW in the marine industry can result in significant weight reduction, which can improve fuel efficiency and reduce emissions. A study conducted by Arya et al. (2022) found that FSW produced high-quality welds in aluminum and magnesium alloys used in the marine industry, making it suitable for joining lightweight materials.

The marine industry requires welding processes that can repair damaged structures efficiently. FSW is an effective technique for repairing marine structures, because of its capacity to generate high-quality welds while minimizing distortion. Additionally, FSW can repair structures that are difficult to access, such as underwater pipelines. A study conducted by Amavisca et al. (2023) found that FSW produced high-quality welds in the repair of clad pipes in the context of the oil and gas industry, making it a suitable method for repairing marine structures.

Rail industry

The rail industry requires welding processes that can join rail tracks efficiently. This process is highly effective for connecting rail tracks, as it can generate high-quality welds with minimal distortion. FSW can join rails with thicknesses up to 50mm in a single pass, ensuring that the

rails maintain their strength and durability. A study conducted by Hoyos et al. (2019) found that FSW produced welds with high strength and ductility in rail tracks, making it suitable for joining rail tracks.

The rail industry requires welding processes that can join dissimilar metals efficiently. FSW has been substantiated as an effective method for uniting dissimilar metals, such as aluminum and stainless steel. FSW produces high-strength welds with minimal distortion, ensuring that the rail's integrity is maintained. A study conducted by Ghosh et al. (2014) found that FSW produced high-quality welds in aluminum and stainless steel used in the rail industry, making it suitable for joining dissimilar metals.

The rail industry requires welding processes that can repair damaged rails efficiently. FSW has demonstrated its efficacy as a reliable technique for repairing rail structures by delivering high-quality welds with minimal distortion. Additionally, FSW can repair rails that are difficult to access, such as those in tunnels.

Electrical industry

In the electrical industry, FSW has been used in the manufacture of electrical components, such as transformers and motors, owing to its capability of generating superior welds with minimal flaws.

Transformers are essential components in the electrical industry, and they require welding processes that can join them efficiently. Traditional welding techniques such as arc welding can produce welds that are susceptible to imperfections like porosity, cracking, etc. These defects can result in transformer failures, leading to significant losses. FSW has proven to be an efficient method for joining transformers owing to its capability of producing high-quality welds with minimal defects.

The electrical industry requires welding processes that can join motor components efficiently. FSW has been validated as an effective technique for connecting motor components because it can generate high-quality welds with minimal distortion. Additionally, FSW can join dissimilar metals, reducing the need for expensive welding techniques such as explosion welding. A study conducted by Ouyang et al. (2006) found that FSW produced high-quality welds in aluminum and copper used in the manufacture of electrical motors, making it a suitable method for joining motor components.

The electrical industry requires welding processes that can join electrical conductors efficiently. FSW has demonstrated its efficiency in joining electrical conductors. Additionally, FSW can join dissimilar materials such as copper and aluminum, reducing the need for expensive welding techniques such as explosion welding.

Medical industry

The medical industry has been exploring the use of FSW for various applications, including the manufacturing of implants, medical instruments, and equipment. FSW can join various materials, including commonly utilized titanium and stainless steel, which are used in producing implants. This technique can produce strong and durable joints, which are crucial for implant success (Moghadasi et al., 2022). FSW has been used to join thin sheets of metals used in the manufacturing of surgical instruments, such as scissors and forceps. This technique can produce welds with high strength, ductility, and corrosion resistance, which are crucial for medical instruments (Wu et al., 2022). FSW has been used to manufacture equipment such as X-ray tube components and MRI coils. This technique can produce welds with high mechanical strength, which is crucial for the safe and reliable operation of medical equipment.

Nuclear applications

The nuclear industry requires welding processes that can join components efficiently and produce high-quality welds with minimal defects. FSW has proven to be an efficient method for joining nuclear components due to its ability to create welds that exhibit decreased residual stress levels and enhanced joint strength.

Nuclear fuel rods are essential components in the nuclear industry, and they require welding processes that can join them efficiently. Traditional welding techniques such as arc welding can produce welds that are susceptible to defects like porosity, cracking, etc. These defects can result in fuel rod failures, leading to significant losses.

Nuclear waste containers are essential components in the nuclear industry, and they require welding processes that can join them efficiently. FSW can join dissimilar materials, reducing the need for expensive welding techniques such as explosion welding. A study conducted by Cederqvist et al. (2012) found that FSW produced high-quality welds in nuclear waste containers, making it a suitable method for the manufacture of nuclear waste containers.

1.3 CHALLENGES IN FRICTION STIR WELDING OF STEEL

FSW of steel is still challenging because of several factors. The challenges are discussed in this section:

Material properties

Steel is extensively employed across diverse industries owing to its exceptional mechanical characteristics, such as remarkable strength and toughness. However, these properties also make it challenging to weld using FSW. Steel requires high input during the welding process, as its melting point is high. This high heat input can result in thermal distortion, which can affect the quality of the weld. Moreover, the high carbon content in steel can cause hardening and cracking during welding, which can further reduce the weld quality.

Tool material

It is crucial for the tool utilized in the welding process to exhibit exceptional wear resistance to withstand the high temperatures and mechanical stresses involved. Nonetheless, the substantial wear rate of the tool poses a significant challenge when welding steel using FSW. The tool material must be able to withstand high temperatures and pressures while maintaining its structural integrity. Furthermore, the high wear rate can cause tool degradation, which can affect the weld quality.

Process parameters

The weld quality is impacted by the process parameters, and achieving optimal parameter settings for the FSW of steel remains a challenging task. The substantial heat input necessary for steel welding can lead to excessive material deformation and recrystallization, thereby influencing the mechanical properties. Moreover, the high carbon content present in steel may result in hardening and cracking while welding, posing difficulties in fine-tuning the process parameters.

Joint design

The design of the joint plays a crucial role in steel FSW, as it directly influences the weld's strength and quality. The joint design must ensure that the material is sufficiently plasticized and that the tool can access the joint without creating excessive distortion. However, the joint design for steel is still a challenging task, as the high strength and material toughness can cause difficulty for the same.

1.4 FORMAT OF THE THESIS

Chapter-1: Introduction

This chapter provides a thorough explanation of the FSW process, its functioning, its application, and the difficulties associated with welding steel. Additionally, it outlines the thesis chapters.

Chapter-2: Literature review

A review of research conducted on different materials utilizing the FSW process is discussed in this chapter. It also includes an overview of the steel materials that are welded using the FSW technique. This chapter also includes references to newly published studies on tool geometry optimization, process optimization, and material flow. The objectives of the study and gaps in the literature are also mentioned in this chapter.

Chapter-3: Experimental setup

This chapter provides an outline of the FSW equipment employed for conducting the experimental work. Additionally, the welding fixture, tool, and other materials needed for the present study are also described in this chapter. The chapter also describes the basis of the selection of tool material and the suitability of tungsten carbide as tool material is also discussed.

Chapter-4: Experimentation

This chapter deals with the basis for the selection of process parameters and their levels to obtain satisfactory welds. The planning for experimentation as per the design of experiments is also described in the chapter. Additionally, the details of finding the welding run for experimentation are described in this chapter.

Chapter-5: Testing weld integrity and analysis of results

This chapter presents the outcomes of mechanical tests performed on the welds, including the procedures for preparing samples for tensile testing, reduced section tensile testing, impact testing, and fatigue testing. The chapter also describes the influence of input variables on weld integrity through statistical analysis.

Chapter-6: Optimization of process parameters

Single objective optimization using Taguchi is described in this chapter. This indicates the optimum machine settings for optimizations of the single response parameters. Multi-objective Optimization is also performed using GRA and the weighted GRA method. The results of both Optimization techniques are compared in this chapter.

Chapter-7: Metallurgical testing of welds

Different metallurgical tests were done on the weld like spectroscopic analysis, microstructural examination, and microhardness testing have been described in this chapter. This chapter includes the presentation of micrographs depicting the welds fabricated under optimal parameters, as well as the presentation of the results obtained from microhardness testing.

Chapter-8: Conclusion and scope of future work

This chapter presents the key findings derived from the research conducted, with potential future research directions in the same field.

CHAPTER 2   LITERATURE REVIEW

2.1 INTRODUCTION

Ferrous alloys are primarily composed of iron, with varying amounts of carbon and other elements. These alloys possess excellent mechanical properties, making them widely utilized in various industries. There are two main categories of ferrous alloys: steel and cast iron, each with its unique characteristics and applications. Steel is a versatile ferrous alloy that can be categorized into four major groups: carbon steel, alloy steel, stainless steel, tool steel, and specialty steel.

Carbon steel is composed primarily of iron and carbon. Carbon steel is further divided into three subcategories based on carbon content: steel with a low carbon content, steel with medium-carbon steel, and steel with high carbon content. Low-carbon steel, which has a carbon content of up to 0.25%, is known for being very weldable, formable, and ductile. It finds widespread use in construction, automotive manufacturing, and general engineering applications. Medium carbon steel, with a moderate carbon content (between 0.25% and 0.60%), offers increased strength and hardness compared to low carbon steel. It is commonly used for machinery, axles, and gears. High carbon steel, with a higher carbon content (between 0.60% and 2.0%), possesses exceptional hardness, wear resistance, and strength. It is utilized in specialized applications such as cutting tools, knives, and springs.

Another significant category is alloy steel, which contains iron along with additional alloying elements like manganese, chromium, nickel, or molybdenum. These elements contribute to improving specific characteristics of the steel, including its strength, hardness, resistance to corrosion, and ability to withstand high temperatures. Alloy steel can be further classified into various subcategories. One notable subcategory is stainless steel, which contains a minimum of 10.5% chromium. Stainless steel is highly resistant to corrosion and is widely used in kitchenware, medical equipment, construction, and automotive parts. Tool steel belongs to a distinct group of alloy steels that are intentionally formulated to exhibit exceptional toughness, wear resistance, and high hardness. It is employed in the production of cutting tools, molds, and dies. Additionally, high-strength low-alloy (HSLA) steel is an alloy steel with improved mechanical properties, commonly used in structural applications.

Stainless steel, though a subcategory of alloy steel, is often considered a separate category due to its distinct properties and widespread use. Its remarkable corrosion resistance is attributed to the chromium content, which is typically at least 10.5%. Stainless steel offers high strength, durability, and aesthetic appeal, making it suitable for various applications such as kitchen utensils, medical instruments, architectural structures, and automotive components. Stainless steel is further categorized into different grades, including austenitic, ferritic, martensitic, and duplex stainless steel, each with its own unique chemical composition and specific properties.

Tool steel is a distinct classification renowned for its exceptional hardness, wear resistance, and toughness. It finds wide application in the manufacturing of cutting tools, molds, dies, and various other tools that necessitate the capability to shape or cut materials. Tool steel is available in various grades tailored to meet specific application requirements. Examples include high-speed steel (HSS), which can withstand high temperatures during cutting operations, and cold work steel, which maintains its hardness at lower temperatures.

Lastly, specialty steel comprises a wide range of steel alloys designed for specific applications or industries. These steels are formulated to exhibit distinct characteristics like resistance to high temperatures, durability against wear, or specific magnetic properties. Heat-resistant steel is used in high-temperature environments, such as furnaces and power plants. Electrical steel, on the other hand, has low electrical resistance and is utilized in electrical appliances and transformers.

2.1.1 Welding of steel

Welding steel is a critical process that is used to join steel components and create robust structures. Fusion welding processes have long been employed for steel welding. Arc welding utilizes an electric arc formed between an electrode and the workpiece to accomplish the welding process. This arc generates intense heat, causing the metal to melt and form a weld pool. Steel welding often involves various arc welding techniques like shielded metal arc welding (SMAW), gas metal arc welding (GMAW), and gas tungsten arc welding (GTAW). These methods employ either consumable or non-consumable electrodes and inert gases to safeguard the weld against atmospheric impurities.

In contrast, solid-state welding methods present an alternative approach to joining steel. These methods do not rely on melting the base materials but instead utilize heat and pressure to

establish connections. Among these techniques, FSW has attracted considerable interest in recent times.

When compared to welding aluminum, steel welding presents unique challenges that initially discouraged researchers from exploring FSW as a viable option. In contrast to aluminum, steel has a higher melting point and requires higher temperatures to reach a molten state for effective welding. This poses a challenge for FSW, as the process relies on generating heat through frictional forces. Achieving the necessary plasticized state for stirring and joining steel using FSW becomes more difficult due to the elevated temperatures involved. Moreover, the increased heat input required for steel welding can lead to thermal distortion and metallurgical changes in the base material, which may compromise the quality and integrity of the weld. While initially overlooked by researchers for steel welding due to the mentioned challenges, FSW has gained recognition for its ability to produce high-quality welds in aluminum.

When it comes to the need for greener welding technologies in steel welding, it is essential to consider the environmental impact of traditional welding processes. Many conventional methods rely on consumable electrodes, shielding gases, and fluxes that can emit hazardous fumes and contribute to environmental pollution. Additionally, these processes often require a significant amount of energy, which is predominantly derived from non-renewable sources. To address these concerns, the industry has been actively exploring greener alternatives for steel welding.

2.1.1.1 Challenges in steel fusion welding

Fusion welding is a widely employed technique for joining steel components, but it is not immune to challenges and problems. One common problem associated with the fusion welding of steel is thermal distortion. During welding, the high heat leads to localized expansion and subsequent contraction upon cooling. This can lead to warping and distortion in the welded joint, affecting its dimensional accuracy and overall structural integrity.

Secondly, fusion welding of steel leads to the formation of solidification cracks. As the molten metal cools and solidifies, it undergoes a phase change that can result in the development of cracks. This issue is particularly prominent in steels containing high levels of sulfur and phosphorus, which are known to promote crack formation. Proper material selection and control of welding parameters are essential to mitigate the risk of solidification cracks.

Furthermore, it causes alterations in the microstructural composition and mechanical characteristics of the joined region. Due to the rapid temperature fluctuations during welding, undesirable phases such as brittle martensite or coarse grain structures may develop. These changes can significantly impact the weld's toughness and ductility. Heat-affected zones adjacent to the weld can also experience alterations in hardness and grain structure, affecting the overall performance of the welded component.

Additionally, the use of consumable electrodes, filler metals, and shielding gases in the fusion welding of steel presents its own set of challenges. Consumable electrodes require constant replacement, leading to increased material and operational costs. The selection and use of appropriate filler metals are critical to achieving desired weld properties and avoiding issues such as brittleness or inadequate strength. Shielding gases, if not properly controlled, can contribute to atmospheric pollution and require careful handling to ensure a high-quality weld. To address these challenges and enhance the fusion welding process for steel, researchers and industry professionals have explored various techniques and innovations.

2.1.1.2 Problems associated with welding steel using solid-state welding processes

Several solid-state welding methods are utilized for steel welding. However, most of these techniques have certain limitations that hinder their practical application. In this section, we will explore specific solid-state welding processes and their respective limitations:

Explosive welding: Explosive welding employs controlled explosive forces to join materials together. While it can be employed for welding steel, it is associated with several drawbacks. Achieving precise control over the explosive energy can be challenging. Additionally, explosive welding is typically suited for joining large-scale components and may not be suitable for intricate or small-scale applications. The high-pressure and high-velocity nature of the process can also result in surface irregularities and interfacial defects in the welded joint.

Ultrasonic welding: Ultrasonic welding employs high-frequency mechanical vibrations to generate heat and weld materials. Although commonly used for joining plastics and non-ferrous metals, its application to steel welding is limited due to certain constraints. Welding steel using ultrasonic methods often requires high power levels and longer welding times, making it less efficient compared to other welding techniques. Also, achieving consistent welds in thick steel plates can be challenging, and the weld quality can be influenced by the thickness of the steel being joined.

Magnetic pulse welding: This process utilizes magnetic forces for welding. While it offers advantages such as high joining speeds and the absence of consumables, it does have its drawbacks. Magnetic pulse welding is primarily employed for joining dissimilar materials, and its applicability to steel welding is limited because of the possibility of material blending and the creation of intermetallic compounds. The efficiency of the method also depends significantly on material characteristics and the design of the joint, which can influence the integrity and durability of the weld.

Diffusion welding: Diffusion welding achieves the fusion of surfaces by applying pressure and raising the temperature. Before welding, meticulous cleaning of the surfaces is essential. This technique does not involve any significant deformation or movement of the parts. It can join metals that are alike or different, with or without the use of an intermediary substance. Some research has been conducted on specific applications of diffusion welding. However, a major drawback of this process is the requirement for precise joint preparation, often necessitating extremely tight tolerances. The difficulty and expense of execution are further increased by the requirement for a vacuum or inert environment. Its procedure can be time-consuming, which limits its viability for a variety of real-world uses.

Cold welding: This technique achieves metal fusion by applying pressure at ambient temperature, causing considerable deformation during the welding process. This method depends on applying substantial pressure to thoroughly prepared metal surfaces to achieve the welding. While thin materials can be joined using simple tools that generate adequate pressure, welding thicker sections often requires the use of a large press to exert the necessary force. However, the practicality of using such equipment may be limited in certain situations.

Friction welding: It involves the alignment of two parts in an axial configuration for welding. The parts are brought into light contact and subjected to relative rotary motion. Increasing the applied axial force generates frictional heat at the interface, which enables the formation of a joint without melting the materials. The successful execution and evaluation of the welding process depend on effective process management and the appropriate selection of welding equipment. The parameters for friction welding are specific to each machine, making the process highly dependent on the equipment. Therefore, conducting a study on process parameters is not justifiable. One limitation of friction welding is that at least one part must have rotational symmetry in its cross-sectional area. This restriction narrows the applicability

of the process to specific scenarios. Typically, friction welding is primarily used for creating flat and angular butt joints, limiting its versatility in other types of joints or configurations.

2.2 FRICTION STIR WELDING PROCESS

Section 1.2 of the preceding chapter provided a detailed explanation of the fundamental idea behind FSW. The next sections provide a thorough analysis of the literature.

2.2.1 Different materials welded by FSW

Since its invention in 1991 (Thomas et al., 1991), FSW has transformed the field of materials engineering by facilitating the welding of a broad spectrum of engineering materials. Initially, extensive feasibility studies showcased the capabilities of the FSW process in welding various materials. Subsequently, rigorous research was undertaken, subjecting the FSW welds to comprehensive testing. FSW has emerged as an exceptionally adaptable technique, overcoming previous challenges, and enabling the joining of materials that were previously deemed difficult or even impossible using conventional methods. The extensive adoption and effective utilization of FSW can be credited to its remarkable capability to maintain the intrinsic characteristics of the materials, such as their strength, hardness, and resistance to corrosion.

2.2.1.1 Friction stir welding of aluminum and its alloys

Aluminum is widely used in sectors like marine, aerospace, etc due to its corrosion resistance, ductility, and other advantageous properties. However, the fusion welding of aluminum poses challenges (AWS Handbook,1996). Initial research on the FSW of aluminum was conducted by Rhodes et al. (1997). Subsequent studies focused on specific alloys and welding conditions. For instance, Liu et al. (1997) examined 6061-T6 aluminum alloy and found variations in hardness and grain size based on welding and rotational speeds.

Other researchers explored different aspects of FSW. Colligan et al. (1999) studied plastic deformation in the nugget zone, noting its dependence on the tool's pin. Sato et al observed microstructural changes in the FSW of Aluminum 6063, including coarse equalized grains, fine recrystallized grain, and reduced hardness due to density and precipitate dissolution. Jata et al. (2000) investigated the correlation between strain rate, temperature, and grain evolution within the nugget zone. They also assessed the effects of FSW on the characteristics of Aluminum welds, observing alterations in fatigue crack resistance.

Studies expanded to other aluminum alloys. Su et al. (2003) investigated aluminum 7xxx alloy and analyzed its microstructural properties. Charit et al. (2002) explored superplastic behavior in the heat-affected zone, resulting in increased strength. Lim et al. (2004) studied the FSW of 6xxx alloy, noting changes in weld ductility with tool rotation. Schmidt et al. (2006) conducted research on butt joints for 2024 T3, calculating material flow velocities using the shear layer.

Chen et al. (2006) examined how the initial state of the base metal influences the FSW of 2219 T6 and 2219 O aluminum alloys. They found better tensile strength efficiency in 2219 O and observed differences in microstructure between the weld nugget and TMAZSalari et al. (2014) conducted a study to examine how the geometry of the tool pin and shoulder affected FSW. Similarly, Scialpi et al. (2007) analyzed the correlation between the shoulder profile and grain size in the nugget zone. Elongovan et al. (2008) conducted a study on the influence of tool geometry on 6061 aluminum alloy. Their findings indicated that using a squared pin profile resulted in satisfactory welds and improved strength. Hwang et al. (2008) examined temperature distribution in FSW of Aluminum 6061 alloy, reporting consistent hardness on both sides of the weld. Rodrigues et al. (2009) compared conical shoulder and scroll shoulder tools, finding reduced elongation with the conical shoulder.

Palanivel et al. (2012) used different pin profiles and rotational speeds for FSW of 5083 and 6351 aluminum alloys, noting changes in material flow and resulting properties. Xu et al. (2009) investigated the temperature distribution profile of FSW in 2219 O aluminum alloy and observed complete recrystallization in the stir zone. Lu et al. (2011) analyzed the FSWed 2219 O, 6061, and 2219 aluminum alloys. The authors obtained an increased tensile strength with a decrement of strength with feed rate.

Costa et al. (2012) conducted a study on the FSW of 6082 aluminum alloy, examining the influence of defects, such as tunnels, on fatigue strength. Fahimpour et al. (2012) compared FSW with tungsten inert gas (TIG) welding, noting higher corrosion resistance in FSW joints but lower than the parent metal. Xu et al. (2012) compared fusion welding with FSW, finding better fatigue strength in fusion welded joints due to the hooking effect. Salari et al. (2014) examined pin profiles in lap joint FSW, emphasizing their significant influence on process performance. Guo et al. (2013) studied input characteristics in FSW of 6061 and 7075 aluminum alloys, noting the effectiveness of mixing and grain size variations based on the feed rate. Kranswoski et al. (2015) investigated the impact of backing plates and weld

21

configurations, observing enhanced micro-hardness and strength with the use of composite plates.

Recent research has extensively examined the influence of process parameters, including tool rotational speed, traverse speed, and axial force, on the microstructure and mechanical properties of FSWed joints in aluminum alloys. (Demirel et al., 2020; Ghiasvand et al., 2021; Dorbane et al., 2023).

2.2.1.2 Friction-stir welding of copper and its alloys

Copper is widely used in diverse industries owing to its outstanding characteristics, including high electrical conductivity, resistance to corrosion, and malleability. Nevertheless, the welding of copper using conventional fusion welding methods is challenging due to its high susceptibility to oxidation and rapid heat diffusion. In recent years, FSW has emerged as a promising technique for joining copper and its alloys. Initial research conducted by Lee et al. (2004) focused on copper FSW and demonstrated successful welds without any defects using tool steel with a rotational speed of 1250 rpm and a welding speed of 61 mm/min. Although a refined microstructure was achieved in the SZ, HAZ exhibited larger grain sizes than the base material, decreasing the strength of the transverse joints.

Subsequent investigations carried out by Xie et al. (2007) and Sakthivel & Mukhopadhyay (2007) demonstrated the formation of fine-grained structures in the stir zone while encountering challenges in controlling the grain size in the HAZ. Further exploration of FSW in the context of joining copper canisters was conducted by Cederqvist & Oberg (2008) and Muller et al. (2006). Lui et al. (2009) specifically examined the influence of tool rotation speed on the microstructure and mechanical properties. Additionally, researchers such as Shen et al. (2010), Sun & Fuji (2010), and Teimournezhad & Masoumi (2010) have investigated the impact of welding parameters on the microstructure and mechanical properties of FSWed joints. Walley et al. (2010) focused on the post-processing effects on the creep behavior and microstructure of rolled Cu-8cr-4Nb, revealing no degradation of creep properties following the FSW process.

In addition, the literature includes studies on the FSW of brass and other copper alloys. Park et al. (2004) examined FSWed 60-40 brass and observed the formation of extremely fine grains in the stir zone, along with elongated grains in the TMAZ. Other researchers, such as Meran

(2006), Cam et al. (2008), and Xei et al. (2008), have evaluated the mechanical properties of various Cu-Zn alloys.

Khodaverdizadeh et al. (2012) examined the work-hardening behavior of FSWed copper alloys. The study focused on analyzing the resulting mechanical properties and metallurgical effects. It was observed that the grain size in the HAZ decreased with the increase in rotational speed and the decrease in welding speed.

Lin et al. (2014) conducted a comparative study where they produced friction stir-welded (FSW) joints of copper plates and compared them with tungsten inert gas (TIG) welding. The FSW joints exhibited a 13% higher efficiency compared to TIG welding. Azizi et al. (2016) performed FSW on pure copper plates with a thickness of 10 mm. The experiment involved a fixed 700 rpm rotational speed and variable traverse speeds ranging from 50 to 200 mm/min, using a square pin profile tool. Thermocouples were used to monitor the thermal cycles and peak temperatures during the welding process. The study found that faster traverse speeds lead to decreased heat input, resulting in the creation of finer grains in the joints. The ultimate tensile strength of the joints first rose with increasing traverse speed, reaching a maximum value before decreasing.

Several research studies have focused on investigating the FSW of copper, aiming to optimize process parameters for effective material joining (Kumar et al., 2012; Nagamalleswara Rao et al., 2017; Rzaev et al., 2019; Boitsov et al., 2020).

In a recent study conducted by Wang et al. (2023), the issue of precipitate coarsening and its impact on joint strength in Cu–Cr–Zr alloys during the welding process was addressed. The studies suggested strategies to reduce the welding temperature below the aging temperature to mitigate precipitate coarsening. The results revealed the difficulty in achieving a lower FSW temperature without using coolants. By softening the Cu–Cr–Zr alloys to a supersaturated solid solution state before FSW, the peak temperature during FSW was reduced to a level close to the aging temperature of the alloy. Consequently, high joint strength equivalent to the peak-aged base metal was achieved. Moreover, the FSW zone exhibited a higher electrical conductivity compared to the peak-aged base material.

2.2.1.3 Friction stir welding of magnesium alloys

Several researchers have investigated FSWed magnesium alloys, such as AZ31B and AZ91D. Esparza et al. (2002) conducted a study on the microstructure of AZ31B alloy using TEM and

SEM and observed that the microstructural changes during FSW of magnesium alloys resemble other materials. Lee et al. (2003) welded AZ91D alloy and observed the complete replacement of the original microstructure by finer grains, leading to improved mechanical properties. Johnson & Threadgrill (2016) FSWed various magnesium alloys (AM50, AM60, AZ31) and determined the critical range of process parameters required for successful welding. Failure to meet these parameters resulted in unsuccessful welding. Zhang et al. (2006) proposed a mathematical model to obtain defect-free joints in the FSW of magnesium alloys. Park et al. (2003) studied the microstructural evolution during FSW of AZ91D alloy and investigated the effect of welding on the Hall-Petch relationship. The study revealed that the impact of grain size on hardness was less important in conventional and rapidly solidified AZ91 alloys.

Esparza et al. (2003) and Zhang et al. (2005) conducted FSW experiments on magnesium alloy AM60. They reported that the microstructural changes observed in FSW of magnesium alloys exhibit similarities to those observed in other materials. Zhang et al. (2005) also welded Mg-Al-Cu alloy and found that the intermetallic compound in the parent material remained undissolved during welding, transforming into fine particles dispersed within the dynamically recrystallized magnesium grains.

Aydin & Bulut (2010), Chowdhury et al. (2010), Yu et al. (2010), Cao & Jahazi (2011), and Singh et al. (2018) conducted studies that yielded consistent results regarding the strength ratio between the joint and the parent material. They concluded that this ratio was influenced by the presence of flaws during FSW, while the effect of process parameters on weld integrity was found to be minimal.

Singh & Kuriachen (2022) recently conducted a comprehensive investigation on the microstructural and mechanical behavior of AZ31 magnesium alloy joined through FSW. The study utilized various characterization techniques, such as EBSD, SEM, XRD, and optical microscopy, to analyze the weld integrity. Mechanical properties were assessed through tensile, microhardness, and bending tests. The findings revealed the presence of twins and second-phase particles induced during the welding process. The intermetallic compounds (IMCs) formation was influenced by both grain orientations and boundaries. Higher travel speeds resulted in a smaller average grain size within the stirred zone, and the TMAZ also experienced grain refinement. Bending tests indicated maximum and minimum bending stresses, with fracture occurring in HAZ and parent material regions, which exhibited lower hardness values.

The weld strength improved with increased travel speed due to reduced recrystallization in the stirred zone resulting from lower heat inputs.

2.2.1.4 Friction stir welding of other materials

FSW has been explored for joining various materials such as titanium, brass, and plastics. Lee et al. (2005) attempted to join high-strength titanium alloy plates using FSW. They observed the formation of deformational twins and varying nugget zone density, with higher density at the top and decreasing towards the bottom. The tensile strength of the weld nugget was less compared to the parent metal, and fractures were predominantly observed in the HAZ. Another investigation by Zhang et al. (2008) focused on the FSW of titanium alloy plates and examined the microstructure of the weld. In the nugget zone and the HAZ, respectively, there was a formation of lamellar and bimodal structures. It was observed that the HAZ had lower hardness and tensile strength than the parent material.

Fractures were mostly seen in the HAZ, and the weld nugget's tensile strength was determined to be lower than that of the parent metal. Another investigation by Zhang et al. (2008) focused on the FSW of titanium alloy plates and examined the microstructure of the weld. They identified a lamellar structure in the nugget zone and a bimodal structure in the HAZ. The tensile strength and hardness of the HAZ were found to be inferior to the parent metal.

In another study, Panneerselvam & Lenin (2014), joined nylon sheets using FSW and modeled the effect of tool direction. They observed that using left-hand threaded pin profiles with counter-clockwise rotation and right-hand threaded pin profiles with clockwise rotation produced better weld quality, whereas other configurations resulted in the formation of blow-holes and large cavities.

Schneider et al. (2015) conducted a study where nickel-based alloys were welded using FSW, resulting in a defect-free process compared to fusion welding. The grain size was significantly decreased by approximately 85%, but the tensile strength was inferior to the base metal.

Küçükömeroğlu et al. (2016) conducted a study to examine the possibility of utilizing FSW for the joining of 9 mm thick cast Nickel-Aluminum Bronze (NAB) alloy. The results showed that all the produced joints exhibited a refined grain structure with equiaxed fine grains. These alterations in the microstructure resulted in increased proof stress values over the base material. In the research, approximately half of the samples demonstrated enhanced tensile strength

relative to the base plate, while the remaining half experienced a reduced tensile strength due to the presence of weld flaws, specifically cold bonding and/or tunnel defect.

In a recent study, Bilici et al. (2022) examined the influence of input parameters on the welding defects of FSWed high-density polyethylene (HDPE) sheets. The study primarily aims to identify the welding defects occurring at the joints, investigate their causes, and explore prevention methods. Macrostructure analysis is employed to assess welding quality, defects, and performance, while tensile strength measurements are conducted on selected joints.

2.3 FRICTION STIR WELDING OF STEEL

While extensive research has been conducted on aluminum and its alloys, the study of steels in the context of FSW has been relatively limited. The initial exploration of FSW for steel was documented by Thomas et al. (1998). Additionally, 'The Welding Institute' conducted a feasibility study in 1999 (Thomas et al.,1999), which examined the process's viability while taking into consideration the impact of tool wear.

2.3.1 Friction stir welding of carbon and alloy steels

FSW has been utilized on different steel types, but the extent of research in this area is comparatively restricted when compared to its application on aluminum and its alloys. One of the earliest works on FSW of steels was reported by Lienert et al. (2003) wherein successfully produced defect-free welds on 0.25-inch-thick mild steel (AISI 1018). Molybdenum and tungsten-based alloys were employed as tool materials. The study demonstrated tool wear during welding and emphasized the need to address this issue by refining tool geometry. Furthermore, the research suggested that mild steel can be FSWed with intact tensile properties.

Ueji et al. (2006) utilized low-carbon steel for the evaluation of microstructure transformation and its weld integrity. The study incorporated a martensite process to prepare the base metal, subjecting it to numerous thermo-mechanical workings to produce 1.5 mm thick sheets with ultrafine grains. Tungsten carbide was utilized as the tool material. Although the study extensively employed TEM, mechanical testing of the welds was not carried out.

A study was also conducted on FSWed 1012 and 1035 carbon steel with a plate thickness of 1.6 mm by Fuji et al. (2006). Additionally, the welding of ultra-low carbon (20 ppm carbon) interstitial-free steel was investigated by Fuji et al. (2006). Load-controlled FSW was utilized for the experimentation. The weld integrity was studied particularly to analyze the effect of the welding speed on the UTS of the welds.

Miles et al. (2006) performed welding on dual-phase steel (DP 590) containing less than 0.1% carbon and 10-15% martensite distributed throughout the ferrite matrix having a thickness of 1.6 mm using a polycrystalline cubic boron nitride (PCBN) tool. The study revealed that the formability of the FSWed joints was similar to that of the laser welds.

Gan et al. (2007) focused on welding high-strength pipe steel (L80) and evaluated the performance of different tool materials. Potassium-doped commercially pure tungsten was employed as the tool material, and it was observed to experience significant wear during the welding operation. Based on finite element analysis, they suggested that a tool having tungsten with 25% rhenium would be more effective.

Konkol and Mruczek (2007) conducted a study to examine the applicability of FSW for high-strength low-alloy steel (HSLA-65). They performed welding on 6 mm thick plates using two different types of tool materials: a tungsten-rhenium alloy pin and a Mo-TMZ (molybdenum-1%, titanium-0.3%, and zirconium-0.15% carbon) tool shoulder. The study revealed significant deformation in the tool and concluded that the tool material used was not suitable. The authors also assessed tool wear, weld distortion, and mechanical properties. Barnes et al. (2008) conducted FSW on rolled, quenched, and tempered steel (RQT-701) with a carbon content of 0.14%. The plate thickness was 12.5 mm, and a tungsten-rhenium alloy was employed for welding. The study included microstructural examinations and residual strain measurements. In contrast to the findings of Konkol & Mruczek (2007) the tungsten-rhenium alloy tool was found to be suitable, likely due to its composition containing 25% rhenium.

Cui et al. (2007) conducted butt welding experiments on 1.6 mm thick plates made of 0.72% carbon steel (AISI 1070). Tungsten carbide was used as the tool material in experiments conducted on a load-controlled FSW. The findings of the study indicated that welds produced using high-carbon steel exhibited superior joint strength compared to the base material.

Sato et al. (2007) successfully conducted FSWed ultra-high carbon steel with a thickness of 2.3 mm, utilizing the PCBN tool. Although fusion welding techniques are not effective for joining this steel due to its poor weldability, FSW has proven to be a successful method for achieving welds. Chung et al. (2009) examined the welding process of high-carbon steel with a carbon content of 0.85% at temperatures both above and below the eutectoid temperature. The study concluded that conducting the welding process above the eutectoid temperature led to the formation of a microstructure comprised entirely of martensite. Conversely, welding below the eutectoid temperature resulted in a combination of ferrite and martensite. When welding below

the eutectoid temperature, the weld integrity was found to be similar. In another work, Chung et al. (2010) performed FSW on high-carbon steel (AISI 1080) and concluded that welds exhibited excellent toughness when welding below the eutectoid temperature.

Miles et al. (2009) conducted a study on the impact of FSW conditions on high-strength and ultra-high-strength steels used in automotive applications. They observed that adjusting the process parameters, specifically a welding speed of 100 mm/min and a tool rotation of 300-350 rpm, resulted in the desired weld integrity. Ghosh et al. (2010) analyzed the microstructural changes in friction stir lap-welded high-strength M190 steel using a hybrid carbide tool material and evaluated parameters such as microhardness and grain size.

Cho et al. (2012) conducted FSW studies on API X100, 10 mm thick, which were successfully joined by a PCBN tool. The study primarily focuses on the evaluation of the feasibility of FSW for joining API X100 steel. The researchers examined the influence of the welding process on weld integrity. By assessing the quality of the resulting welds, the study provided valuable insights into the potential application of FSW as an efficient method for API X100 steel. Santos et al. (2010) specifically investigated the fracture toughness of X80 steel plates with a thickness of 12 mm. Unlike the study conducted by Gan et al. (2007), which focused solely on single-pass welding without testing the mechanical properties, Santos et al. (2010) emphasized the evaluation of mechanical properties. The paper concluded that input parameters significantly affected fracture toughness, and optimal parameters for achieving the best fracture toughness were determined. The authors observed dynamic recrystallization and subsequent phase transformation in the microstructure, with bainitic ferrites observed in SZ. In another study on FSW of medium carbon steel, Ghosh et al. (2012) analyzed the influence of input parameters on weld integrity. The findings indicated that the weld's stir zone exhibited higher strength than the parent material, whereas the HAZ displayed the lowest strength.

Azevedo et al. (2016) addressed the research gaps in the FSW of ship buildings. The study focused on the analysis of GL-A36 steel plates coated with a zinc-based primer. The objective was to investigate the impact of various characteristics on weld integrity. Through their analysis, the authors provided valuable insights into the effects of different factors on the quality and performance of FSW in shipbuilding applications.

Miura et al. (2016) performed a research investigation on the application of FSW to join low-carbon Cr-Mo steel, utilizing a tool made of tungsten carbide. They observed the microstructure of the welds and provided insights into the underlying mechanisms of plastic deformation and

strain accumulation in low-carbon Cr-Mo Steel during FSW. Their findings contribute to the understanding of the metallurgical processes occurring during FSW of this specific steel alloy, providing valuable information for optimizing welding parameters and improving the weld quality.

Husain et al. (2017) conducted FSW on C-Mn steel considering tool rotation speeds as a process parameter considering Traverse speed as a constant input factor. The objective of the research was to examine how the microstructure and texture of the weld nugget are affected by thermal conditions and deformation. The analysis revealed that the weld nugget comprised ferrite, bainite/ Widmanstatten ferrite, and exhibited varying grain sizes corresponding to the peak temperature. The development of a fine equiaxed grain structure was responsible for the continuous dynamic recrystallization.

In a recent study, Wang et al. (2021) investigated the weld integrity of FSWed weathering mild steel. The mechanical properties are evaluated using digital image correlation (DIC). The results demonstrate that defect-free joints are achieved for both SMA490-AW and SPA-H materials, with no observed softening in the HAZ. In the study conducted by Ahmed et al. (2022), FSW was carried out on mild steel samples that had a thickness of 5 mm. The research utilized a constant rotational speed of 500 rpm and two different welding speeds, namely 20 mm/min and 50 mm/min. Additionally, a tool tilt angle of 3° was employed during the welding process. The study primarily focuses on evaluating the effects of process parameters on the resulting weld characteristics and properties. The study aimed to gain insights into the optimal machine setting to achieve high-quality mild steel welds.

Korkmaz & Meran (2023) investigated the weld integrity and microstructural characterization of XPF800 steel, using a tungsten carbide (WC) tool. The results indicate an increase in strength, as evidenced by a maximum hardness value of approximately 350 HV. On the other hand, HAZ undergoes a reduction in strength and hardness due to the occurrence of softening. The tensile strength and hardness of the HAZ decrease by approximately 8% and 20%, respectively, compared to the base material.

2.3.2 Friction stir welding of stainless steel

Parallel to the beginning of the carbon steel welding process, FSW for stainless steel was explored. This section explores the examination of various stainless-steel grades within the scope of FSW research.

Reynolds et al. (2003) conducted initial research on FSW of stainless steel using 304L grade. The study involved butt welding 3.2 mm thick plates with a tool steel backing plate. The research involved the utilization of optical microscopy, tensile testing, and residual stress measurements. The study primarily investigated the grain size of 304 stainless steel welds using optical microscopy.

Park et al. (2003) analyzed FSWed 304 stainless steel using a PCBN tool. They conducted bead-on-plate welding on a 6 mm thick plate with a 4.75 mm long tool pin. The authors investigated the rapid formation of the sigma phase during FSW using TEM and optical microscopy. Additionally, they examined the corrosion behavior of the weld under similar conditions (Park et al., 2004). Two studies conducted by Park et al. were dedicated to examining the progression of microstructure. They examined the sigma phase on the advancing side comparing them to gas tungsten arc welding (GTAW).

Sato et al. (2005) welded duplex stainless steel using a PCBN tool. The plate thickness was 4 mm, and Argon shrouding was employed during welding to prevent oxidation. The authors studied the microstructural evolution and conducted tensile testing of the base metal. A similar study on duplex stainless steel was performed by Saeid et al. (2008) focusing on the effect of welding speed on weld integrity. The plate thickness in this study was 2 mm, and a tungsten carbide tool was used.

Klingensmith et al. (2005), employed FSW to join super austenitic stainless steel. The researchers performed double-sided welding on plates measuring 6.35 mm in thickness. They utilized a tungsten-based tool material of undisclosed composition. An extensive analysis of the microstructure was carried out utilizing advanced microscopy techniques.

Mathon et al. (2009) employed a PCBN tool to perform FSW on ODS plates,1.3 mm thick. The use of the PCBN tool allowed for the effective joining of the ODS steel, and the study aimed to explore the specific details and outcomes of this welding process. Legendre et al. (2009) performed FSW on the same material and investigated the microstructural characteristics. Chen et al. (2010) performed a comprehensive study on ODS, examining the microstructural evolution during welding using EBSD, TEM, and SEM. Miyano et al. (2011) analyzed the weld integrity of hydrogen-containing austenitic stainless steel with a Si_3N_4 tool. They found that the hardness and tensile strength of the welds were superior to the base metal. The authors also identified the optimal process parameters based on thermal profile measurements.

AISI 430 ferritic stainless steel was investigated in the study by Bilgin & Meran (2011). The study utilized a tungsten carbide tool to friction stir weld two plates with a thickness of 3 mm, employing different levels of process parameters. The study's findings indicated that FSW could effectively address the issue of sigma phase formation, a challenge commonly encountered in fusion welding techniques.

Han et al. (2014) examined the FSW of stainless-steel plates for mechanical testing and found that the welds exhibit better weld integrity over the base material. Zhou et al. (2015) conducted a study that aimed at mitigating the keyhole formation issue in FSW. The study focused on the FSW of 316L stainless steel. The researchers noted the development of a fine-grained microstructure within the weld nugget, while also detecting void defects on the lower surface of the weld.

Li et al. (2017) conducted a study on the changes in microstructure and mechanical properties of friction stir-welded super-austenitic stainless steel (S32654) using a tungsten-rhenium tool. The study revealed band structures containing tungsten and rhenium resulted in the wear of the tool probe. The hardness and strength improved, but the plastic deformation capacity of the joints was reduced.

Ramesh et al. (2019) joined 3-mm-thick plates made of 316L austenitic stainless steel (ASS) using FSW. The research aimed to analyze the relationship between changes in microstructure and variations in mechanical properties, considering different welding conditions. A tungsten alloy (W-Re) tool was used for the welding process. Successful joints were achieved within a range of traverse speeds (45-85 mm/min). Various zones were observed across the joint line.

Johnson & Murugan (2020) welded 3 mm-thick AISI 321 stainless steel sheets using FSW. The welding process involved joining rectangular sheets with specific parameters. The primary objective of the research was to establish a correlation between the properties of the weld joint. The study aimed to investigate how the chosen process parameters influenced the microstructural and mechanical characteristics of the welded AISI 321 stainless steel sheets. The researchers focused on analyzing the resulting weld joint properties, such as the microstructure, hardness, tensile strength, and impact toughness. In a recent study, Hammood et al. (2023) welded 2101 lean duplex stainless steel (LDSS) using FSW. The welds were analyzed to examine changes in crystalline phases. The study reveals that the rotational speed was found to have a positive linear correlation with corrosion resistance, indicating a

connection between the balanced microstructure or grain refinement and improved corrosion resistance.

Gaddam et al. (2023) present a novel approach to joining 12 mm thick N40 plates using the double-sided FSW technique. The objective is to obtain weld joints that possess favorable qualities, such as a reduced amount of δ ferrite (an unfavorable ferromagnetic phase), high joint efficiency, prevention of sensitization and hardness reduction in the HAZ, and minimal loss of nitrogen from the weld nugget. The findings reveal that the double-sided FSW approach outperforms fusion welding methods, yielding superior weldments suitable for application in tokamak devices.

2.3.3   Welding dissimilar metals with steel

Welding researchers have investigated the feasibility of combining steel with different alloys like aluminum, magnesium, and copper. FSW is widely utilized in the welding of aluminum and steel, creating numerous dissimilar joints. (Tanaka et al., 2009; Chen et al., 2008; Kimapong et al., 2004; Watanabe et al., 2006; Chen, 2009; Chen et al., 2008).

Various researchers have investigated the welding of aluminum and carbon steel, along with stainless steel and aluminum. (Uzun et al., 2005; Lee et al., 2006; Ghosh et al., 2012; Habibnia et al., 2015; Yazdipour and Heidarzadeh, 2016; Zandsalimi et al., 2019; Beygi et al., 2022; Datta et al., 2023; Newishy et al., 2023). Fusion welding of steel and magnesium alloys has proven challenging, but FSW has provided a viable solution. (Schneider et al., 2011; Venkateswaran et al., 2012; Singh et al., 2019; Meng et al., 2021; Khalaf et al., 2023)

Many studies have even focused on joining steel with titanium, where the process parameters were adjusted to achieve successful joint formation (Fazel et al., 2010; Gao et al., 2015; Li et al., 2019). These investigations have served as preliminary studies, shedding light on the optimal process parameters required for producing high-quality welds without defects.

2.4 GAPS IN LITERATURE

While research on FSW of steel continues to pose challenges, the majority of studies conducted thus far have focused on demonstrating the feasibility of the process rather than addressing its practical applications. After reviewing the existing literature, several gaps in knowledge have been identified:

- **Insufficient studies on tool material evaluation:** There is a scarcity of research that explores the evaluation of different tool materials for welding steel using FSW. Understanding the impact of tool material on the welding process and resulting joint quality is essential for enhancing the overall efficiency and effectiveness of the technique.

- **Limited information on defects in FSWed steel:** The literature provides limited details regarding the specific defects that may occur during the process. Identifying and comprehending these defects is crucial for developing strategies to mitigate their occurrence and improve the overall weld quality.

- **Inadequate investigation of welding parameter effects on weld integrity:** A limited number of studies have focused on investigating the effects of varying input parameters on weld integrity. It is essential to understand how changes in parameters impact the weld integrity.

- **Limited reporting of defect-free process parameters:** Few researchers have reported a comprehensive range of process parameters that yield defect-free welds in steel but the underlying rationale for selecting these specific parameters has not been sufficiently explained. A deeper understanding of the relationships between process parameters and weld quality is important to establish the guidelines and optimize the process.

2.5 PROBLEM STATEMENT AND OBJECTIVE OF THE RESEARCH WORK

The research aims to address the current research gaps and challenges in the field of FSW of carbon steel (AISI 1018) by conducting a comprehensive investigation into the application of this technique. The problem is formulated as follows:

 "SOME INVESTIGATIONS IN FRICTION STIR WELDING OF CARBON STEEL"

The present research problem aims to accomplish the following objectives:

- To develop a procedure to obtain sound friction stir weld for carbon steel (AISI 1018).

The objective is to develop a robust procedure that can consistently yield high-quality friction stir-welded carbon steel. This entails addressing the existing issues and limitations associated with the process, such as the occurrence of defects and the need for process optimization.

2.6 METHODOLOGY TO ACHIEVE THE OBJECTIVE

To achieve the objective of developing a procedure to obtain sound friction stir welds for carbon steel (AISI 1018), the following methodology with the following steps was employed:

- **Tool Material and profile selection:** The initial stage involved the meticulous tool material selection and configuration for FSW of steel joints. This entailed a thorough evaluation of various tool materials, taking into account their characteristics including wear resistance, thermal conductivity, and longevity. The selection was based on the specific requirements of welding carbon steel and the desired weld quality. The tool profile, including the geometry and dimensions, was determined to ensure optimal material flow and joint formation.

- **Process parameter selection and range determination:** The next step was to select the appropriate process parameters. The ranges for these parameters were determined through systematic experiments and analysis. The objective was to identify the parameter ranges that resulted in defect-free welds and desired weld characteristics.

- **Investigation of process parameter effects:** Once the process parameters and their ranges were established, the effect of these parameters on the weld integrity was thoroughly investigated. This involved conducting experiments with different combinations of parameters within the determined ranges. The resulting welds were evaluated for their quality, including factors such as defect formation, microstructural properties, mechanical properties, and joint strength. The objective was to assess the impact of each parameter on weld quality and determine the most effective parameter configurations for obtaining defect-free friction stir welds in carbon steel.

CHAPTER 3   EXPERIMENTAL SETUP

3.1 INTRODUCTION

The high strength and elevated softening temperature of steel pose significant challenges when it comes to FSW, making it a complex undertaking. Conducting experiments on steel necessitates the utilization of a well-designed setup capable of effectively handling the entire experimental process. The experimental setup must encompass a robust machine capable of withstanding the substantial vertical forces and providing ample torque for the welding operation. Since the plates being welded will experience significant forces, a secure fixture is essential to firmly hold them in position.

FSW generates elevated temperatures, which can adversely impact the spindle of the machine and potentially harm the lubrication system of the spindle bearing. To safeguard the machine, it is imperative to insulate the tool from the machine spindle. A suitable tool holder is necessary to securely hold the tool in place and prevent slippage when applying torque.

Selecting the appropriate tool material is of utmost importance in steel FSW, as it directly impacts tool performance and durability. To ensure effective experimentation, it is essential to select a suitable tool material that provides optimal results and a sufficient lifespan. Extensive quantities of tools are needed for trial runs, necessitating a grinding facility to swiftly produce tools with the necessary dimensions.

3.2 MACHINE TOOL SELECTED FOR EXPERIMENTATION

The dedicated design of the Friction stir welding equipment enables the smooth execution of the process through the provision of essential tools and operational controls. It consists of several key components that work together to create a stable and controlled welding environment. One of the critical components is the spindle, which houses the rotating tool used for stirring and joining the steel materials.

The experiments were performed using a Friction stir welding apparatus located at Delhi Technological University, Delhi. Figure 3.1 illustrates the appearance of the Friction stir welding machine. Detailed information regarding the specifications of the machine can be found in Table 3.1.
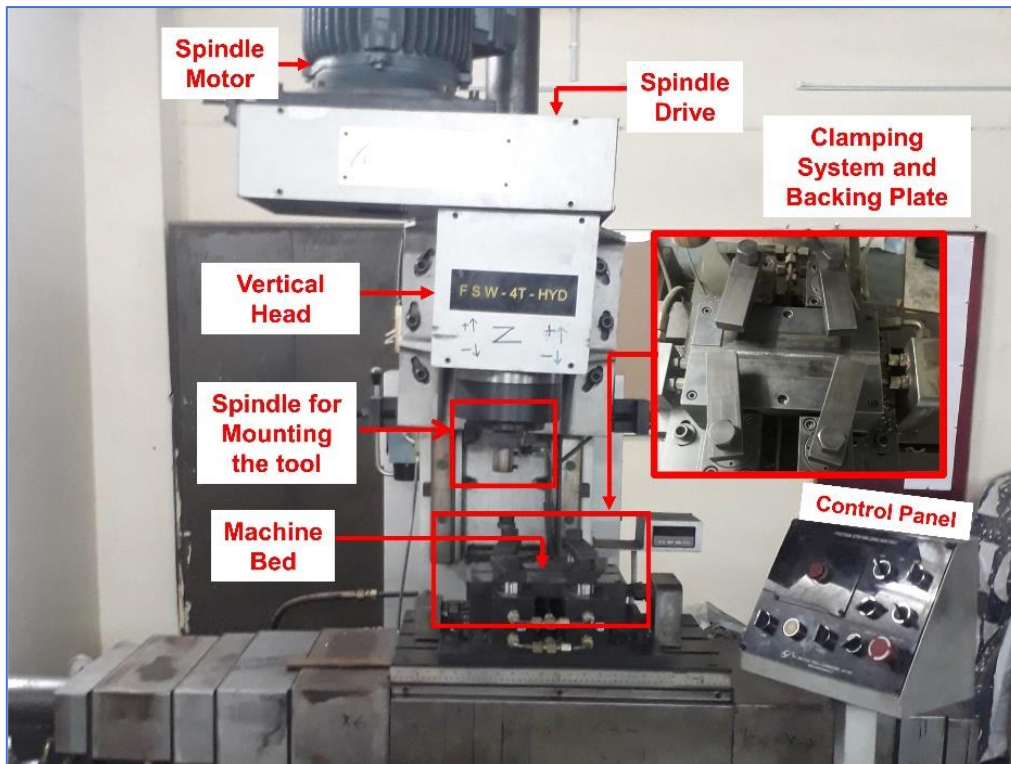
Figure 3.1: FSW setup employed in the present study

One of the primary reasons for using the FSW machine for welding steel is its ability to produce welds with superior mechanical properties. Conventional fusion welding techniques, like arc welding, commonly involve the application of excessive heat input, leading to the development of coarse grains and heat-affected regions. FSW, on the other hand, operates at a lower temperature, minimizing the formation of these undesirable features and ensuring excellent weld quality (AWS Handbook,1996). The machine's precise control over the welding parameters further enhances the quality and consistency of the welds.

Another reason for using the FSW machine is its versatility in joining various types of steel alloys. Steel materials with different compositions and properties can be effectively joined using FSW, including high-strength steels, stainless steels, and even dissimilar steel combinations. This versatility makes the FSW machine an attractive option for industries that require the welding of steel components with diverse applications, such as automotive, aerospace, and construction.

Table 3.1: Specification of the FSW machine employed in the present study

Spindle motor	Rated Power: 11 kW
	Maximum Speed: 1440 rpm
	Voltage: 440 V
	Phase: 3-phase
	Drive Type: AC Drive
	Mounting: Flange mount (STARK).
Spindle housing tilting	Range of adjustable angles: -5° to 5°
Spindle pulley type	Timing Pulley
Z-axis	Stroke Length: 300 mm
	Feed Rate: 0-2000 mm/min
	Range of thrust capacity: Adjustable from a minimum of 400 Kgf to a maximum of 4000 Kgf, with customizable increments.
	Feedback: Load cells with a capacity of 5000 Kg and a resolution of 1 kg are used to measure feed force.
X-axis	Stroke Length: 600 mm
	Feed Rate: 0-5000 mm/min
	Thrust capacity range: Adjustable from a minimum of 250 Kgf to a maximum of 2500 Kgf, with 50 Kgf increments.
Y-axis	Stroke Length: 200 mm
Table	Size: 600 mm x 400 mm
	T-Slot Dimensions: 18 x 3 mm
Tool Holder	Type: ISO 40 Taper-Side lock holder
Controller	The machine utilizes a PC-based control system.

Efficiency and productivity are also significant factors contributing to the preference for FSW in steel welding applications. The process does not require the use of consumables like filler materials or shielding gases. This eliminates the need for additional material preparation and reduces the overall costs associated with welding operations. Furthermore, FSW offers a high welding speed, that allows rapid production of welded steel components. The machine's ability to consistently deliver high-quality welds also minimizes the need for post-welding inspections and rework, further optimizing the efficiency of the welding process.

Its robust construction and durability are additional factors that make it an ideal choice for welding steel. Steel materials are known for their high hardness and resistance to wear, which can pose challenges to conventional welding equipment. The FSW machine, constructed with robust components, including hardened ceramics for the welding tool, can withstand the demands of welding steel materials over extended periods. Moreover, the machine's stability and precision contribute to its long-term reliability and ensure consistent welding results.

3.3 SELECTION OF TOOL MATERIAL

The careful choice of suitable tool material is crucial when it comes to the FSW of steel. The tool operates under harsh conditions of temperature and forces, necessitating a material capable of withstanding such demands. Specific material characteristics significantly impact the suitability of the chosen tool material. These properties include strength, hardness, wear resistance, fatigue resistance, thermal conductivity, toughness, and chemical stability. By considering these factors, the selection of the tool material can be made in accordance with the specific demands of the FSW procedure, guaranteeing excellent functionality and longevity.

The majority of steels exhibit a yield strength exceeding 250 MPa and can reach as high as 700 MPa. Moreover, they do not undergo significant softening below 1000 °C, which presents significant challenges in selecting an appropriate material for the tool. The chosen tool material must possess the capability to withstand elevated temperatures without undergoing any chemical alterations, either independently or due to atmospheric reactions. Nevertheless, the primary concern lies in ensuring that the tool material maintains its mechanical characteristics, including strength, hardness, toughness, and fatigue resistance, even when subjected to high temperatures during the welding process. The tool material must be carefully selected to meet these requirements and withstand the demanding conditions of FSW.

3.3.1 Potential tool materials for FSW of steel

The materials that have been tried by researchers for welding steel are tabulated in Table 3.2. The types of materials that have proven results to satisfactory weld steel using the FSW process are refractory metals and super abrasive tools.

Table 3.2: Overview of the tool material selection for steel FSW

Welding performed on the base metal	Joint type	Thickness	Tool material	Reference
AISI 1018	Butt joint	0.25 inch	Tungsten based alloys	(Lienert et al., 2003b)
Low carbon steel	Butt joint	1.5 mm	Tungsten Carbide	(Ueji et al., 2006)
DP590 steel	Butt Joint	1.5 mm	PCBN	(Miles et al., 2006)
L80 steel	Lap Joint	-	Tungsten Rhenium alloy and Potassium-doped pure alloy	(Gan et al., 2007)
AISI 1012 and AISI 1035	Butt joint	1.6 mm	Tungsten carbide	(Fujii et al., 2006)
RQT-701	Butt joint	12.5 mm	Tungsten-rhenium alloy	(Barnes et al., 2008)
High-strength steel and ultrahigh-strength steel	Butt joint	--	PCBN	(Miles et al., 2009)
M190 steel	Butt joint	1 mm	Hybrid carbide	(Ghosh et al., 2010)
304 stainless steels	Butt joint	6 mm	PCBN	(Park et al., 2003)
Super austenitic stainless steel	Butt joint	6.35 mm	Tungsten carbide	(Sato et al., 2005)
Duplex stainless steel	Butt joint	4 mm	PCBN	(Klingensmith et al., 2005)
Oxide-dispersed strengthened (ODS) Steel	Butt joint	--	PCBN	(Legendre et al., 2009)
AISI 304 austenitic stainless steel	Butt Welded	2.95 mm	Tungsten carbide with cobalt	(Siddiquee & Pandey, 2014)
DH36 steel plates.	Butt Welded	300 mm × 100 mm × 4 mm.	WC-6 weight percent cobalt and WC-10 weight percent cobalt	(Tiwari et al., 2019)
SC45 steel	Butt welded	2.4 mm thick	WC-12Co	(Avettand-Fènoël et al., 2019)

3.3.1.1 Refractory metals

This category of tool material includes tungsten carbide, tungsten carbide cobalt alloy, silicon nitride, and tungsten lanthanide (Muhammad et al., 2018). Table 3.3 presents the characteristics of refractory tool materials.

Table 3.3: Properties of refractory materials

Tool material	Property			
	Melting point (°C)	Boiling point (°C)	Young's modulus (GPa)	Vicker's hardness (MPa)
Tungsten	3422	5555	411	3430
Rhenium	3200	5560	460	2500
Molybdenum	2625	4640	330	1530

In the early phases of FSW, tungsten, and molybdenum were employed because of their favorable attributes, including excellent hot hardness, resistance to creep, and high tensile strength. However, these materials had a significant drawback of tool fracture occurring during the plunging stage (Lienert et al., 2003). The brittle fracture of the tool resulted from plunging at room temperature, necessitating the preheating of the workpiece material above the ductile-brittle transition temperature before the initial plunge of the tool. Subsequently, a tungsten-rhenium tool was introduced for FSW of steel, which exhibited a reduced ductile to the brittle transition temperature. This eliminated the need for preheating the tool when using the tungsten-rhenium alloy. Nonetheless, the addition of rhenium led to a decrease in tool wear resistance, posing a challenge in terms of tool wear. This resulted in the inclusion of tungsten in the weld, impacting the mechanical properties. In recent times, refractory materials such as tungsten carbide and tungsten carbide with cobalt have gained prominence as tools for FSW (Bhatia & Wattal, 2021).

Researchers commonly prefer tungsten carbide as a tool material for steel FSW because of its excellent heat resistance, hardness, and wear resistance properties. (Siddiquee & Pandey, 2014; Tiwari et al., 2019; Avettand-Fènoël et al., 2019; Majeed et al., 2021). However, its brittleness poses difficulties in its direct application. To address this, cobalt is often incorporated into the composite at a range of 5-25%. The composite of tungsten carbide with cobalt has become a

popular choice among researchers (as indicated in Table 3.2), offering a balance of desirable properties for effective FSW applications.

3.3.1.2 Synthetic materials

PCBN is an exceptionally hard material, ranking second to diamond in terms of hardness. Its remarkable hardness allows it to withstand extremely high temperatures. The properties of PCBN material are described in Table 3.4.

Table 3.4*: Properties of PCBN tool

Density (kg/m³)	Fracture toughness ($MPa\sqrt{m}$)	Thermal conductivity (W/m °C)	Vicker's hardness (HV)
3400	7.9	120	10000

PCBN tool materials are manufactured using high-pressure high-temperature technology, where cubic boron nitride crystals are bonded together with metallic or ceramic binders to form a substrate, imparting strength to the PCBN composite. PCBN stands out as the most promising material for fabricating friction-stir welding tools, as supported by several researchers (Table 3.3). However, one limitation of PCBN is its vulnerability to tool breakage when subjected to non-uniform loads.

3.3.2   Tungsten carbide as a tool material

Tungsten carbide has emerged as a favored tool material for FSW of steel because of its unique properties and excellent performance. The choice of the right tool material is essential in achieving high-quality and durable welds. This section will delve into the reasons why tungsten carbide is extensively used as a tool material for FSW of steel.

One of the key reasons for the preference for tungsten carbide is its exceptional hardness. Tungsten carbide is renowned for its high hardness, ranking among the hardest materials known. It exhibits remarkable resistance to wear, making it highly suitable for the severe conditions encountered during FSW (Gong et al.,2018). The hardness of tungsten carbide enables it to withstand the abrasive forces and high temperatures generated during the welding process, ensuring longevity, and reducing the need for frequent tool replacements.

Additionally, tungsten carbide possesses excellent thermal stability and a high melting point. It can withstand the elevated temperatures experienced during FSW without significant

softening or deformation (Yarlagadda et al., 2018). This property ensures the stability and integrity of the tool, minimizing the risk of tool failure or deformation under harsh welding conditions.

Moreover, tungsten carbide exhibits good thermal conductivity, enabling efficient dissipation of heat generated during the welding process. Efficient heat dissipation helps maintain the desired temperature distribution and prevents excessive localized heating, which could lead to distortion or other weld defects (Yarlagadda et al., 2018). The high thermal conductivity of tungsten carbide contributes to the overall control and stability of the welding process, resulting in high-quality welds with minimal thermal distortion.

Another advantage of tungsten carbide is its chemical stability. It demonstrates excellent resistance to chemical reactions with the steel being welded or the surrounding atmosphere. This prevents the tool from undergoing chemical changes (Gong et al., 2018). The chemical stability of tungsten carbide ensures the purity of the weld, maintaining the desired mechanical properties and structural integrity.

Furthermore, tungsten carbide is known for its high strength and toughness, which are critical for withstanding the mechanical stresses and forces encountered during FSW. Its inherent strength and toughness enable the tool to endure the vigorous stirring and forging actions involved in the process (Yarlagadda et al., 2018). This results in a stable tool structure, ensuring consistent weld quality and reducing the risk of tool failure or breakage.

3.3.3   Selecting the correct grade of tungsten carbide

Tungsten carbide is a well-known material recognized for its remarkable hardness, elevated melting point, and excellent wear resistance. It consists of tungsten and carbon atoms and is available in two main forms: cemented carbide and solid carbide.

Cemented carbide, also referred to as tungsten carbide-cobalt (WC-Co), is the most common form of tungsten carbide. It is produced by combining tungsten carbide particles with a metallic binder, typically cobalt. The tungsten carbide particles contribute to the material's hardness and wear resistance, while the cobalt binder enhances toughness and strength. The combination of these components results in a composite material with excellent properties suitable for various applications.

Solid carbide, on the other hand, refers to pure tungsten carbide without any metallic binder. It is a dense and brittle material that exhibits exceptional hardness and wear resistance. Solid

carbide is often utilized in specialized applications where maximum hardness and resistance to wear are required. However, its brittleness makes it less suitable for applications that involve high-impact or shock loading.

Tungsten carbide is available in a wide range of grades, each designed to meet specific requirements. The grades are typically distinguished by their composition and the addition of other elements or compounds to enhance particular properties. The most common grading system for tungsten carbide is the ISO standard, which categorizes the grades based on grain size, cobalt content, and hardness.

ISO grades for tungsten carbide include ISO P, M, K, and N, among others. Each grade exhibits a unique combination of hardness, toughness, and wear resistance, allowing for customized applications across different industries. For example, ISO P grades have a fine grain size and high cobalt content, making them suitable for applications requiring high wear resistance. On the other hand, ISO M grades have a medium grain size and are often utilized for general-purpose applications that require a balance between hardness and toughness.

For the present work, two grades of tungsten carbide available in the market were evaluated for their performance, and the best suited was selected for subsequent experimentation. For the present study, two grades of tungsten carbide tools used are designated as 'Tool A' and 'Tool B' respectively. Figures 3.2 (a and b) display the EDAX outcomes of the tools. 'Tool A' consists of Tungsten carbide with approximately 7% cobalt and 'Tool B' consists of 12% cobalt.

a) TOOL A

Element	Series	Unn C [Wt%]	Norm C [Wt %]	Atoms C	Error
Tungsten	L-Series	91.02	83.00	33.17	2.5
Cobalt	K-Series	6.75	6.16	7.68	0.2
Carbon	K-Series	6.72	6.13	37.44	1.1
Oxygen	K-Series	5.18	4.73	21.67	0.9

b) TOOL B

Element	Series	Unn C [Wt%]	Norm C [Wt %]	Atoms C	Error
Tungsten	L-Series	86.77	77.67	30.97	2.5
Cobalt	K-Series	13.71	12.28	15.27	0.4
Carbon	K-Series	5.67	507	30.97	1.4
Oxygen	K-Series	5.56	4.98	22.80	1.4
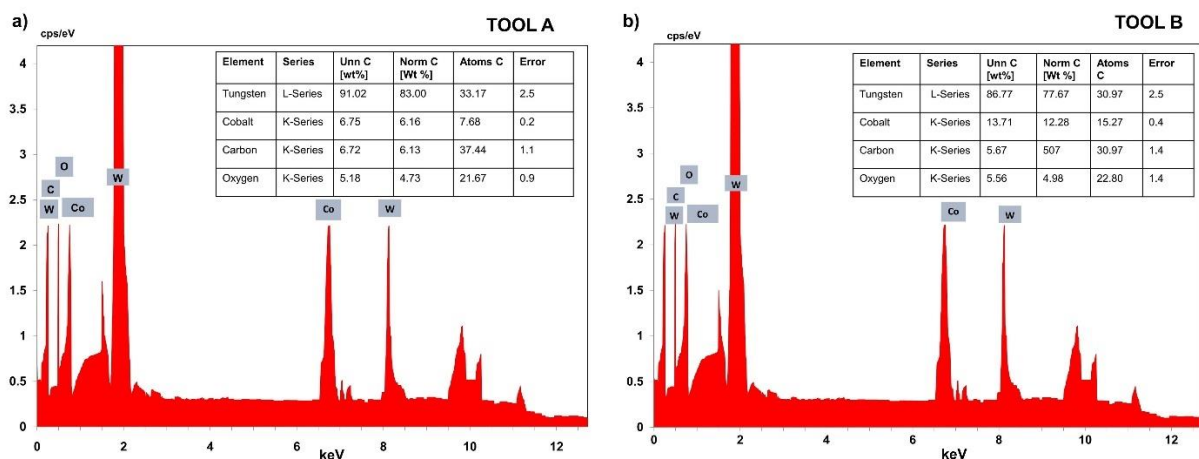
Figure 3.2: a) EDAX results for 'Tool A', and b) EDAX results for 'Tool B'

3.3.3.1 Tungsten carbide with approximately 7% cobalt

Figure 3.3 (a) represents 'Tool A' used for the study. When FSW was tried using this tool, blue-colored powder appeared on the surface after a few trials. This was a result of the oxidation of tungsten. The most notable oxidation was observed on the shoulder periphery. There was no sign of oxidation on the tool pin or the flat shoulder surface which was in contact with the workpiece. The probable reason for this was no exposure of the surfaces to the atmosphere and there is very little plastic deformation on the tool's surface. Figure 3.3 (b) illustrates the tool's condition after multiple welding runs were conducted and tested.
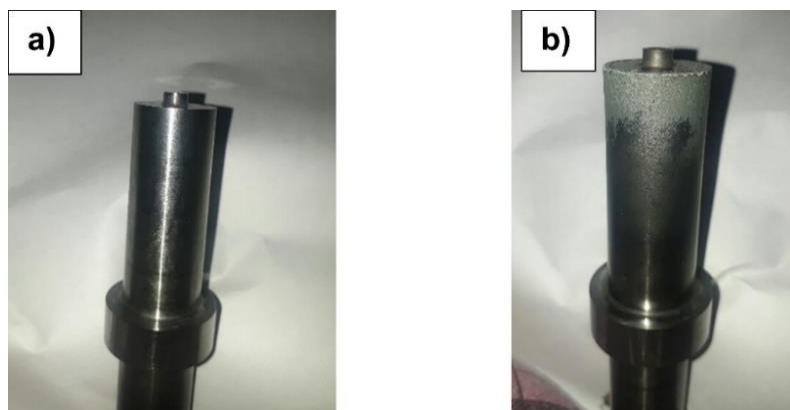
Figure 3.3: a) Undeformed 'Tool A' used for the present study, and b) 'Tool A' after performing welding.

The arrangement of tungsten carbide grains and the cobalt binder phase has an impact on the welding process and it plays a significant role in determining the material's mechanical properties and overall performance. The microstructural analysis of 'Tool A' is described in Figure 3.4. It provides valuable insights into the tungsten carbide-cobalt composite used in cemented carbide materials.

Tungsten carbide and cobalt are the main constituents of cemented carbide, and their arrangement in the microstructure has a significant role in determining the material's properties. Figure 3.4 (a) represents the microstructure of tungsten carbide-cobalt (WC-Co). The final tool material had good compaction and there is very little evidence of porosity. The bigger regular-shaped grains are tungsten carbide particles and the white matrix is cobalt.
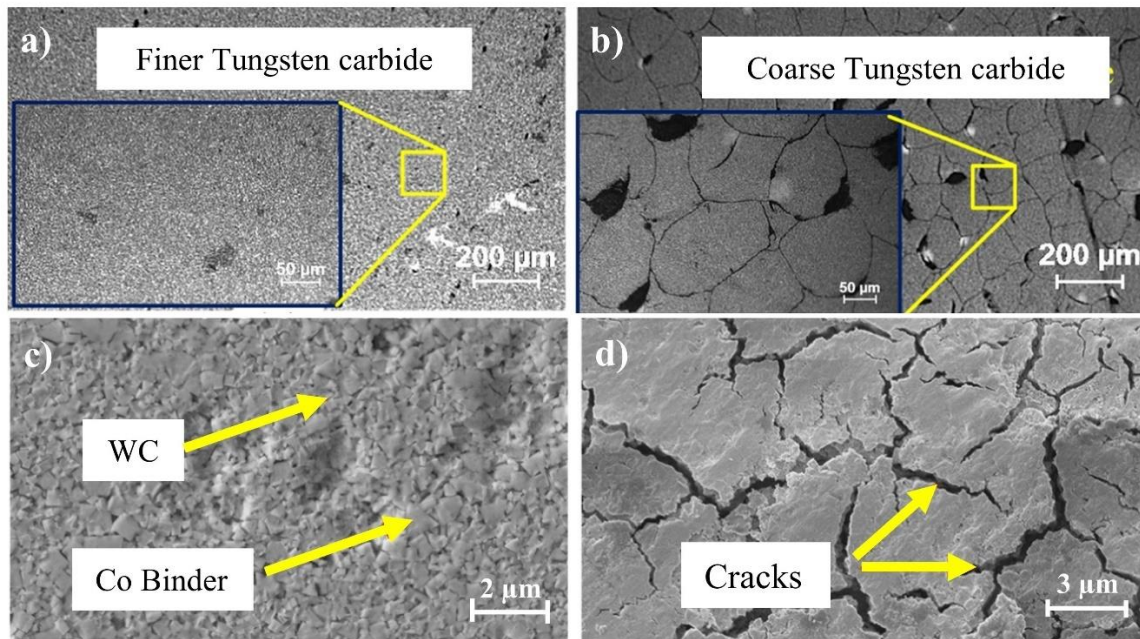
Figure 3.4: SEM image of 'Tool A' (a) before welding; (b) after welding and FESEM image of the 'Tool A' at 10000X (c) before welding, and (d) after welding

Also, an excessive change in the grain morphology is observed in Tool 'A' after a considerable amount of welding due to the weld thermal cycle as illustrated in Figure 3.4 (b). Friction-stir welding involves the application of heat and mechanical forces, which can result in significant temperature gradients and mechanical deformation. These conditions can lead to alterations in the grain structure of the tungsten carbide-cobalt composite, as observed in the microstructure. Figure 3.4 (c) depicts a closer look at the microstructure indicating the presence of closely packed brittle tungsten carbide (WC) grains embedded in a ductile cobalt binder. This combination of hard and ductile phases is essential for achieving the desired mechanical properties of the cemented carbide. The presence of WC grains provides hardness and wear resistance, while the cobalt binder enhances toughness and strength. Figure 3.4 (d) indicates a potential decrease in the bonding strength between the tungsten carbide and cobalt phases after a significant number of welding operations. The diminished strength of the bond can be attributed to the thermal and mechanical impacts of the welding process. The weakening of the bond can have implications for the overall integrity and performance of the material.

The product of oxidation was a very brittle non-adherent powder. The corresponding FESEM image for the same is shown in Figure 3.5. The powder falls continuously from the tool surface. The product of oxidation is tungsten oxide (WO_3) as illustrated by equation (3.1). This finding aligns with the research conducted by Wu et al. (2021).

$$WC + 2.5\ O_2 = WO_3 + CO_2 \tag{3.1}$$

The developed porous oxide layer further enhances the oxidation process in the neighboring layer. This, in turn, leads to the confinement of CO_2 within the WC grains. The presence of porous tungsten oxide (WO_3) and the exceptionally high CO_2 gas pressures are responsible for the formation of cracks as the ductile cobalt binder separates.
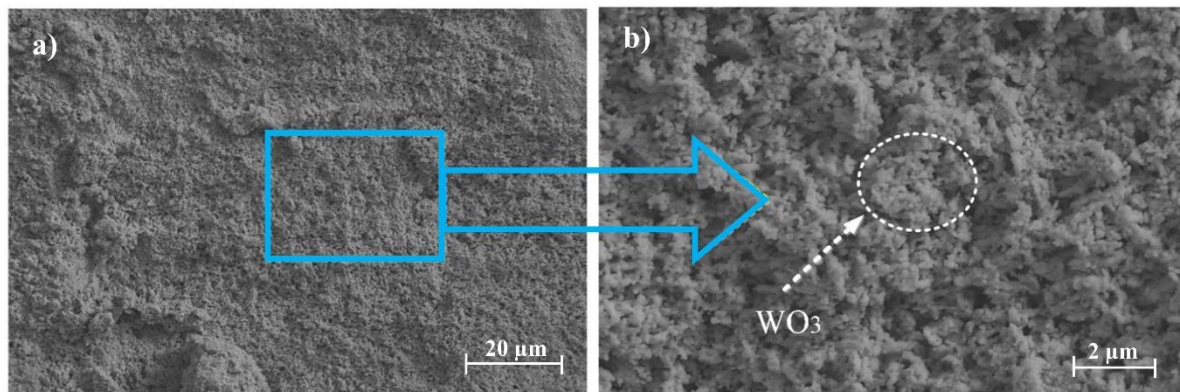
Figure 3.5: FESEM image of the oxidized layer at a) 1000X magnification, and b) 6000X magnification.

3.3.3.2 Tungsten carbide with 12% cobalt

When welding is performed using this type of tool, the products of oxidation are different as in the previous case. The oxides that are formed were blue. The rate of oxidation was lesser and there was an observation of swelling after the oxidation. The outer edge of the shoulder exhibited a noticeable bulge, as depicted in Figure 3.6 (a and b).
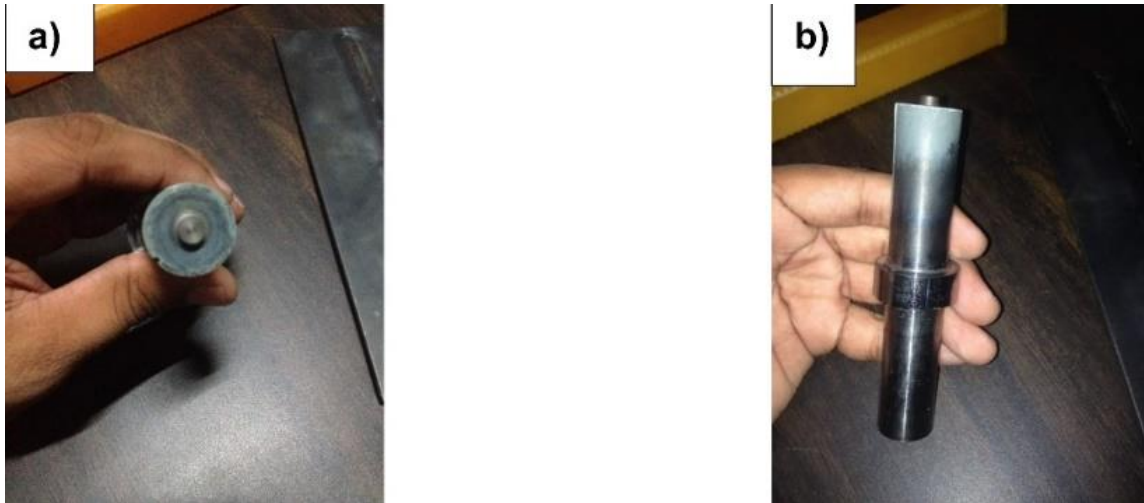
Figure 3.6: a) and b) show different views of 'Tool B' after performing welding.

The concentration of cobalt binder plays a crucial role in influencing the oxidation characteristics of tungsten carbide, which in turn affects the observed reaction between the oxide and tungsten carbide, leading to swelling. The product of oxidation in this case is different from 'Tool A'. The oxide layer is highly porous and swelled. The swelling could be because of the result of the reaction of oxide grain with cobalt, leading to the formation of $CoWO_4$ as illustrated by equation (3.2).

$$Co+WC+3O_2=CoWO_4+CO_2 \tag{3.2}$$

The periphery of 'Tool B' was bulged out which leads to an increment in shoulder diameter thereby making the shape of the tool convex, hence welding is not possible with a deformed tool. This deformation is because of the result of Co drift and movement of WC grains at high temperatures under the action of stress. These findings are consistent with the research conducted by Roa et al. (2015). They discovered that the quantity of cobalt binder plays a crucial role in influencing the oxidation characteristics of tungsten carbide. Their study highlighted the interaction between the oxide and cobalt, resulting in swelling effects.

A qualitative examination of the various precipitates formed on the tool surface was conducted through XRD phase analysis. Figure 3.7 (a, b) illustrates the X-ray diffraction patterns of the tool before and after the welding process, encompassing the 2-theta range of 10°–80°. In Figure 3.7(a), the prominent and smaller peaks correspond to tungsten carbide and cobalt, respectively. Figure 3.7(b), represents the emergence of distinct carbide phases such as WC, Fe_6W_6C, and Cr_3C_2 on the shoulder surface due to the welding thermal cycle's interaction with the tool

material and workpiece. Additionally, tungsten oxide (WO_3) and cobalt tungstate ($CoWO_4$) oxide phases are detected. Notably, WO_3 exhibits a weak texture formation due to substantial degradation, highlighting oxidation as the primary contributor to the weakening of the Co binder phase and, consequently, a reduction in the strength of the WC-Co alloy.
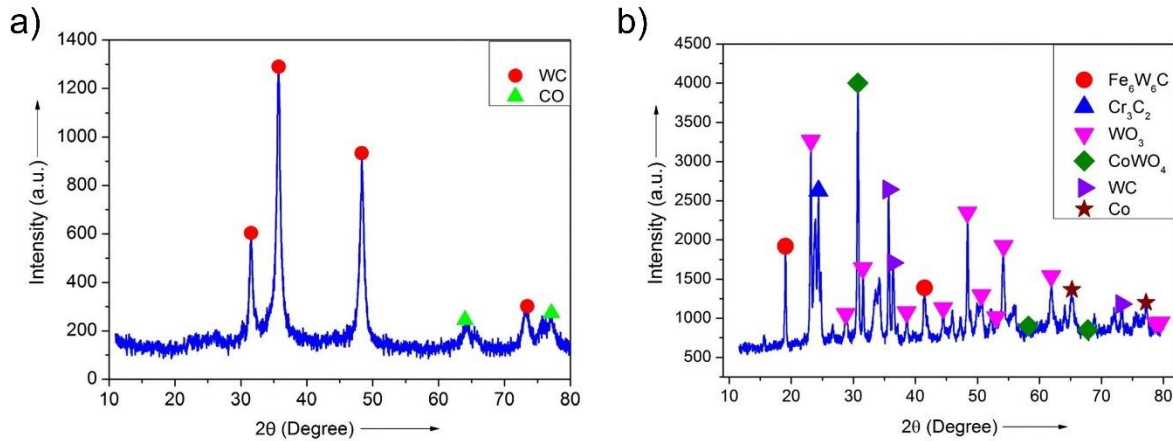
Figure 3.7:XRD patterns depicting distinct phase formations on the tool (a) before welding and (b) after welding.

Based on the above findings, the behavior of tool materials during the FSW of steel can be summarized as follows:

- **Oxidation of tool material:** 'Tool A' with a lesser amount of cobalt resulted in the formation of WO_3. The oxide formed in 'Tool B' reacted with cobalt and formed a porous and highly swelled $CoWO_4$.

- **Tool life:** For 'Tool B', the tool shoulder's periphery expanded, resulting in an enlarged diameter and a convex shape. Welding was not possible with this deformed tool and regrinding of the tool was necessary. The deformation was not observed in the case of 'Tool A', it performed well for a good amount of welding.

- **Suitability of tool material:** 'Tool B' was not suitable for the current application as it deformed quickly. This required very frequent regrinding that may not be very practical in real-life industrial situations. Although, 'Tool A' is expected to be more wear-resistant and stronger as the oxidation was also slow in the case of 'Tool A'.

Therefore, for the rest of the experimentation, the tool material selected was tungsten carbide with approximately 7% cobalt binder.

CHAPTER 4   EXPERIMENTATION

4.1 INTRODUCTION

Experimentation is a critical component of scientific research, allowing researchers to test hypotheses, explore causal relationships between variables, and collect empirical data to support their theories. Through experimentation, researchers can design controlled environments to observe and measure the effects of a specific intervention or treatment, helping to provide evidence for or against a particular hypothesis. By systematically manipulating independent variables and measuring the dependent variables, researchers can identify patterns and draw meaningful conclusions about the relationship between different factors. Experimentation is not only important for advancing scientific knowledge but also for informing policy decisions and improving the lives of individuals by providing evidence-based interventions and treatments. As such, experimentation is a fundamental aspect of research in many fields, including psychology, biology, chemistry, physics, and social sciences.

4.1.1 Types of experimentation approaches

Experimental approaches are crucial in scientific research as they allow researchers to test hypotheses and draw conclusions based on empirical evidence. There are several types of experimental approaches, and the choice of approach depends on the research question, the complexity of the system under investigation, and the resources available. In this article, we will discuss three main types of experimental approaches: the best gauge approach, the varying variable at a time approach, and the DOE approach.

The best gauge approach involves testing a range of variables simultaneously to determine the optimal set of conditions that produce the desired outcome. This approach is often used in complex systems where it is difficult to isolate individual variables. The best gauge approach is useful when multiple variables interact, and it allows researchers to identify the most effective combination of variables quickly.

The varying one variable at a time approach involves testing one variable at a time while holding all other variables constant. This approach is useful for identifying the individual effects of each variable on the outcome and determining the optimal level for each variable. The varying variable at a time approach is often used in scientific research to understand the relationship between variables. For example, a study by Zhang et al. (2018) used the varying

variable at a time approach to investigate the effect of four variables on the production of glycerol by a bacterium. By testing each variable independently, the researchers were able to identify the optimal level of each variable for maximum glycerol production.

The design of the experiment approach involves systematically varying multiple variables simultaneously using a predefined experimental design. This approach allows researchers to identify the effects of individual variables and their interactions systematically. The utilization of the design of experiments (DOE) approach is common in industrial and manufacturing contexts to enhance production processes and optimize product design. For example, a study by Wong et al. (2019) used the design of experiments approach to optimize the production process of biodegradable plastic. By systematically varying multiple variables such as temperature, mixing speed, and reaction time, the researchers were able to identify the optimal combination of variables for maximum product yield.

4.2 DESIGN OF EXPERIMENT

DOE is a systematic and structured approach to planning, conducting, analyzing, and interpreting experiments. It is a powerful tool for optimizing processes, improving quality, and reducing costs in various fields such as manufacturing, engineering, medicine, and social sciences.

DOE involves identifying the factors that may affect the outcome of the experiment, determining their levels, and then designing a series of experiments to systematically vary the levels of these factors while keeping all other factors constant. By analyzing the results of these experiments, DOE can determine which factors have the most significant impact on the outcome, and at what levels they should be set to achieve the desired result.

There are several key steps involved in DOE, including:

- **Defining the problem:** Clearly defining the problem or objective of the experiment is crucial to designing a successful experiment. The problem should be specific, measurable, achievable, relevant, and time-bound (SMART).
- **Identifying the factors:** Identifying the factors that may affect the outcome of the experiment is the next step. These factors can be either qualitative (e.g., color, shape) or quantitative (e.g., temperature, pressure). It is important to choose the right factors and levels to obtain accurate and relevant results.

- **Designing the experiment:** The design of the experiment should be carefully planned to ensure that all relevant factors are included and that the experiment is conducted in a controlled and consistent manner. There are several types of experimental designs, including full factorial, fractional factorial, and response surface.

- **Experimenting:** Once the experiment has been designed, it should be conducted in a controlled and consistent manner. Data should be collected and recorded accurately, and any deviations from the experimental plan should be noted.

- **Analyzing the results:** The data collected during the experiment should be analyzed using statistical methods to determine the significance of the factors and their interactions. The results should be interpreted in the context of the problem or objective of the experiment.

DOE has numerous benefits, including:

- **Increased efficiency:** DOE can help optimize processes by identifying the factors that have the greatest impact on the outcome and the levels at which they should be set to achieve the desired result. This can lead to increased efficiency, reduced waste, and improved quality.

- **Improved product quality:** By identifying the key factors that affect product quality, DOE can help improve product design and manufacturing processes, leading to higher-quality products and increased customer satisfaction.

- **Cost savings:** DOE can help identify cost-saving opportunities by optimizing processes and reducing waste. This can lead to significant cost savings over time.

- **Better decision-making:** By providing data-driven insights, DOE can help decision-makers make informed decisions about product design, manufacturing processes, and other critical areas.

4.2.1 Types of design of experiments

There are several types of experimental designs, including the following:

4.2.1.1 Full factorial design

Full factorial design is a powerful and widely used experimental design method that allows researchers to systematically investigate the effects of multiple variables on a response or

outcome of interest. It involves testing all possible combinations of the levels of each factor and is particularly useful when the number of factors and levels is relatively small. In this design, each factor is varied at each of its levels, resulting in a complete set of treatment combinations. When there are two factors, A and B, with two levels each (low and high), there are four potential combinations of treatments: A at the low level and B at the low level, A at the low level, and B at the high level, A at the high level and B at the low level, and A at the high level and B at the high level. The main advantage of a full factorial design is the ability to estimate the main effects, interaction effects, and quadratic effects of each factor on the response variable. This allows researchers to identify important factors and their optimal levels for achieving the desired outcome. Additionally, a full factorial design allows for efficient use of resources by testing all possible combinations of factors and levels in a single experiment. Nevertheless, the number of factors and levels in a full factorial design may impose limitations as the possible combinations of treatments can rapidly increase with an increasing number of factors and levels. In addition, if any confounding factors are not accounted for in the design, the results may be biased.

4.2.1.2 Factorial design with center points

Factorial design with center points is an experimental design method that allows researchers to investigate the effects of multiple factors on a response variable, while also incorporating replicates at a central point to test for curvature or nonlinearity. In a factorial design, each factor is varied at multiple levels, and the response variable is measured for each combination of factor levels. The design with center points includes additional runs at a central point, where all factors are set to their middle levels, to provide a reference point for measuring curvature. The center points are used to estimate the pure error variance, which can then be used to test for curvature or nonlinearity using a quadratic model. If the quadratic term is found to be significant, this suggests that there is a curvature in the relationship thereby, it cannot be modeled using a linear function.

The main advantage of a factorial design with center points is its ability to estimate both linear and quadratic effects of the factors on the response variable, as well as the ability to test for curvature in the relationship between the factors and the response. This allows researchers to identify optimal factor settings for achieving the desired outcome, even when the relationship is nonlinear. However, one potential limitation is that it assumes that the effects of the factors on the response are independent and additive. If there are interactions between the factors, this

assumption may not hold, and the results may be biased. Additionally, the use of center points adds extra runs to the experimental design, which may increase the time and cost of the experiment.

4.2.1.3 Fractional factorial design

A fractional factorial design is a partial representation of a full factorial design employed to examine the impact of multiple factors on a response variable. It involves selecting a subset of factors to be tested instead of testing all possible combinations, thus reducing the number of experimental runs required. This approach is particularly useful when the number of factors is large, and conducting a full factorial design would be impractical. The fractional factorial design is a method used to create an experimental design matrix by selecting a subset of rows from a full factorial design matrix. Each row in the design matrix represents a distinct combination of the factors being investigated, while the columns indicate the levels of each factor. The number of columns in the design matrix is equal to the number of factors being tested, and the number of rows is determined by the level of fractionalization.

The level of fractionalization is represented by a notation such as $2^{(k-p)}$, where k represents the number of factors under investigation, while p signifies the number of factors that remain fixed at a specific level. For example, a $2^{(4-1)}$ design would involve testing four factors at two levels each, while holding one factor at a fixed level. This would result in eight experimental runs, instead of the 16 runs required for a full factorial design.

The advantages of using fractional factorial designs include reduced cost and time required for experimentation, as well as the ability to identify the most important factors affecting the outcome variable. However, it is important to note that this approach does not allow for the estimation of interactions between factors, and may result in some important factors being missed if they are confounded with other factors in the design.

4.2.1.4 Response surface design

A response surface design is an experimental design in which the levels of several factors are varied to determine the optimal combination of factor levels that produce the desired response. It involves creating a model that relates the response of interest to the input variables and then using the model to predict the optimal combination of input variables for achieving the desired response. The fundamental concept of response surface design involves conducting a sequence of experiments with varying combinations of input variables and assessing the corresponding

response of interest. The data obtained from these experiments is then used to build a model that predicts the response as a function of the input variables. The model can then be used to identify the optimal combination of input variables that maximizes or minimizes the response.

There are two main types of response surface design: central composite design (CCD) and Box-Behnken design (BBD). CCD is a commonly used design that involves varying the input variables at three levels (-1, 0, 1), while BBD uses a smaller number of experiments to estimate the curvature of the response surface.

The success of response surface design depends on the quality of the model used to predict the response. The model can be linear or nonlinear, and it can be fitted using various regression techniques such as least squares, maximum likelihood, or Bayesian methods. The model can also include interaction terms between the input variables to capture the nonlinearity of the response.

Response surface design is a powerful tool for optimizing processes and systems. It allows engineers and scientists to identify the optimal combination of input variables that maximizes or minimizes the response of interest. As a result, substantial cost reductions, enhanced product quality, and an increase in efficiency can be achieved. However, the success of response surface design depends on the quality of the model used to predict the response. Therefore, it is important to carefully design the experiments, collect high-quality data, and use appropriate statistical techniques to build the model.

This design is useful for determining the curvature of the response surface, which can help identify the optimal factor levels. However, it may not be useful for identifying interactions between factors.

4.2.1.4.1 Central composite design

Central composite design (CCD) is a widely used experimental design technique in statistics and engineering. It is used to find the optimal combination of input variables that will maximize the output response of a system or process. CCD involves creating a design matrix that includes a set of experimental runs with different combinations of input variables. The matrix includes a set of center points that help estimate the curvature of the response surface and a set of axial points that allow for a more complete exploration of the input space.

Afterward, the design matrix is employed to construct a response surface model, which describes the relationship between the input variables and the corresponding output response. The model can then be used to predict the response at different points in the input space, allowing for the optimization of the system or process.

4.2.1.4.2 Box-Behnken design

It is a response surface methodology that is commonly used for experimental design to develop and optimize the process. It is a design that uses a set of predetermined experimental points that can efficiently estimate the response surface and determine the optimal levels of independent variables to achieve the desired response. It involves the use of a set of experimental points that are arranged in a balanced block design. The design uses three levels of the independent variables, typically coded as -1, 0, and +1, which represent the low, medium, and high levels of the factors, respectively. The design includes a set of central points at the center of the design space, which is used to estimate the pure error and determine the experimental variability.

One of the significant advantages of the Box-Behnken design is its efficiency in estimating the response surface with fewer experimental runs compared to a full factorial design. The design includes a minimum number of experimental points, while still providing an accurate estimation of the response surface. Also, it is more robust to the presence of outliers or experimental noise compared to a full factorial design. The design includes a central point that can help detect any lack of fit in the model, which can be due to experimental errors or other uncontrolled factors. It is useful for identifying the significant factors and their interactions, as well as the optimal factor levels that produce the desired response.

4.2.1.5 Plackett-Burman design

The Plackett-Burman design is a widely employed experimental design strategy utilized for screening numerous factors to identify the influential variables that impact the response. This design is efficient and cost-effective, as it allows researchers to identify the critical factors that influence the response, without conducting a large number of experiments.

The Plackett-Burman design uses a set of experimental points that are arranged in a balanced block design. The design includes a set of binary-coded independent variables, which are typically coded as -1 and +1. Each experimental run involves only a subset of the independent

variables, and their combinations are determined using a predetermined design table. One of the significant advantages of the Plackett-Burman design is its efficiency in identifying the significant factors with a minimum number of experimental runs. The design includes a minimal number of experimental runs, which is typically equal to twice the number of factors being screened. Therefore, for many factors, the Plackett-Burman design can be a more efficient and cost-effective alternative to the full factorial design. It is robust to the presence of noise or experimental errors. The design can identify the significant factors, even in the presence of experimental errors or noise, due to the use of binary-coded independent variables.

4.2.1.6 Taguchi design

Taguchi's OAs are a popular form of experimental design extensively applied in diverse domains, such as manufacturing, engineering, and product design. This design was developed by Dr. Genichi Taguchi, a Japanese engineer, who sought to create a more efficient and effective method for quality improvement and optimization of product and process design.

Taguchi's orthogonal array (OA) design involves a systematic variation of the levels of each factor, based on a predetermined OA. The main reason for choosing Taguchi as DOE in this research work is that it offers flexibility in choosing the range of levels a non-numerical value can be taken as a level, which is not the case for CCD and other designs available. The design is characterized using a small number of experimental runs, while still providing statistically significant results. This makes the design a cost-effective and time-efficient method for testing many factors. One of the main advantages of the Taguchi OA design is its robustness to variations and noise in the system. The design includes experiments that are performed at different levels of each factor, including the mean and the extremes. This allows for the identification of the optimal levels of each factor, even in the presence of variations and noise, thereby improving the quality and reliability of the product or process. Moreover, it facilitates the recognition of the crucial factors that impact the quality of the product or process. The design allows for the systematic variation of the levels of each factor, enabling the identification of the significant factors impacting the output.

Taguchi's OA design is widely used in the industry for quality improvement and optimization of product and process design. The design has been used in various fields, including manufacturing, engineering, and product design. This tool is highly effective in pinpointing the vital factors influencing the product or process quality and in establishing the ideal levels of each factor to attain the desired quality.

4.2.2   Taguchi's design of experiments

This involves several steps that are followed systematically to optimize the product or process design. The following are the steps involved in Taguchi's design of experiments:

- **Define the problem and identify the response variables:** In Taguchi's design of experiments, the initial stage involves outlining the problem and determining the response variables that hold the utmost significance in the performance of the product or process.

- **Determine the factors influencing the response variables:** The subsequent stage involves identifying the factors that have an impact on the response variables. These factors can be classified as controllable and uncontrollable.

- **Determine the levels of the factors:** The third step is to determine the levels of the factors that will be tested in the experiment. The levels are selected based on the range of values that are likely to be encountered in real-world situations.

- **Design the orthogonal array:** The fourth step is to design the OA. The OA is a matrix that is used to systematically vary the levels of the factors. The design ensures that each factor is tested at different levels, and the interactions between the factors are systematically varied.

- **Conduct the experiments:** The fifth step is to conduct the experiments according to the design. The experiments are performed at the predetermined levels of the factors, as specified in the OA.

- **Analyze the results:** The analysis of the experimental outcomes constitutes the sixth step, encompassing the identification of the influential factors impacting the response variables and ascertaining the optimum levels of each factor required to accomplish the desired performance.

- **Verify the results:** The ultimate step involves the verification of the experimental outcomes, wherein the optimized design is subjected to real-world conditions to validate the attainment of the desired performance.

4.3 METHODOLOGY FOR CONDUCTING THE EXPERIMENTS

4.3.1 Cause and effect diagram

In the present study, a cause-and-effect diagram was used as a tool to analyze the potential causes of a problem. This diagram, also known as a fishbone diagram or Ishikawa diagram, is a graphical representation that helps to identify and organize the possible causes of a particular effect. The diagram was prepared after a thorough brainstorming session with a peer group and experts in the field as shown in Figure 4.1. All the possible causes of the problem are listed and grouped into categories such as Tool-related parameters, machine-related problems, and other parameters. This approach helped to systematically identify and analyze the root cause of the problem, and to develop effective solutions to address it.
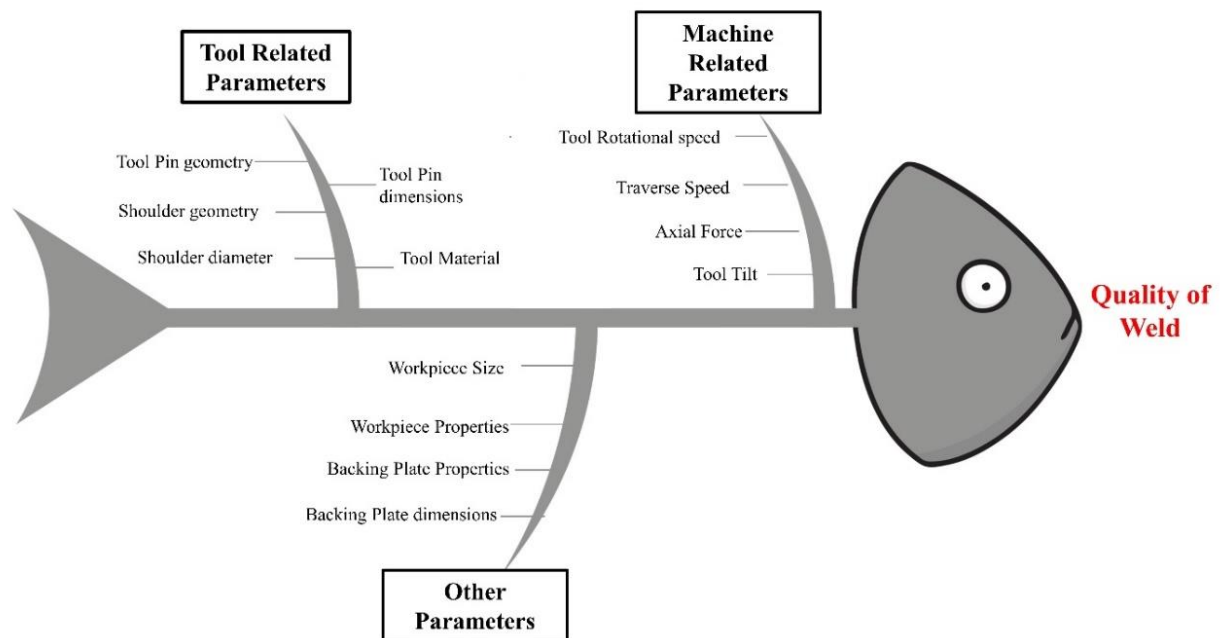
Figure 4.1: Cause and effect diagram to identify the significant input parameters affecting the weld integrity

4.3.2 Identification of the process parameters affecting the quality of the weld

To establish a reliable procedure for achieving a successful friction stir weld, it is crucial to investigate the impact of input parameters on weld integrity. Therefore, identifying the input parameters that influence the characteristics of weld holds significant importance. Section 4.3.3 provides an overview of the key parameters, as reported in the existing literature.

4.3.3 Important input parameters of FSW

The welding process and the resulting weld quality are significantly impacted by the chosen process parameters in FSW. This section provides a comprehensive examination of the different process parameters utilized in FSW and their influence on the welding process.

- **Tool geometry:** The tool configuration plays a vital role in determining the quality of the weld in FSW. Consisting of a shoulder and a pin, the tool's diameter is a crucial parameter that affects both the HAZ and the material displacement during the welding process. Increasing the shoulder diameter can result in an expansion of the HAZ while reducing the diameter of the pin can help minimize material displacement. Furthermore, the tool design also affects heat transfer to the workpiece, influencing the weld's microstructure.

- **Rotational speed:** This is a critical parameter in FSW as it directly influences heat generation during welding. Proper adjustment of the rotational speed is essential for maintaining control over the temperature during the process. Higher rotational speeds result in increased temperatures, leading to softening and potential weakening of the material. Conversely, lower rotational speeds may not generate sufficient heat, resulting in incomplete weld formation. Determining the appropriate rotational speed is based on considerations such as the specific material, tool design, and welding parameters.

- **Traverse speed:** The traverse speed in FSW refers to the speed at which the tool moves along the joint line, impacting both heat input and material deformation. The choice of traverse speed directly affects the amount of heat applied and the level of plastic deformation in the material. Higher traverse speeds result in reduced heat input, leading to a smaller HAZ and minimal plastic deformation. Conversely, lower traverse speeds increase heat input, resulting in a larger HAZ and more significant plastic deformation.

- **Axial force:** It refers to the force applied by the tool onto the workpieces. It directly influences the amount of material displacement and the depth of tool penetration into the workpieces. A higher axial force promotes greater material flow and deeper tool penetration, while a lower axial force leads to less material flow and shallower tool penetration. Determining the appropriate axial force depends on factors such as the specific material being welded, the design of the tool, and the welding parameters.

- **Tool tilt angle:** It refers to the angle between the tool axis and the workpiece surface, and plays a significant role in FSW by affecting material flow and the contact area

between the tool and the workpiece. Modifying the tilt angle can directly impact the degree of material flow, with a higher angle encouraging increased flow and a lower angle leading to reduced flow.

- **Workpiece material:** The characteristics of the workpieces, including their composition, microstructure, and mechanical properties, can have an impact on the welding process. Materials with high melting temperatures, low thermal conductivity, and low ductility can be difficult to weld using FSW. Materials that are prone to deformation or distortion during welding, such as aluminum alloys, require a careful selection of process parameters to achieve a high-quality weld.

- **Welding environment:** The welding environment, such as the presence of a shielding gas or a vacuum environment, can affect the welding process. The use of shielding gas protects the weld by preventing contamination and oxidation, while a vacuum environment helps prevent the formation of oxide layers on the surface of the weld. The selection of the welding atmosphere is typically based on the specific material being welded and the desired weld properties.

4.4 PILOT RUNS TO FINALISE THE RANGE OF PROCESS PARAMETERS

Preliminary experiments were performed to determine the appropriate values for the process parameters. Numerous process parameters exhibited limited possibilities for variation. Trial and experimentation can be employed to ascertain the appropriate levels for the process parameters. Any deviation from the ideal value results in a faulty weld. The process parameters and the values at which the final experiments would be conducted were chosen as a result of the experiments' findings.

4.4.1 Tool pin geometry characteristics

The tool geometry, including its shape and dimensions, directly impacts the contact area between the tool and the workpiece, which in turn affects the heat generation in FSW. A wider contact area increases heat generation, which can sometimes be advantageous. However, it can also result in excessive plastic deformation, which leads to defects

The geometry of the tool in FSW has a substantial impact on the material flow during the process. A tool with a small diameter and a narrow shoulder can produce a more concentrated and vigorous stirring action, resulting in superior material mixing and weld quality. On the

contrary, utilizing a tool with a large diameter and a wider shoulder can lead to a more even distribution of temperature and decrease the likelihood of material defects.

Furthermore, the configuration of the tool pin, in addition to the diameter and shoulder size, influences the material flow during FSW. A tapered pin can create a more gradual stirring action, while a cylindrical pin can create a more intense stirring action. The shape of the pin used in FSW can also influence the extent of material displacement during the process, which, in turn, can impact the strength and weld quality.

4.4.1.1   Tool pin shape

The geometry of the tool pin can impact the flow of material during FSW. Various research studies have investigated the influence of different tool pin configurations on the mechanical properties of the welds. Cylindrical pins are the most commonly used tool pin shape in FSW, but this can create several problems during the process. Some of the main issues associated with cylindrical pins in FSW are as follows:

- **Excessive material flow:** Cylindrical pins have been associated with excessive material flow during FSW, as reported in previous studies, resulting in defects such as tunneling, porosity, and voids in the weld zone (Mishra et al., 2003).
- **Poor mixing and stirring:** The cylindrical pin shape does not provide an adequate mixing and stirring action, leading to incomplete mixing of the materials and resulting in a weak weld joint (Mishra et al., 2005).
- **High tool wear:** The use of cylindrical pins in FSW can lead to significant tool wear as a result of the elevated levels of friction and plastic deformation experienced during the process. (Ravi Kumar et al., 2007).
- **Uneven temperature distribution:** The cylindrical pin shape can result in an uneven temperature distribution across the weld zone, leading to inconsistent mechanical properties (Palanivel et al., 2012).

To address these challenges, researchers have introduced different tool pin shapes, including conical, triangular, square, trapezoidal, and threaded pins, to enhance the efficiency and effectiveness of the FSW process. These tool pin shapes can provide better mixing and stirring action, reduce tool wear, and produce more uniform temperature distributions during the welding process. Figure 4.2 presents different shapes tried for experimentation in the present study.
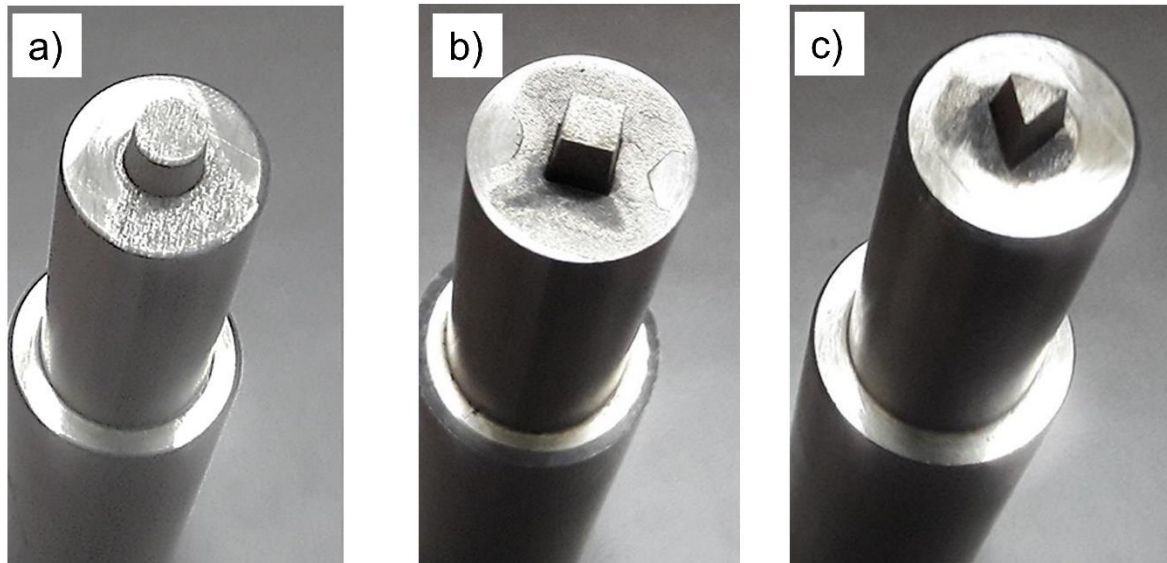
Figure 4.2: Different types of pin profiles tried in the present study

There was a problem of frequent pin breakage in the case of cylindrical shapes as shown in Figure 4.3 and all other profiles lost their shapes after 100 mm of welding. These types of pin shapes got worn out and assumed the shape of a truncated cone. When this truncated cone was used for welding, it gave defect-free welds. This became the motivation to use a truncated cone profile for the rest of the experimentations.

Figure 4.3: Wearing of tool pin when cylindrical pin profile was used.

4.4.1.2   Tool pin diameter

The diameter of the tool pin is a crucial parameter in this process and has a substantial impact on the weld quality. The criteria of selection are based on the thickness of the material being welded. In general, a smaller pin diameter is suitable for thinner materials, while a larger pin diameter is better for thicker materials. A smaller pin diameter results in reduced heat generation during welding, which is advantageous for thinner materials. Conversely, a larger

pin diameter facilitates better material mixing during the welding process, which is critical for thicker materials.

The relationship between the pin diameter and the shoulder diameter is also essential. To provide adequate support for the pin during welding, the diameter of the shoulder should be twice the diameter of the pin or larger. Insufficient shoulder diameter can result in pin failure and negatively impact the weld quality.

The relationship between the pin diameter and the shoulder diameter may vary depending on the specific application and the materials being welded. It is important to consider these factors when determining the appropriate correlation between the two dimensions. Therefore, it is crucial to conduct trials to determine the optimal pin and shoulder diameter for a given application. Welding experiments were conducted using tool pins with diameters ranging from 3 mm to 8 mm. The findings indicate that tool pins with a diameter of 5 mm or less were ineffective as they experienced shearing. However, when employing an 8 mm diameter tool pin and a 25 mm shoulder diameter, a groove defect was observed due to difficulties in material flow and filling the gap created by the advancing pin. The groove defect is illustrated in Figure 4.4.
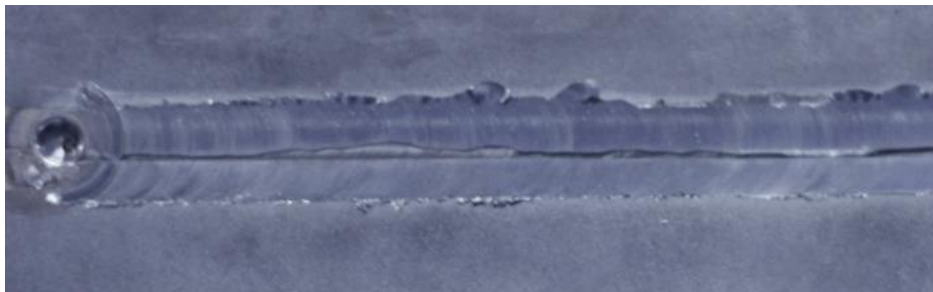
Figure 4.4: Defect due to large pin and regular shoulder diameter

The welding process was successful when using a 6 mm diameter tool pin, as it remained intact throughout the welding process without experiencing shearing.

4.4.1.3 Tool pin length

The tool pin length shall be such that it allows complete penetration. Various length of the tool pins was tried but the tool pin with 2.8 mm worked well. When the tool pin is less than this length, there is a problem of incomplete penetration. Tool pin with a length of more than 2.8 mm resulted in sticking the plate with the backing plate, thus it became very difficult to take out the plate from the backing plate. The problem of plates getting stuck on the backing plate

also has taken place with a length of 2.8 mm as shown in Figure 4.5. The probable reason for the same is due to low welding speed and high tool rpm produced an enormous amount of heat. In most situations, the removal of plates took place by light hammering.
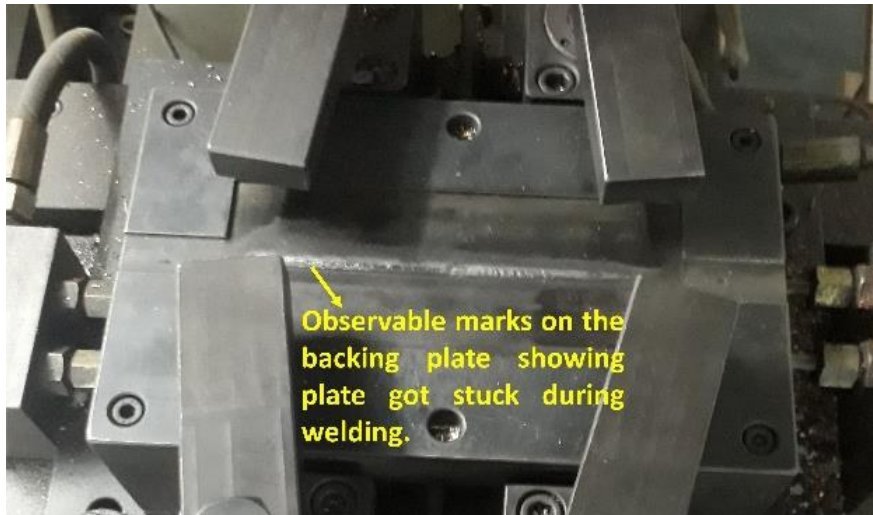
Figure 4.5: Picture of the backing plate showing observable marks after the removal of welded plates

4.4.2   Profile of the tool chosen for the experimentation

Tool pins should closely conform to a specific shape and size to provide defect-free welding. As a result, the tool profile cannot be considered a process parameter that can be changed during welding. The present study utilizes a tapered pin profile due to the numerous advantages it offers in the FSW of steels. The advantages and implications of these benefits are presented and examined in the subsequent section.

- **Enhanced material displacement and blending:** The utilization of a tapered pin profile enables enhanced material flow and blending during welding. The gradually decreasing diameter of the pin reduces the amount of material that needs to be displaced, resulting in a more uniform and consistent mixing of the material. This, in turn, leads to a better-quality weld with fewer defects. (Elangovan et al., 2009)

- **Enhanced heat dissipation:** The tapered pin profile also helps to dissipate heat more effectively. The smaller diameter at the tip of the pin allows for more efficient heat transfer from the welding zone to the surrounding material. This reduces the risk of overheating and distortion and also helps to prevent the formation of unwanted phases, such as brittle intermetallic compounds. (Tekkaya et al., 2005)

- **Increased weld strength:** The use of a tapered pin profile has been shown to increase the strength of the weld in FSW of steels. This is due to the improved material flow and mixing, which leads to a more homogeneous microstructure and better bonding between the materials. The strength of the weld can be further enhanced by optimizing the taper angle and other parameters of the pin. (Emamian et al, 2017)

- **Reduced tool wear:** Ultimately, the implementation of a tapered pin profile in FSW of steels can effectively decrease tool wear. This reduction in tool wear is a result of the smaller contact area between the tool and the material, particularly at the pin's tip. As a result, tool wear is minimized throughout the welding process. This advantage contributes to an extended tool lifespan and a reduction in overall welding costs. (Rameshbabu et al., 2011)

Figure 4.6 displays the selected tool profile for the current investigation. The tool pin is designed as a truncated cone, featuring a pin diameter of 6 mm and a pin length of 2.8 mm.

All dimensions are in mm
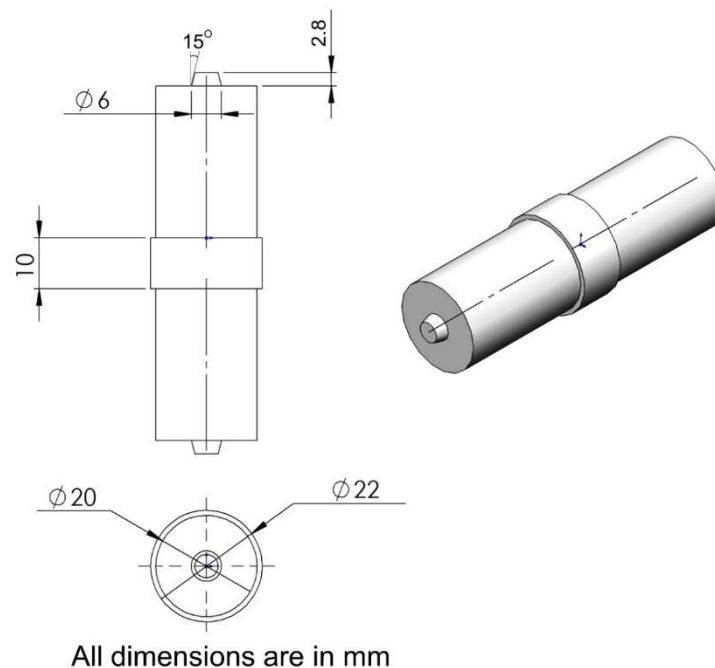
Figure 4.6: Final profile of the tool selected for experimentation

4.4.3 Tool tilt

This pertains to the inclination of the tool with respect to the workpiece surface. This angle significantly influences material flow, heat generation, contact between the tool and workpiece, material mixing, and weld integrity. Moreover, the tool tilt angle directly affects the mechanical properties of the joint.

Choosing the appropriate tool tilt angle in steel FSW is dependent upon various factors, including the material type, thickness, tool geometry, and welding parameters. These considerations give rise to a spectrum of tilt angle choices. In general, the tool tilt angle ranges from -2° to +2° for low-carbon and medium-carbon steels (Li et al., 2018). However, for high-strength steels, a negative tool tilt angle of up to -3° may be used to improve the weld quality and mechanical properties (Zhang et al., 2019).

A tool tilt of 2° or more proved inadequate for effectively consolidating the material stirred behind the tool. The leading edge of the tool displaced the material in front of it instead of gathering it beneath the shoulder, resulting in a deficiency of material behind the tool. The remaining material was unable to fill the void created by the advancing pin. Since the advancing side of the weld received the material last, it remained unfilled. This defect is known as 'shoulder void'. The defect is shown in Figure 4.7.

Figure 4.7: Shoulder void defect due to insufficient tool tilt

This defect could be reduced by increasing the shoulder plunge depth. The excessive plunging compensated for the tool tilt, in a sense that now the stirred material is held down and consolidated. Thus, the shoulder void is eliminated and defect-free welds are produced. But this increased shoulder plunge leads to excess material getting thrown out in the form of a flash. This excessive flash requires additional machining as well as thinning of the workpiece. This material thinning is not acceptable as per the design.

Excessive flash also occurred when the tool tilt was very high (4° or above). As illustrated in Figure 4.8, when the tool tilt was high, the front of the tool got excessively plunged (D x tan θ) even when the tool shoulder plunge was just right on the tool's back side. This led to excessive

material flushing out and resulted in a weld that is not acceptable. While the tool shoulder plunge was found to be suitable on the front side of the tool, it was insufficient on the backside, resulting in a defective weld. Figure 4.9 indicates the thinning of the workpiece material when welding was performed with excessive tool tilt.
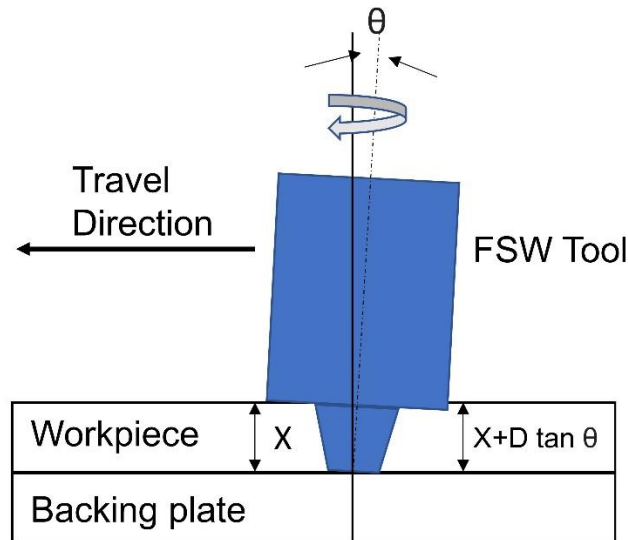
Figure 4.8: Extra plunge required because of excessive tool tilt

Figure 4.9: Thinning of material because of excessive flash

Thereby, tool tilt is not considered a variable parameter, rather its value is kept constant which is 1.5° to obtain defect-free welds. This choice is in agreement with Li et al. (2018) that demonstrates a positive tool tilt angle of 1.5° produced a defect-free weld with a fine equiaxed grain structure and excellent mechanical properties.

67

4.4.4 Welding speed

This is a critical parameter that has a substantial impact on the quality of the weld. It refers to the linear speed at which the tool moves along the weld line during the welding process. The welding speed directly affects the amount of heat input, and influences the microstructure and mechanical properties of the resulting weld.

Welding speed directly influences the heat input during the process. The heat input refers to the amount of heat generated during welding and is affected by the welding speed. Increasing the welding speed results in a lower heat input since the exposure time to the generated heat is reduced. The heat input directly influences the weld's microstructure, where higher heat input can lead to larger grain size and decreased mechanical properties.

In addition to affecting the heat input, the welding speed also affects the material flow during FSW. A higher welding speed leads to a more rapid and shallow material flow, while a lower welding speed leads to a deeper and broader material flow. The weld quality is influenced by the material flow, wherein a more extensive and deeper material flow results in an improved blending of the materials and a more uniform microstructure.

Therefore, choosing the appropriate welding speed is critical to ensure high-quality welds. A balance between the heat input and material flow must be achieved to produce a weld with desirable mechanical properties. The optimal welding speed should be determined by considering factors such as tool design, and weld quality.

A study conducted by Dinda et al. (2019) analyzed the effect of welding speed on the weld integrity of FSWed high-carbon steel. The observation revealed that as the welding speed increased, there was a corresponding decrease in UTS and elongation. The decrease in weld quality was attributed to the existence of larger regions with coarse grains in the weld. Experimental tests were performed with different welding speeds to investigate this effect. Defects appeared when the welding speed exceeded 210 mm/min. Lower than 60 mm/min welding speeds resulted in excessive heat production and too-slow welding. Therefore, the speed range chosen for the studies was between 60 mm/min and 210 mm/min. The welding speed could not be altered continuously since the machine's feed motor was a constant-speed induction motor. The speed was changed by picking a gear combination from the gearbox. As a result, only a few discrete values of speed were feasible, and the welding speed was picked from there.

In recent research conducted by Song et al. (2023), the influence of welding speed on the microstructure and mechanical properties of FSWed high-strength low-alloy (HSLA) steel was examined. The study found that higher welding speeds resulted in larger grain sizes and decreased mechanical properties, which can be attributed to the reduced heat input.

4.4.5 Rotational speed

The rotational speed is an important parameter in FSW as it directly affects the heat generation during the process. A higher rotational speed leads to increased friction between the tool and the workpiece, resulting in higher temperatures at the weld interface. This elevated temperature promotes material softening, facilitating material flow and mixing between the workpieces. However, it is important to note that excessive heat input can have negative effects such as excessive grain growth and reduced weld strength.

Several studies have indicated that higher tool rotational speeds can result in improved weld quality in steel FSW. For instance, a study conducted by Nandan et al. (2007) examined the impact of tool rotational speed on the microstructure and mechanical properties of FSW in mild steel. The findings revealed that increasing the rotational speed led to finer grain sizes, increased hardness, and enhanced mechanical properties. Similarly, Choudhary et al. (2013) conducted a study on the effect of tool rotational speed on the FSW of high-strength steel. Their research demonstrated that higher rotational speeds resulted in a narrower heat-affected zone, finer grain structure, and improved mechanical properties. Moreover, it is essential to note that increasing the rotational speed can also lead to reduced material flow and improper mixing between the two pieces of material. Therefore, the tool rotational speed should be optimized to obtain the desired weld quality.

The tool rotational speed is an important process parameter that has a significant impact on the quality of FSW in steel. Increasing the rotational speed can improve weld quality, but it is essential to find the optimal speed to avoid excessive heat input and hindered material flow.

The range of process parameters that result in a weld without defects was determined after extensive testing. Excessive heat was produced at rotating speeds of 750 rpm and higher. This heat had a deteriorating effect on the tool pin. A tunnel defect with excessive flash was also observed, owing to high rotational speed. When the rotational speed was less than 430 rpm, very little heat was produced, and the work material did not soften properly. As a result, the machine required a lot of torque. This torque requirement could be just met as the tool spindle

was rotating at low rpm. There was also a greater risk of tool breakage and the pin entirely shearing off.

Therefore, during the rest of the experiment, the tool rpm values of 430, 550, and 750 were utilized. It was not possible to adjust the tool rpm continuously, so the available rotational speed options from the machine were chosen. This was similar to the welding speed, where there were specific values that could be selected.

4.4.6   Tool shoulder diameter

The diameter of the tool shoulder is a critical factor in steel FSW and has a substantial impact on the welding process and the quality of the resulting weld joint. This parameter directly impacts heat generation during welding. When the shoulder diameter is larger, it generates more heat through friction, leading to enhanced plastic deformation and increased thermal input into the material. As a result, this can lead to a more uniform and refined microstructure within the welded area, thereby enhancing the mechanical characteristics of the joint. (Reynolds et al., 2004).

The diameter of the tool shoulder also influences the material flow during welding. A larger shoulder diameter creates a larger region of plastic deformation and mixing, known as the stir zone (SZ). This promotes better uniformity of the material and aids in the elimination of defects like voids and porosity. (Murr et al., 1999). Thus, the tool shoulder diameter affects the joint strength and fatigue performance. A larger shoulder diameter can produce a stronger joint, but may also lead to more residual stress and distortion. On the other hand, a smaller shoulder diameter can reduce distortion and residual stress but may result in a weaker joint (Zhang et al., 2019).

Therefore, choosing the right tool shoulder diameter is essential to attain the desired weld quality in steel FSW. It is important to consider the specific application and material properties when selecting the shoulder diameter to ensure optimal results. When a shoulder diameter of less than 15 mm was used then a surface defect became evident. This occurs due to the decrease in the space between the pin on the shoulder and the diameter of the shoulder, resulting in a subsequent decrease in material flow. Using a tool with a shoulder diameter larger than 20 mm resulted in the formation of a defect known as a tunnel defect. This problem occurred as a result of excessive heat generation and insufficient material movement.
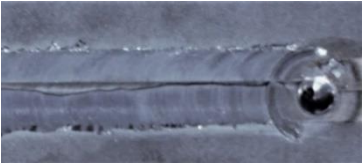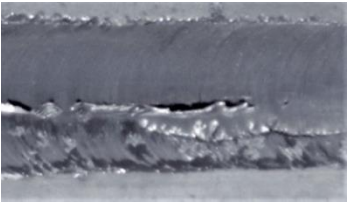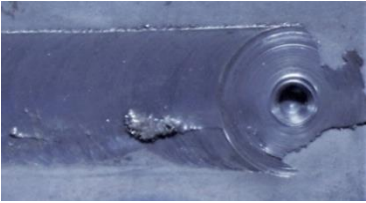
Thus, for the rest of the experimentation, tools of shoulder diameter between 15 mm and 20 mm were used. Tools of 15 mm, 18 mm, and 20 mm were available in the market and were used for the present study.

4.5 SELECTION OF INPUT PARAMETERS AND THEIR VALUES

The process parameters chosen for the pilot study included welding speed, tool rotational speed, and tool shoulder diameter. The experimental results are presented in Table 4.1, while the allowable range of these parameters, based on the production of welds without defects, is indicated in Table 4.2.

The influence of these elements is not simply linear, hence at least three levels are required to assess the linear and quadratic effects of these components. It is self-evident to split the available area into equal portions for experimenting. However, there was a constraint with the levels chosen in this case. Because the rpm was altered by selecting a specific combination of gears, the tool rpm could not be varied constantly. As a result, the closest middle-level rotational speed was 550 rpm. Similarly, the tungsten carbide rod's size was commercially available only at 18mm, and thus, it was chosen as the middle level. The middle level of welding speed selected from the available range was 110 mm/min. Table 4.3 presents the selected process parameters along with their respective levels.

Table 4.1: Findings recorded during the selection of the range of input parameters.

Variable factor	Process Variables	Macrostructure	Observations
Welding speed	V <60 mm/min N=430 rpm D=20 mm		The root became firmly attached to the surface due to the prolonged duration of contact between the heated metal and the backing plate.
	V >210 mm/min N=430 rpm D=20 mm		An imperfection in the shape of a groove was observed. This occurred because of the interaction between the heat produced by friction and the movement of material.
Tool rotational speed	N <430 rpm V=60 mm/min D=20 mm		Significant tool pin deterioration was noted, which can be attributed to the fracture of the pin caused by excessive generation of heat.
	N >750 rpm V=60 mm/min D=20 mm		A defect in the form of a tunnel, accompanied by an excessive presence of flash, was detected. The occurrence of this excessive flash can be attributed to the elevated rotational velocity.
Shoulder diameter	D <15 mm V=60 mm/min N=430 rpm		The surface defect was observed. This is a result of reducing the space between the pin and shoulder diameter, leading to a consequent decrease in the material's flow.
	D>20 mm V=60 mm/min N=430 rpm		A defect in the shape of a tunnel was observed on the welded sample. This occurrence is due to excessive heat generation and insufficient flow of material.

Table 4.2: Table showing selected input parameters with their upper and lower limits.

Input Variable	Notation	Units	Lower Limit	Upper Limit
Welding speed	V	mm/min	60	210
Tool rotational speed	N	rpm	430	750
Tool shoulder diameter	D	mm	15	20

Table 4.3: Selected process parameters with their levels

Selected parameter	Notation	Units	Levels		
			1	2	3
Welding speed	V	mm/min	60	110	210
Tool rotational speed	N	rpm	430	550	750
Shoulder diameter	D	mm	15	18	20

4.6 SELECTION OF ORTHOGONAL ARRAY

Taguchi's OA is a highly effective approach in experimental design for determining the most favorable combination of factors and their respective levels to achieve optimal outcomes. This approach can help researchers minimize the cost of experimentation while maximizing accuracy. In the current study, 3 factors with 3 levels are there. To choose an OA, a few options to choose from in Taguchi's OA, but choosing the right one depends on the desired outcome and the available resources.

One of the most common OAs used in experimental design is the L9 array. The L9 array is suitable when there are only a few factors that need to be tested, and each of these factors has only a few levels. The L9 array is designed to accommodate up to 3 factors, each with 3 levels. This design can efficiently produce an accurate analysis of the experimental results by minimizing the number of required experiments, which can help reduce the overall cost of experimentation. In addition, the L9 array has an efficient structure that allows for a straightforward analysis of the results, which can help save time. The L9 OA by Taguchi was selected as the experimental design method for the current research. Table 4.4 presents the OA, with the coded and actual values.

Table 4.4: Design matrix used for the experimentation

Run order	Coded values			Original values		
	V	N	D	V	N	D
1	1	1	1	60	430	15
2	1	2	2	60	550	18
3	1	3	3	60	750	20
4	2	1	2	110	430	18
5	2	2	3	110	550	20
6	2	3	1	110	750	15
7	3	1	3	210	430	20
8	3	2	1	210	550	15
9	3	3	2	210	750	18

While the L27 OA can also be used for testing variables with three levels, the number of required experiments becomes very large, especially if three replicates are used. Therefore, the L9 OA is often preferred as it provides sufficient information without conducting an excessively large number of experiments.

4.6.1 Finalizing the number of replicates

The determination of the suitable number of replicates in an FSW experiment relies on multiple factors, such as the variability of the welded material, the desired level of accuracy, and the available resources for experimenting.

One of the primary considerations when determining the number of replicates in an FSW experiment is the variability of the material being welded. Another important factor to consider when determining the number of replicates in an FSW experiment is the desired level of precision. Precision can be measured in several ways, including repeatability and reproducibility. Repeatability refers to the ability to obtain consistent results from the same operator using the same equipment, while reproducibility refers to the ability to obtain consistent results across different operators and equipment. To achieve high levels of repeatability and reproducibility in FSW experiments, a larger number of replicates may be required. (Liu et al., 2014)

The resources available for the experiment are also an important consideration when determining the number of replicates in an FSW experiment. Resources such as time, equipment, and funding can limit the number of replicates that can be performed. In some cases, it may be necessary to balance the desired level of precision with the available resources when deciding on the number of replicates.

In general, it is recommended to use at least three replicates in FSW experiments to achieve statistically significant results. It is important to ensure that the replicates are independent and randomly assigned to treatment groups to minimize bias and increase the accuracy of the results. For this study, three replicates were chosen for each condition. Thus, a total of 27 welding runs were conducted.

4.6.2 Run order

The 27 plates were welded in a specific order determined by a computer program after being randomized. Table 4.5 shows the run order followed for experimentation.

To prevent the impact of uncontrolled factors like tool wear, voltage fluctuation, the non-uniform surface of plates being welded, and ambient temperature, it is advisable to randomize the sequence of experimentation. These variables, which can vary with time, may have a considerable impact on the outcome. In case the order of experimentation is not randomized, the DOE may falsely indicate the influence of factors that are caused by uncontrolled variables that coincidentally change at the same time.

The welding process took place over three working shifts, with attempts made to maintain identical working conditions each day. The machine's lubrication, cleanliness, and other conditions were kept constant. The machine was operated by the same operator on all three days, and there were no significant changes in meteorological conditions. This eliminated the possibility of any ambient factors influencing the results.

Table 4.5: Run order and the process parameters corresponding to the run order

Run order	Welding speed (mm/min)	Rotational speed (rpm)	Tool shoulder diameter (mm)	Run order	Welding speed (mm/min)	Rotational speed (rpm)	Tool shoulder diameter (mm)
1	110	750	15	15	110	550	20
2	60	550	18	16	210	550	15
3	210	550	15	17	210	750	18
4	60	430	15	18	210	750	18
5	210	430	20	19	60	750	20
6	210	430	20	20	110	430	18
7	110	430	18	21	110	430	18
8	60	430	15	22	110	750	15
9	60	750	20	23	60	550	18
10	210	750	18	24	60	550	18
11	210	430	20	25	60	750	20
12	110	550	20	26	60	430	15
13	210	550	15	27	110	750	15
14	110	550	20				

4.7 PROCEDURE FOR CARRYING OUT THE EXPERIMENT

The experimentation phase involved three different types of experiments. The initial experiments focused on selecting the appropriate tool material and geometry to assess the feasibility of the process. Subsequently, a second set of experiments was conducted to determine the optimal input parameters and their respective levels to achieve defect-free welds. Finally, a series of experiments based on the experimental design were performed to examine the influence of process parameters on the weld quality.

The next section will discuss the workpiece material, the material of the backing plate, the procedure followed to conduct the experiments, the visual examination procedure followed for testing the weld quality, and taking the test coupons for final testing of weld integrity.

4.7.1 Workpiece material

The experimental material selected for the study was a 3 mm thick carbon steel plate, specifically AISI 1018 steel. The chosen steel grade, produced by the Steel Authority of India Limited (SAIL), was characterized by its chemical composition and mechanical properties, as outlined in Table 4.6.

Table 4.6: Chemical composition (wt%) and mechanical properties of the base metal

C	S	Mn	P	Fe	Ultimate tensile strength (MPa)	Yield strength (MPa)	% elongation
0.18	0.03	0.65	0.04	Bal	435	280	18

The plates that needed to be welded had dimensions of 200 x 40 x 3 mm as illustrated by Figure 4.10. These plates were cut from a larger plate with a standard size of 6'x4', which is provided by SAIL. A shearing machine was used to cut the plates to the desired size, and care was taken to ensure that the direction of shearing was consistent to balance out any differences in the properties of the material. The sharp edges of the plates were smoothed out. A butt joint was prepared by keeping the two plates of the same dimensions together using a fixture.
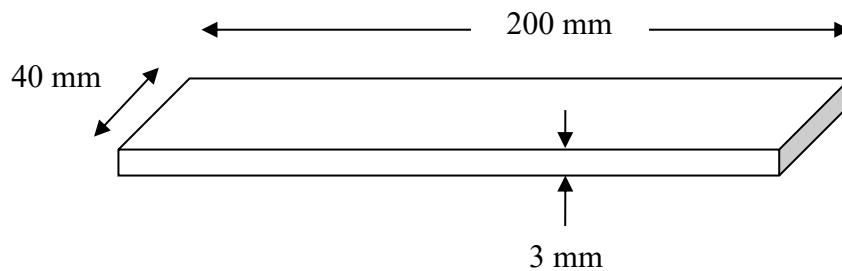
Figure 4.10: Dimensions of the plates used for welding

Originally, the plates were made using a rolling process, which resulted in the presence of mill scales on them. These scales are difficult to get rid of and can negatively impact welds. However, the decision was made to remove the scales from the relevant area of the workpiece, specifically the material that would be subjected to the tool shoulder. To do this, a surface grinder was used to remove the material, and the plates were manually pressed against them to remove the mill scales. Care was taken to ensure that the scales were also removed from the

back of the plates and the transverse section. Figure 4.11 shows the cleaned plate after the process was completed.

Figure 4.11: Plate with the edges cleaned and ready for welding

4.7.2   Specifications of the backing plate

In the FSW process, it is common to utilize a backing plate during welding. This is because FSW involves the joining of two materials using a rotating tool that generates frictional heat and mechanical pressure to soften and mix the material. As a result, there is a need for a backing plate to be used to help contain and support the materials during the welding process.

The backing plate serves the dual role of providing support to the weld and facilitating the dissipation of generated heat. When a backing plate is used, it helps to reduce the amount of heat that is transferred to the adjacent material, preventing it from reaching its melting point or undergoing any undesirable thermal effects. It is crucial because excessive heat can result in material deformation or undesired alterations in its properties.

Furthermore, the backing plate also helps to maintain the alignment and material's positioning during FSW. This is especially crucial when working with thin materials or when attempting to join materials with different thicknesses. The presence of a backing plate offers a stable foundation for the materials being joined and helps prevent any potential warping or distortion that could arise during welding.

The backing plate utilized in the process was composed of mild steel and measured 220 x 100 x 6 mm. To simplify the removal of the plates after welding, the backing plate was extended slightly. The surface grinder was used to eliminate the mill scales from the backing plate. It is crucial to remove the mill scale and thoroughly clean the backing plate surface because welding on an unclean surface can result in a Lazy S defect (Chen et al., 2006)

4.7.3 Friction-stir welding of the plates as per DOE

The 27 plates were welded using the same experimental conditions. The plates were fixed, and then a tool was placed directly over the intended path. The welding speed and tool rotation was set using the machine. The tool was rotated and then lowered into the workpiece at one end until it penetrated 0.2 mm into the material. Once in position, the tool rotated in the same spot for 10 seconds. Next, the tool was moved along the joint's path at the desired speed until it reached the end of the plates, after which it was removed and stopped.

After the welding, the plate was left to cool for a while before being removed from the fixture. Monitoring the tool position using a digital readout system was implemented to ensure precise control over the tool shoulder plunge in the x, y, and z axes. The digital display had excellent resolution, which made it possible to control the shoulder plunge accurately. To avoid the initial tool temperature from affecting the next experiments, the tool, tool holder, and fixture were allowed to cool until the beginning of the next experiment. Figure 4.12 (a) indicates the setup of FSW and Figure 4.12 (b) indicates the welded plate.
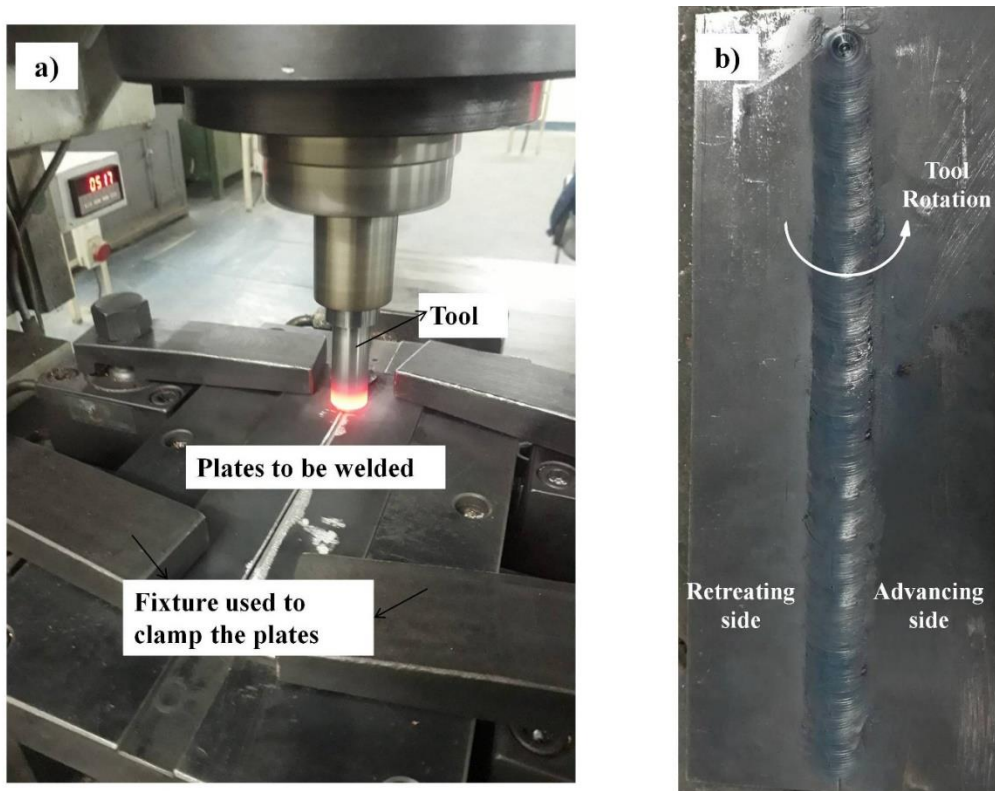
Figure 4.12: a) Friction stir welding setup b) Friction stir welded steel plate

4.8 TESTING OF THE WELDS

Testing of friction stir welds is a critical step in ensuring the quality and reliability of the weld. There are various types of testing methods available for friction stir welds, including destructive and non-destructive testing methods. The selection of the testing technique is influenced by the specific needs of the application, the characteristics of the material being welded, and the desired level of accuracy.

Non-destructive testing methods, on the other hand, do not require the destruction of the specimen and are used to evaluate the integrity of the weld without causing damage. One commonly used non-destructive testing method is visual inspection. Visual inspection is an essential quality control technique used to verify the weld quality and detect any defects in the weld. The visual inspection procedure entails inspecting the surface of the weld for visible flaws, including cracks, air pockets, incomplete fusion, and other surface irregularities. It is a non-destructive testing approach that enables the detection of potential problems before subjecting the weld to additional testing or practical use.

Destructive testing methods involve testing the weld by destroying the specimen to evaluate its mechanical properties. Tensile testing is a widely utilized method for evaluating the strength of friction stir welds. This test allows for the assessment of critical parameters including the UTS elongation, and the reduction in the weld area. Another destructive testing method is the bend test, which involves bending the sample to determine the ductility and soundness of the weld.

Selecting the appropriate testing method for friction stir welds depends on various factors, such as the material category, weld thickness, and desired level of accuracy. It is also essential to follow established standards and guidelines for testing friction stir welds to ensure consistency and accuracy in the testing process.

4.8.1 Visual examination of the welds

The welds were subjected to a visual examination test, which is a powerful tool that should not be underestimated. This examination involves scrutinizing the weld for any visible flaws, either with the naked eye or with a magnifying instrument. Inspecting the surface of the welded joint is essential to determine its overall acceptability. After welding the plates, they underwent careful inspection for any defects. Despite using a magnifying glass, no flaws were detected in

any of the welds. Furthermore, there was no distortion or significant flash on any of the plates, and all 27 welds were thoroughly penetrated.

4.8.2 Test coupon for further testing

To make accurate comparisons of various welds, it's crucial to extract test specimens from the same spots for each weld being tested. This is necessary to eliminate any discrepancies that may arise due to reasons like machine bed misalignment or varying amounts of deflection in the machine bed under the vertical thrust experienced during welding. By consistently extracting the test pieces from the same locations, any effects of such variations can be balanced out for all the plates that have been welded.
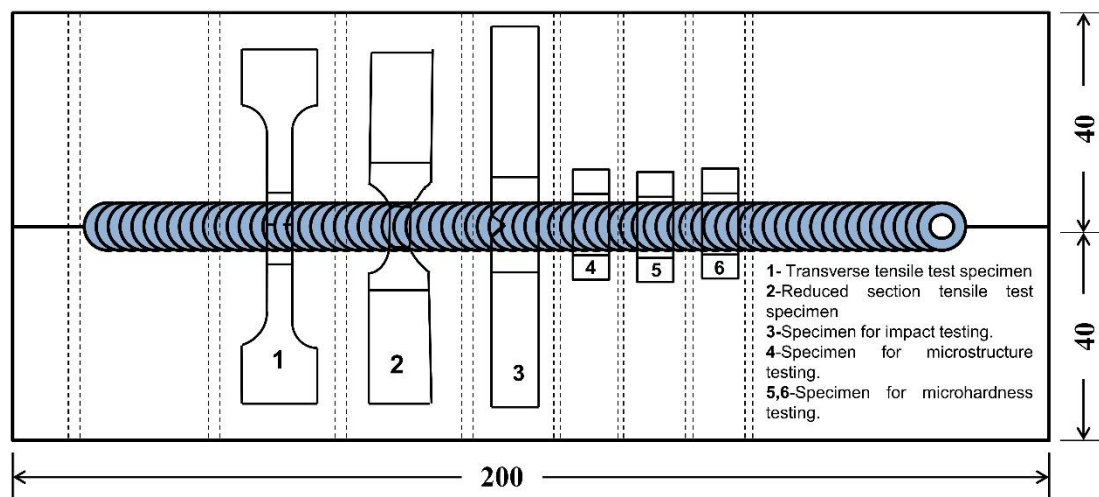
Figure 4.13: Sample extraction for weld integrity testing

To evaluate the integrity of the weld, samples were collected from the plates as per the plan depicted in Figure 4.13, with the initial 25 mm of the welded specimen discarded. This is because the process may take some time to stabilize, and so the samples were extracted from the section where the process is expected to be well-established. The test samples were intended to be obtained from the regions beyond this initial segment. An allowance of 3 mm was provided for the material wasted during the sawing of the test plate. For the preparation of tensile test specimens, two strips of 15 mm each were taken out, while another strip of 15 mm was used for creating an impact test specimen. Three strips, one of 5 mm and the other two of 8 mm each, were removed to produce the test pieces for microscopic examinations and microhardness testing.

CHAPTER 5   TESTING WELD INTEGRITY AND ANALYSIS OF RESULTS

5.1 TESTING WELD INTEGRITY

When a weld is in use, it is crucial to monitor its behavior over time. Once initial testing is completed, it is vital to examine the weld integrity to ensure that it is safe and strong. These testing methods are standardized and provide valuable information about weld characteristics. Assessing the integrity of the weld metal yields qualitative data that can be compared to mechanical properties for further analysis.

The three most frequently employed tests for welding evaluation are tensile, impact, and fatigue testing. Tensile testing serves to assess the mechanical strength and ductility of the welded joint, gauging its ability to withstand tensile forces without succumbing to failure. This evaluation is critical in applications where the anticipated loads are predominantly tensile, such as in structural components within the aerospace, automotive, or maritime sectors. In parallel, impact testing assumes an equally pivotal role as it aids in the assessment of a welded joint's resilience when subjected to sudden or impulsive loads. This becomes especially crucial in scenarios where components may encounter dynamic stresses, such as ensuring crashworthiness in automotive structures or enhancing the impact resistance of marine and offshore installations. Fatigue testing is vital for evaluating the long-term durability and reliability of FSW joints. It helps determine how well a welded joint can withstand repeated loading and cyclic stress without experiencing fatigue failure.

Although there exist other methods like creep testing, wear testing, and torsion testing, they are primarily used to assess welds in specialized service environments. For a welding procedure to be deemed fit for industrial applications, it must undergo the three most common tests: tensile, impact, and fatigue. Conducting metallurgical tests along with mechanical tests yields a comprehensive understanding of the process, which is essential for determining its suitability for widespread industrial use.

All 27 welds were tested using both tensile testing and impact testing, as per DOE requirements. However, the fatigue test was specifically carried out to compare the weld's response to fatigue loading with the base material.

5.1.1 Tensile testing of welds

Tensile testing plays a significant role in assessing the mechanical characteristics of FSW. During welding, a tool with rotational motion is employed to generate frictional heat and transform the material through mechanical deformation, resulting in bond formation. Tensile testing is essential to ensure that welds have sufficient strength to withstand the stresses they will be subjected to in their intended application.

Tensile testing of the welded specimen is typically conducted according to the ASTM E8 standard (ASTM E8, 2017), which provides guidelines for preparing and testing specimens. The standard specifies the dimensions of the specimen, the testing procedure, and the equipment required to conduct the test. Typically, the FSW sample is extracted from the welded joint and processed according to the specific guidelines.

During the tensile test, the FSW specimen is gripped at each end by the testing machine's jaws, and a tensile load is applied. As the load is increased, the specimen experiences deformation until it reaches its maximum load capacity. At this point, the specimen fractures, and the load is recorded as the ultimate tensile strength. The examination also yields important mechanical properties, including yield strength, elongation, and percentage reduction in the area.

The tensile test results for FSW can be influenced by various factors, including the chosen welding parameters, tool design, and specimen preparation. Adjusting the welding parameters, such as the rotational speed of the tool, the traverse speed, and the axial force, can impact both the weld quality. For instance, higher tool rotational speeds can result in a more refined grain structure and increased strength (Sharma et al., 2019; Sundar Raju et al., 2020), while higher traverse speeds may lead to reduced strength and ductility (Muthu & Jayabalan, 2015; Fotouhi et al., 2014; Bisadi et al., 2015; Liu et al., 2008)

The strength and mechanical properties of the FSW can also be greatly impacted by tool design. The specific tool characteristics like the dimensions of the shoulder and pin, can impact heat generation and material displacement during the welding process, ultimately affecting the weld quality. Furthermore, the preparation of the specimen plays a crucial role in obtaining accurate test results. If the specimen is not adequately prepared, including the presence of surface defects or excessive residual stress, it can have an impact on the outcome of the test.

Tensile testing of welds is an important quality control measure for many industries, including aerospace, automotive, and marine. The results of the test can help to ensure that the FSW is suitable for its intended application and meets the required specifications. Furthermore, it can also help to identify any defects or weaknesses in the FSW, which can be corrected before the final product is produced.

5.1.1.1 Transverse tensile testing of weldments

To successfully implement any welding technology, it is crucial to ensure that the joint it produces is highly efficient. It is expected that a weld joint, which is free of defects and produced according to the welding procedure specification, should be stronger than the original base metal. When subject to a load, the fracture is expected to happen either in the HAZ or the base material area, rather than within the weld itself. To identify the weakest area within the weldment, transverse tensile test specimens are created, with the gauge length of the specimen including the weld nugget, heat-affected zone, and a section of the unaffected base metal.

The American Society of Testing of Materials (ASTM) standard E-8 (M) was utilized to prepare transverse tensile test specimens. As the specimen was 3 mm thick, therefore a sub-size specimen specified in the ASTM standard was chosen. Figure 5.1 depicts the sub-size specimens, which had a width of 6mm and a gauge length of 32 mm. The specimens were fabricated in such a way that the weld nugget was positioned centrally within the gauge length. The transverse tensile testing was performed as per the ASTM E8 standard.
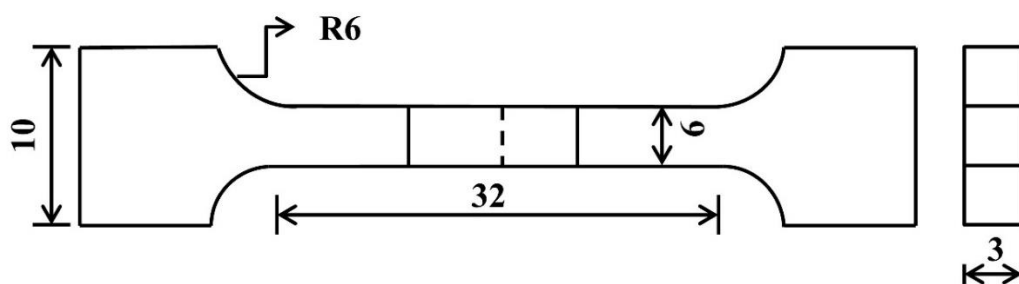
Figure 5.1: Dimensions of the prepared test specimen for transverse tensile

A total of 28 tensile test samples were created, with 27 being extracted from the welded plates and one exclusively prepared from the base metal. Figure 5.2 presents the transverse tensile test specimen before and after fracture, denoted as (a) and (b) respectively.
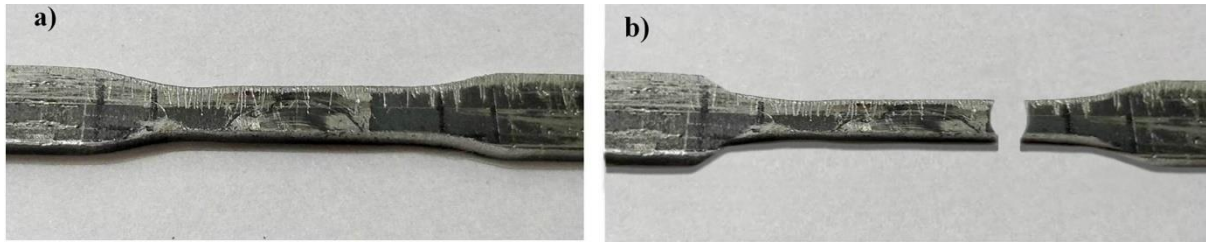
Figure 5.2: a) Test specimen for transverse tensile testing; b) broken transverse tensile test specimen

5.1.1.2 Testing procedure

Tensile testing was performed following the E-8(M) standard of ASTM on a Zwick/Roell tensile testing machine, which had a capacity of 250 kN. The testing procedures adhered to ISO 9000 and CE Conformity standards. The specimens were gripped in a manner that ensured the gripping length was identical in all cases and slightly less than the gripping section of the specimen.

Due to the 32 mm gauge length of the specimen, the testing speed was limited to a range of 1.5 mm/min to 15 m/min. A testing speed that is too slow wastes machine time without enhancing results, whereas a speed that is too fast produces inconsistent results. Therefore, the testing speed was set to 10 mm/min, which delivered reliable and consistent outcomes.

5.1.1.3 Testing results

All 27 tensile test specimens fractured in the base metal region and HAZ was the strongest region than the base metal. The specimens broke in the unaffected base metal area on either side of the weld and HAZ, without a preference for a specific side. The fractures occurred randomly on one of the two sides, and the precise location of the fracture within the unaffected base metal area was unpredictable.

Tensile test specimens made from base metal (having no welding in its entire gauge length) were also tested along with the specimens taken from welds.

When the specimen was made only from the base metal, it broke at the center of the gauge length. The results of the tensile tests conducted on transverse tensile test specimens are displayed in Table 5.1.

Table 5.1: Results of ultimate tensile strength for transverse tensile test specimen

Run Order	Welding speed(mm/min)	Rotational speed (rpm)	Tool shoulder diameter (mm)	Ultimate tensile strength (MPa)	Percentage elongation
1	110	750	15	407.7	22.22
2	60	550	18	445.7	22.66
3	210	550	15	409.8	21.75
4	60	430	15	410.8	22.78
5	210	430	20	409.7	20.78
6	210	430	20	407.3	21.34
7	110	430	18	443.2	22.88
8	60	430	15	407.8	20.72
9	60	750	20	416.5	19.63
10	210	750	18	417.8	20.31
11	210	430	20	410.8	21.63
12	110	550	20	402.3	20.41
13	210	550	15	404.7	21.44
14	110	550	20	426.8	21.59
15	110	550	20	405.7	20.81
16	210	550	15	415.8	21.81
17	210	750	18	416.6	22.19
18	210	750	18	418.9	21.53
19	60	750	20	406.2	21.32
20	110	430	18	423.3	25.69
21	110	430	18	366.6	21.38
22	110	750	15	405.4	23.22
23	60	550	18	425.3	20.11
24	60	550	18	417.9	20.13
25	60	750	20	419.5	22.78
26	60	430	15	405.1	19.29
27	110	750	15	410.8	21.20
Base metal				419.20	20.27

5.1.2 Reduced section tensile testing of welds

To evaluate the strength of weld nuggets under different welding conditions, it is suggested that all the weld metal tensile test samples should be prepared and examined. However, due to the limited thickness of the welded plates, it becomes challenging to prepare all the test specimens. To tackle this issue, reduced section tensile test specimens are prepared which are widely used by researchers in this field. These specimens are crucial in determining the properties of the weld nugget and have gained significant popularity among researchers (Lakshminarayanan et al., 2010; Babu et al., 2017).

To ensure fracture occurred within the weld nugget, the section of the specimen at the weld nugget was appropriately reduced. The length of the reduced section, also known as the gauge length, was set in a way that it consisted entirely of the weld nugget. Since the tool pin diameter was 3 mm, it was certain that the width of the weld nugget would be at least 3 mm. Thus, the reduced section's length was determined as 3 mm. The fillet's radius used for connecting the reduced section to the grip length was kept at 6 mm, which was the same as the fillet used in the ASTM standard tensile test specimen.

Figure 5.3 showcases the reduced tensile test specimen used for evaluation. The UTS of the weld nuggets was found to surpass that of the base metal. Nevertheless, there was considerable variation in the UTS values of the welds when different process parameters were employed.
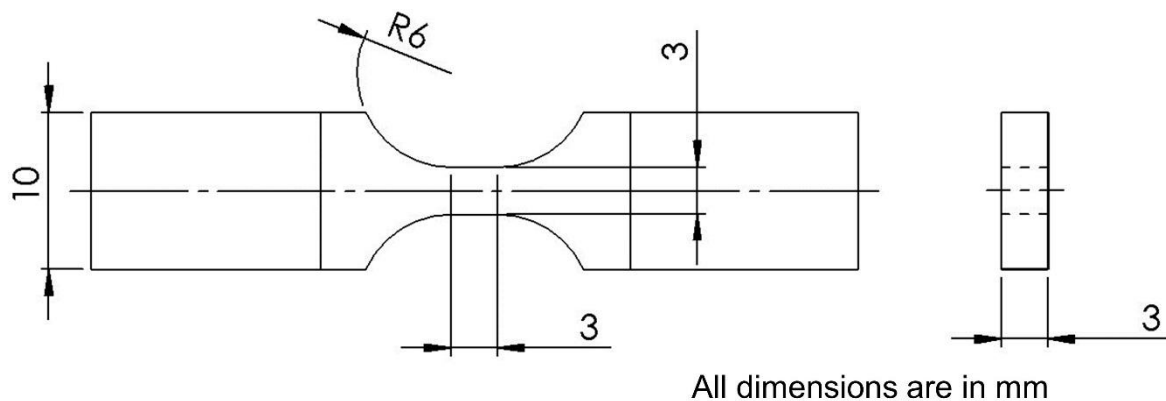
Figure 5.3: Dimensions of the reduced section tensile test specimen

5.1.2.1 Test procedure

The tensile testing was carried out as per the E-8 standard of the ASTM (ASTM E8, 2017) on Zwick/ Roell testing machine. The testing machine provided the measurements for ultimate strength and percentage elongation. The percentage elongation was calculated by measuring the final length of the fractured specimens. The broken pieces of the specimens were carefully aligned, and the final gauge length was measured using vernier calipers. The percentage reduction in area was also measured as mentioned above (i.e., by individually putting the broken ends of the specimens together and measuring the area of the cross-section at the necked section.

5.1.2.2 Results

The tensile testing performed on the reduced section test specimens consistently resulted in consistent and predictable outcomes, demonstrating that the UTS of the weld nugget consistently exceeded that of the base metal. However, notable discrepancies were found in the UTS values produced under different welding process parameters. To evaluate this further, a total of 27 reduced section tensile test specimens were subjected to tensile testing, and outcomes were recorded in Table 5.2.

The observed variations in the UTS values of the welds can be attributed to the different welding conditions used during the testing procedure. Examining the data presented in Table 5.2 will offer valuable insights into the correlation between welding process parameters and the resulting UTS values. Analyzing the data may reveal patterns and trends that can enhance our understanding of the ideal conditions for attaining the desired weld strength.

Table 5.2: Results of UTS, % elongation, and % reduction in area for reduced section tensile specimens

Run Order	V	N	D	UTS (MPa)	% elongation	% reduction in area	Run Order	V	N	D	UTS (MPa)	% elongation	% reduction in area
1	110	750	15	571.34	25.27	51.98	15	110	550	20	534.88	25.94	25.29
2	60	550	18	455.40	21.67	50.03	16	210	550	15	520.34	27.77	77.48
3	210	550	15	523.80	23.21	69.87	17	210	750	18	551.67	22.67	69.42
4	60	430	15	543.78	21.34	40.86	18	210	750	18	574.64	26.10	50.39
5	210	430	20	556.56	22.44	47.84	19	60	750	20	520.34	21.27	37.83
6	210	430	20	551.80	27.96	77.70	20	110	430	18	524.67	29.63	72.16
7	110	430	18	539.70	21.27	51.87	21	110	430	18	523.52	23.27	53.64
8	60	430	15	529.80	19.57	48.44	22	110	750	15	527.34	23.27	38.69
9	60	750	20	539.80	18.13	31.33	23	60	550	18	462.80	22.31	54.57
10	210	750	18	567.67	25.56	79.42	24	60	550	18	472.60	20.77	32.67
11	210	430	20	568.92	27.67	57.92	25	60	750	20	531.45	19.93	59.90
12	110	550	20	518.52	22.37	69.70	26	60	430	15	533.65	22.77	46.74
13	210	550	15	531.30	23.00	44.69	27	110	750	15	551.75	21.93	53.34
14	110	550	20	527.45	22.67	64.92	Base metal				436.54	21.78	54.72

5.1.3   Impact testing of welds

There is a tendency for ductile material to fail in a brittle manner in certain situations. The brittleness of ductile materials can be attributed to the presence of a tri-axial stress state, low temperatures, and high rates of strain. The study of this behavior of the material is particularly important for a welded structure since many failures of this nature have occurred in welded structures. The failure of the welded liberty ships and T-2 tankers led to the belief that the welded constructions were not good enough for critical applications. It becomes very important that a new welding process or procedure must be thoroughly checked for its tendency to fail in a brittle manner. The difference in the quality of the weld, based on the tendency to fail in a brittle manner, cannot be known through tensile testing. Thus, impact testing of welds becomes essential whenever the quality of a weld is to be judged.

5.1.3.1 Charpy impact testing of welds

The tri-axial state of stress often exists in service due to a notch present on the surface. The effect of such a notch in making the material susceptible to brittle fracture is accentuated if the rate of loading is high. Keeping in mind, various types of notched impact tests are designed and used in practice, to ascertain the tendency of a material to fail in a brittle manner. Although the results of the notched impact tests are not directly used in the design of components, it is very useful when comparing the behavior of different materials.

Two types of tests namely the Charpy test and the Izod test have been standardized. Essentially in an impact test a suitable specimen is placed between a set of anvils to receive the blow of the moving mass. The blow is usually given by a heavy mass swinging like a pendulum. The moving mass has sufficient energy to break the specimen placed in its path. A device is used for measuring the energy absorbed by the specimen during fracture. Charpy tests with V-notch specimens are very popular for ferrous alloys and were used in the present study.

5.1.3.2 Test procedure

The Charpy impact test was conducted as per the E23 standard of ASTM (ASTM E23, 2016), using a Zwick/Roell computer-controlled impact testing machine. Since the available material for testing was obtained from 3 mm thick welded plates, subsidized specimens were fabricated for the purpose. The test specimens were manufactured according to section A3 of the ASTM standard E23-07a, which outlines the specifications for reduced-size impact test samples. The

specimens had measurements of 10 mm in width, 2.5 mm in thickness, and 55 mm in length, with a centrally located notch within the weld nugget. Figure 5.4 depicts the dimensions of the fabricated test specimen.
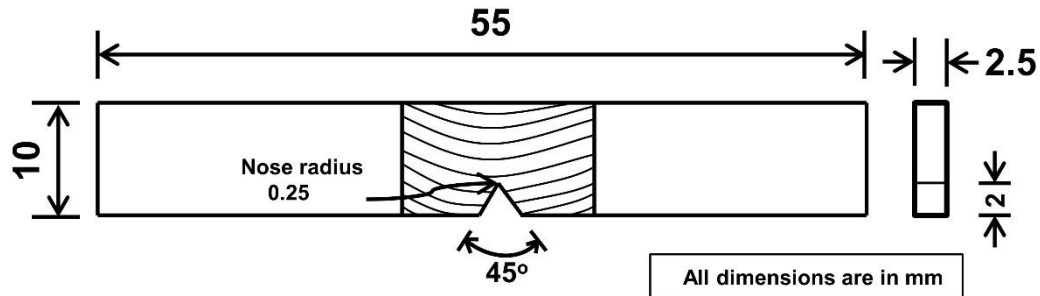
Figure 5.4: Dimensions of the subsidized impact test specimen

The specimens were obtained from the test coupon using a power saw. The initial dimensions of the specimens were shaped using a shaper machine, and the final dimensions were achieved using a surface grinder. Precautions were taken to ensure that the temperature of the specimens remained unaffected during the machining process. The 2 mm deep notch with a radius of 0.25 mm was fabricated on a horizontal milling machine. All 27 specimens were clamped together in a vice and processed to eliminate any irregularities in the dimensions of the notch.

The Zwick impact testing machine is equipped with various hammer sizes, offering energies ranging from 15 J to 50 J. In this particular test, a 50 J hammer was utilized. The use of smaller hammers was not suitable since impact test results are considered unreliable if the energy absorbed during fracture exceeds 80% of the hammer's rated energy. To account for friction and air resistance, the machine was initially calibrated by swinging the hammer without a specimen on the anvil. This measurement was stored in the computer and adjusted during the actual impact tests.

The 27 test specimens underwent impact testing in a randomized sequence. The impact testing machine registered the impact energy absorbed during fracture, taking into account the correction factor for factors like friction. The recorded energy absorption values were also presented as a percentage of the total energy (rated energy of the hammer) to identify any readings surpassing 80% of the hammer's rated energy.

5.1.3.3 Results

The results of the impact test conducted on all 27 specimens have been compiled and presented in Table 5.3.

Table 5.3: Results of impact testing of welds

Run Order	V	N	D	Impact energy (J)	Impact energy (%)	Run Order	V	N	D	Impact energy (J)	Impact energy (%)
1	110	750	15	32.97	64.98	15	110	550	20	30.42	60.84
2	60	550	18	27.92	53.82	16	210	550	15	33.15	66.30
3	210	550	15	33.10	66.20	17	210	750	18	31.98	63.96
4	60	430	15	27.39	54.78	18	210	750	18	32.02	64.04
5	210	430	20	32.63	65.26	19	60	750	20	30.58	61.16
6	210	430	20	36.35	72.70	20	110	430	18	30.81	61.62
7	110	430	18	28.52	57.04	21	110	430	18	28.30	56.60
8	60	430	15	29.71	59.42	22	110	750	15	34.90	69.80
9	60	750	20	27.28	50.36	23	60	550	18	27.45	54.90
10	210	750	18	32.34	64.68	24	60	550	18	31.97	63.94
11	210	430	20	33.64	67.28	25	60	750	20	28.46	56.94
12	110	550	20	30.94	61.88	26	60	430	15	31.82	63.64
13	210	550	15	32.80	65.60	27	110	750	15	33.87	67.74
14	110	550	20	33.00	66.00	Base metal				26.29	52.59

All 27 impact specimens were subjected to the test and experienced bending without fracturing into separate halves, as depicted in Figure 5.5. None of the cases surpassed 80% of the hammer's rated energy in terms of absorbed impact energy. The welds exhibited a significant improvement in energy absorption compared to the base metal. It should be emphasized that there was considerable variation in the impact energy measurements among the specimens.
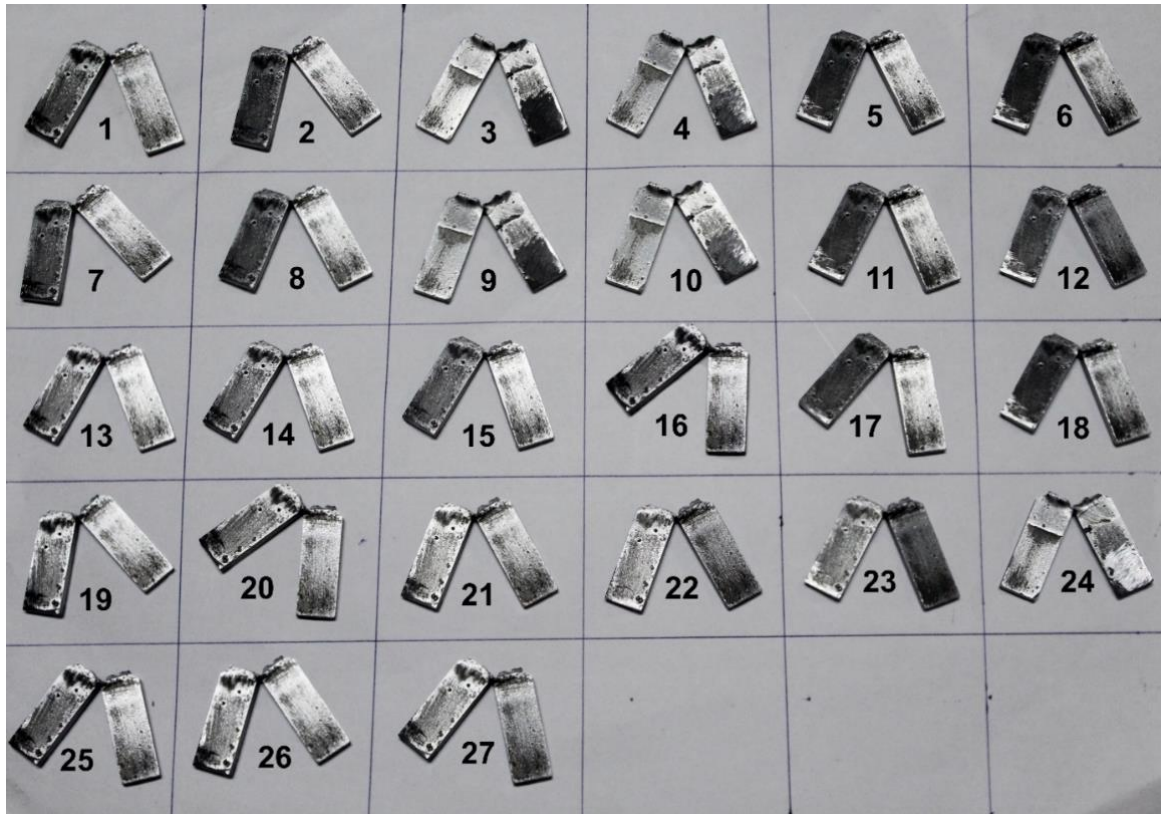
Figure 5.5: Fractured impact test specimens.

5.1.3.4 Analysis of the fractured surface of the impact test specimens

SEM is a powerful tool commonly used to investigate the fractography of fractured specimens. In the case of fractured specimens resulting from an impact test on friction-stir welding of steels, the SEM can reveal valuable information about the nature and mode of the fracture. When observing the specimens under a magnification of 800X, pronounced dimpled regions were observed as shown in Figure 5.6, which are indicative of ductile fracture.
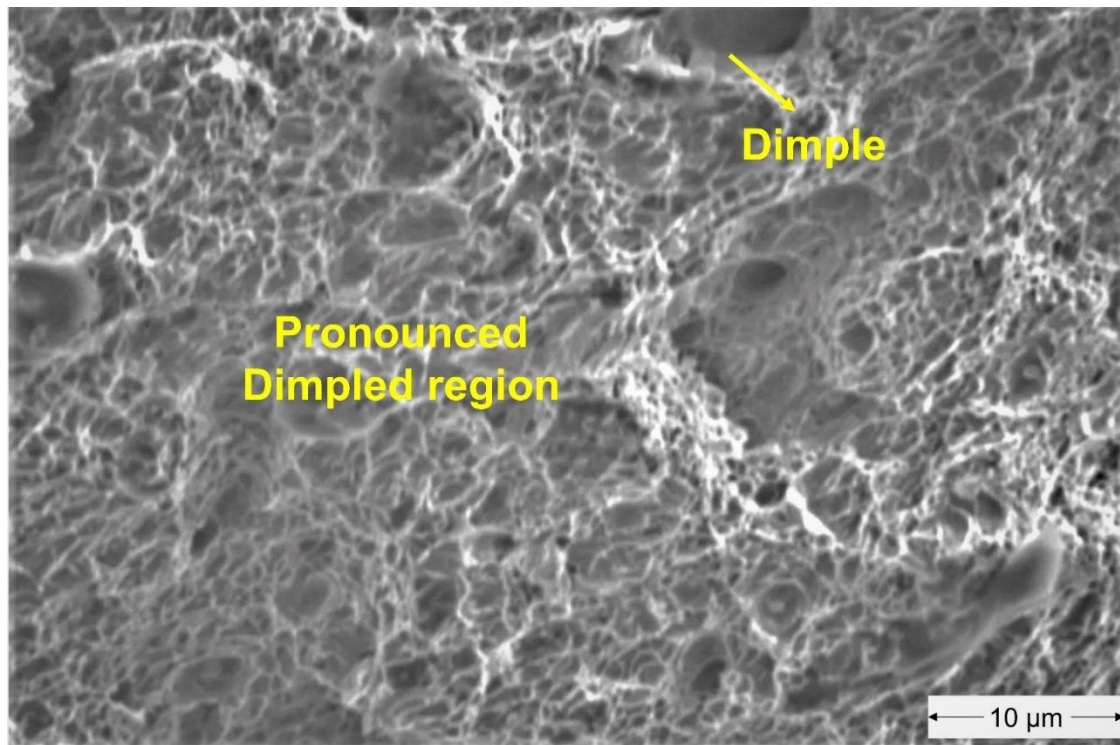
Figure 5.6: Fractography of the weld specimen broken during impact testing (800X)

5.1.4 FATIGUE TEST

The fatigue strength analysis utilized a material testing machine (MTM) with the ability to apply tensile loads for measuring the fatigue stress intensity of welds and the base metal. The MTM employed a closed-loop single servo hydraulic controller with a load capacity of ±10 tonnes. Specifically designed for testing materials under static and dynamic conditions, the digital system of the MTM was utilized. Two compact tension (C(T)) specimens, prepared according to ASTM E647 (ASTM E647,2018), were employed for the fatigue strength test. The C(T) specimen was chosen due to its advantage of requiring a minimal amount of test material while evaluating crack growth behavior. Conforming to the ASTM standard, a single-edge notch was incorporated into the C(T) specimen. Figure 5.7 (a) and Figure 5.7 (b) present the dimensional details and an isometric view of the prepared specimen, respectively. To facilitate in-plane rotations of the loaded specimen, a clevis-pin assembly was employed at the top and bottom. It's important to note that this specimen and loading arrangement were solely used for tension-tension loading. The assembly of the clevis and pin for the fatigue test is depicted in Figure 5.7 (c). The specimens underwent testing at stress ratios (R) of 0.1 and 0.2, with a frequency of 10 Hz and a yield strength of 286 MPa. The maximum load applied was 6.5 kN, while the minimum loads for both conditions were set at 0.65 kN and 1.30 kN. The specimens were securely gripped using a high-power hydraulic system within the MTM.

Tensile loads were then applied to the samples, resulting in crack initiation at the single-edge notch and subsequent shearing of the specimens. The stress intensity factor (ΔK) and fatigue crack growth rate (da/dN) for the C(T) specimens were calculated using equation (5.1) and equation (5.2), respectively, following the ASTM standards. The fractured fatigue test specimens are illustrated in Figure 5.8.
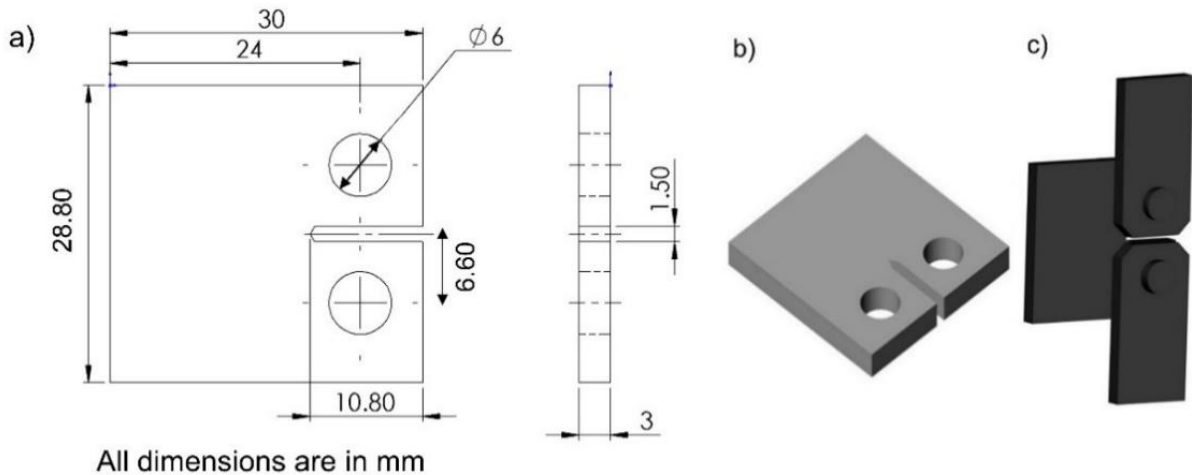
Figure 5.7: a) Dimensions of the fatigue test sample, b) Isometric illustration of the fatigue test sample, and c) Clevis and pin setup used for fatigue testing.

$$\Delta K = \frac{\Delta P(2+\beta)}{\beta\sqrt{w}(1-\beta)^{3/2}}(0.866+4.64\beta-13.32\beta^2+14.72\beta^3-5.6\beta^4) \tag{5.1}$$

Where, $\beta=\frac{a}{w}$

$\Delta P = P_{max} - P_{min}$

The fatigue crack growth rate (da/dN) is determined by calculating the ratio between the change in crack length and the difference in the number of cycles.

$$\frac{da}{dN}=\frac{a_f-a_i}{N_f-N_i} \tag{5.2}$$

Where a_f is the final crack length

a_i is the initial crack length

N_f is the final number of cycles

N_i is the initial number of cycles
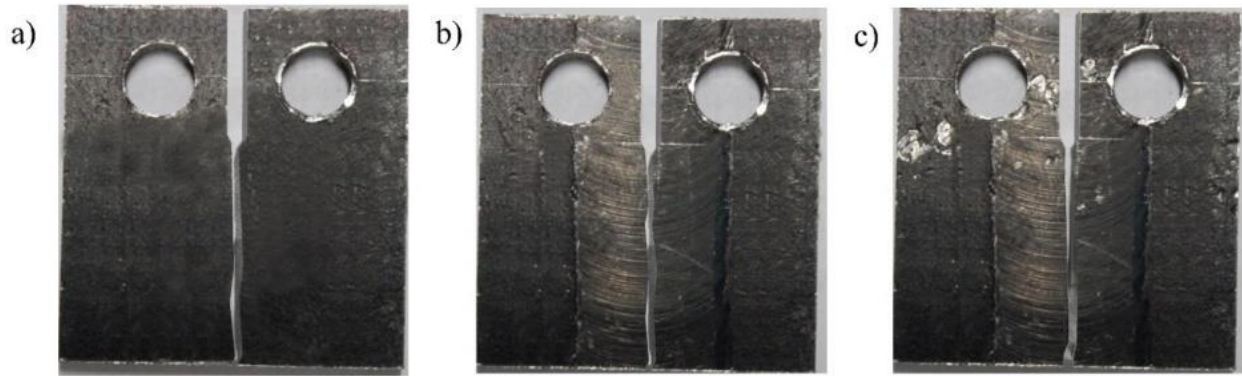
Figure 5.8: a) Fractured fatigue test specimen of BM b) Fractured fatigue test welded specimen with stress ratio=0.1 c) Fractured fatigue test welded specimen with stress ratio=0.2

5.2 ANALYSIS OF RESULTS

The study involved conducting various experiments using different parameters, with each combination of process parameters being repeated three times to ensure accuracy. However, the results of the mechanical testing were not consistent across each trial run. This could be due to uncontrolled factors, indicating inherent variability in the results. Alternatively, the changes made in the process parameters could also be responsible for the variation in results. The study aims to determine the root cause of the variability, whether it is due to changes made in the process parameters or inherent variability.

The present study proposes a general non-linear model, as shown in equation (5.3), that links mechanical properties to process parameters.

$$\text{Effect} = \text{Constant} + b_1(V) + b_2(V)^2 + b_3(N) + b_4(N)^2 + b_5(D) + b_6(D)^2 \tag{5.3}$$

The regression equation considered up to second-order terms due to having three levels of process parameters. The process parameters were expressed using coded notation. The three levels of parameters were assigned codes 1, 2, and 3 to represent the lowest, middle, and highest values, respectively. The reason for using coded values instead of actual values is to remove the influence of differences in parameter magnitudes on regression coefficients. The term "Effect" in the equation represents the mechanical properties being analyzed, such as UTS, % elongation, % reduction in area, and impact energy absorbed.

When performing the regression analysis, certain coefficients can be zero, indicating that those specific parameters have no impact on the mechanical property being analyzed. To carry out

this analysis, we used MINITAB 19 software along with standard t-tests, and we confirmed the software's results through independent calculations. Furthermore, a confidence level of 95% was employed to conduct an F-test, ensuring the adequacy of the data's conformity to the proposed model.

5.2.1 Analysis of tensile testing of welds

Based on the results of the transverse tensile testing, it was clear that the weld strength was higher than that of the base material, irrespective of the chosen process parameters. However, to accurately determine the strength of the weld nugget, reduced section tensile tests were conducted. The subsequent section presents a statistical analysis of the test results, including UTS, % elongation, and % reduction in area.

5.2.1.1 Influence of input parameters on the UTS of welds

To investigate the influence of different process parameters on the UTS of welds, ANOVA was employed. The results of this analysis are presented in Table 5.4, providing a comprehensive understanding of the relationship between the process parameters and the UTS of the welds.

Table 5.4: ANOVA table to identify the most influential factors affecting the UTS

Source	DF	Seq SS	Contribution	Adj SS	Adj MS	f-value	p-value
Regression	7	7162.60	99.25%	7162.60	1023.23	18.82	**0.176**
V	1	2411.61	33.42%	24.19	24.19	0.44	0.625
N	1	22.54	0.31%	3830.79	3830.79	70.47	0.075
D	1	3.07	0.04%	1025.37	1025.37	18.86	0.144
V*V	1	118.63	1.64%	118.63	118.63	2.18	0.379
N*N	1	3366.65	46.65%	3366.65	3366.65	61.93	0.080
D*D	1	621.52	8.61%	1116.97	1116.97	20.55	0.138
V*N	1	618.58	8.57%	618.58	618.58	11.38	0.183
Error	1	54.36	0.75%	54.36	54.36		
Total	8	7216.96	100.00%				

After analyzing Table 5.4, it becomes apparent that the model lacks statistical significance, as indicated by the p-value exceeding the threshold of 0.05 (with a 95% confidence level).

Moreover, the model incorporates insignificant terms that need to be pooled to determine their significance. Consequently, to address this issue, a more refined two-way interaction ANOVA was done, and the outcomes are presented in Table 5.5. This updated ANOVA approach allows for a more precise assessment of the significant factors influencing the UTS, aiding in the development of effective strategies for improving weld strength.

Table 5.5: ANOVA table for refined two-way interaction model for UTS

Source	DF	Seq SS	Contribution	Adj SS	Adj MS	f-value	p-value
Regression	3	5800.81	80.38%	5801	1933.6	6.83	**0.032**
V	1	2411.61	33.42%	2412	2411.6	8.51	0.033
N	1	22.54	0.31%	3220	3220.5	11.37	0.020
N*N	1	3366.65	46.65%	3367	3366.6	11.89	0.018
Error	5	1416.16	19.62%	1416	283.2		
Total	8	7216.96	100.00%				
$R_E=0.8965; R_E{}^2=0.8037; R_E{}^2 (adj)=0.6860$							

During the statistical analysis, the suitability of a model is evaluated through two indicators: the coefficient of determination ($R_E{}^2$) and the square root of the coefficient of determination (R_E). $R_E{}^2$ quantifies the portion of the variability in the data that can be accounted for in the regression model. A higher value of $R_E{}^2$ indicates a better model fit. To account for the number of terms in the model, an adjusted version of $R_E{}^2$, called $R_E{}^2$ (adj), is used. Unlike $R_E{}^2$, which always increases when a new term is added, $R_E{}^2$ (adj) only increases if the new term enhances the model beyond what would be expected by chance. The p-value indicates the likelihood of the independent variable occurring by chance rather than indicating an actual connection between the variables and the mechanical property under consideration. The p-value for the entire model is 0.032, indicating its adequacy as it is below the significance level of 0.05.

After analyzing the ANOVA results, it was observed that the UTS of the weld is influenced by both the welding speed and tool rotational speed. The effect of tool rotational speed on UTS was found to be nonlinear, as indicated by the significance of both the tool rotational speed and its square in the analysis of variance. In contrast, the welding speed showed a linear effect on UTS, with the square of the welding speed being deemed insignificant during the analysis. The

study also revealed that the tool shoulder diameter had no significant effect on UTS. Further analysis using regression yielded significant coefficients for the parameters that impact UTS, as outlined in Table 5.6.

Table 5.6: Values of coefficients of parameters for modeling UTS of welds

Term	Coefficient	Standard error	t-value	p-value
Constant	624.1	44.5	14.02	0.000
V	20.0	6.87	2.92	0.033
N	-162.2	48.1	-3.37	0.020
N*N	41.0	11.9	3.45	0.018

The statistical model for the UTS of the weld, based on regression analysis considering the coded process parameters, is presented by equation (5.4).

UTS= 624.1 + 20.0 V - 162.2 N + 41.0 N*N   (5.4)

The values of the process parameters in the statistical model are in coded form (1 for the lowest value, 2 for the middle value, and 3 for the highest value of process parameters).

Residual plots are useful tools for assessing the goodness of fit of a statistical model, and they can be especially informative when analyzing the UTS of welded joints. The residual plot is shown in Figure 5.9. The normal probability plot, 'versus fits' plot, histogram, and 'versus order' plot are commonly employed residual plots for analyzing the UTS. The four different residual plots are represented in Figure 5.9 (a, b, c, and d respectively). A normal probability plot reveals deviations from normality, with an ideal plot showing a straight line. 'Versus fit' plots typically identify patterns in the residuals, with a random scatter of points indicating a good fit. Finally, 'versus-order' plots reveal any trends in the residuals, with a horizontal line indicating no trend.
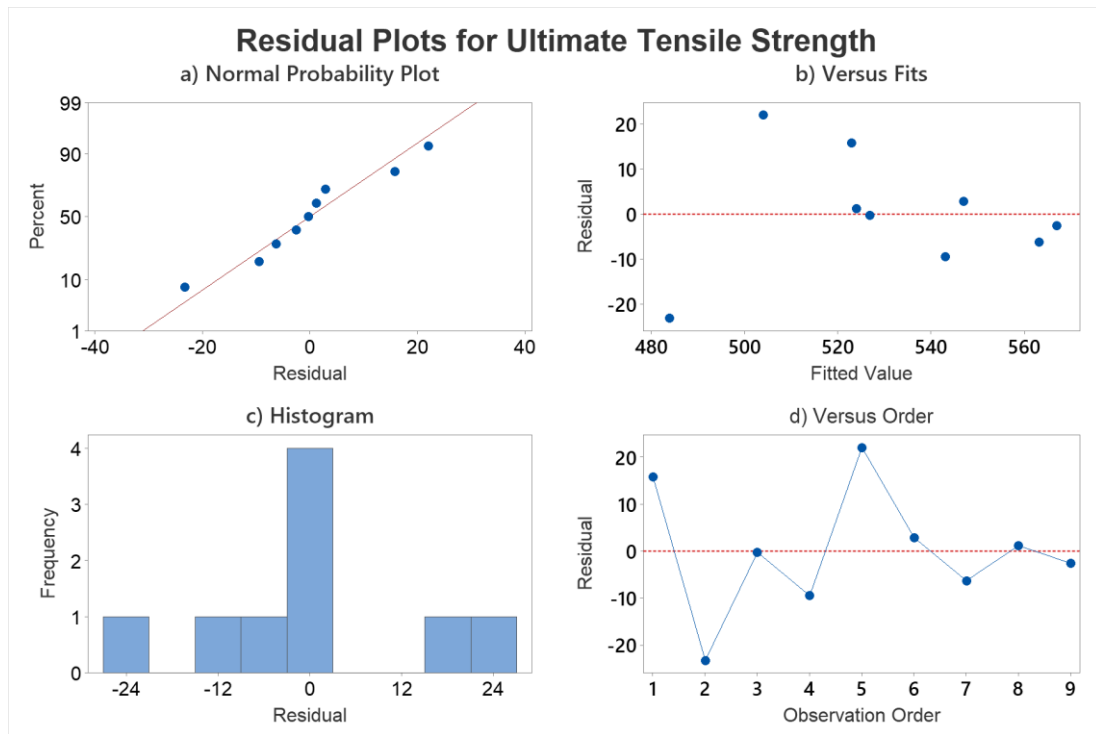
Figure 5.9: Residual plots for UTS of welds

A comparison between experimental and model-predicted values is also an important aspect of evaluating the accuracy of a statistical model used in analyzing the behavior of welded joints. This comparison is critical to determine whether the model can predict the UTS accurately and can provide insights into the factors affecting UTS. The comparison helps identify whether the model can capture the variability and underlying trends in the data, and if the error is less than a certain threshold, it indicates a good fit for the model. A good fit model can help optimize welding processes and improve the strength of welded joints. Based on the values presented in Table 5.7, the percentage error between the experimental and predicted values is below 10%, suggesting a satisfactory fit of the model. The comparison between the same is also illustrated with the help of Figure 5.10.
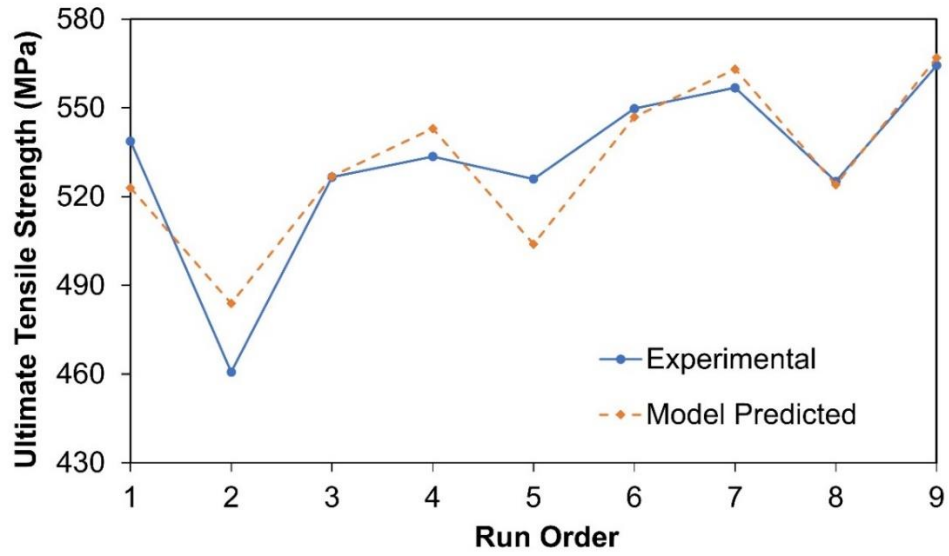
Figure 5.10: Comparison of experimental and predicted UTS values of welds

Table 5.7: Comparative table between experimental and model-predicted values for UTS of welds.

Run Order	V	N	D	Experimental value (MPa)	Model Predicted value (MPa)	% Error
1	1	1	1	538.73	522.98	2.92
2	1	2	2	460.7	483.89	5.03
3	1	3	3	526.6	526.86	0.05
4	2	1	2	533.56	543.03	1.77
5	2	2	3	525.96	503.94	4.19
6	2	3	1	549.76	546.91	0.52
7	3	1	3	556.8	563.08	1.13
8	3	2	1	525.16	523.99	0.22
9	3	3	2	564.36	566.96	0.46

Figure 5.11 illustrates the relationship between the UTS and the coded values of the significant process parameters, demonstrating their variation.
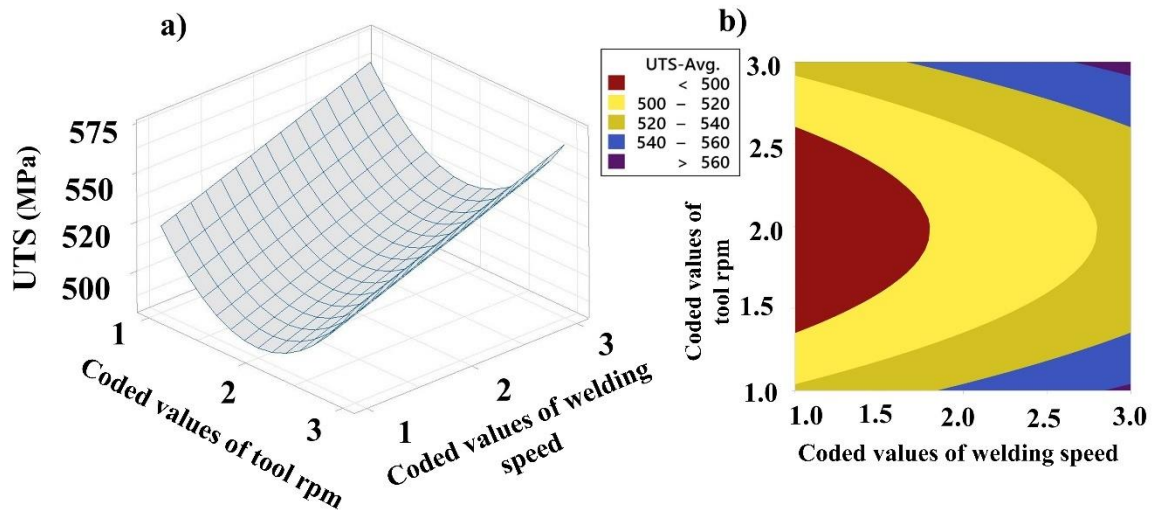
Figure 5.11: a) Surface plot depicting the changes in UTS based on variations in the input parameters; b) Contour plot showing the alterations in UTS as influenced by the input parameters.

The temperature generated during welding exhibits an inverse relationship with welding speed. Consequently, when welding is performed at higher speeds, recrystallization occurs at a lower temperature, thereby restricting grain growth after recrystallization and resulting in a finer grain structure. Consequently, the welding speed has a substantial impact on the UTS, where an increase in speed leads to an enhancement in the strength of the weld nugget. However, it is important to consider that there is a threshold for the welding speed, beyond which its impact on the tensile strength decreases. Therefore, to achieve the highest possible tensile strength, it is recommended to maintain a high welding speed.

The relationship between temperature due to friction and tool rpm is directly proportional, meaning that an increase in rotational speed results in a subsequent temperature rise. This elevated temperature causes the material to undergo softening, leading to a reduction in flow stress. Additionally, increased strain rates can be achieved by increasing the rotational speed. Initially, when the rotational speed is raised, the impact of this factor is less significant compared to the temperature increase, which mainly determines the size of the recrystallized grain. However, as the rotational speed is further increased, a higher strain rate becomes more prominent, increasing strength, as depicted in Figure 5.11 (a).

By increasing the tool shoulder diameter, more heat is generated during welding; however, a larger tool diameter also facilitates heat dissipation through conduction. As a result, the heat is

distributed over a broader region due to the larger tool shoulder. Therefore, this factor has a minimal effect on the UTS of the weld.

The corresponding contour plot is depicted in Figure 5.11 (b), illustrating that maintaining the welding speed and tool rotational speed at their maximum levels will yield the UTS exceeding 560 MPa.

5.2.1.2 Influence of process parameters on percentage elongation of welds

Statistical analysis was conducted to evaluate the impact of process parameters on the elongation percentage of the welds. ANOVA was performed to identify the significant parameters that have an impact on the elongation percentage. The findings of the ANOVA can be observed in Table 5.8, offering valuable information regarding the significance of the identified parameters.

Table 5.8: ANOVA table to find out the significant parameters affecting % elongation of welds.

Source	DF	Seq SS	Contribution	Adj SS	Adj MS	f-value	p-value
Regression	6	34.5087	89.79%	34.5087	5.75146	2.93	0.276
V	1	32.4803	84.51%	3.3025	3.30254	1.68	0.324
N	1	0.2688	0.70%	0.0854	0.08537	0.04	0.854
D	1	0.1568	0.41%	0.5071	0.50709	0.26	0.662
V*V	1	1.0272	2.67%	1.0272	1.02722	0.52	0.544
N*N	1	0.1369	0.36%	0.1369	0.13694	0.07	0.816
D*D	1	0.4387	1.14%	0.4387	0.43867	0.22	0.683
Error	2	3.9230	10.21%	3.9230	1.96148		
Total	8	38.4317	100.00%				

Table 5.8 illustrates that the model lacks significance, as the p-value associated with the model is 0.276 (greater than 0.05), which is the threshold for a 95% confidence level. Additionally, the model consists of terms that are not statistically significant and should be pooled to determine their collective significance. As a result, a more refined ANOVA table was generated, specifically focusing on the two-way interactions between variables. The refined ANOVA table

with R_E, R_E^2, and R_E^2 (adj) values is presented in Table 5.9. This provides a clearer understanding of the significant factors and their interactions, shedding light on their impact on the percentage elongation of the welds.

Table 5.9: ANOVA table for refined two-way interactions for percentage elongation of welds.

Source	DF	Seq SS	Contribution	Adj SS	Adj MS	f-value	p-value
Regression	1	32.480	84.51%	32.480	32.4803	38.20	0.000454
V	1	32.480	84.51%	32.480	32.4803	38.20	0.000454
Error	7	5.951	15.49%	5.951	0.8502		
Total	8	38.432	100.00%				
$R_E=0.9192$; $R_E^2=0.8451$; R_E^2 (adj)=0.8230							

Table 5.9 reveals that among the factors examined, only welding speed significantly influences the percentage elongation of the weld. The regression analysis further determined the coefficients associated with the significant parameters impacting the percentage elongation, as outlined in Table 5.10. Significantly, the p-value of the entire model is 0.000454, which is below the significance level of 0.05. This suggests that the model is statistically appropriate for the analysis.

Table 5.10: Coefficients of the refined two-way interaction model of percentage elongation of welds

Term	Coefficient	Standard error	t-value	p-value
Constant	17.90	0.813	22.01	0.000000
V	2.32	0.376	6.18	0.000454

Based on the regression analysis, the following statistical model for percentage elongation of the weld in terms of coded values of process parameters is proposed in equation (5.5).

% elongation= 17.90 + 2.32 V   (5.5)

The process parameters in the statistical model are expressed using coded notation, where a value of 1 represents the lowest level, a value of 2 represents the middle level, and a value of 3 represents the highest level.

The four different residual plots are represented in Figure 5.12 (a, b, c, and d respectively). A normal probability plot reveals deviations from normality, with an ideal plot showing a straight line. Versus fit plots typically identify patterns in the residuals, with a random scatter of points indicating a good fit. Finally, versus-order plots reveal any trends in the residuals, with a horizontal line indicating no trend.
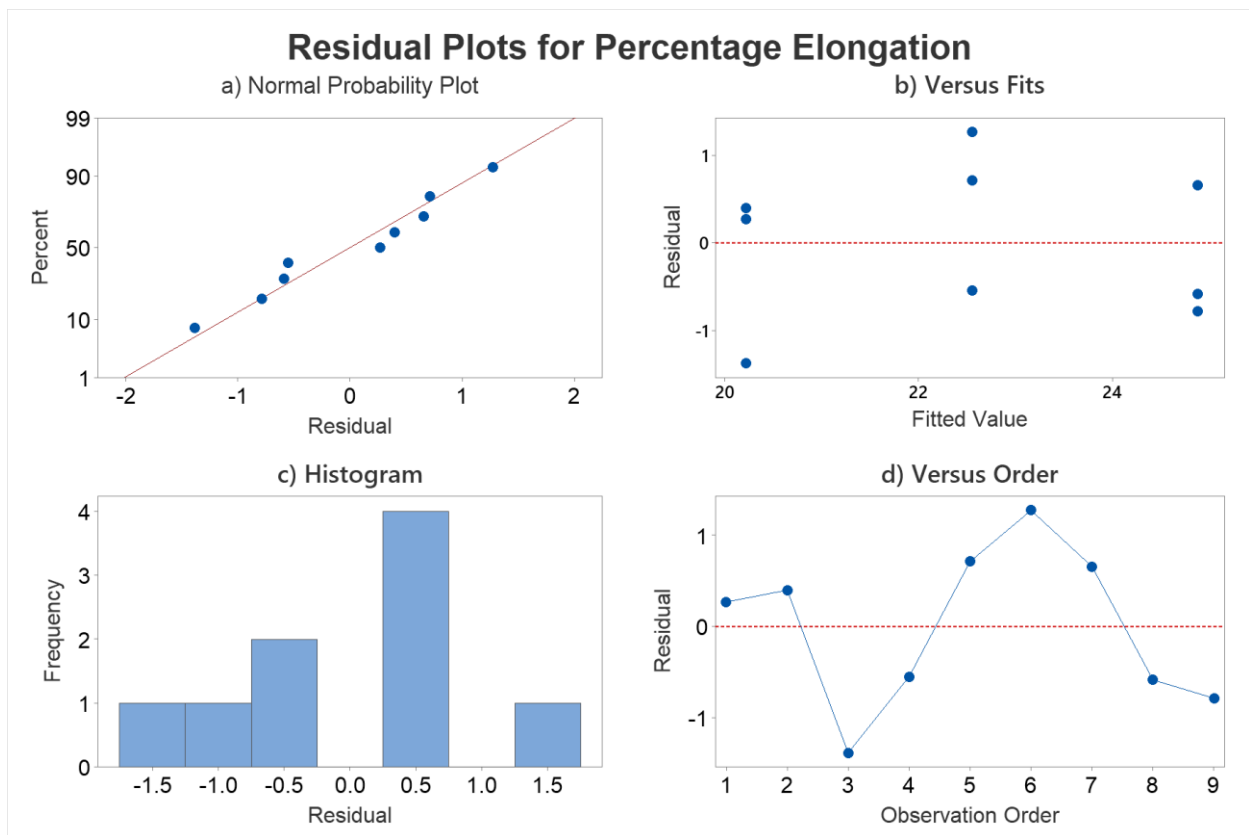
Figure 5.12: Residual plots for percentage elongation of welds

As observed in Table 5.11, the percentage deviation between the experimental and predicted values is below 10%, indicating a satisfactory fit of the model. The comparison between the same is also illustrated with the help of Figure 5.13.
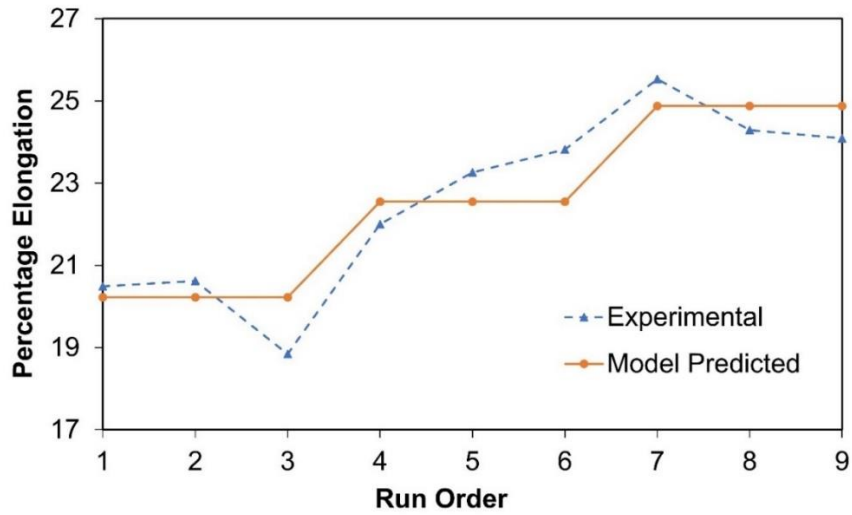
Figure 5.13: Comparison of experimental and model-predicted percentage elongation of welds

Table 5.11: Comparative table between experimental and model-predicted values for percentage elongation of welds

Run order	V	N	D	Experimental values (%)	The model predicted values (%)	% Error
1	1	1	1	20.49	20.22	1.31
2	1	2	2	20.62	20.22	1.93
3	1	3	3	18.84	20.22	7.34
4	2	1	2	22	22.55	2.49
5	2	2	3	23.26	22.55	3.06
6	2	3	1	23.82	22.55	5.34
7	3	1	3	25.53	24.88	2.56
8	3	2	1	24.29	24.88	2.41
9	3	3	2	24.09	24.88	3.26

Figure 5.14 illustrates the correlation between the coded values of the significant process parameters and the associated changes in percentage elongation.
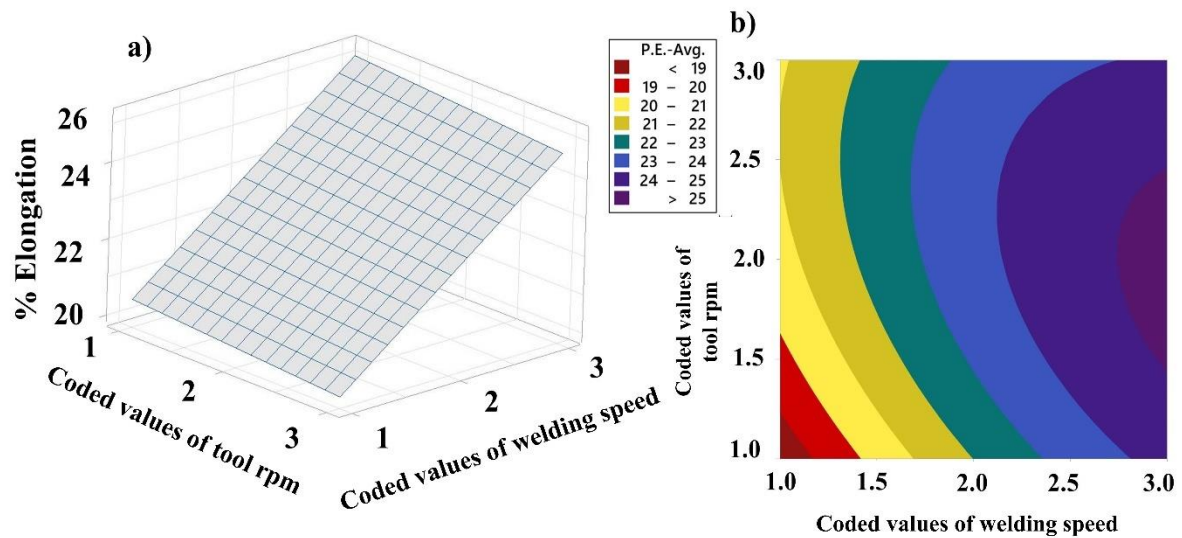
Figure 5.14: a) Surface plot showing the variations in the 'percentage elongation' as influenced by the input parameters; b) The contour plot showcasing the fluctuations in the 'percentage elongation' while considering different input parameters.

The percentage elongation is influenced by the material's strain-hardening behavior, which is determined by the grain size. Figure 5.14 (a) clearly shows that a higher welding speed leads to an increase in percentage elongation. The observed reduction in grain size is attributed to the increased strain rates experienced during the welding process. It appears that the effects of tool rotational speed on strain rate and temperature are balanced within the observed range, indicating that tool rotational speed remains independent of these variations. Additionally, the larger tool diameter spreads heat over a wider area, resulting in no significant effect on the percentage elongation.

Figure 5.14 (b) presents the contour plot illustrating that a percentage elongation exceeding 25% can be achieved by maximizing the welding speed and maintaining the rotational speed at an intermediate level.

5.2.1.3 Influence of process parameters on percentage reduction in area of welds

The statistical analysis investigated how the percentage reduction in area of welds is influenced by different process parameters. An analysis of variance (ANOVA) was performed to determine the significant parameters influencing the percentage reduction in area. The results of the ANOVA are displayed in Table 5.12.

Table 5.12: ANOVA table for two-way interaction model of 'percentage reduction in area' of welds

Source	DF	Seq SS	Contribution	Adj SS	Adj MS	f-value	p-value
Regression	6	605.275	96.05%	605.275	100.879	8.11	0.114
V	1	548.362	87.02%	4.606	4.606	0.37	0.605
N	1	10.881	1.73%	0.629	0.629	0.05	0.843
D	1	0.735	0.12%	39.776	39.776	3.20	0.216
V*V	1	1.468	0.23%	1.468	1.468	0.12	0.764
N*N	1	1.632	0.26%	1.632	1.632	0.13	0.752
D*D	1	42.197	6.70%	42.197	42.197	3.39	0.207
Error	2	24.866	3.95%	24.866	12.433		
Total	8	630.141	100.00%				

Table 5.12 indicates that the model is not significant as its p-value is not less than 0.05 for a 95% confidence level. In addition, there are some insignificant terms included in the model that should be pooled to achieve significance. Therefore, the insignificant terms were removed to create a refined two-way interaction ANOVA table. The refined ANOVA table with R_E, R_E^2, and R_E^2(adj) values is presented in Table 5.13. Based on regression analysis, the coefficients of significant parameters affecting % reduction in the area were found and have been given in Table 5.14. With a p-value of 0.001879, which is below the significance level of 0.05, the entire model demonstrates adequacy.

According to the ANOVA results, both the welding speed and shoulder diameter were observed to have an impact on the percentage reduction in area of the welds. It was found that the shoulder diameter has a non-linear effect on the % reduction in area of the welds, as both the diameter and the square of the shoulder diameter were identified as significant during the analysis of variance. On the other hand, the welding speed has a linear effect on the percentage reduction in area, as the square of the welding speed was found to be insignificant.

Table 5.13: ANOVA table for refined two-way interaction model of percentage reduction in area of welds

Source	DF	Seq SS	Contribution	Adj SS	Adj MS	f-value	p-value
Regression	3	591.294	93.84%	591.29	197.098	25.37	0.001879
V	1	548.362	87.02%	548.36	548.362	70.58	0.000392
D	1	0.735	0.12%	39.78	39.776	5.12	0.073107
D*D	1	42.197	6.70%	42.20	42.197	5.43	0.067168
Error	5	38.847	6.16%	38.85	7.769		
Total	8	630.141	100.00%				
$R_E=0.9687$; $R_E^2=0.9384$; R_E^2 (adj)=0.9014							

Table 5.14: Coefficients of the refined two-way interaction model of percentage reduction in area of welds

Term	Coefficient	Standard Error	t-value	p-value
Constant	19.86	7.37	2.69	0.043166
V	9.56	1.14	8.40	0.000392
D	18.02	7.97	2.26	0.073107
D*D	-4.59	1.97	-2.33	0.067168

Based on the analysis of regression, a statistical model is being proposed to represent the relationship between the coded process parameters and the percentage reduction in area of the weld as shown in equation (5.6).

% reduction in area= 19.86 + 9.56 V + 18.02 D - 4.59 D*D　　　　　　　　(5.6)

The statistical model utilizes coded values for the process parameters, where each value represents the corresponding level of the parameter (1 for the lowest level, 2 for the middle level, and 3 for the highest level).

Figure 5.15 displays the residual plot, which is a commonly used method to analyze the % reduction in area. Different types of residual plots, including the normal probability plot, versus fits, histogram, and versus order, are typically employed for this analysis. The four different

residual plots are represented in Figure 5.15 (a, b, c, and d respectively). A normal probability plot reveals deviations from normal data, with an ideal plot showing a straight line. Versus fit plots typically identify patterns in the residuals, with a random scatter of points indicating a good fit. Finally, versus-order plots reveal any trends in the residuals, with a horizontal line indicating no trend.
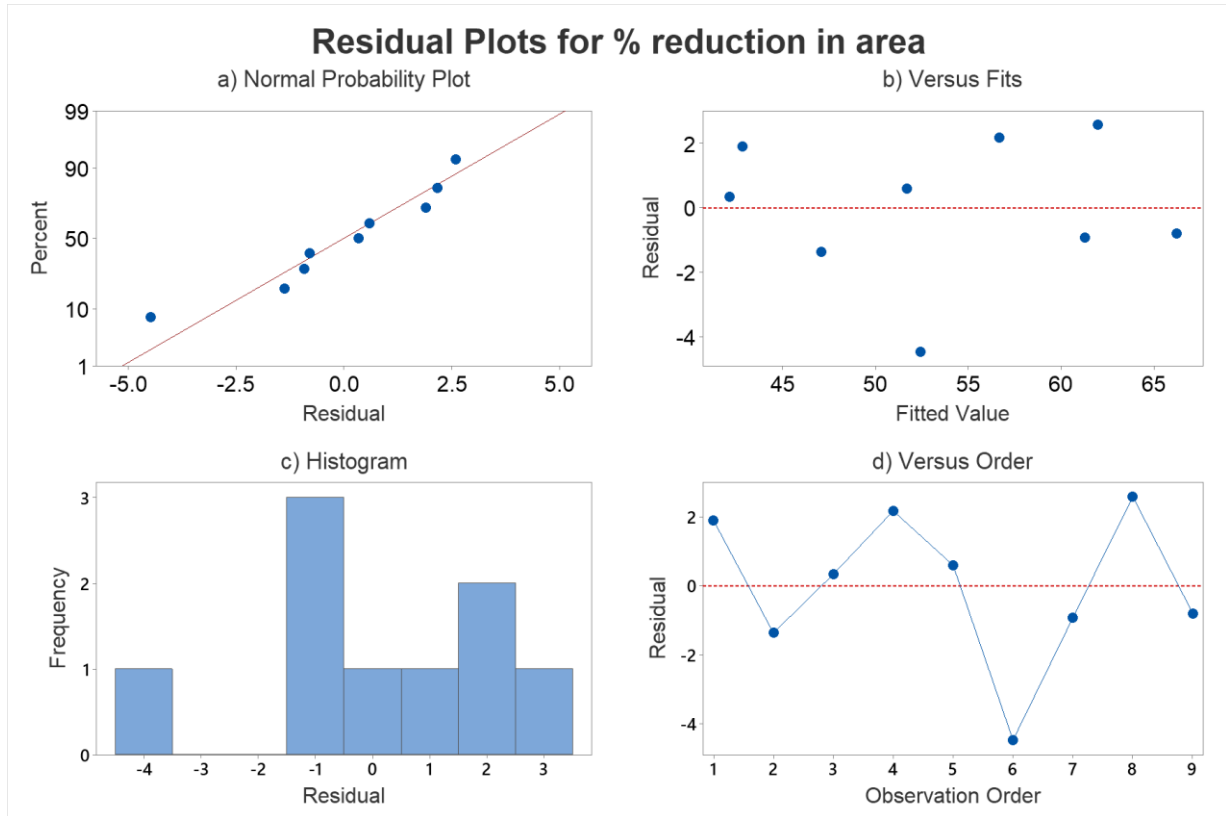
Figure 5.15: Residual plots for 'percentage reduction in area' of welds

The model-predicted values show a percentage error of less than 10% compared to the experimental values, indicating a good fit model, as indicated in Table 5.15. The comparison between the same is also illustrated with the help of Figure 5.16.
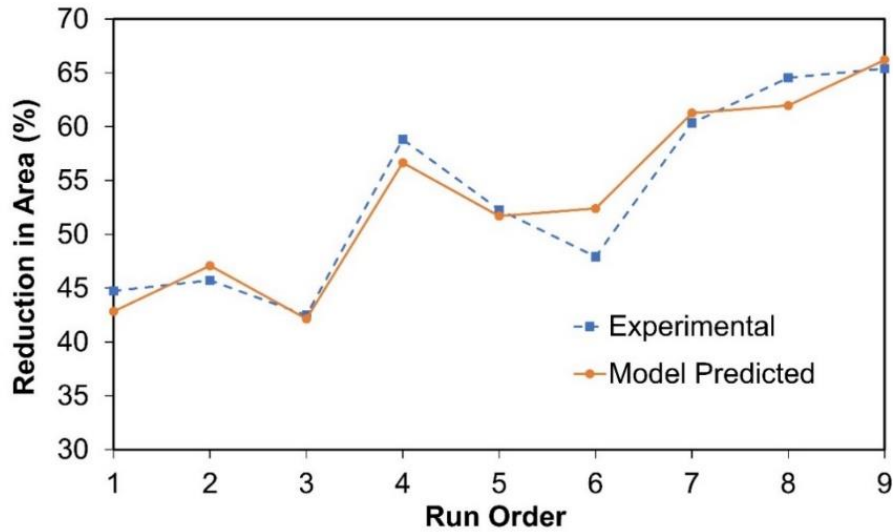
Figure 5.16: Comparison between the experimental and model predicted values for 'percentage reduction in area' of welds

Table 5.15: Comparative table between experimental and model-predicted values for 'percentage reduction in area' of welds

Run Order	V	N	D	Experimental value (%)	Model Predicted value (%)	% Error
1	1	1	1	44.74	42.85	4.23
2	1	2	2	45.72	47.09	3.00
3	1	3	3	42.48	42.15	0.78
4	2	1	2	58.82	56.65	3.69
5	2	2	3	52.3	51.71	1.13
6	2	3	1	47.93	52.41	9.34
7	3	1	3	60.34	61.27	1.54
8	3	2	1	64.55	61.97	4.00
9	3	3	2	65.41	66.21	1.22

Figure 5.17 displays the relationship between the percentage reduction in area and the coded values of the significant process parameters.
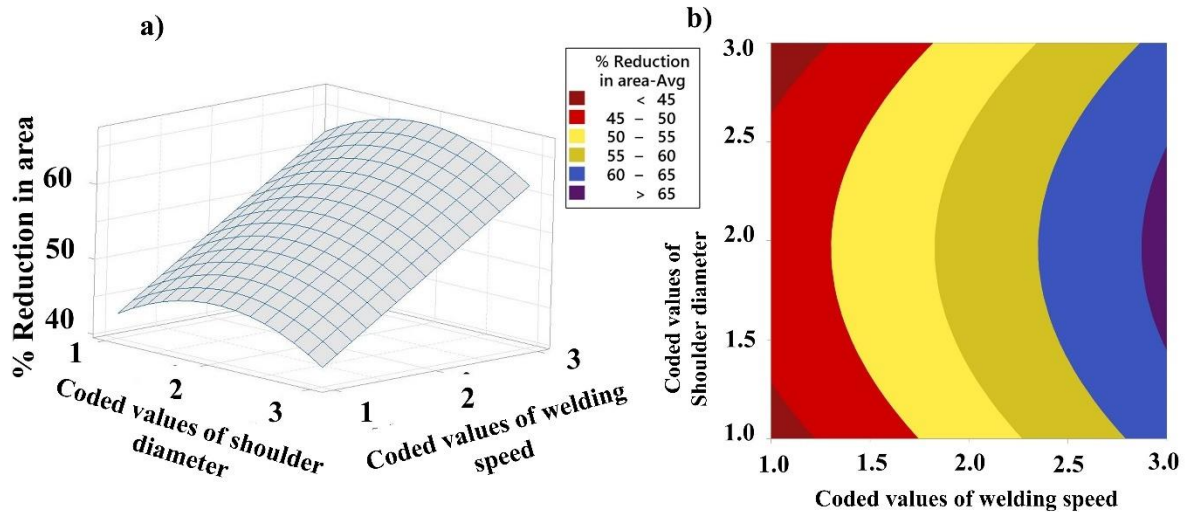
Figure 5.17: a) Surface plot illustrating the relationship between the process parameters and the 'percentage reduction in area'; b) Contour plot representing the variations in 'percentage reduction in area' with the process parameters

As depicted in Figure 5.17 (a), an increase in welding speed results in a higher percentage reduction in area. The decrease in grain size observed can be attributed to the higher strain rate experienced during the process. It seems that the effect of tool rotational speed on strain rate and welding temperature is balanced across the range of process parameters. Furthermore, a slight impact of tool shoulder diameter on the percentage reduction in area is noticed.

Figure 5.17 (b) presents the contour plot, revealing that a welding speed set to the maximum level and a shoulder diameter set to the middle level will yield a 'percentage reduction in area' exceeding 65%.

5.2.2 Analysis of impact testing of welds

The Charpy impact test was conducted on specimens with a notch in the weld nugget to measure the energy absorbed by the weld. Statistical analysis was then performed to assess the impact of process parameters on the absorbed energy. The findings and analysis are presented in the following section.

5.2.2.1 Influence of process parameters on impact energy absorbed by welds

To determine the influential factors affecting impact energy, an analysis of variance (ANOVA) was conducted. The results of ANOVA have been shown in Table 5.16, the results indicate that the model is not significant as its p-value is not less than 0.05 for a 95% confidence level.

Table 5.16: ANOVA table for finding the significant factors affecting the impact energy of welds

Source	DF	Seq SS	Contribution	Adj SS	Adj MS	f-value	p-value
Regression	6	30.5322	82.09%	30.5322	5.08870	1.53	0.447
V	1	23.2460	62.50%	1.4957	1.49572	0.45	0.572
N	1	0.5065	1.36%	0.0035	0.00352	0.00	0.977
D	1	0.7609	2.05%	6.1891	6.18909	1.86	0.306
V*V	1	0.2913	0.78%	0.2913	0.29134	0.09	0.795
N*N	1	0.0265	0.07%	0.0265	0.02645	0.01	0.937
D*D	1	5.7009	15.33%	5.7009	5.70094	1.71	0.321
Error	2	6.6598	17.91%	6.6598	3.32988		
Total	8	37.1919	100.00%				

In addition, there are some insignificant terms included in the model that should be pooled to achieve significance. Therefore, the insignificant terms were removed to create a refined two-way interaction ANOVA table. The refined ANOVA table with R_E, R_E^2, and R_E^2 (adj) values is presented in Table 5.17.

Table 5.17: ANOVA table for refined two-way interaction model for impact energy of welds

Source	DF	Seq SS	Contribution	Adj SS	Adj MS	f-value	p-value
Regression	1	23.25	62.50%	23.25	23.246	11.67	0.011198
V	1	23.25	62.50%	23.25	23.246	11.67	0.011198
Error	7	13.95	37.50%	13.95	1.992		
Total	8	37.19	100.00%				
$R_E=0.7905$; $R_E^2=0.6250$; R_E^2 (adj)=0.5715							

The impact energy of the weld is primarily influenced by the welding speed, as indicated by the ANOVA results. The impact energy was assessed through regression analysis, revealing the coefficients of the significant parameters that influence it. These coefficients are outlined in Table 5.18. The model's p-value is 0.011198, indicating adequacy in predicting the impact energy as it is less than 0.05.

Table 5.18: Coefficients of the refined two-way interaction model for impact energy of the welds

Term	Coefficient	Standard Error	t-value	p-value
Constant	27.33	1.24	21.96	0.000000
V	1.97	0.576	3.42	0.011198

The regression analysis has led to the development of a statistical model to predict the impact energy of FSWed joints. This model is based on the coded values of the process parameters as illustrated by equation (5.7).

Impact energy = 27.33 + 1.97 V   (5.7)

The process parameters in the statistical model are represented using coded values, where the lowest value is assigned as 1, the middle value as 2, and the highest value as 3.

The residual plot is shown in Figure 5.18. Four types of residual plots that are commonly used to analyze impact energy are the normal probability plot, versus fits, histogram, and versus

order. The four different residual plots are represented in Figure 5.18 (a, b, c, and d respectively). A normal probability plot reveals deviations from normal data, with an ideal plot showing a straight line. Versus fit plots typically identify patterns in the residuals, with a random scatter of points indicating a good fit. Finally, versus-order plots reveal any trends in the residuals, with a horizontal line indicating no trend.
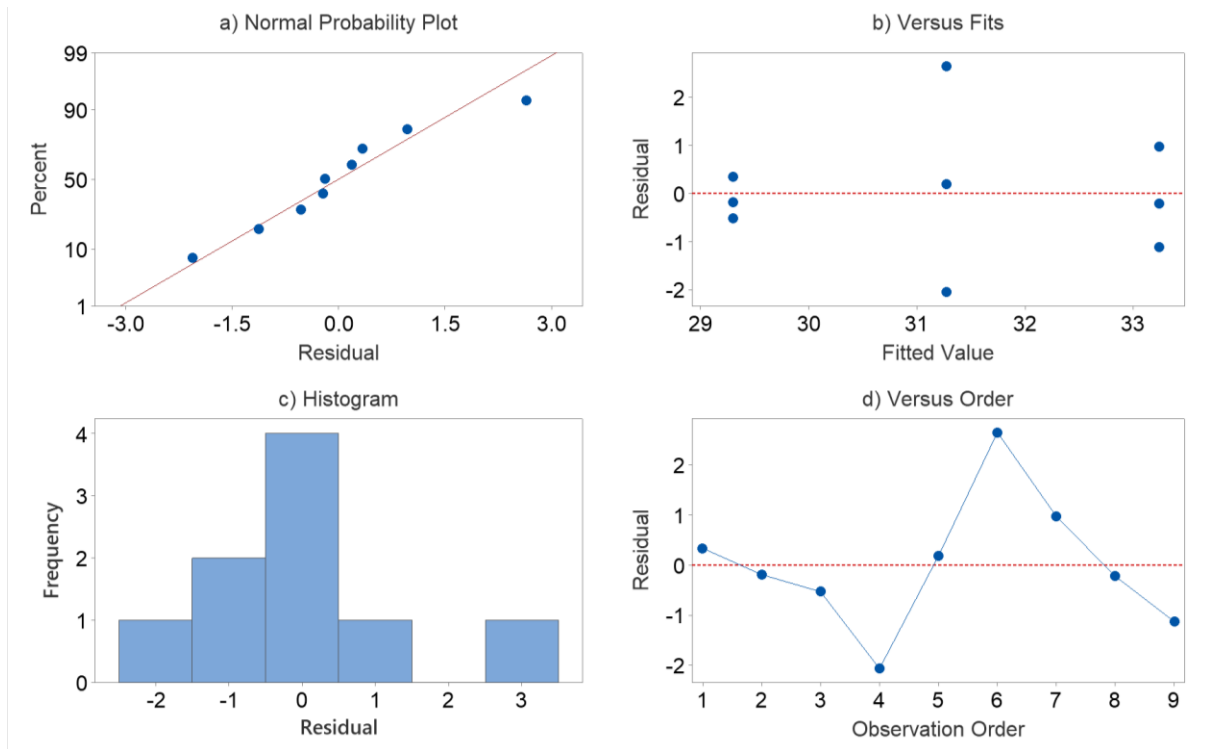
Figure 5.18: Residual plots for impact energy of welds.

As seen from Table 5.19, the percentage error between the experimental and model-predicated values is less than 10 % which indicates a good fit model. The comparison between the same is also illustrated with the help of Figure 5.19.
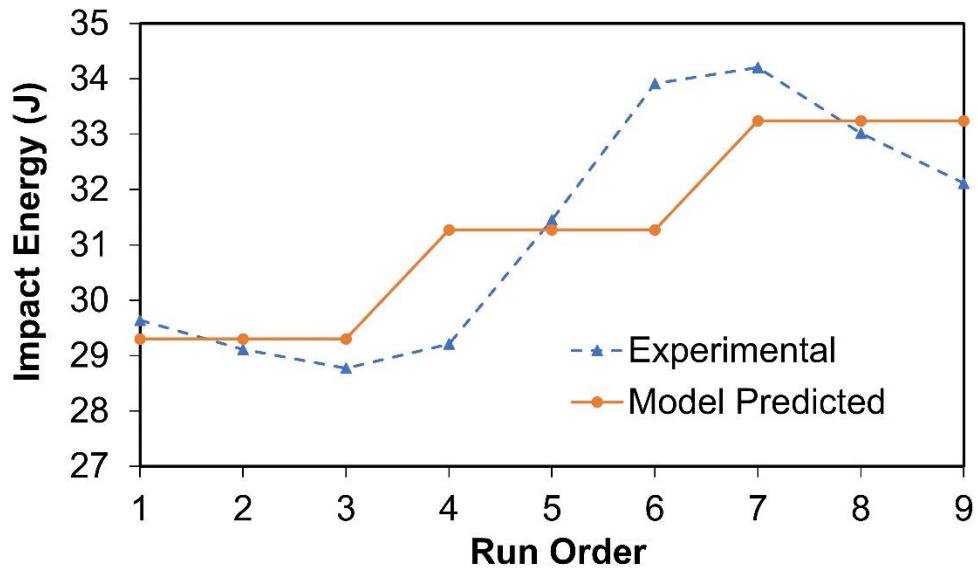
Figure 5.19: Comparison of experimental and model-predicted values for impact energy of welds

Table 5.19: Comparative table between experimental and model-predicted values for impact energy of welds

Run order	V	N	D	Experimental value (J)	Predicted value (J)	% error
1	1	1	1	44.74	42.85	4.23
2	1	2	2	45.72	47.09	3.00
3	1	3	3	42.48	42.15	0.78
4	2	1	2	58.82	56.65	3.69
5	2	2	3	52.3	51.71	1.13
6	2	3	1	47.93	52.41	9.34
7	3	1	3	60.34	61.27	1.54
8	3	2	1	64.55	61.97	4.00
9	3	3	2	65.41	66.21	1.22

Figure 5.20 displays how the impact energy changes in response to the coded values of the significant process parameters.
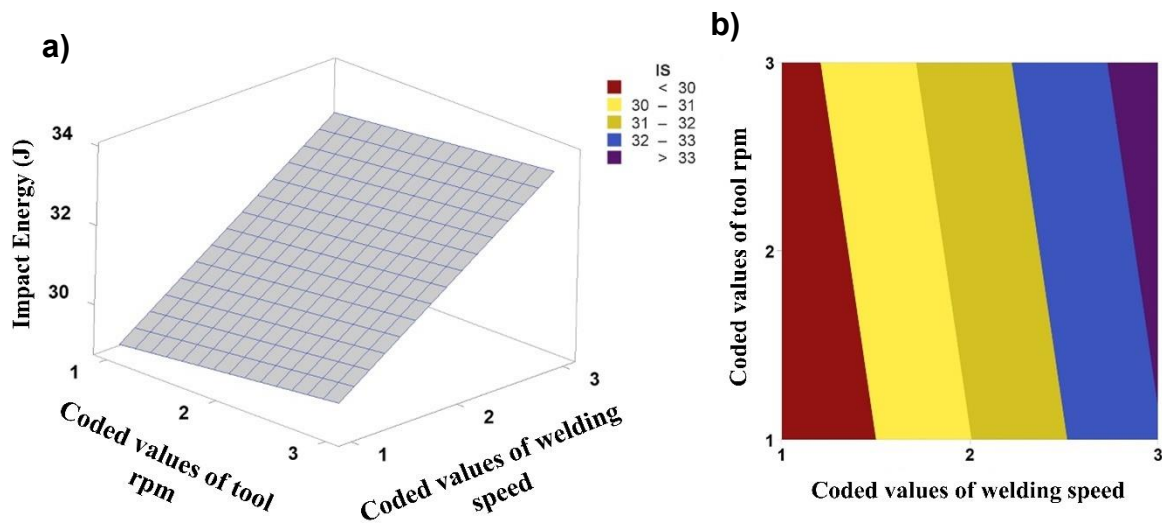
Figure 5.20: a) The surface plot showcasing the fluctuations in impact energy as influenced by the process parameters; b) Contour plot showing the changes in impact energy across different process parameters.

The relationship between welding temperature and welding speed is well-established, as lower temperatures and higher speeds result in the formation of recrystallized grains and restrict grain growth. Increased welding speed contributes to smaller grain size and enhanced ductility, leading to higher absorbed impact energy. The temperature rise during welding and the influence of tool rpm on strain rate have counterbalanced each other in the process. Similarly, altering the shoulder diameter affects heat generation and conduction away from the region, but these opposing effects also compensate for each other. Consequently, impact energy is solely influenced by welding speed and remains unaffected by variations in tool rpm and shoulder diameter as shown in Figure 5.20 (a).

The contour plot shown in Figure 5.20 (b) illustrates that maintaining the welding speed at its maximum level and the tool rotational speed at its maximum level will result in an impact energy exceeding 33 J.

5.2.3 Effect on fatigue strength

The stress intensity factor (ΔK) and the rate of crack propagation (da/dN) were computed using equations (5.1) and (5.2), respectively. The obtained values were then plotted on log-log axes in Figure 5.21 and Figure 5.22, representing stress ratios of 0.1 and 0.2 for both the weld and base metal (BM).

The fatigue life of the friction stir-welded (FSWed) plate was determined to be 60300 cycles at a stress ratio of 0.1 and 67700 cycles at a stress ratio of 0.2. In comparison, the base metal (BM) exhibited a fatigue life of 50200 cycles at a stress ratio of 0.1 and 56500 cycles at a stress ratio of 0.2. This indicates a 20% increase in fatigue life for the FSWed joints compared to the base metal. To analyze the crack growth rate, a best-fit line was plotted as indicated in Figure 5.21 and Figure 5.22, resulting in the equation $da/dN = C \, (\Delta K)^m$. The values of C and m were found to be lower for the welds than for the base metal, demonstrating a lower fatigue crack growth rate in the weld nugget.
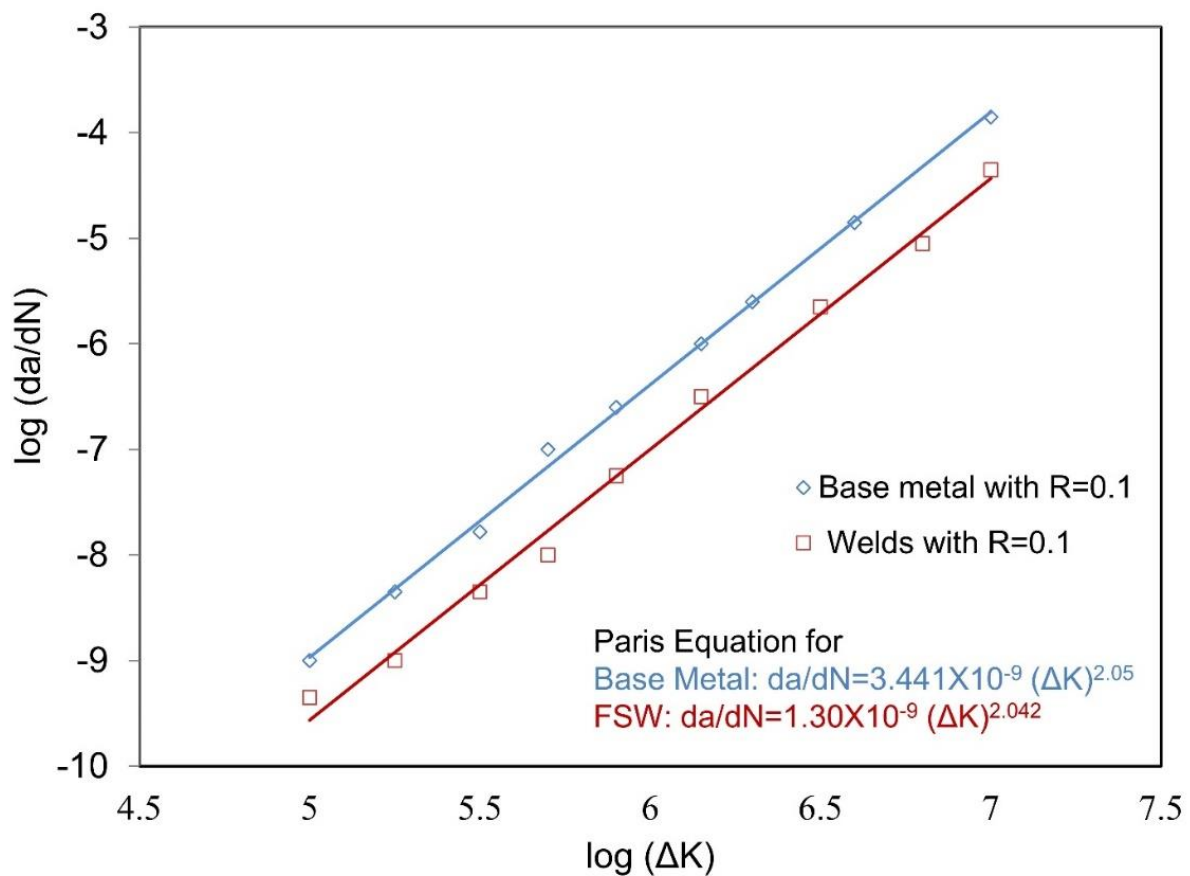
Figure 5.21: Comparison of fatigue crack growth rate and stress intensity factor at R=0.1 for base metal and welds.
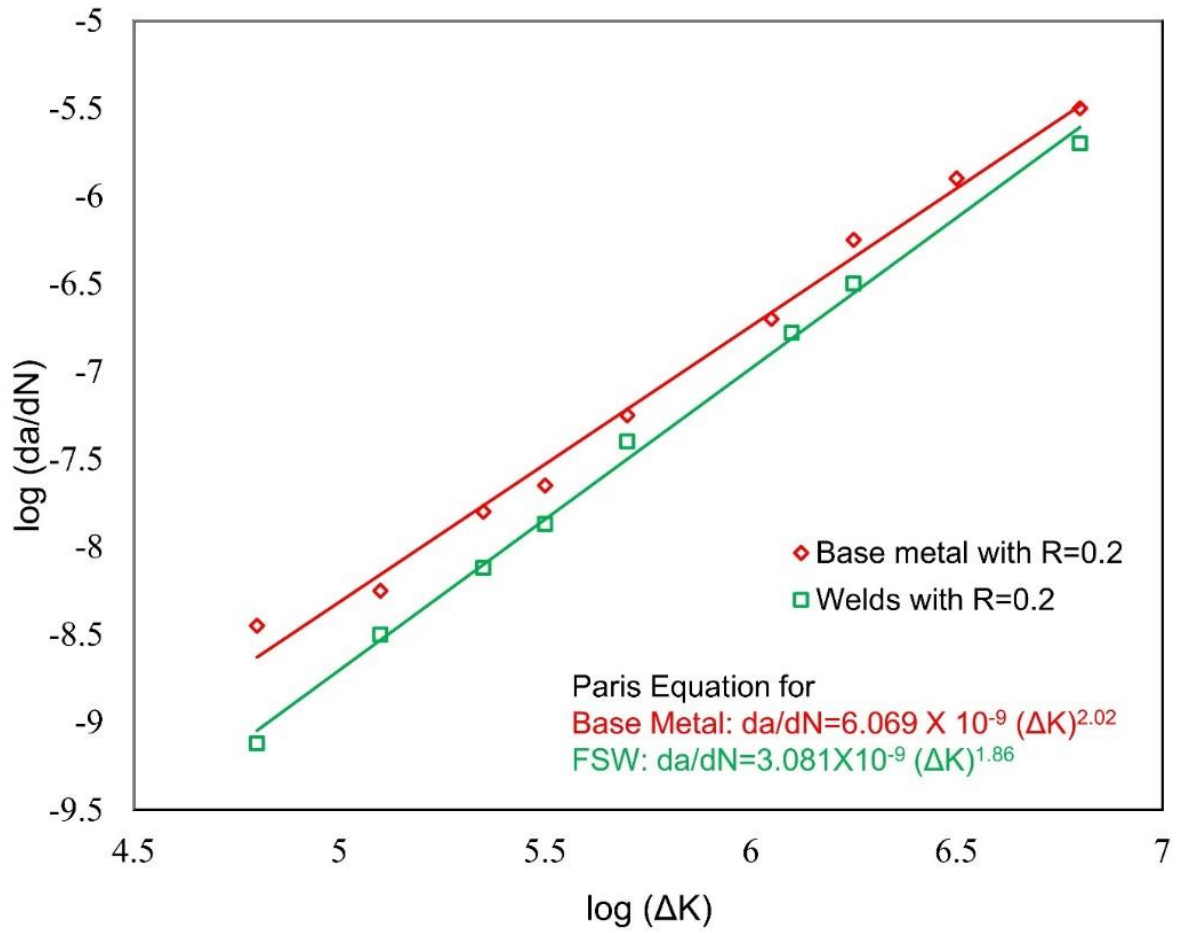
Figure 5.22: Comparison of fatigue crack growth rate and stress intensity factor at R=0.2 for base metal and welds.

CHAPTER 6   OPTIMIZATION OF PROCESS PARAMETERS

6.1 INTRODUCTION

Process parameter optimization of FSW is critical as it can obtain the desired weld quality and properties. Parameters affecting frictional heat, cooling rate, and deformation behavior of the metal during welding, are to be critically analyzed thereby, it is required to optimize each parameter for obtaining high-quality welded joints. Optimization is necessarily required for the following reasons:

- Primarily, it is required to ensure that the welded joint has the required mechanical properties. Steel is a complex material, and its properties vary depending on several factors, including its chemical composition, microstructure, and heat treatment. Welding steel can alter its microstructure, which affects its mechanical properties. Therefore, it is essential to find the optimal process parameters to control the welding conditions and reduce any adverse effects on the microstructure and characteristics of the steel.

- Additionally, it contributes to enhancing the effectiveness of the procedure. FSW is a highly energy-demanding method, and by optimizing the input parameters, it becomes possible to decrease the energy usage and duration needed for welding. For example, increasing the welding speed while maintaining the required joint quality can reduce the time and energy required for welding, This can lead to financial advantages for the manufacturer, as it can result in cost reductions.

- The optimization of input parameters can enhance the replicability and uniformity of the welded joint. FSW is a relatively recent technique, and still, a significant amount of knowledge is to be gained regarding the ideal process parameters for various steel types. However, by optimizing the process parameters, manufacturers can ensure that the welding process is consistent and reproducible, which can help to reduce variability in weld quality.

- This aids in diminishing the occurrence of flaws within the welded joint. Insufficient process control or unsuitable process parameters can lead to defects like cracks, porosity, and inadequate fusion. Nonetheless, through the optimization of process parameters, manufacturers can guarantee that the welding conditions align with the specific steel type being welded. This, in turn, aids in reducing defects and enhancing the weld quality.

6.2 OPTIMIZATION TECHNIQUES

Optimization techniques are widely used in modern manufacturing processes to achieve optimal results with minimum effort and cost. FSW is a complex process that requires a careful balance of several process parameters to achieve a high-quality weld. Achieving improved welding quality and enhanced efficiency in the FSW of steel necessitates process parameter optimization. In this section, various optimization techniques that are commonly used in FSW are discussed.

6.2.1 Taguchi optimization

This is a popular optimization technique used in many industries. It is a statistical approach to control the quality parameters that help to identify which variables are most significant in achieving optimal results. In the context of FSW, the Taguchi method is often used to optimize the process parameters to achieve the desired weld quality. The Taguchi method is especially useful for optimizing single-response problems, which have only one quality characteristic of interest. Through the utilization of this approach, it becomes possible to identify the ideal blend of process parameters that will yield the desired weld quality. Numerous research works have documented the effective utilization of the Taguchi method for process parameter optimization in FSW of steel, leading to enhanced weld quality and heightened efficiency.

6.2.2 Response surface methodology (RSM)

This is another statistical optimization technique commonly used in engineering. RSM is a technique that assists engineers in determining the correlation between the input variables and the output response, enabling the identification of the most favorable process parameter combination. RSM uses experimental data to build a mathematical model that can predict the response for any given combination of input variables. In connection with FSW, RSM is often used to optimize multiple process parameters simultaneously, resulting in improved weld quality and productivity. Numerous research studies have documented the effective implementation of RSM to optimize process parameters in FSW of steel.

6.2.3 Artificial neural networks (ANNs)

Artificial neural networks (ANNs) are machine learning algorithms that draw inspiration from the structure and functionality of the human brain. They offer valuable modeling capabilities for complex systems and have proven effective in optimizing process parameters within FSW.

ANNs possess the unique ability to identify hidden patterns within data that may elude human perception, making them instrumental in determining the optimal process parameter configuration. Numerous studies have successfully utilized ANNs to optimize process parameters in steel FSW, leading to notable advancements in weld quality and operational efficiency.

6.2.4 Genetic algorithm (GA)

This technique draws inspiration from natural selection by mimicking the process of evolution. GA efficiently searches for optimal solutions to complex problems. GA excels in optimizing multiple parameters concurrently, making it highly applicable to the optimization of process parameters in FSW. Several studies have effectively employed GA to optimize process parameters in steel FSW, leading to notable enhancements in weld quality and operational efficiency.

6.2.5 Grey relational analysis (GRA)

It is a mathematical technique utilized for assessing the correlation between input and output variables within a system. This method proves highly valuable in situations with limited or noisy data. In the context of FSW, GRA serves as a powerful tool for optimizing process parameters by determining the ideal configuration that achieves the desired weld quality. Numerous studies have successfully employed GRA to enhance process parameters in steel FSW, leading to notable improvements in weld quality and operational efficiency.

6.2.6 Particle swarm optimization

It is a type of optimization algorithm that mimics the behavior of birds flocking or fish schooling. Particle swarm optimization is employed in the field of FSW to discover the optimum configurations of process parameters that yield the utmost weld quality. By employing particle swarm optimization, the optimization of process parameters in steel FSW becomes highly effective, leading to enhanced welding quality and improved operational efficiency.

6.3 PROCEDURE FOLLOWED FOR OPTIMIZATION OF PROCESS PARAMETERS

The Taguchi method utilizes an OA within the framework of experimental design to minimize the required number of experiments for studying the impact of process variables on

performance metrics. The orthogonal design matrix is a fractional design that allows for the evaluation of all levels and factors individually and equally but with a minimum subset of factor and level combinations. This method entails gathering the essential data needed to ascertain the notable impact of process factors on the quality of the output. This methodology is illustrated in Figure 6.1. The process of optimization is further illustrated in detail by the following sequential steps.

Step 1: Defining the response parameters: To begin the optimization process, the initial stage involves establishing the desired performance goals for a given process. The response variables examined in this study included UTS, % elongation, % reduction in area, and impact energy. This initially involves optimizing each of the four individual responses as mentioned above using a single-response optimization approach, followed by multi-response optimization of the combined UTS, % elongation, % reduction in area, and IE.

Step 2: Identifying the input parameters and their levels: Three process parameters, namely welding speed, tool rotational speed, and shoulder diameter, are taken into account in the study. The values of V, N, and D can be varied within a range, where V ranges between 60 to 210 mm/min, N ranges between 430 to 750 rpm, and D ranges between 15 to 20 mm. Each of these factors is categorized into three levels as indicated in Table 4.3. After conducting optimization, the responses for UTS, % elongation, % reduction in area, and impact energy, obtained using the optimized set of factors, will be compared to those obtained using the initial set of factors.

Step 3: Finalising the orthogonal array: The OA is a framework for conducting multi-factor experiments. In this research, three parameters, each having three levels, are examined. Therefore, L9 OA is utilized, as illustrated in Table 4.4. Additionally, the data's reliability is improved by conducting three trials for each experiment.

Step 4: Conducting the experiments: The assessment of the UTS, % elongation, % reduction in area, and impact energy responses is conducted by performing a total of nine experiments, each comprising three trials. The data is displayed in Table 5.2 and Table 5.3 correspondingly.
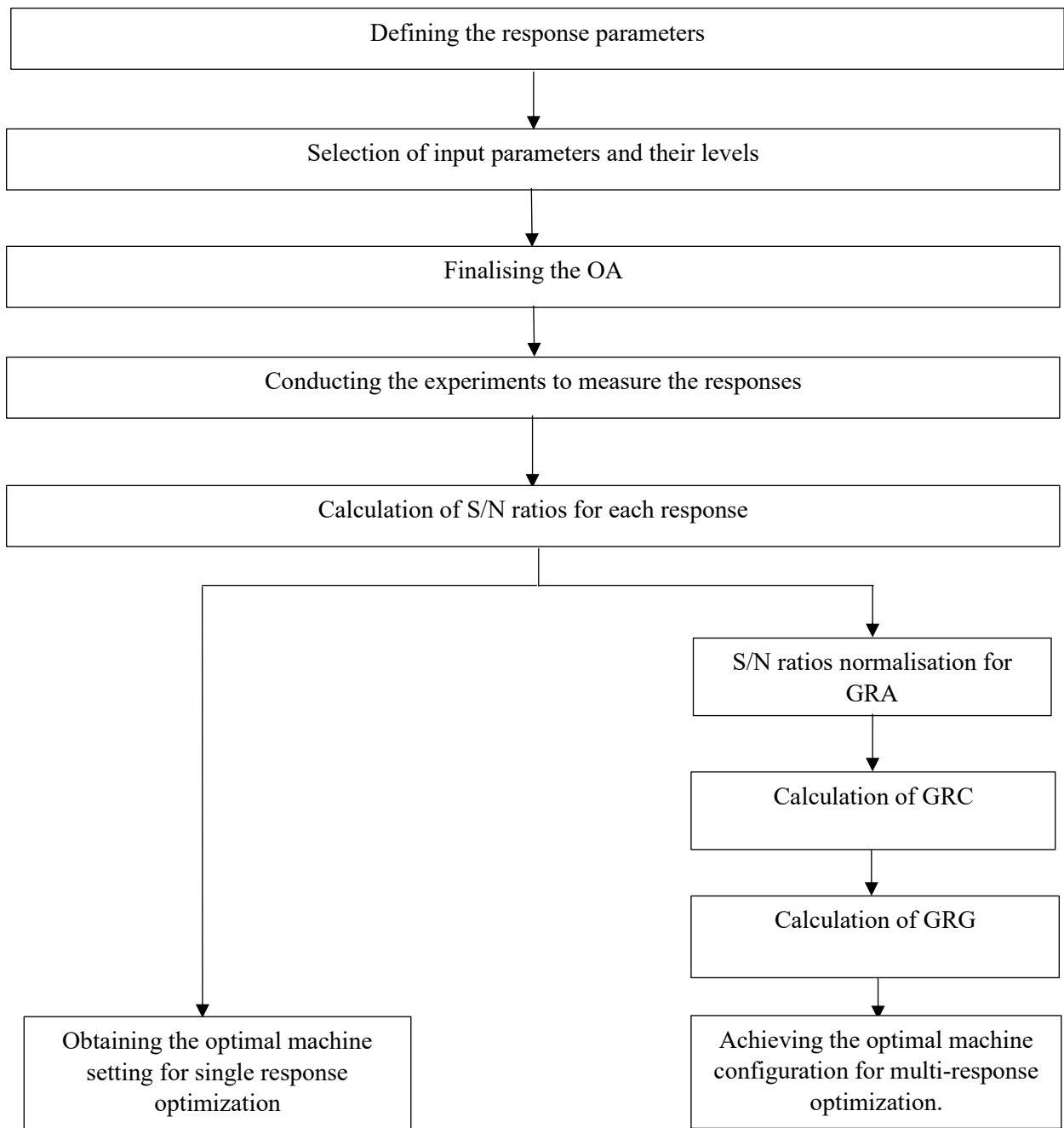
Figure 6.1: Flowchart showing the methodology of single/multi-response optimization of process parameters

Step 5: Data analysis for determining the effect of process parameters: The Signal-to-noise ratio (S/N) is a metric that signifies the influence of each parameter on the overall performance. The factor set is considered optimal when its S/N is the highest. To calculate S/N, Taguchi suggested the use of three loss functions, which depend on the type of performance characteristics being assessed, namely, smaller-the-better (STB), larger-the-better (LTB), and nominal-the-best (NTB). To maximize the performance characteristics, such as UTS, %

elongation, % red in area, IE, and a combination of all, the LTB loss function is used and determined using equation (6.1) (Ross, 1996).

$$S/N_i = -10\log \left(\frac{1}{n_{tr,i}} \sum_{u=1}^{n_{tr,i}} \frac{1}{y_u^2} \right)$$

(6.1)

where S/N_i is the signal-to-noise ratio of a given experiment, $n_{tr,i}$ is the number of trials of the experiment i[th], u is the order of trials, i is the experiment number, y_u is the value of the measured performance characteristic for a given trial. The value of $n_{tr,i}$ is 3, and the value of i is 9 in this study. Note that equation (6.1) is used to calculate S/N for the single-response optimization. For the multi-response optimization with a simultaneous maximum of UTS, % elongation, % reduction in area, and IE, grey relational analysis (GRA) is used as an alternative approach for data processing. Firstly, using grey relational generation normalizes experimental data of responses to the values between zero and one. A linear data pre-processing equation to normalize experimental data for the LTB response is expressed by equation (6.2) (Achuthamenon et al, 2018).

$$y'_i(k) = \frac{y_i(k) - \min[y_i(k)]}{\max[y_i(k)] - \min[y_i(k)]}$$

(6.2)

where $y_i'(k)$ is normalized experimental data based on the grey relational generation for response k[th] of experiment i[th]. $y_i(k)$ is the mean value of the kth response of ith experiment, while the smallest and the highest values of $y_i(k)$ are denoted by min $[y_i(k)]$ and max $[y_i(k)]$. Subsequently, the grey relational coefficient (GRC) is calculated based on the normalized set to determine the correlation between the desired data and the experimental data. GRC $\xi_i(k)$ is presented by equation (6.3).

$$\xi_i(k) = \frac{\Delta_{min} + \Psi\Delta_{max}}{\Delta_{0i}(k) + \Psi\Delta_{max}}$$

(6.3)

where $\Delta_{0i}(k) = |y_{0i}(k) - y_i(k)|$ shows the discrepancy of desired data ($y_{0i}(k) \sim 1$) and normalized experimental data $y_i(k)$ in absolute value. $\Psi \in [0, 1]$ is the distinguishing coefficient and is typically set at a value of 0.5. Δ_{min} and Δ_{max} are the minimum and maximum values of $y_i(k)$. Note that the initially measured responses cannot be comparable together because of the difference in evaluated units, thus they must be converted to GRCs and can be comparable. However, these responses still represent different responses. To use the loss function LTB, the GRCs must be converted to a single value called the grey relational grade (GRG) by adding weighting factors. The GRG can be calculated by using equation (6.4).

$$\gamma_i = \sum_{k=1}^{r} \omega(k)\xi i(k) \tag{6.4}$$

Where γ_i is the GRG of all responses at the ith experiment. $\omega(k)$ is the weighting factor of each response k^{th} with. $\sum_{k=1}^{r} \omega(k) = 1$. r is the total of responses.

The welding process has multiple responses and welding quality sturdily depends upon optimizing all responses simultaneously. Therefore, researchers frequently employ GRA coupled with PCA for the optimization of multiple responses simultaneously. These techniques are entirely different from traditional single-response optimization. These are effective statistical methods and offer quite successful results in obtaining a combination of parameters for multiple response optimizations.

PCA is a powerful multivariate statistical technique for multi-objective optimization that reduces the complexity, correlation, vagueness, and dimensions of information by simplifying and combining numerous allied arrays into a few uncorrelated arrays and principal components. PCA employs linear permutation for conserving unique information to the maximum extent. Thus, it converts multi-response optimization to single-response optimization without compromising original information. It begins by setting a structure of linear combinations arrays of multi-responses. The GRCs are computed for response variables and are employed to form a matrix, presented as equation (6.5).

$$y = \begin{bmatrix} y_1(1) & y_1(2) & \cdots & y_1(k) \\ y_2(1) & y_2(2) & .. & y_2(k) \\ \vdots & \vdots & \cdots & \vdots \\ y_j(1) & y_j(2) & \cdots & y_j(k) \end{bmatrix} \tag{6.5}$$

where $y_p(q)$ is GRC of each quality responses, p = 1, 2, . . . j, experiments, and q = 1,2, . . . k, quality responses. In this work, j = 9 and k = 3. Thereafter, the coefficient correlation matrix can be generated by equation (6.6).

$$R_{jl} = \left(\frac{Cov(y_p(q), y_p(l))}{\sigma_{yp}(q) * \sigma_{yp}(l)} \right) \tag{6.6}$$

where $Cov(y_p(q), y_p(l))$ is the covariance of sequences $y_p(q)$ and $y_p(l)$. $\sigma_{yp}(q)$ is standard deviation of sequence $y_p(q)$ and $\sigma_{yp}(l)$ is standard deviation of sequence yp(l). The eigen values and eigen vectors are computed by R_{jl} array using equation (6.7).

$$(R - \lambda_k I_j)V_{pk} = 0 \tag{6.7}$$

Thereafter, eigenvalues (λ_k) and eigenvectors (V_{pk}) of square matrix R are used to determine the uncorrelated principal components (PCs) by using equation (6.8).

$$Z_{jk} = \sum_{i=1}^{n} Y_j(p) * V_{pk} \tag{6.8}$$

where Z_{jk} corresponds to k^{th} principal component. Eigenvalues and principal components are arranged in descending order concerning explained variance, therefore, the first eigenvalue associated with the first PC accounts for the largest variance contribution.

After obtaining the S/N_i for both single-response and multi-response problems, an average S/N_i value for each level i^{th} of each factor f (f= [V; N; D]) is notated by $\overline{S/N}_{i,f,l}$ and expressed by equation (6.9).

$$\overline{S/N}_{i,f,l} = \frac{1}{m} \sum S/N_{i,f,l} \tag{6.9}$$

where m is the total observation of level l^{th} of factor f, $S/N_{i,f,l}$ is the S/N_i value corresponding to the factor f for level l^{th}. Then, delta values (Δ) are calculated by the highest value of $S/N_{i,f,l}$ minus the lowest value of $S/N_{i,f,l}$ of each factor f as follows:

$$\text{Delta } \Delta = \max(S/N_{i,f,l}) - \min(S/N_{i,f,l}) \tag{6.10}$$

The rank of Δ is in order from high to low corresponding to an order of factors' significant effect on the process performance. Lastly, the optimal value of factor f and its l levels were chosen based on the highest mean value of $S/N_{i,f,l}$.

Step 6: Variance analysis (ANOVA): Percentage contribution of control factors to the responses determined through ANOVA of S/Ns. Estimating the error variance for the effects and variance of the prediction error are also obtained by using ANOVA.

Step 7: Confirmatory test: After optimization of the process factors, the final step is using the optimal level of factors to predict and confirm the improvement of responses.

6.4 SINGLE RESPONSE OPTIMIZATION

The optimization of individual responses is achieved by taking into account the S/N values. The objective of this study is to maximize the individual responses, namely the UTS, % elongation, % reduction in area, and impact energy. The quality characteristic, which follows the larger-the-better principle, is applied to these response parameters using equation (6.1).

Optimal levels are determined by calculating the average S/N values for each response at different levels, as depicted in Figure 6.2. High S/N indicates better quality characteristics. Table 6.1 presents the higher S/N ratios for UTS, % elongation, % reduction in area, and impact energy, which are 55.03, 28.14, 36.31, and 30.68, respectively.

Table 6.1: S/N values for different response parameters

Exp No.	S/N of responses			
	UTS	Percentage elongation	Percentage reduction in area	Impact energy
1	54.63	26.23	33.01	29.44
2	53.27	26.29	33.20	29.28
3	54.43	25.50	32.56	29.18
4	54.54	26.85	35.39	29.31
5	54.42	27.33	34.37	29.95
6	54.80	27.54	33.61	30.61
7	54.91	28.14*	35.61	30.68*
8	54.41	27.71	36.20	30.37
9	55.03*	27.64	36.31*	30.13
Optimum	$V_3N_3D_1$	$V_3N_2D_1$	$V_3N_1D_2$	$V_3N_3D_1$
* Optimized setting for the individual response parameters				

For UTS, the experimental run 9 with welding speed at a high level, tool rotational speed at a high level, and shoulder diameter at a low level yielded the highest S/N. In the case of percentage elongation, the highest S/N is obtained from experimental run 7 with welding speed at a high level, tool rotational speed at mid-level, and shoulder diameter at a low level. Similarly, for percentage reduction in area, the highest S/N is observed for experimental run 9 with welding speed at a high level, tool rotational speed at a low level, and shoulder diameter at mid-level. Finally, for impact energy, the highest S/N is found in experiment 7 with welding speed at a high level, tool rotational speed at a low level, and shoulder diameter at a low level.

Figure 6.2 (a,d) shows the optimal levels for UTS and IE which are welding speed at a high level, tool rotational speed at a high level, and shoulder diameter at a low level. Figure 6.2 (b) shows optimal levels for percentage elongation which are welding speed at a low level, tool rotational speed at mid-level, and shoulder diameter at a low level. Whereas Figure 6.2 (c) depicts the optimal levels for 'percentage reduction in area' having welding speed at a high level, tool rotational speed at a low level, and shoulder diameter at mid-level.
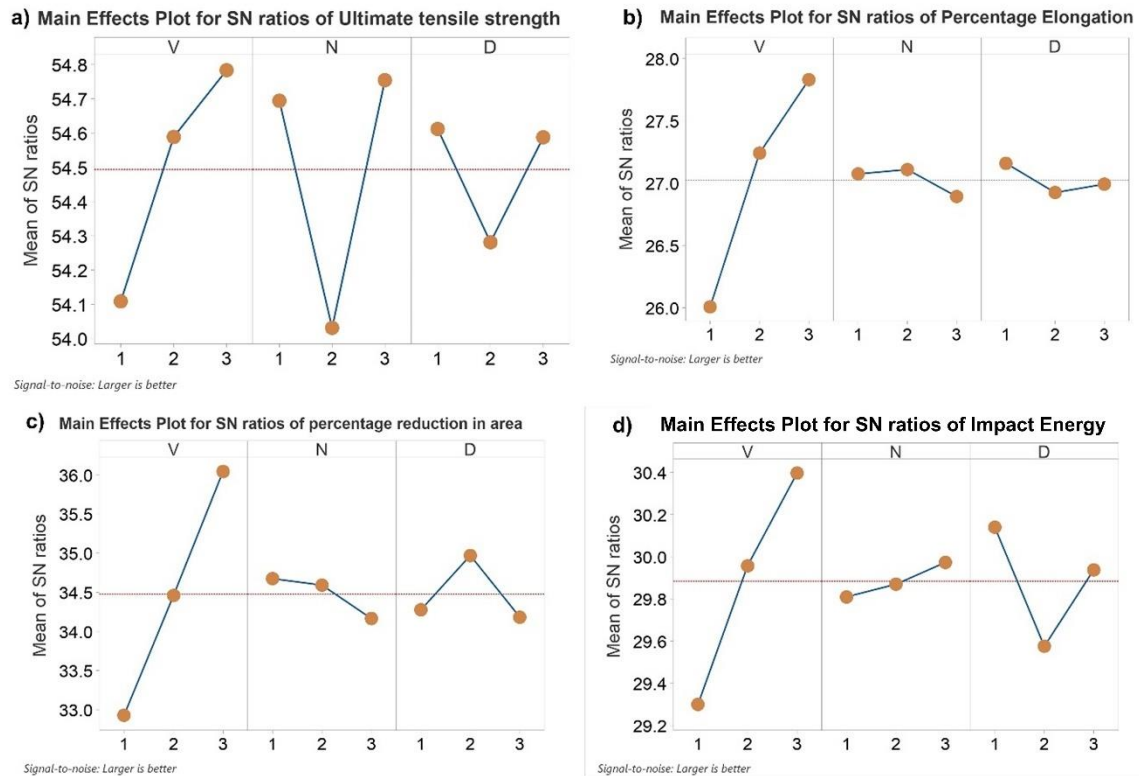
Figure 6.2: Plots depicting the main effects of S/N for a) UTS b) % elongation c) % reduction in area d) impact energy

6.4.1 Probability plots

Probability plots serve as a valuable tool in analyzing the distribution of experimental data. Anderson-Darling test (ADT) is a particular statistical test widely employed for outlier detection and verification of normality assumptions. The main purpose of the ADT is to assess whether the observed data can be reasonably assumed to follow a normal distribution. (Stephens et al., 1974)

Figure 6.3 provides a visual representation of the relationship between the experimental data and the fitted line. The experimental data points demonstrate a notable alignment with the fitted

line, indicating a strong indication of normal distribution. This visual evidence supports the subsequent statistical analysis conducted using ADT.

To quantitatively validate the normality assumption, ADT computes specific statistics and derives a p-value. The ADT statistics, in the present study, demonstrate relatively low values. This indicates that the observed data does not deviate significantly from the expected values under a normal distribution. Additionally, the p-value resulting from the ADT exceeds the conventional threshold of 0.05. Hence, based on the chosen level of significance, there is insufficient evidence to reject the assumption of normality for the data. These findings provide reassurance regarding the validity of assuming a normal distribution for the dataset under consideration.
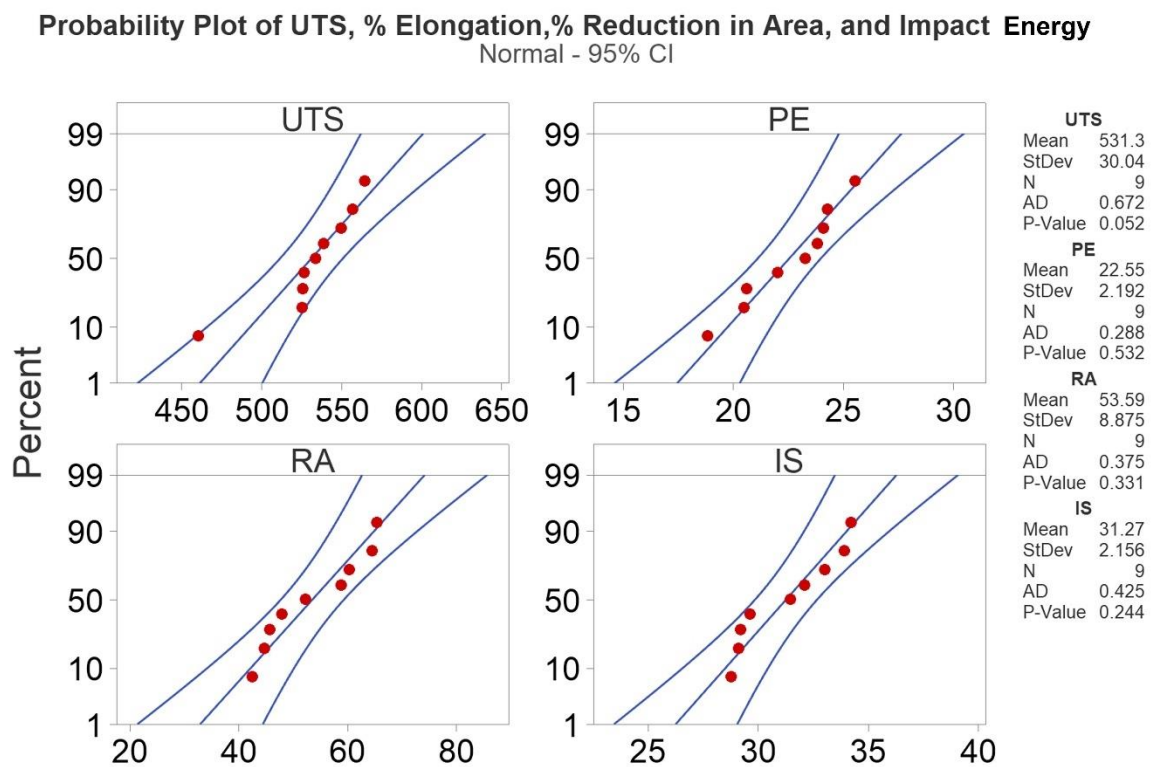
Figure 6.3: Normal probability plots of the response parameters

6.4.2 ANOVA and main effect plots of means for individual responses

Exploring the influence of input parameters on individual responses through ANOVA with a 95% confidence interval. This statistical method enables a thorough analysis of the primary influences of process parameters. The ANOVA results for key response variables i.e. UTS, % elongation, % reduction in area, and impact energy were compiled and presented in Tables 6.2,

6.3, 6.4, and 6.5, respectively. The main effect plots of means for response parameters are presented in Figure 6.4.

Table 6.2: ANOVA table for UTS of welds

Source	DF	Seq SS	Adj SS	Adj MS	% Contribution
V	2	2530.2	2530.2	1265.1	35.06%
N	2	3389.2	3389.2	1694.6	46.96%
D	2	624.6	624.6	312.3	8.65%
Error	2	672.9	672.9	336.5	9.32%
Total	8	7217.0			100.00%
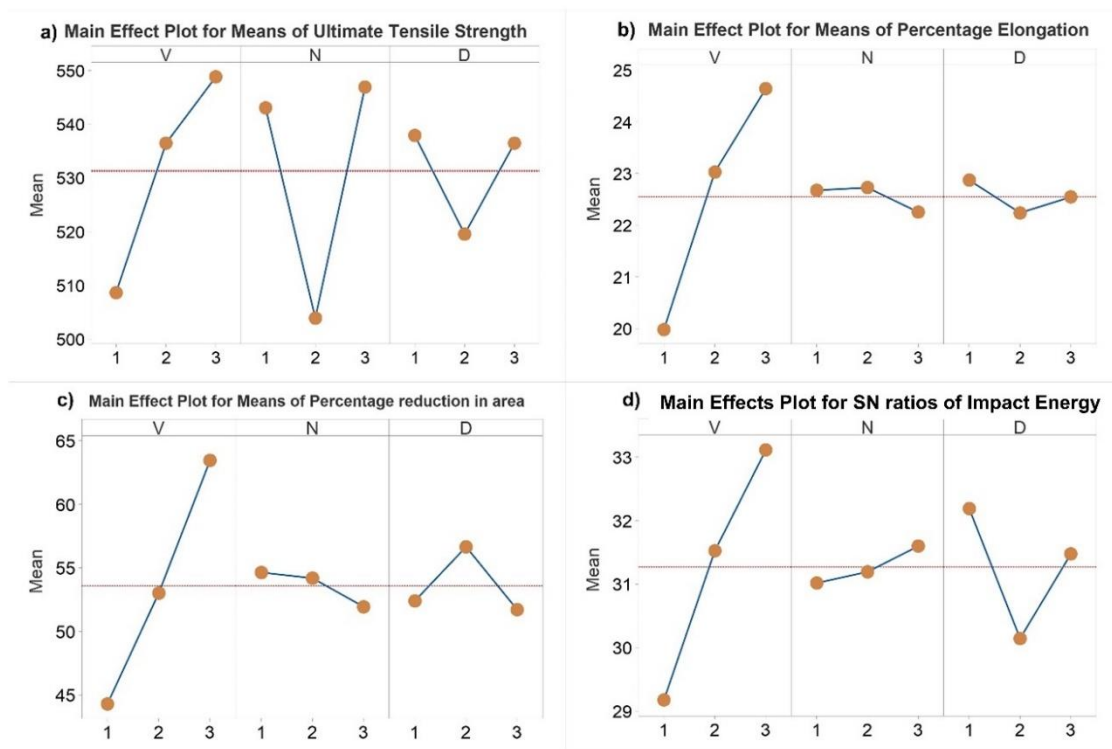
Figure 6.4: Main effect plot of means for a) UTS (b) % elongation c) % reduction in area d) Impact energy.

Based on the information presented in Table 6.2 concerning UTS, it is clear that tool rotational speed stands out as the influential factor, making a significant contribution of 46.96%. This suggests that changes in the tool rotational speed have a significant impact on the UTS.

131

Following closely is the welding speed with a contribution of 35.06%, signifying its noteworthy influence on the UTS as well. Conversely, shoulder diameter is observed to have a relatively insignificant impact, contributing a mere 8.65% to the UTS. These findings shed light on the varying degrees of importance among the input parameters, emphasizing the crucial role of tool rotational speed and welding speed in determining the UTS.

Figure 6.4 (a) exhibits the main effect plots depicting the characteristics of UTS. The plot demonstrates a positive correlation between UTS and welding speed. It suggests that an increase in welding speed corresponds to an increase in UTS. This relationship can be attributed to the fact that higher welding speeds contribute to the formation of a finer microstructure, resulting in reduced defects and improved joint strength (Zhang et al., 2018; Chen et al., 2016).

On the contrary, the main effect plot shows a negative correlation between UTS and tool rotational speed. An increase in the tool's rotational speed corresponds to a decrease in the UTS. This phenomenon can be explained by the adverse effects of high rotational speeds on the weld joint. Increased rotational speed generates additional frictional heat, which in turn leads to excessive plastic deformation and the formation of defects, thereby compromising joint strength (Chen et al., 2016).

Additionally, the plot indicates that UTS decreases with an increase in shoulder diameter. The correlation between UTS and shoulder diameter is linked to the heat produced during welding. A greater shoulder diameter leads to a larger contact area, causing higher heat generation. Excessive heat can lead to thermal degradation and adversely affect the mechanical properties of joints, resulting in a reduction in UTS. (Li et al., 2019).

Upon examining the percentage elongation, it becomes apparent that welding speed holds the utmost influence, exhibiting a significant contribution of 87.19%. This implies that variations in the welding speed have a substantial impact on the percentage elongation. In contrast, both the tool rotational speed and shoulder diameter are considered to have negligible contributions to the percentage elongation, with meager percentages of 1.06% and 1.55%, respectively. These findings suggest that variations in the tool rotational speed and shoulder diameter have minimal impact on the percentage elongation. To provide a visual representation and facilitate a comprehensive understanding, the ANOVA table corresponding to these findings is presented in Table 6.3. According to these outcomes, it is evident that the welding speed has a substantial effect on the percentage elongation, while the influence of the tool rotational speed and shoulder diameter is comparatively insignificant.

Table 6.3: ANOVA table for % elongation of welds

Source	DF	Seq SS	Adj SS	Adj MS	Contribution
V	2	33.5075	33.5075	16.7537	87.19%
N	2	0.4058	0.4058	0.2029	1.06%
D	2	0.5955	0.5955	0.2977	1.55%
Error	2	3.9230	3.9230	1.9615	10.21%
Total	8	38.4317			100.00%

Figure 6.4 (b) illustrates the main effect plots concerning percentage elongation, a measure of the ductility of a material. The plots indicate important trends regarding the relationship between percentage elongation and various factors in the welding process. Primarily, the findings reveal that the percentage elongation rises alongside an augmentation in welding speed. This can be attributed to the notion that elevated welding speeds often yield a finer microstructure, thereby enhancing the joint's ductility and capacity for deformation. (Zhang et al., 2018; Chen et al., 2016).

Moreover, the plot illustrates a more complex association between the percentage elongation and the tool rotational speed. Initially, as the tool rotational speed increases, there is a corresponding increase in the percentage elongation. This can be explained by the heightened heat input at higher rotational speeds, which enhances the material's ductility. However, beyond a certain point, further increases in tool rotational speed led to a decrease in percentage elongation. This decrease can be attributed to excessive heat input, which can induce grain growth and reduce ductility (Chen et al., 2016). While examining the ANOVA results for percentage reduction in area, an insight is presented in Table 6.4.

Notably, the factor that exerts the most substantial influence is welding speed, contributing significantly with a percentage contribution of 87.26%. This finding underscores the significant impact of variations in welding speed on % reduction in area. Conversely, both the tool rotational speed and shoulder diameter are observed to have relatively insignificant contributions. Tool rotational speed contributes a mere 1.99%, while shoulder diameter closely

contributes 6.81%. The findings indicate that variations in the tool rotational speed and shoulder diameter have minimal impact on the % reduction in area.

Table 6.4: ANOVA table for percentage reduction in area

Source	DF	Seq SS	Adj SS	Adj MS	Contribution
V	2	549.83	549.83	274.915	87.26%
N	2	12.51	12.51	6.257	1.99%
D	2	42.93	42.93	21.466	6.81%
Error	2	24.87	24.87	12.433	3.95%
Total	8	630.14			100.00%

The main effect plots of % reduction in area are shown in Figure 6.4 (c). The main effect plot reveals that an increase in welding speed correlates with a higher % reduction in area. This correlation can be explained by the greater energy input and plastic deformation experienced by the material during higher welding speeds. Consequently, the material exhibits greater deformation and reduction in cross-sectional area (Zhang et al., 2018; Chen et al., 2016). The plot further illustrates that the 'percentage reduction in area' initially rises as the tool rotational speed increases, but eventually reaches a peak and subsequently decreases. At lower rotational speeds, the increased tool rotational speed contributes to enhanced plastic deformation and subsequent reduction in area. However, beyond a certain point, further increases in rotational speed led to excessive heat input and material softening, resulting in reduced plastic deformation and a decrease in the percentage reduction in area (Chen et al., 2016).

Lastly, the % reduction in area exhibits an upward trend with an increase in shoulder diameter up to a certain threshold, beyond which it begins to decline. Initially, the larger shoulder diameter provides increased contact area and improved heat generation, resulting in enhanced plastic deformation and a higher percentage reduction in area. However, beyond a certain shoulder diameter, factors such as increased heat dissipation and potential defects begin to limit the plastic deformation, leading to a decrease in the percentage reduction in area (Li et al., 2019).

Table 6.5 illustrates the ANOVA results for impact energy, providing valuable insights into the influential factors. Among these factors, welding speed emerges as the most prominent, exerting a significant influence with a substantial contribution of 63.29%. This finding underscores the crucial role of welding speed in determining the Impact strength. Following welding speed, shoulder diameter exhibits a noteworthy contribution of 17.37%, indicating its considerable impact on the measured variable. Conversely, tool rotational speed is observed to have an insignificant effect on Impact strength, contributing a mere 1.43%.

Table 6.5: ANOVA table for impact energy of welds

Source	DF	Seq SS	Adj SS	Adj MS	Contribution
V	2	23.537	23.537	11.7687	63.29%
N	2	0.533	0.5330	0.2665	1.43%
D	2	6.461	6.4618	3.2309	17.37%
Error	2	6.659	6.6598	3.3299	17.91%
Total	8	37.191			100.00%

Figure 6.4 (d) presents the main effect plots for the parameter of impact energy indicating that an increase in welding speed corresponds to a higher impact energy. As the welding speed increases, the material undergoes more intense deformation, resulting in higher impact energy (Chen et al., 2016; Li et al., 2019). Likewise, as the tool rotational speed increases, there is a corresponding rise in the impact energy. This higher rotational speed generates additional heat and plastic deformation, resulting in an elevation in impact energy. The higher rotational speed facilitates enhanced material flow and deformation, leading to improved impact energy (Ma et al., 2003; Zhang et al., 2018). Additionally, impact energy decreases with an increase in shoulder diameter up to a certain level, after which it starts to increase. Initially, the smaller shoulder diameter allows for better heat generation and material flow, resulting in higher impact energy, but beyond a certain threshold, an increase in shoulder diameter leads to reduced heat input and limited plastic deformation, resulting in reduced impact energy. Nevertheless, as the shoulder diameter continues to increase, the expanded contact area facilitates better material flow and heightened plastic deformation, resulting in a subsequent increment in the impact energy. (Zhang et al., 2018; Chen et al., 2016).

6.5 MULTI-RESPONSE OPTIMIZATION

Grey relational analysis (GRA) is a method that assigns equal weights to variables, but this approach can introduce uncertainty in the decision-making process. To address this drawback, principal component analysis (PCA) is utilized in this study to ascertain the relative weights of the response parameters. Employing PCA enables a more precise evaluation of the significance of each parameter, facilitating improved decision-making.

The objective is to compare the effectiveness of multi-objective optimization using GRA alone versus GRA combined with PCA. To quantify the relationship between variables, grey relational coefficients (GRC) for individual responses are calculated using equation (6.3). These coefficients provide insights into the degree of correlation and influence between the variables. Additionally, the unweighted grey relational grade, determined using equation (6.4), is employed as an indicator of the overall performance of the system under study. The results of these calculations are summarized and presented in Table 6.6.

Table 6.6: Table showing normalized values of GRC, and GRG for the response parameters

Exp No.	Normalized values				Grey relational coefficients				GRG	Rank
	UTS	PE	% RIA	IE	UTS	PE	% RIA	IE		
1	0.77	0.28	0.12	0.17	0.69	0.41	0.36	0.38	0.46	7
2	0.00	0.30	0.17	0.07	0.33	0.42	0.38	0.35	0.37	9
3	0.66	0.00	0.00	0.00	0.59	0.33	0.33	0.33	0.40	8
4	0.72	0.51	0.75	0.09	0.64	0.51	0.67	0.35	0.54	6
5	0.65	0.69	0.48	0.51	0.59	0.62	0.49	0.51	0.55	5
6	0.87	0.77	0.28	0.95	0.79	0.69	0.41	0.91	0.70	4
7	0.93	1.00	0.81	1.00	0.88	1.00	0.73	1.00	0.90	1
8	0.65	0.84	0.97	0.80	0.58	0.75	0.94	0.71	0.75	3
9	1.00	0.81	1.00	0.63	1.00	0.72	1.00	0.58	0.83	2

For PCA, the eigen values with their respective variance contributions and eigen vectors are computed using equation (6.7) and provided in Table 6.7.

Table 6.7: Principal component analysis

Component	PC1	PC2	PC3	PC4
Eigen value	0.14890	0.04207	0.01899	0.00199
Proportion	0.703	0.199	0.090	0.009
Cumulative	0.703	0.901	0.991	1.000
	0.381	0.028	-0.923	-0.043
	0.527	-0.137	0.251	-0.8
Eigen vector	0.506	0.79	0.22	0.266
	0.567	-0.596	0.191	0.536

From Table 6.7, it is evident that the first PC accounts for as high as 70.3% variance contribution for four quality characteristics. Table 6.8 presents the squares of eigenvectors of the first PC that are chosen as weights of quality responses that are found to be equal to 0.145, 0.2777, 0.2560, and 0.3214 for UTS, % elongation, % reduction in area, and impact energy.

Table 6.8: Variance contribution of response variables for the first principal component

Response variable	Contribution
UTS	0.1451
% elongation	0.2777
% reduction in area	0.2560
Impact energy	0.3214

Using the calculated weights from PCA and GRCs, weighted grey relational grades (W-GRGs) are computed for nine experiments using equation (6.4). The W-GRGs are ranked and presented in Table 6.9. The highest GRG and W-GRG value is obtained at sample no. 7.

Table 6.9: Table showing normalized values of GRC, GRG, and W-GRG for the response parameters.

Exp No.	Normalization				Grey relational coefficients				GRG	Rank	W-GRG	Rank
	UTS	PE	% RIA	IE	UTS	PE	% RIA	IE				
1	0.77	0.28	0.12	0.17	0.69	0.41	0.36	0.38	0.46	7	0.43	7
2	0.00	0.30	0.17	0.07	0.33	0.42	0.38	0.35	0.37	9	0.37	8
3	0.66	0.00	0.00	0.00	0.59	0.33	0.33	0.33	0.40	8	0.37	9
4	0.72	0.51	0.75	0.09	0.64	0.51	0.67	0.35	0.54	6	0.52	6
5	0.65	0.69	0.48	0.51	0.59	0.62	0.49	0.51	0.55	5	0.55	5
6	0.87	0.77	0.28	0.95	0.79	0.69	0.41	0.91	0.70	4	0.70	4
7	0.93	1.00	0.81	1.00	0.88	1.00	0.73	1.00	0.90	1	0.91	1
8	0.65	0.84	0.97	0.80	0.58	0.75	0.94	0.71	0.75	3	0.76	3
9	1.00	0.81	1.00	0.63	1.00	0.72	1.00	0.58	0.83	2	0.79	2

The response table for average GRG and W-GRG is indicated in Table 6.10, which depicts identical optimal conditions. Thus, based on GRG and W-GRGs, the optimum set of input parameters levels for quality responses is $V_3N_3D_1$, indicating welding speed 210 mm/min (level 3), tool rotational speed 750 rpm (level 3), and shoulder diameter 15 mm (level 1).

Table 6.10: Response table for average GRG and W-GRG

Parameters	Average of GRG			Delta	Rank	Average of W-GRG			Delta	Rank
	Levels					Levels				
	1	2	3			1	2	3		
V	0.41	0.60	**0.83***	0.42	1	0.39	0.59	**0.82***	0.43	1
N	0.63	0.56	**0.64***	0.09	2	0.61	0.56	**0.62***	0.06	3
D	**0.64***	0.58	0.62	0.06	3	**0.63***	0.56	0.61	0.07	2
* Optimized setting for response parameter										

6.6 CONFIRMATORY TESTS

Tables 6.11, 6.12, 6.13, and 6.14 present the experimental data for both the optimized factor set and the current factor set for UTS, % elongation, % reduction in area, and impact energy respectively. These tables also provide the predicted data and the improvement in response before and after optimization.

In terms of optimizing UTS as a single response, there was an improvement of 3.73% as the value increased from 549.76 MPa to 570.27 MPa. The enhanced UTS can be credited to the optimized process parameters. By carefully adjusting these parameters, it is possible to promote better bonding and strengthen the weld, leading to an increase in UTS.

Table 6.11: Single response optimization table for UTS

Response parameter	Initial condition	Optimal factors		Response improvement from an initial condition (%)	
		Predicted	Experiment	Predicted	Experiment
	$V_2N_3D_1$	$V_3N_3D_1$	$V_3N_3D_1$		
Ultimate Tensile Strength	549.76	570.39	570.27	3.75	**3.73**
Percentage Elongation	23.82	-	25.56	-	7.30
Percentage reduction in area	47.93	-	59.02	-	23.13
Impact Energy	33.91	-	34.71	-	2.35

Similarly, the percentage elongation showed a 1.97% improvement, with an increase from 23.82 to 24.29. Notably, there was a significant enhancement in the percentage reduction in area, which experienced a substantial increase from 47.93 to 65.41, indicating a remarkable improvement of 36.46%. Factors such as optimized process parameters, tool design, and

material properties can contribute to this improvement. By reducing defects and promoting better flow of material during FSW, the joint becomes more ductile.

When focusing on the single response optimization for IE, its value increased from 33.91 J to 34.71 J, resulting in a 2.35% improvement. This can be achieved through factors such as optimized welding conditions, which lead to the formation of finer grain structures and a reduction in brittleness.

Table 6.12: Single response optimization table for percentage elongation

Response parameter	Initial condition	Optimal factors		Response improvement from initial condition (%)	
		Predicted	Experiment	Predicted	Experiment
	$V_2N_3D_1$	$V_3N_2D_1$	$V_3N_2D_1$		
Ultimate tensile strength	549.76	-	525.16	-	-4.47
Percentage elongation	23.82	25.13	24.29	5.49	**1.97**
Percentage reduction in area	47.93	-	64.55	-	36
Impact energy	33.91	-	33.02	-	-2.62

Table 6.13: Single response optimization table for percentage reduction in area

Response parameter	Initial condition	Optimal factors		Response improvement from initial condition (%)	
		Predicted	Experiment	Predicted	Experiment
	$V_2N_3D_1$	$V_3N_1D_2$	$V_3N_1D_2$		
Ultimate tensile strength	549.76	-	562.34	-	2.28
Percentage elongation	23.82	-	24.09	-	1.13
Percentage reduction in area	47.93	67.55	65.41	40.93	**36.46**
Impact energy	33.91	-	32.07	-	-5.42

Table 6.14: Single response optimization table for impact energy

Response parameter	Initial condition	Optimal factors		Response improvement from initial condition (%)	
		Predicted	Experiment	Predicted	Experiment
	$V_2N_3D_1$	$V_3N_3D_1$	$V_3N_3D_1$		
Ultimate tensile strength	549.76	-	570.27	-	3.73
Percentage elongation	23.82	-	25.56	-	7.30
Percentage reduction in area	47.93	-	59.02	-	23.13
Impact energy	33.91	34.36	34.71	1.32	**2.35**

Table 6.15 illustrates the outcomes of multi-response optimizations for response parameters-UTS, % elongation, % reduction in area, and impact energy. The results indicate that there is a percentage improvement of 3.73%, 7.30%, 23.13%, and 2.35% for the respective responses. The observed experimental values correspond to the predicted models, validating the general pattern.

The experimental data consistently demonstrate enhanced performance characteristics when utilizing the optimal set of factors on the FSW machine.

Table 6.15: Multi-response optimization table

Response parameter	Initial condition	Optimal factors using GRA/W-GRA		Response improvement from initial condition (%)	
		Predicted	Experiment	Predicted	Experiment
	$V_2N_3D_1$	$V_3N_3D_1$	$V_3N_3D_1$		
Ultimate tensile strength	549.76	-	570.27	-	3.73
Percentage elongation	23.82	-	25.56	-	7.30
Percentage reduction in area	47.93	-	59.02	-	23.13
Impact energy	33.91	-	34.71	-	2.35
Grey relational grade	0.70	-	0.85		

CHAPTER 7   METALLURGICAL TESTING OF WELDS

7.1 INTRODUCTION

Metallurgical testing plays a crucial role in scientific studies, providing valuable insights into the properties and behavior of metallic materials. It serves as a fundamental tool for researchers across various disciplines, enabling them to understand the characteristics, composition, and performance of metals. In the context of welding, metallurgical testing is very significant, as it allows for the assessment of the quality, integrity, and structural properties of weldments.

Metallurgical testing for welds involves various essential examinations such as chemical analysis, microstructural analysis, phase evaluation, and microhardness testing. These tests provide valuable insights into the weld's composition, internal structure, and mechanical properties. Additionally, specific assessments like corrosion testing may be conducted on particular alloy compositions. The combination of metallurgical and mechanical testing enables a comprehensive understanding of the welding process and facilitates accurate predictions regarding the weld's performance in real-world service conditions.

7.2 SPECTROSCOPIC ANALYSIS

Spectroscopic analysis is a powerful scientific technique that plays a crucial role in understanding and improving various industrial processes. It involves the study of the interaction between electromagnetic radiation and matter, providing valuable insights into the composition, structure, and properties of different substances.

One of the key areas where spectroscopic analysis is utilized in FSW is the evaluation of the thermal and chemical changes in the weld zone. In the process of FSW, the rotational tool generates heat, leading to localized heating and plastic deformation. As a consequence, a distinctive weld nugget with specific microstructural traits is formed. Spectroscopic techniques such as infrared (IR) spectroscopy and Raman spectroscopy enable the analysis of thermal signatures and chemical transformations in the weld zone. These methodologies offer valuable information regarding the development of intermetallic compounds, modifications in the crystal structure, and variations in the elemental composition of the material.

Spectroscopic analysis is essential in monitoring and controlling process parameters during FSW. In-situ monitoring techniques, such as laser-induced breakdown spectroscopy or optical

emission spectroscopy, enable real-time analysis of the plasma plume generated during welding. These techniques can provide information about the temperature, composition, and elemental distribution in the weld zone, facilitating process optimization and ensuring consistent quality in production.

7.2.1 Test procedure

Spectroscopic analysis plays a vital role in materials science and industrial applications, providing valuable insights into the elemental composition of metallic samples. The Foundry master spark spectrometry machine, based on OES, is a widely used instrument for such analyses. By generating a spark on the sample surface, the foundry master collects and analyzes the emitted light, enabling the identification and quantification of various elements. Before performing the spectroscopic test, the machine needs to be calibrated for specific alloy types. This test procedure outlines the steps involved in conducting a spectroscopic analysis using the foundry master spark spectrometry machine, with a focus on the calibration for ferrous alloys.

Before beginning the testing procedure, the foundry master spark spectrometry machine is calibrated for ferrous alloys. Calibration is necessary to establish a correlation between the measured emission intensities and the known concentrations of elements in a set of reference samples. The calibration process involves analyzing a series of standard reference samples with known compositions and determining the emission intensity for each element of interest.

Once the machine is calibrated, the sample preparation stage begins. A sample is prepared for analysis and carefully loaded onto the holder of the machine. Care was taken to fasten the sample in place to prevent any movement during the analysis.

With the sample in place, the analysis parameters were set on the foundry master machine. This involves configuring the measurement mode, such as direct-reading or calibration mode, and specifying the integration time for acquiring the spectral data. Additionally, the appropriate spectral lines or wavelength ranges to be measured are selected, focusing on the emission lines associated with the elements of interest in ferrous alloys.

Once the analysis parameters were set, samples were sparked on the weld's upper surface, as illustrated in Figure 7.1, that are likely to have tungsten inclusions. The spark excites the atoms in the sample, causing them to emit characteristic light. The emitted light is collected by the machine and passed through a spectrometer, which disperses the light into its constituent

wavelengths. A detector measures the intensity of the emitted light at specific wavelengths. The foundry master spark spectrometry machine provides an analysis of the elemental composition typically found in steels. The machine detects the presence of various elements, including iron, carbon, silicon, manganese, phosphorus, sulfur, chromium, molybdenum, cobalt, niobium, titanium, vanadium, tungsten, tin, boron, calcium, zirconium, and arsenic. Among these elements, iron, carbon, tungsten, and cobalt are particularly crucial and require close monitoring. However, the remaining elements are not commonly added or depleted during the FSW process.
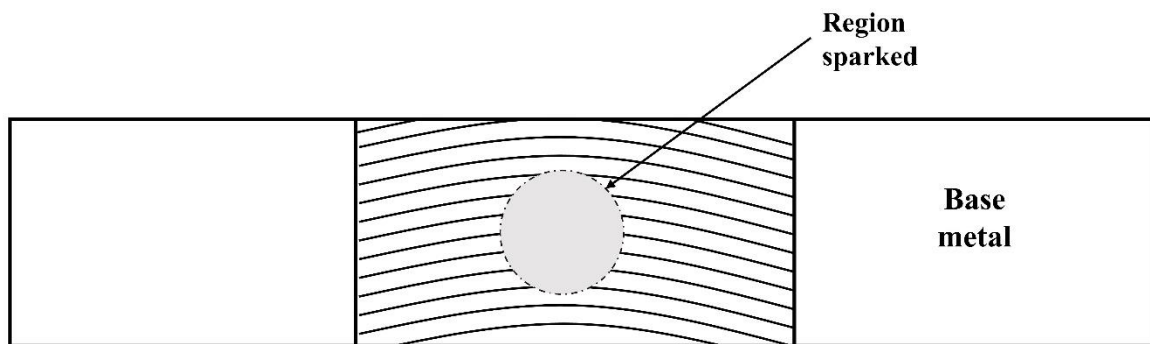
Figure 7.1: Specimen for spectroscopic analysis

7.2.2 Results of spectroscopic analysis

Table 7.1 presents the compositions of weld nuggets extracted from welds produced under different welding parameters. Table 4.6 provides the composition details of the base metal. The base material's composition was determined by averaging the results from six samples taken from various locations of the original supplied base material, which was AISI 1018 steel provided by the Steel Authority of India Limited (SAIL). The spectroscopic analysis of the base metal samples exhibited consistent results, indicating a high level of homogeneity in the original material. Specifically, the weight percentages of carbon, tungsten, and cobalt remained stable. Table 7.1 displays the spectroscopic analysis outcomes for 27 welds produced according to the process parameters outlined in Table 4.5.

Table 7.1: Results of spectroscopic analysis of welds.

Run order	Fe	C	Si	Mn	P	S	Cr	Mo	Co	W
1	99.07	0.178	0.104	0.521	0.038	0.014	0.030	<0.005	0.011	Nil
2	99.01	0.168	0.115	0.532	0.040	0.015	0.030	<0.005	0.011	0.017
3	99.00	0.170	0.123	0.523	0.041	0.013	0.027	<0.005	0.011	0.034
4	98.97	0.168	0.132	0.522	0.038	0.014	0.030	<0.005	0.0114	0.027
5	99.00	0.156	0.097	0.535	0.040	0.015	0.030	<0.005	0.008	Nil
6	99.03	0.166	0.0119	0.526	0.041	0.013	0.027	<0.005	0.007	Nil
7	98.98	0.164	0.124	0.520	0.038	0.014	0.030	<0.005	0.010	0.026
8	98.94	0.176	0.111	0.532	0.040	0.015	0.030	<0.005	0.009	0.074
9	96.61	0.164	0.145	0.523	0.041	0.013	0.027	0.052	>0.35	**>1.5**
10	99.06	0.180	0.108	0.522	0.038	0.014	0.030	<0.005	0.017	0.047
11	97.75	0.154	0.128	0.533	0.040	0.015	0.030	<0.005	>0.35	**>1.5**
12	99.03	0.178	0.112	0.521	0.041	0.013	0.027	0.051	0.012	Nil
13	98.99	0.172	0.118	0.519	0.038	0.014	0.030	<0.005	0.011	0.019
14	98.28	0.160	0.116	0.521	0.040	0.015	0.030	<0.005	0.082	**0.621**
15	97.96	0.165	0.115	0.518	0.041	0.013	0.027	<0.005	0.093	**0.873**
16	99.01	0.178	0.124	0.517	0.038	0.014	0.030	<0.005	0.011	Nil
17	99.02	0.169	0.119	0.516	0.040	0.015	0.030	<0.005	0.011	Nil
18	99.03	0.164	0.103	0.515	0.041	0.013	0.027	<0.005	0.015	0.017
19	99.04	0.171	0.114	0.514	0.038	0.014	0.030	<0.005	0.012	Nil
20	99.06	0.163	0.062	0.532	0.040	0.015	0.030	<0.005	0.009	nil
21	99.03	0.180	0.118	0.523	0.041	0.013	0.027	<0.005	0.010	Nil
22	99.05	0.176	0.098	0.521	0.038	0.014	0.030	<0.005	0.012	Nil
23	99.03	0.177	0.117	0.532	0.040	0.015	0.030	<0.005	0.016	Nil
24	98.99	0.155	0.112	0.523	0.041	0.013	0.027	<0.005	0.008	Nil
25	98.97	0.168	0.119	0.521	0.038	0.014	0.030	<0.005	0.011	0.043
26	99.01	0.166	0.127	0.532	0.040	0.015	0.030	<0.005	0.011	Nil
27	97.89	0.178	0.115	0.523	0.041	0.013	0.027	<0.005	0.012	**0.908**
Base metal	99.03	0.18	0.117	0.65	0.04	0.014	0.030	<0.005	0.009	Nil

In the majority of samples, the composition of the weld nugget closely matched that of the base material. However, in a few instances (samples 9, 11, 14, 15, and 27), the presence of tungsten was detected. It is noteworthy that when tungsten was found in the weld nugget, the corresponding weight percentages of cobalt and carbon also increased. This suggests that the introduction of tungsten resulted from the presence of wear debris from tungsten carbide, including its binder. In other words, the tool damage observed was attributed to wear rather than chemical changes occurring within the tool material. The tool material did not disintegrate due to the welding heat. The smearing of tungsten carbide was observed only when a specific tool was used extensively over a prolonged period, rather than being caused by excessive heat resulting from any combination of process parameters.

7.3 MICROSTRUCTURAL EXAMINATION

Microstructural examination plays a significant role in comprehending the intricacies involved in FSW, especially when dealing with low-carbon steel. By examining the microstructure of FSW welds, valuable insights can be gained regarding the material's transformation throughout the welding process. The complexity of microstructural evolution in FSW of low-carbon steel arises when the welding temperature closely aligns with the recrystallization temperature. Consequently, the temperature during welding can either surpass or fall below the recrystallization temperature, depending on the specific process parameters employed.

It helps characterize the microstructure within the weld zone, heat-affected zone (HAZ), and Base metal (BM), enabling a thorough evaluation of the alterations taking place at various sections of the joint. Optical microscopy is a primary technique used in microstructural examination, enabling the observation of the weld's macrostructure and microstructure. Sample preparation techniques such as cutting, grinding, and polishing are employed to reveal the microstructural details.

7.3.1 Test procedure

To conduct the examination, a specimen was obtained from the welded plate prepared using the optimal machine settings. The specimen was then mounted in a bakelite mold, ensuring stability during the subsequent polishing process. The sample was subjected to polishing using a variable speed grinder-polisher and silicon carbide emery paper with different grit sizes, ranging from P100 to P2000. The polishing speed was adjusted between 250 rpm and 450 rpm to achieve satisfactory results. A mirror-like finish was obtained by using 0.05-micron alumina

powder on a velvet cloth. Subsequently, the sample underwent etching using a 3% Nital solution composed of 97 parts methanol and 3 parts concentrated nitric acid. The sample's microstructure was analyzed and observed using an optical microscope at various magnifications to examine and assess its characteristics.

7.3.2 Results

The microstructural examination of the FSWed samples was conducted using SEM at various magnifications. The results provide valuable insights into the different zones and features present in the welds.

In Figure 7.2 (a), the transition phase between the unaffected parent material and the stirred zone (SZ) is visible, demonstrating the boundary separating the two regions. The image is magnified by 500x to visualize the distinct zones produced during welding. Figure 7.2 (b) highlights the three main zones: the nugget zone, the thermo-mechanically affected zone (TMAZ), and HAZ. Furthermore, Figure 7.2 (c) illustrates the transitional zone between HAZ and TMAZ, wherein TMAZ shows grain refinement and dynamic recrystallization. Within this region, both thermal and mechanical influences play a significant role.

The nugget zone and TMAZ undergo substantial effects due to the frictional heat generated by the shoulder and the deformation induced by the pin. The movement of the pin during welding also affects the crystalline plane orientation in the stirred zones. Additionally, the shoulder surface on the top of the weld exhibits a different microstructure compared to the bottom due to the greater centrifugal force in material flow.

The microstructure of the base metal is represented by Figure 7.3(a). The HAZ, as observed in Figure 7.3(b), is relatively small and consists of a partially transformed zone. The intense plastic deformation and elevated temperatures encountered during the welding process lead to alterations in grain sizes within the stirred microstructure zone, setting it apart from the base metal. Figure 7.3 (c) provides a clear visualization of the interface between the nugget zone and TMAZ.

During the welding process, some precipitate dissolution can occur within and around the stirred zone. This phenomenon further contributes to the microstructural changes observed in the welds. The detailed discussion on these regions obtained in the weld is illustrated in section 7.3.4.
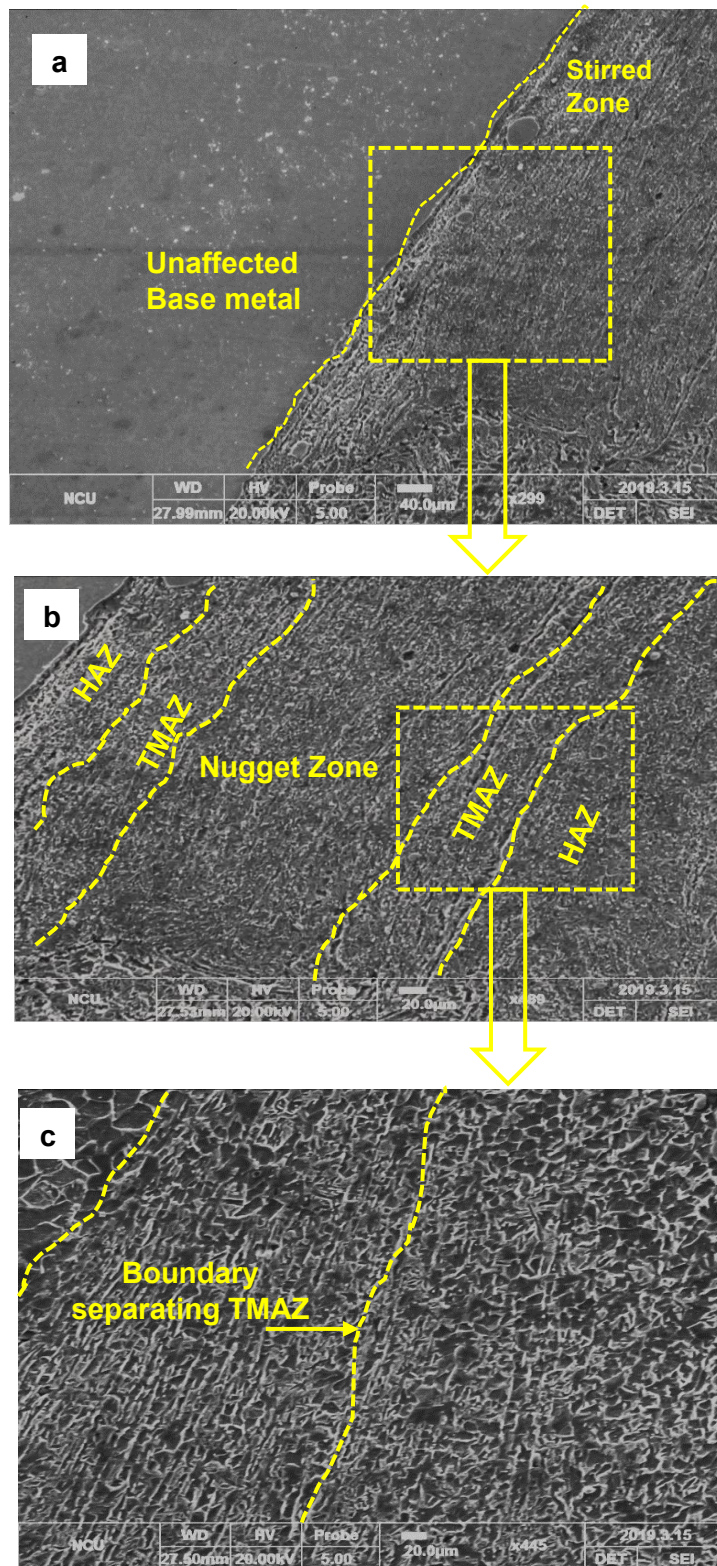
Figure 7.2: Microstructure indicating a) transition between the unaffected base metal and the stirred zone; b) distinct zones identified; and c) transition between TMAZ and HAZ.
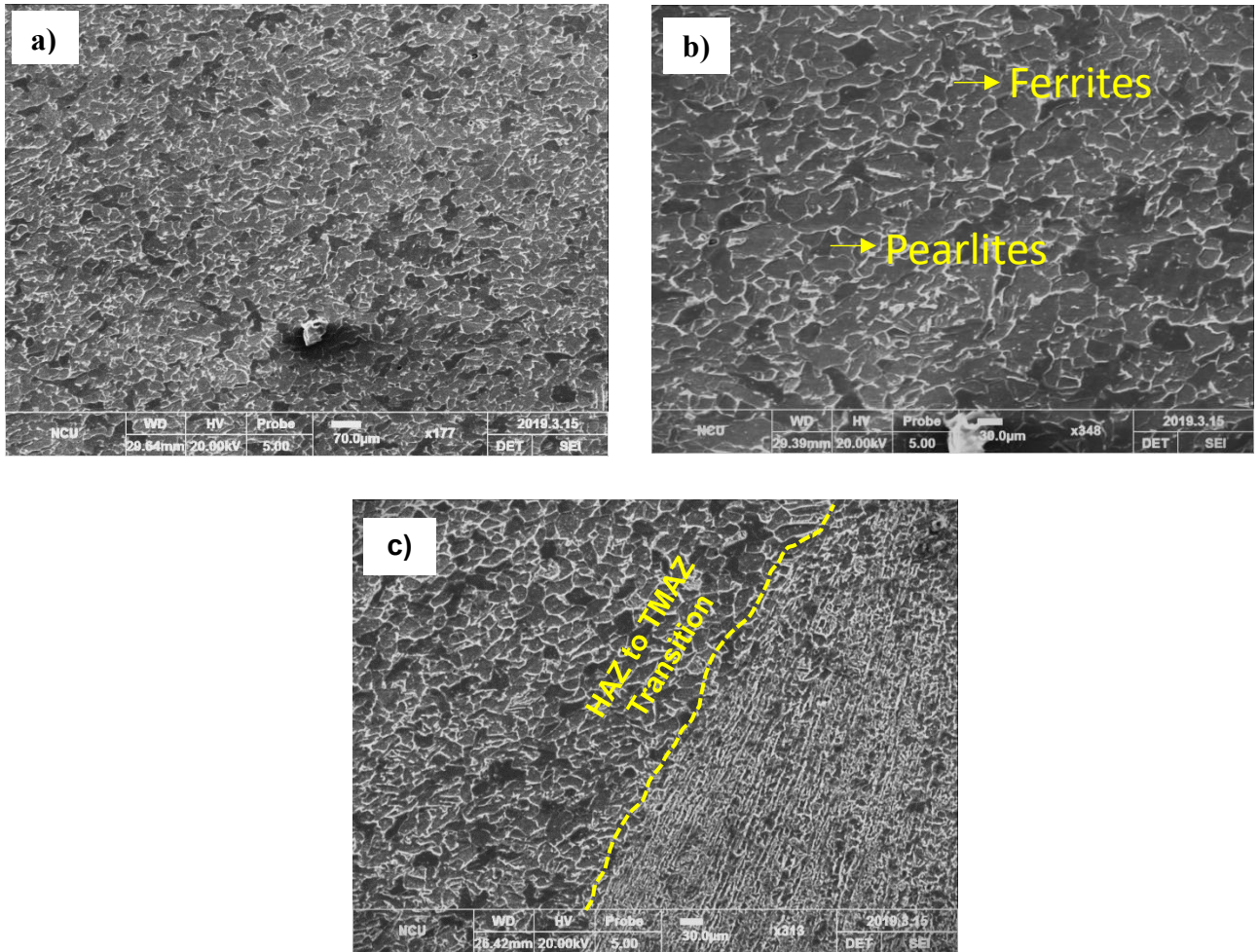
Figure 7.3: Microstructural Characteristics of a) Base metal b) HAZ, and c) HAZ to TMAZ transition

7.3.3 Microstructural evolution in FSW

FSW encompasses the dynamic recovery and dynamic recrystallization of materials. The alterations in microstructure that take place during this procedure are influenced by factors such as deformation temperature and strain rate. To streamline the analysis, the strain rate and deformation temperature are frequently merged into a consolidated parameter referred to as the Zener-Hollomon parameter (Z). This parameter is determined by the equation $Z = \acute{\varepsilon}\ e^{(Q/RT)}$, wherein $\acute{\varepsilon}$ represents the strain rate, Q denotes the activation energy, R is the ideal gas constant, and T represents the temperature.

With higher welding speeds, the temperature in the stir zone tends to decrease, while the strain rate increases, leading to an elevation in the Zener-Hollomon parameter. The tool shoulder diameter and rotational speed directly influence the temperature and strain rate, consequently affecting the value of the Zener-Hollomon parameter. The value of the Zener-Hollomon

150

parameter varies depending on the dominant factor at play. This parameter holds significant importance in determining the size of recrystallized grains.

To comprehend the microstructural changes in FS welds, the principles of dynamic recovery, continuous dynamic recrystallization, and discontinuous dynamic recrystallization are utilized. These theories offer valuable insights into the microscopic transformations taking place during the FSW process.

Dynamic recovery: Dynamic recovery refers to the process that occurs when a material is deformed at elevated temperatures. During this process, various steps take place simultaneously, including the rearrangement and annihilation of dislocations, as well as the formation of subgrains. These steps contribute to the development of a microstructure characterized by low-angle grain boundaries. This phenomenon, known as dynamic recovery, is particularly pronounced in alloys with high stacking fault energy, such as α-iron. In these alloys, dislocation climbs and cross-slips readily occur, leading to rapid and extensive dynamic recovery.

When a material is subjected to deformation at high temperatures, the dislocations present within the crystal lattice undergo dynamic changes. Dislocations are line defects in the crystal structure that result from the deviation from perfect atomic packing. They play a crucial role in the plastic deformation of materials by allowing atomic planes to slide over each other. However, at elevated temperatures, the mobility and interaction of dislocations increase significantly.

During dynamic recovery, the dislocations rearrange themselves within the crystal lattice, causing a reduction in the dislocation density. This rearrangement occurs through processes such as dislocation glide, climb, cross-slip, and annihilation. Dislocation glide involves the movement of dislocations along specific crystallographic planes, while climb refers to their motion in the direction perpendicular to the glide planes. Cross-slip occurs when dislocations change their glide planes. The annihilation of dislocations takes place when dislocations with opposite signs and similar Burgers vectors come into proximity, leading to their mutual cancellation.

The rearrangement and annihilation of dislocations during dynamic recovery result in the formation of subgrains. Subgrains are regions within the material where the crystal lattice has a slightly different orientation compared to the surrounding areas. They are separated by low-

angle grain boundaries, which are interfaces between neighboring subgrains with a misorientation angle typically less than 15°. These grain boundaries with low angles impede dislocation movement, thereby enhancing the strength and mechanical properties of the material. (Kocks et al, 2000)

Continuous dynamic recrystallization: In alloys characterized by high stacking energy, the occurrence of dynamic recovery is facilitated, preventing a significant increase in dislocation density and subsequent nucleation of new grains. However, in these alloys, when subjected to high strain rates, a different mechanism of recrystallization takes place. This mechanism, known as continuous dynamic recrystallization, involves the transformation of subgrains within the deformed original grain into new grains, without distinct nucleation and growth stages.

There are two types of continuous dynamic recrystallization processes:

- Rotational recrystallization
- Geometric dynamic recrystallization

Rotational recrystallization: This type of Continuous dynamic recrystallization is commonly observed in magnesium alloys, aluminum alloys, and geological minerals. This type of recrystallization occurs through the gradual rotation of subgrains neighboring the existing grain boundary. It is particularly prevalent in these alloys and minerals due to their high stacking energy. During dynamic recovery, the formation of subgrains causes the boundaries of the original grain to develop serrations or become distorted. These serrations are similar in size to the subgrains formed during the process. (Liu et al., 2017)

Geometric dynamic recrystallization: Geometric dynamic recrystallization is frequently observed in ferrite steels, where the boundaries of the original grains undergo serrations or become distorted due to the formation of subgrains during dynamic recovery. These serrations are similar in size to the subgrains that are generated. Under substantial deformation, the original grains undergo flattening and thinning due to the material's plastic flow. As the deformation proceeds, the thickness of the initial grain diminishes gradually until it reaches a similar scale as that of the subgrains. Upon reaching this critical point, a sudden transformation takes place. The low-angle grain boundaries of the subgrains swiftly eliminate the high-angle

152

boundaries of the original grains. Consequently, a refined microstructure characterized by a very fine equiaxed pattern with high-angle grain boundaries is formed. (Chen et al, 2016).

Discontinuous dynamic recrystallization (DDRX): In materials with low stacking fault energy, such as γ-iron, the recovery processes occur at a slower rate. Under suitable conditions, these materials undergo a phenomenon known as discontinuous dynamic recrystallization. During this type of dynamic recrystallization, new grains originate at the boundaries of the old grains and begin to grow. With the progression of deformation, the dislocation density within the freshly formed grains intensifies. The increase in dislocation density reduces the driving force for further growth. Eventually, when the dislocation density reaches a sufficient level, the growth of the new grain ceases. Subsequently, new grains nucleate from the grain boundaries of the stagnant grain. This type of recrystallization exhibits distinct stages of nucleation and growth, resulting in fine-grained structures. The size of recrystallized grains, also known as dynamically recrystallized grains (D_R), decreases as the Zener-Hollomon parameter (Z) increases.

Discontinuous dynamic recrystallization (DDRX) initiates at high-angle grain boundaries, which can be either the original grain boundaries or the boundaries of newly recrystallized grains. The mechanism of DDRX can be described as follows: Initially, grains nucleate at the boundaries of existing grains, forming a cluster of growing grains. As previously mentioned, the growth of these grains eventually ceases, giving rise to the initiation of new grains at the boundaries of the recently formed grain. This process results in the thickening of the cluster of recrystallized grains. In scenarios where a substantial disparity in size exists between the initial grain and the grain generated through DDRX, a structure resembling a necklace may emerge. Ultimately, the material undergoes complete recrystallization. Throughout the recrystallization process, the mean size of the recrystallized grains remains constant.

7.3.4 Mechanism of phase transformation in different regions of the weldment

The predominant factors influencing the maximum temperature achieved in the SZ are the rotational speed and welding speed, assuming a constant tool geometry. To address this relationship, researchers (Arbegast et al., 1998) proposed an empirical equation (equation 7.1) that provides an understanding of this dependence.

$$\frac{T'}{T_m} = K_1 \left(\frac{N^2 x 10^4}{V} \right)^{\propto} \tag{7.1}$$

Where, T' is the peak temperature

T_m is the melting point of the alloy

N is the tool rotational speed in rps

V is the welding speed in m/s

K_1=0.7 and α=0.005 are constants.

In the experimentation, it was observed that the peak temperature exceeded 1000 °C for various combinations of welding process parameters. This can be inferred from the color of the tool shoulder, as depicted in Figure 4.12 (a), indicating temperatures above 1000 °C. Assuming this as the maximum temperature attained, Based on the findings, it can be inferred that the temperature within the SZ was adequate to induce the transformation of the base material into austenite.

Different mechanisms of microstructural evolution were observed in the SZ, TMAZ, and HAZ will be further discussed in the following sections.
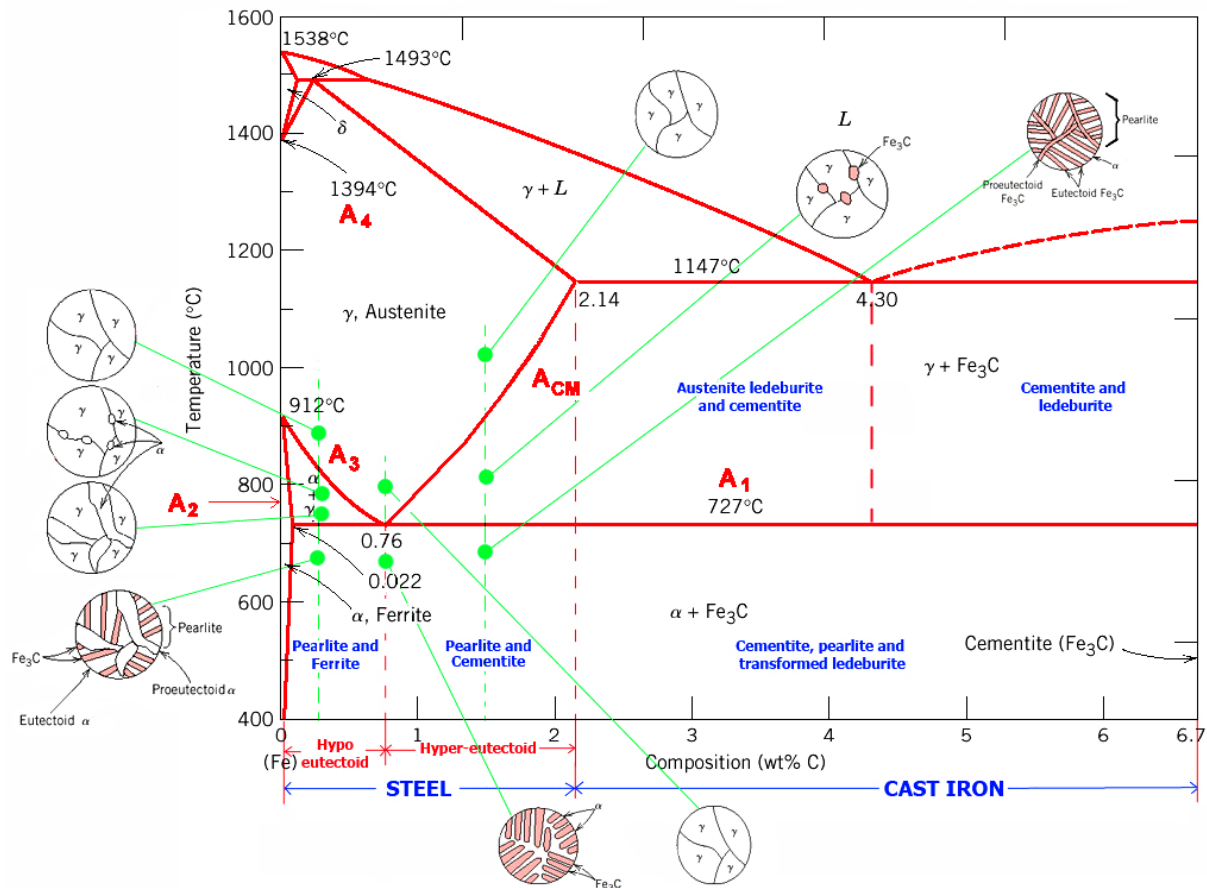
Figure 7.4: Iron-carbon phase diagram. (Callister & Rethwisch, 2018)

7.3.4.1 Microstructural evolution in weld nugget or stir zone (SZ)

During the welding process, where elevated temperatures are present, the deformation leads to dynamic recrystallization within the weld nugget. The microstructural changes in this area are assumed to be influenced by the following mechanisms during FSW

- In all welding scenarios, the attained maximum temperature surpasses the A_3 temperature. With reference to the iron-carbon phase diagram shown in Figure 7.4, at this specific temperature, the material resides within the austenitic (Υ) region of the phase diagram. As the recovery process is sluggish in austenite, dynamic recrystallization takes place. Given the substantial deformation involved in FSW, the conditions necessary for discontinuous dynamic recrystallization are readily met.

- The formation of fine austenite grains is facilitated by the discontinuous dynamic recrystallization (DDRX) phenomenon. The grain size is influenced by a range of process parameters. Higher strain rates, which occur with increased welding speeds and tool rotational speeds, alongside lower temperatures attained through smaller shoulder

155

diameters and higher welding speeds, contribute to an elevated Zener-Hollomon parameter. It is commonly recognized that the steady-state grain size resulting from DDRX decreases as the flow stress increases. Consequently, finer grains are produced when the Zener-Hollomon parameter is increased.

- The fine recrystallized austenite grains transform back into ferrite as the temperature decreases.

7.3.4.2 Microstructural changes in TMAZ

During welding, heat is produced at the weld interface, resulting in localized temperature rises. Nevertheless, heat is dispersed through different means, such as conduction, convection, and radiation. The uppermost part of the weld, being closer to the atmosphere, experiences more pronounced heat dissipation compared to the lower regions. This is due to the absence of direct shielding from the cooling effects of the surrounding environment.

As a consequence of inadequate temperature, the grains in this region experience limited thermal activation and insufficient energy for recrystallization. Instead, the material undergoes plastic deformation, causing grain distortion and the absence of recrystallization. Deformed grain formations are commonly noticed in areas where the temperature is inadequate for the occurrence of dynamic recrystallization.

7.3.4.3 Microstructural changes in HAZ

In comparison to the SZ, the region around the stir zone has a lower temperature. In this zone, a mixed phase of austenite and ferrite $(\alpha+\Upsilon)$ is present, as evidenced by the transformation of pearlite into finely divided perlite. The region near the shoulder, known as the heat-affected zone (HAZ), experiences both strains from the rotating shoulder and the corresponding temperature. These conditions are favorable for the occurrence of continuous dynamic recrystallization (CDRX) in ferrite, as discussed previously. Upon careful examination of the ferrite microstructure using scanning electron microscopy (SEM), it becomes apparent that the original ferrite grains gradually undergo fragmentation and subdivision.

7.4 MICROHARDNESS TESTING

Microhardness testing plays a crucial role in materials science and engineering, as it allows for the precise measurement of hardness values on a microscopic scale. Hardness is a fundamental

mechanical property that relates to a material's resistance to deformation and scratching. By using a microhardness testing instrument, indentations are made on the material's surface under controlled loads. The resulting impressions can then be measured optically to determine the hardness values.

One of the key advantages of microhardness testing is its ability to provide localized hardness information. This is particularly important when investigating the effects of various factors on material properties at small-length scales. For example, during phase transformations, microstructural changes can lead to variations in hardness. By conducting microhardness testing at specific regions of interest, one can assess the impact of these changes on mechanical behaviour. Additionally, microhardness testing can be used to evaluate the hardness gradients within a material, such as in weldments or heat-affected zones.

The principles underlying microhardness testing are based on the indentation size effect (ISE). According to the ISE, the hardness value obtained from a small indentation is higher than that of a larger indentation on the same material. This size-dependent behaviour arises due to the increased influence of material-specific factors, such as dislocation interactions and strain gradients, at smaller length scales. Microhardness testing accounts for this effect by using geometrically defined indenters and appropriate load ranges to ensure accurate and reliable hardness measurements.

7.4.1 Test procedure

Microhardness testing was conducted as per ASTM standards E-92 (ASTM E92-17a) standards. Microhardness testing was performed using a 100-gram load to assess the hardness of the base material, HAZ, and weld nugget. Two sample sets were fabricated to assess the microhardness of welds produced under varying welding conditions. One set of specimens underwent thorough polishing on the welds' transverse section to ensure their suitability for microhardness testing. The second set of specimens was polished on the weld's upper surface

and prepared for subsequent testing. The microhardness evaluations were carried out on the specimens following the indentation patterns depicted in Figure 7.5 (a and b).
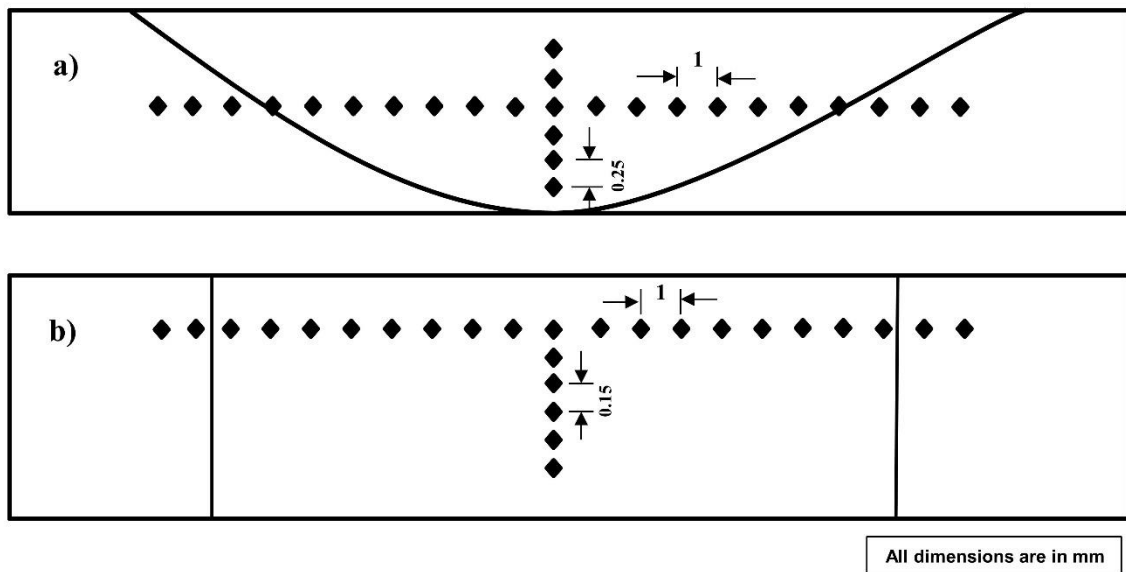
Figure 7.5: a) Indentation methodology employed for microhardness assessment on the cross-sectional area of the welds; b) Indentation procedure employed for microhardness evaluation on the upper surface of the welds.

Indentations were made on the weld's transverse portion in two perpendicular directions. One pair of indentations was spaced 1 mm apart and covered the whole weldment area. A 10 mm span was chosen on either side of the weld center to encompass the weld nugget, HAZ, and base material section, ensuring complete coverage across all welding conditions. The second set of indentations was made exclusively within the weld nugget, oriented from the top to the bottom direction. These indentations were placed at intervals of 0.25 mm, covering the entire depth of the weld nugget.

Indentations were performed on the upper surface of the weld using two perpendicular directions. A 10 mm span was chosen on either side of the weld centre to encompass the weld nugget, HAZ, and base material section, ensuring complete coverage across all welding conditions. In one direction, indentations were placed at 1 mm intervals, perpendicular to the welding direction. A total of 26 indentations were conducted, covering the stir zone, HAZ, and a portion of base material for all welding conditions. Additional indentations were necessary to ensure complete coverage of the wider weld nugget width on the top surface. Along the welding direction, another set of indentations was made parallel to the weld direction. A total

of 12 indentations were carried out, with 0.15 mm spacing between each indentation, ensuring comprehensive coverage along the welding direction. There were ripple formations on the top surface of the weld. The distance between the two indentations was deliberately reduced when indenting along the direction of welding to capture any periodicity in the hardness data induced due to ripple formation. Care was taken to ensure the effect of one indentation was not affecting the hardness value of the adjacent indentation. Also, the established standard of maintaining a minimum distance four times the diagonal length of each indentation was consistently adhered to in all cases.

7.4.2 Results of microhardness testing

The microhardness results obtained from both the transverse section and the top face of the weld are represented in Figures 7.6 to 7.14. Consistent patterns in microhardness were observed across the weld when indentations were made on both the top face and transverse section. Significant enhancements in microhardness, approximately 25%, were observed within the weld nugget region, primarily attributable to refined grains. Notably, no hardness reduction was detected in any of the weldments produced under different process parameters.

Within the transverse section, the microhardness measurements conducted within the stir zone consistently exhibited elevated values. Additionally, slight microhardness variations were identified during the transition from the upper to the lower weld region. Similarly, the weld's upper surface displayed elevated microhardness levels in the stir zone. Microhardness measurements consistently demonstrated higher values within the stir zone, indicating increased hardness in that specific region.
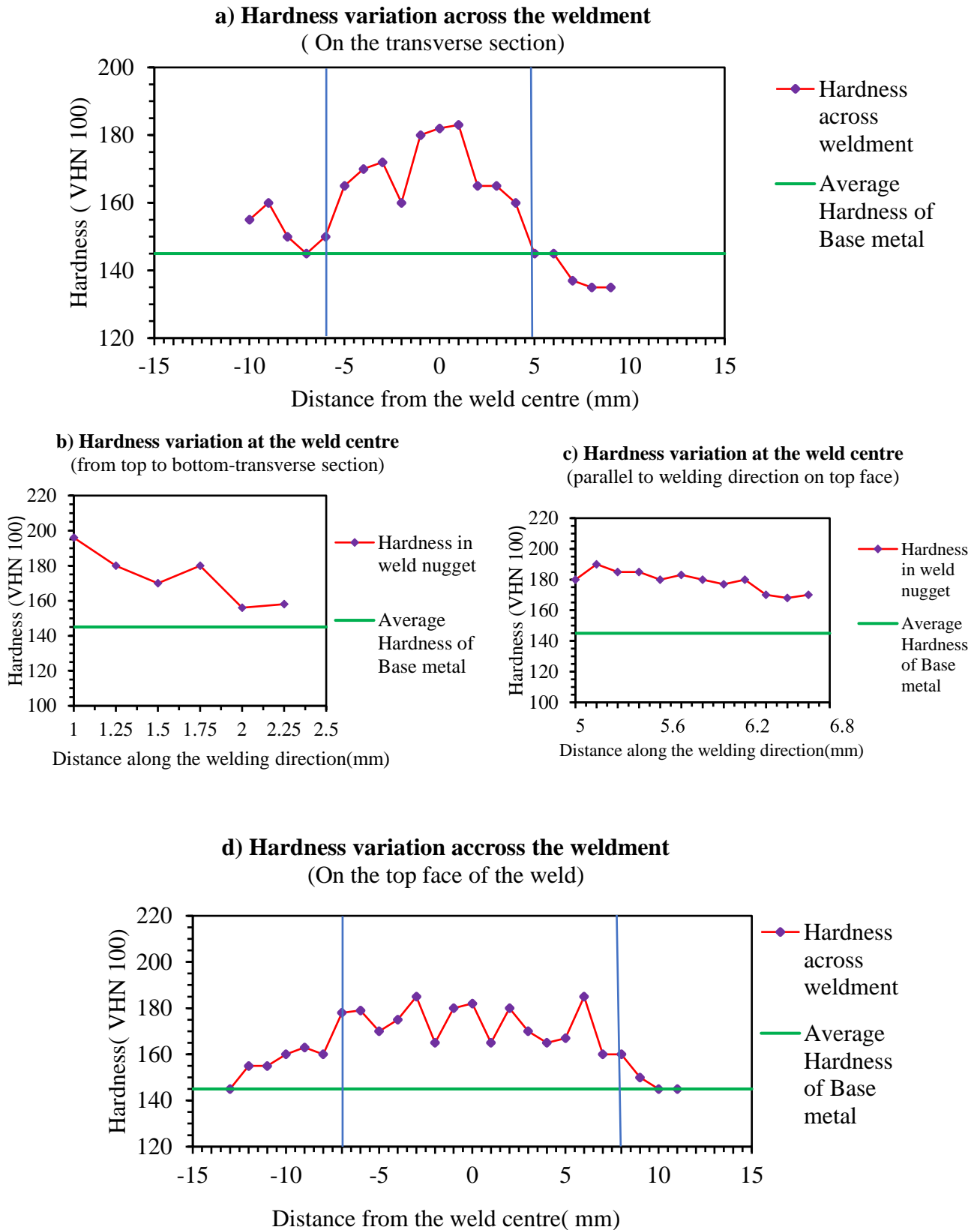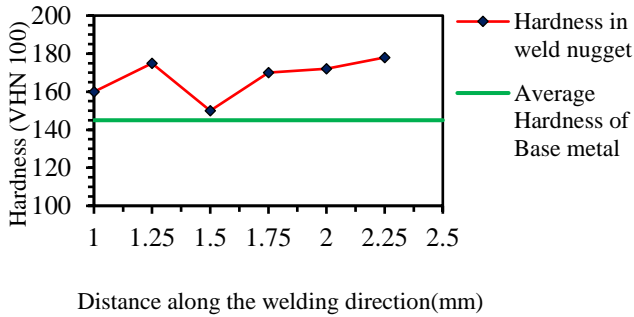
Figure 7.6: Microhardness results obtained from welding conducted at 60 mm/min welding speed, 430 rpm rotational speed, and 15 mm shoulder diameter.
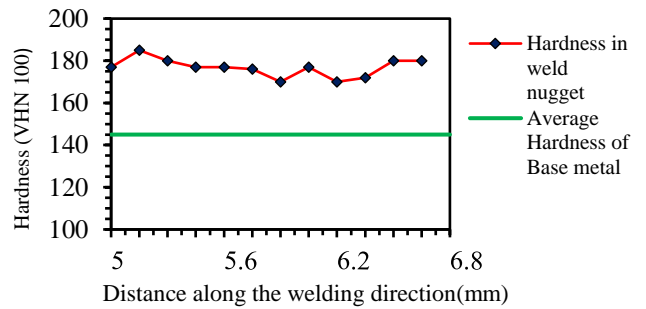
160
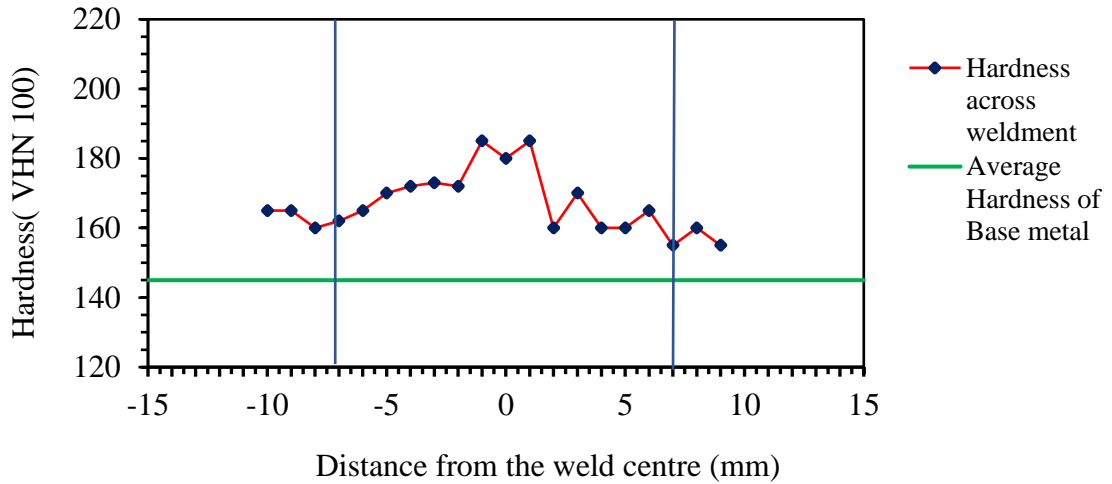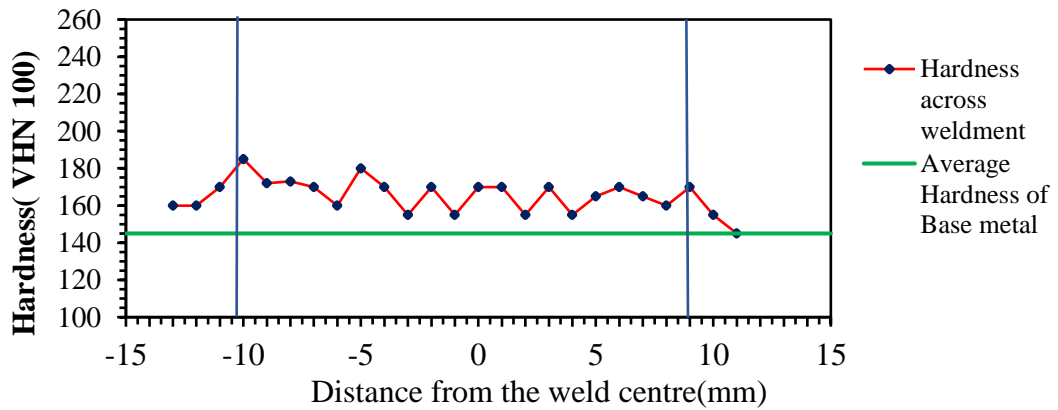
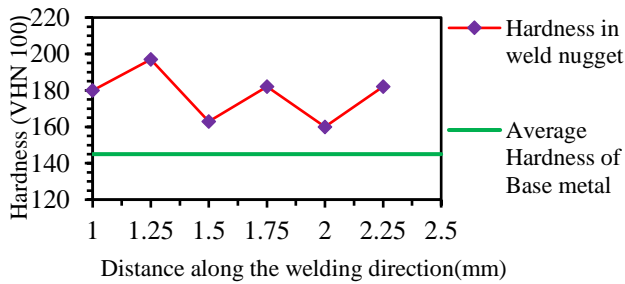**Figure 7.7: Microhardness results obtained from welding conducted at 60 mm/min welding speed, 550 rpm rotational speed, and 18 mm shoulder diameter.**
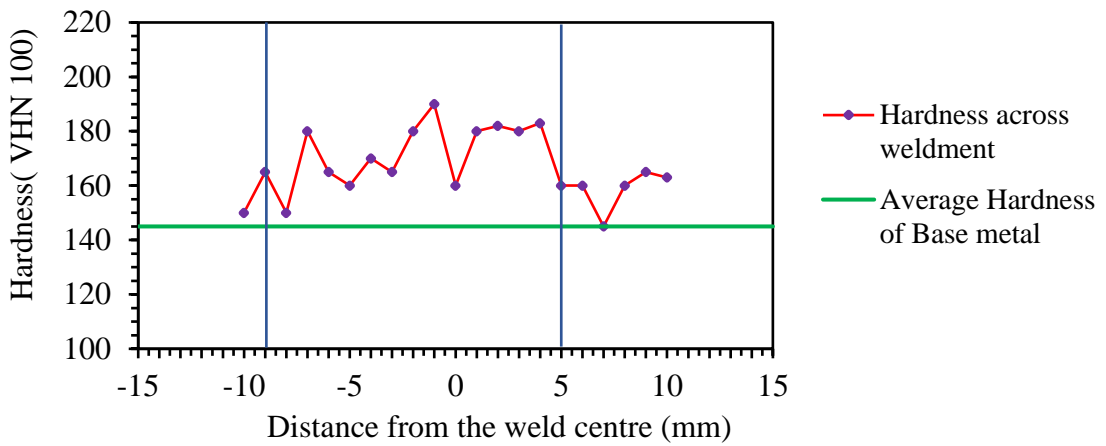
Figure 7.8: Microhardness results obtained from welding conducted at 60 mm/min welding speed, 750 rpm rotational speed, and 20 mm shoulder diameter.
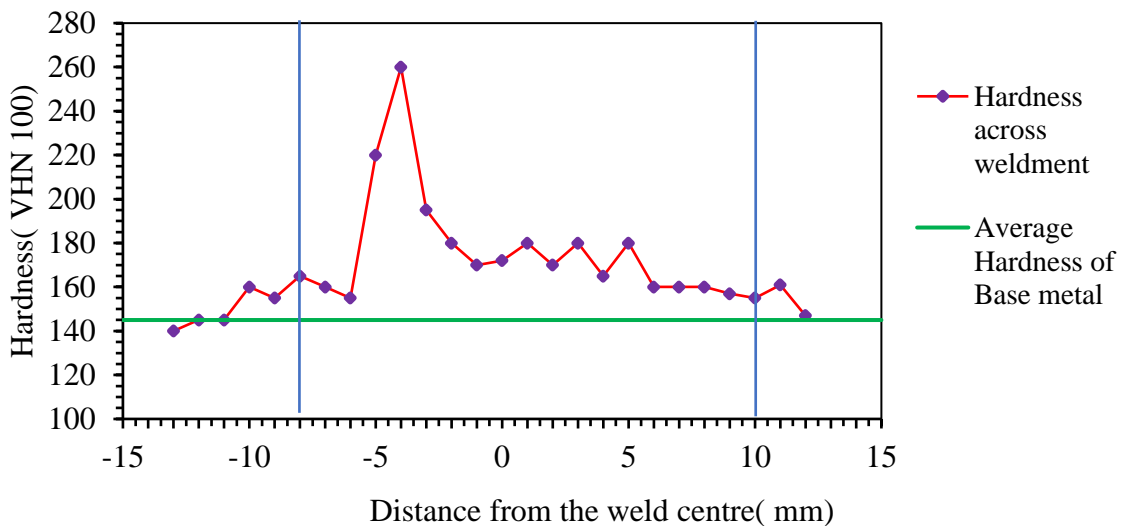
Figure 7.9: Microhardness results obtained from welding conducted at 110 mm/min welding speed, 430 rpm rotational speed, and 18 mm shoulder diameter.
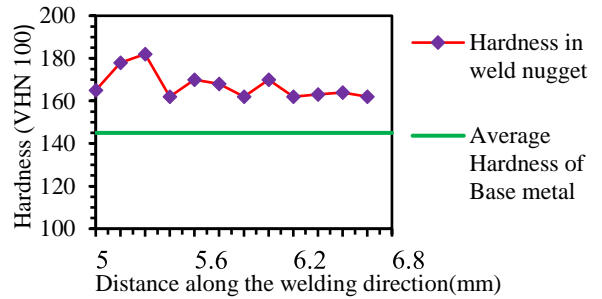
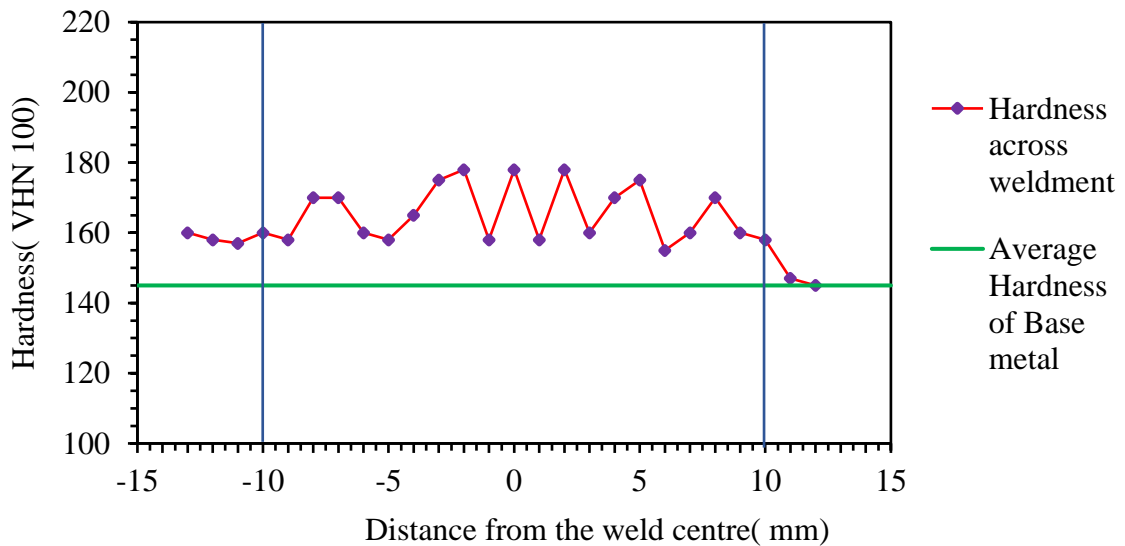**a) Hardness variation accross the weldment**
(On the transverse section)
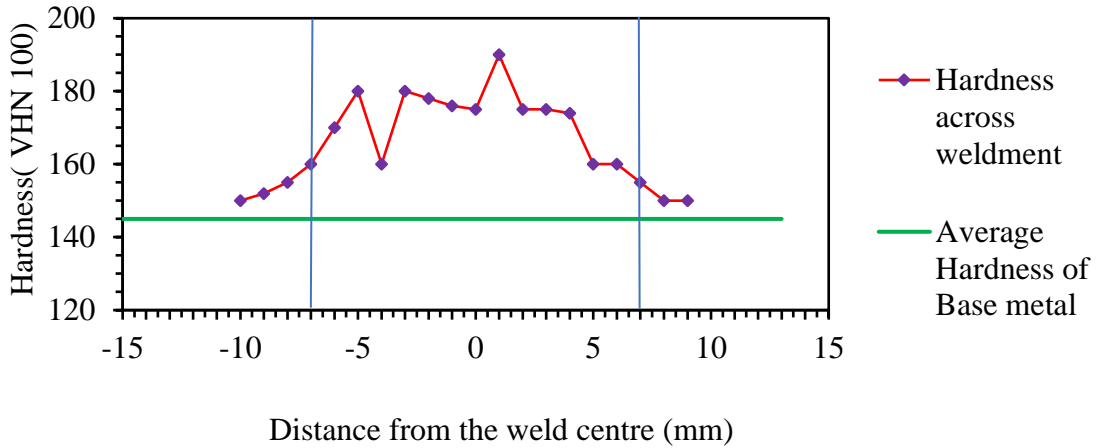
b) Hardness variation at the centre of weld
(from top to bottom-transverse section)
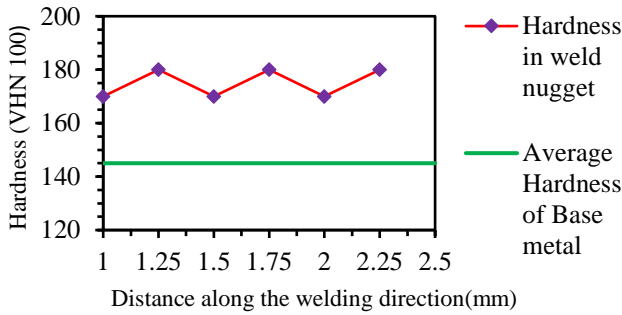
c) Hardness variation at the centre of weld
(parallel to welding direction on top face)
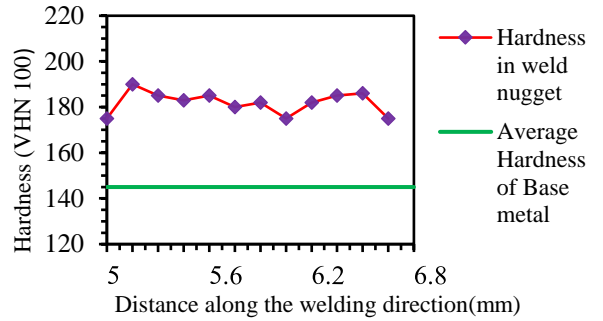
d) Hardness variation accross the weldment
(On the top face of the weld)
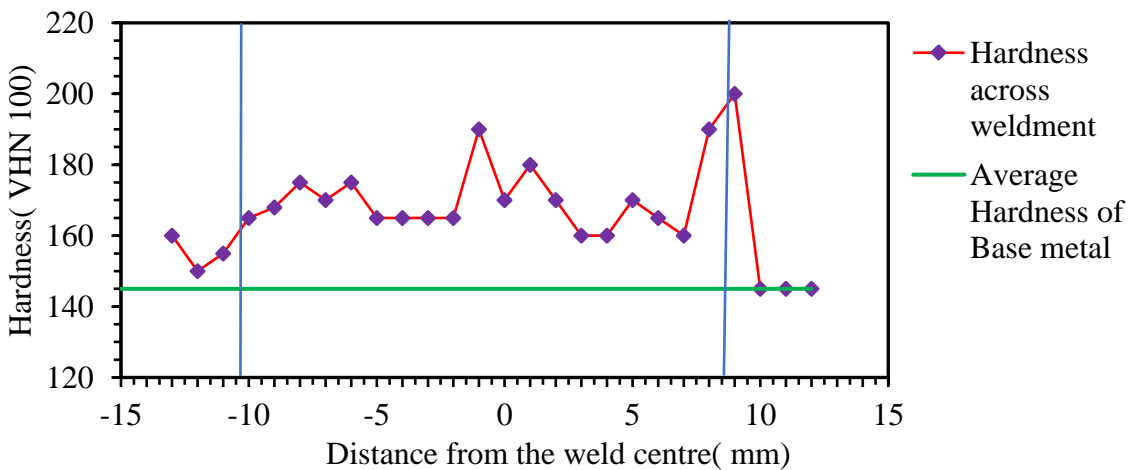
Figure 7.10: Microhardness results obtained from welding conducted at 110 mm/min welding speed, 550 rpm rotational speed, and 20 mm shoulder diameter.

a) Hardness variation accross the weldment

(On the transverse section)
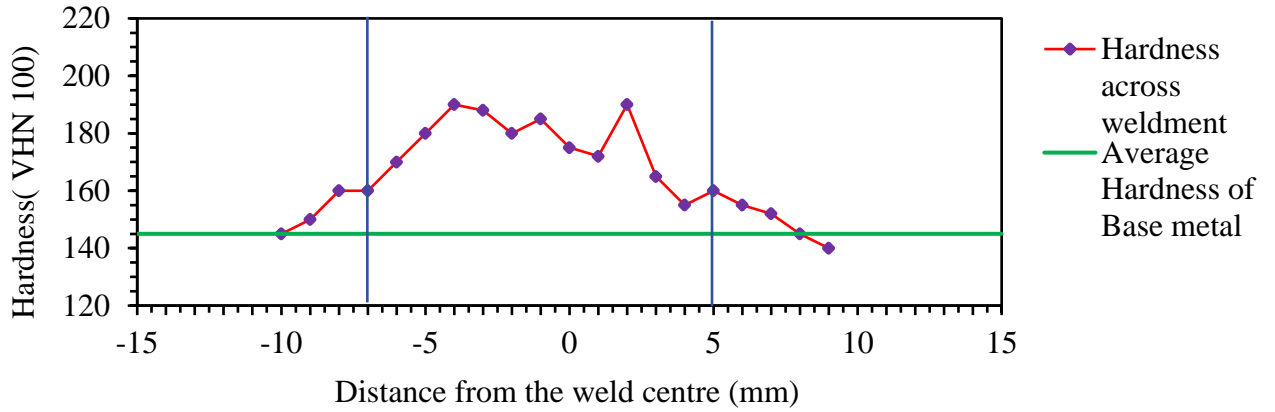
b) Hardness variation at the centre of weld

(from top to bottom-transverse section)
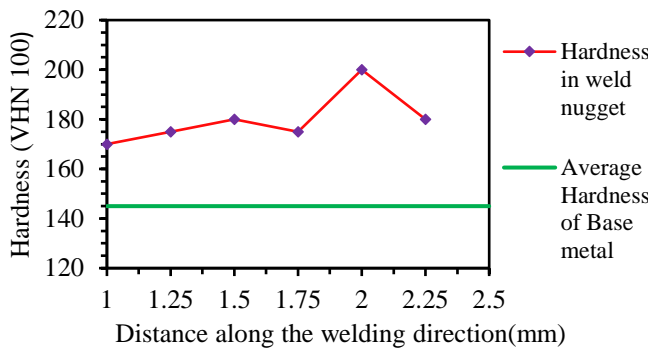
c) Hardness variation at the centre of weld
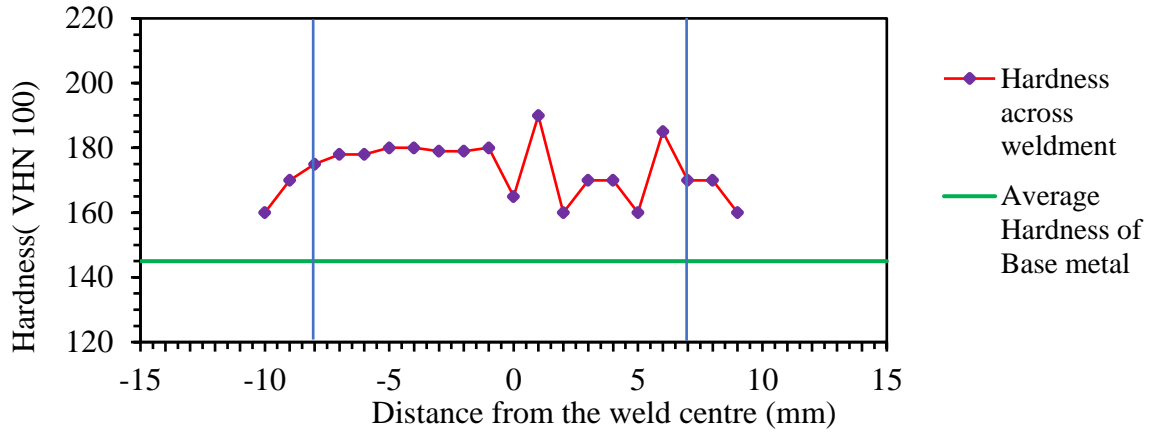
(parallel to welding direction on top face)
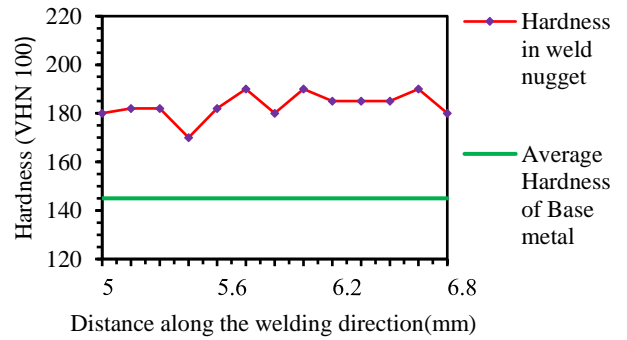
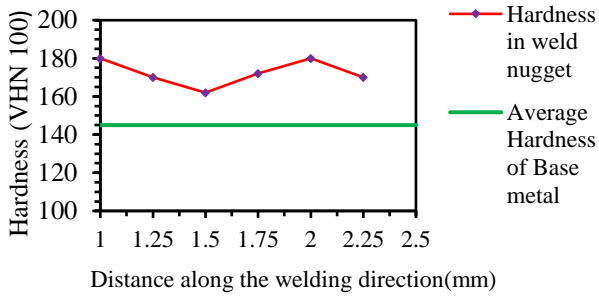**d) Hardness variation accross the weldment**

(On the top face of the weld)
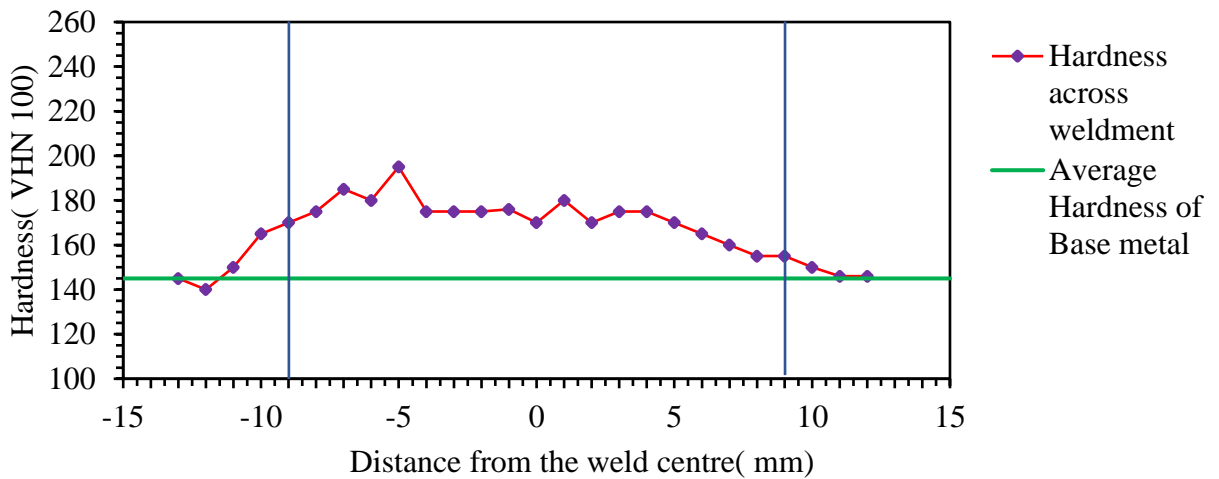
Figure 7.11: Microhardness results obtained from welding conducted at 110 mm/min welding speed, 750 rpm rotational speed, and 15 mm shoulder diameter.
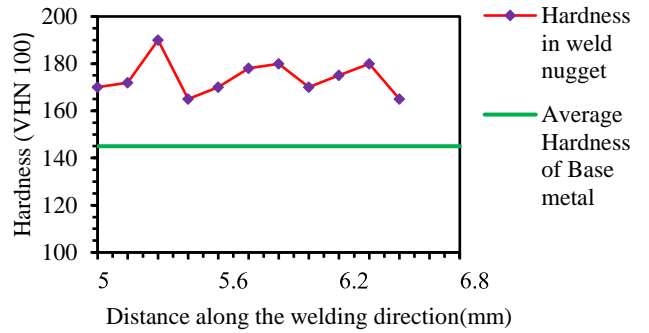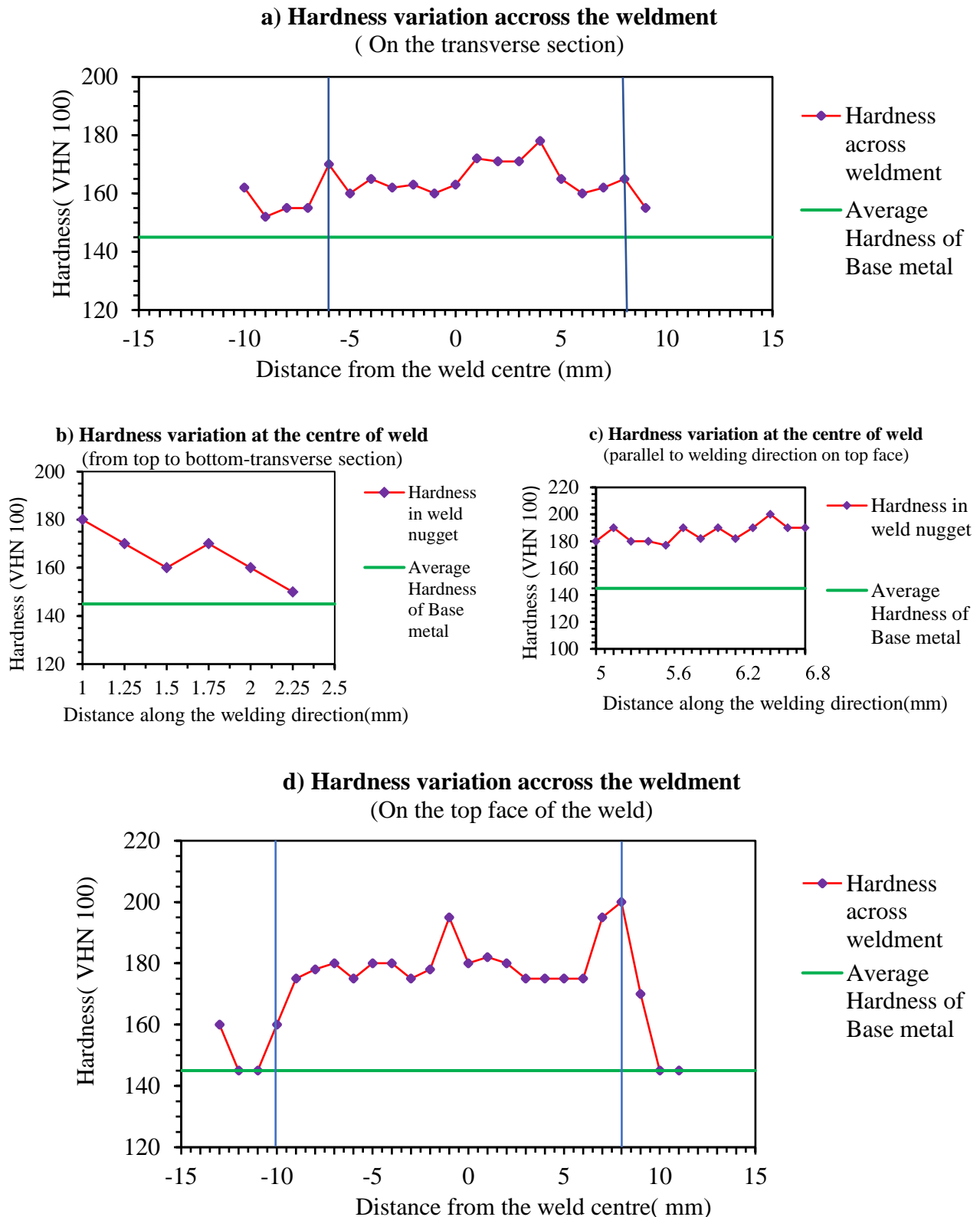
Figure 7.12: Microhardness results obtained from welding conducted at 210 mm/min welding speed, 430 rpm rotational speed, and 20 mm shoulder diameter.
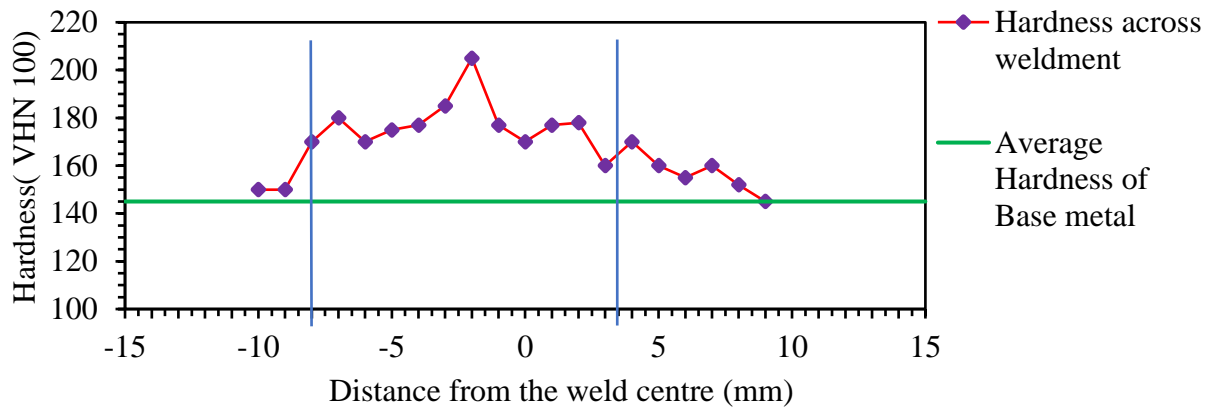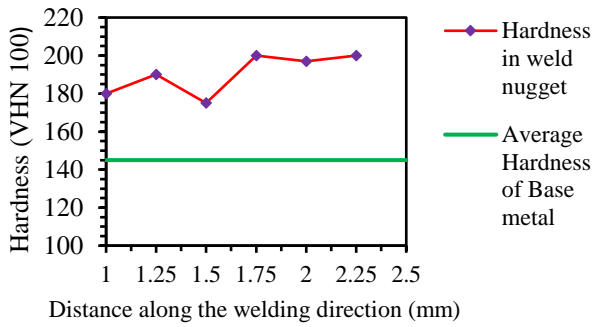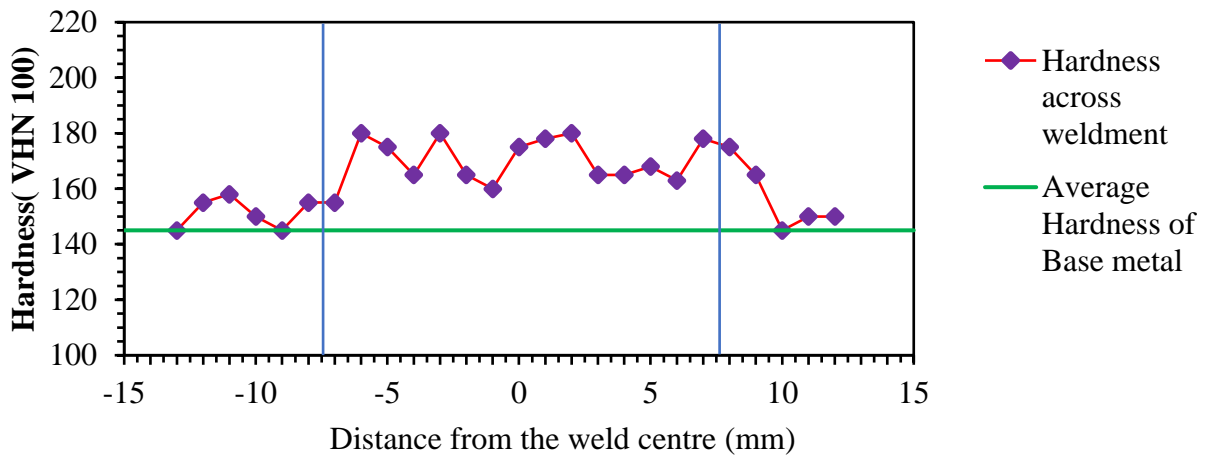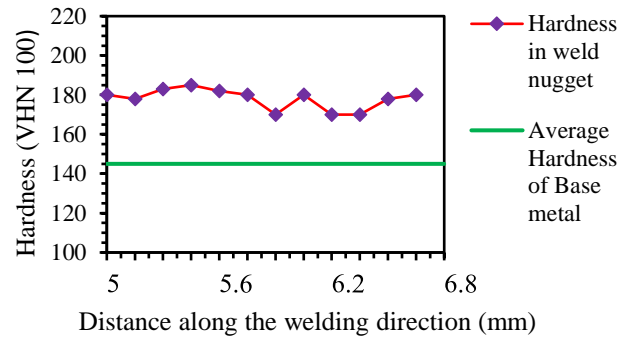
Figure 7.13: Microhardness results obtained from welding conducted at 210 mm/min welding speed, 550 rpm rotational speed, and 15 mm shoulder diameter.
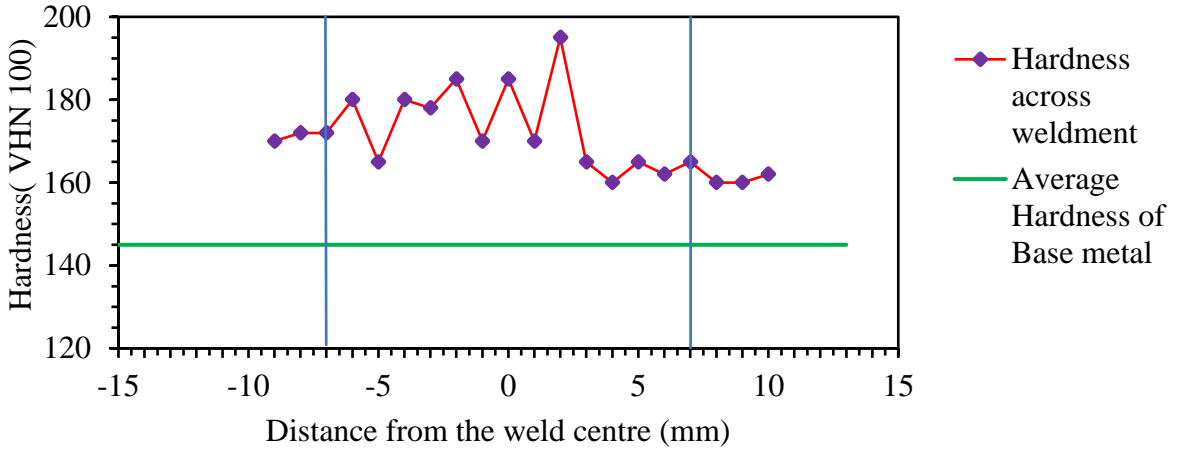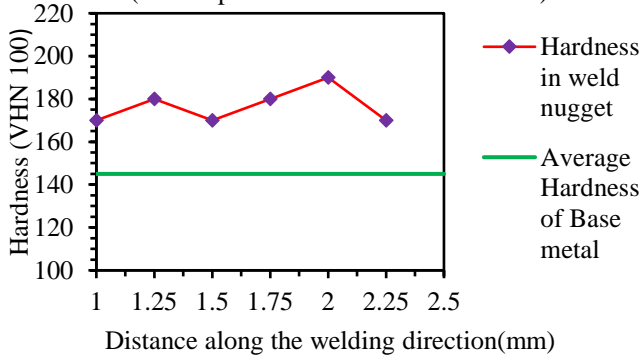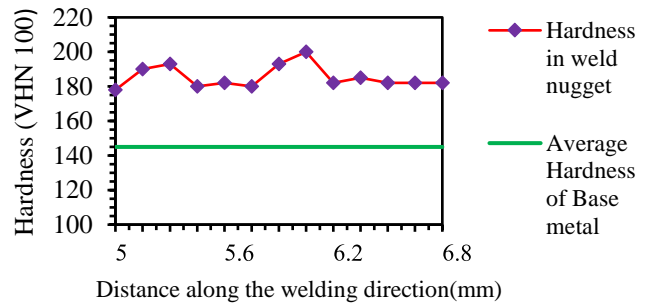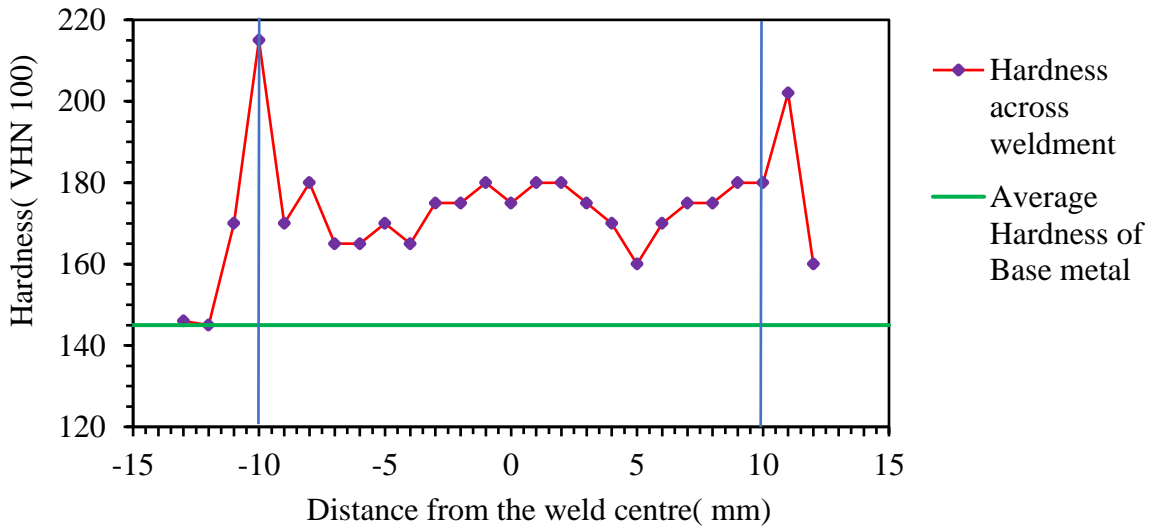
Figure 7.14: Microhardness results obtained from welding conducted at 210 mm/min welding speed, 750 rpm rotational speed, and 18 mm shoulder diameter.

7.4.3 Analysis of microhardness testing of the weldments

When compared to the base metal, the microhardness measurements taken from the weld nugget consistently show higher values. Regardless of how the particular process parameters affect it, the weld nugget's hardness is always above that of the base metal. The presence of fine-grain structures within the weld nugget is what causes the increase in hardness. The reduction in grain size results in an increased number of grain boundaries, contributing to improved resistance against indentation and, consequently, higher hardness. It is noteworthy that no additional alloying elements are introduced during the FSW process, eliminating any other potential sources for this increase in hardness.

The microhardness values within the weld nugget exhibit variability depending on the chosen process parameters. This can be attributed to the influence of the Zener-Hollomon parameter (Z) during the recrystallization process, which in turn affects the resulting grain size. As a result, different process parameter combinations yield distinct microhardness values, reflecting the variations in grain size.

As shown in Figure 7.15 (a and b), the microhardness variations were observed throughout the weld nugget, both on the upper surface and in the transverse section of the weld. While the variation is minimal on the upper face, it becomes more significant on the transverse section. This difference in variation is attributed to the different cooling rates experienced within the weld nugget as one moves from the top to the bottom. The varying cooling rates influence the transformation of austenite into ferrite and pearlite. As a result, the microstructure formed throughout the weld is not uniform, leading to variations in microhardness. There is a decline in microhardness variation, which can be attributed to the accelerated cooling rate experienced on the upper surface.
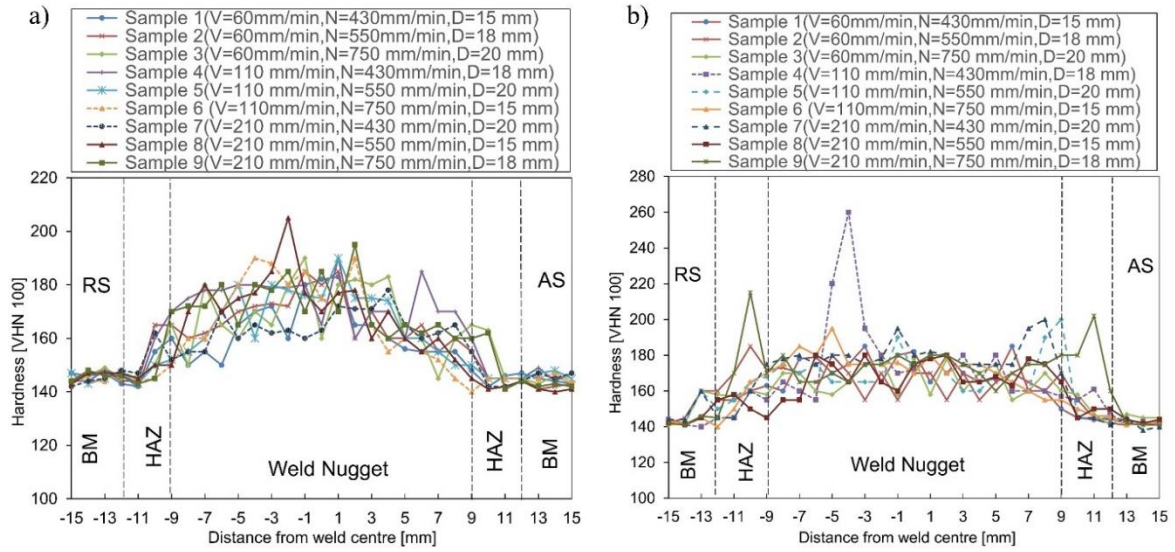
Figure 7.15: (a) Microhardness profiles on the transverse section of the welds and (b) microhardness profiles on the top surface of the weld.

CHAPTER 8   CONCLUSION AND SCOPE OF FUTURE WORK

8.1 CONCLUSIONS

In light of the experimental findings, the following noteworthy conclusions can be drawn:

- Friction stir welding (FSW) of carbon steel AISI 1018, employing a tungsten carbide insert with a 7% cobalt binder, yielded welds with superior mechanical and metallurgical properties compared to the base metal. Approximately 17% increase in cobalt alloy usage, in contrast to the commonly used 6% cobalt inserts in the previous studies, underscores the novelty and effectiveness of this approach in enhancing weld properties in carbon steel joints.

- Tool degradation, characterized by oxide formation near the shoulder and tool bulging in the same region, was predominantly observed. A novel approach to mitigate these issues involves reducing the amount of cobalt binder in the tool.

- The tool's truncated cone pin profile exhibited uniform stirring of the weld material. In contrast, tool pins with sharp cross-sections, such as square or triangular profiles, did not demonstrate any notable improvement. This observation emphasizes effectiveness in achieving a more uniform stirring action during the friction stir welding process.

- The joint efficiency of FSWed steel joints was observed to be more than 100% for all combinations of process parameters. The weldment's strongest region was the weld nugget, whereas the weakest was base metal. This observation highlights the novelty of achieving joint efficiencies exceeding 100%, challenging conventional expectations, and showcasing the unique strength distribution within FSWed steel joints.

- Both the tool rotational speed and welding speed exert a substantial influence on the UTS of the weld nugget. Only the welding speed influences the weld's % elongation, but the tool shoulder diameter and welding speed both significantly affect the weld's percentage reduction.

- The impact strength is directly influenced by the welding speed. Fractured impact test specimens indicated ductile failure as observed from the presence of dimpled regions.

- The application of grey relational analysis in combination with principal component analysis revealed the optimal machine setting as $V_3N_3D_1$ (V= 210 mm/min, N=750 rpm, and D=15 mm), resulting in an ultimate tensile strength of 570.27 MPa, elongation of 25.56%, reduction in area of 59.02%, and impact strength of 34.71 J.

171

- The fatigue life of the steel welds demonstrated a notable improvement of 20% compared to the base metal, as the welded joints exhibited a higher number of cycles to failure than the base metal.

- The microstructural analysis reveals the presence of three distinct regions in the weld: the SZ, HAZ, and TMAZ. The HAZ is relatively narrow and consists mainly of a partially transformed region, exhibiting mechanical properties the same as that of the base material. The upper surface of the weld briefly exhibits the TMAZ.

- For all experimental runs, the microhardness in the SZ is greater than that of the parent material; this is mostly due to grain refinement. The variation in microhardness within the weld nugget is more evident in the transverse region than on the top surface of the weld. This is due to the differential cooling rates experienced across the cross-section of the weld.

8.2 SCOPE OF FUTURE WORK

This section highlights the scope of future work for the benefit of the research community and industry.

- Plates of larger thicknesses can be welded on heavier machines. FSW in other joint configurations such as lap joint, corner joint, etc can be investigated.

- Welding with PCBN can be studied and compared with tungsten carbide for tool wear. An analysis of tool life and optimization of process parameters for extended tool life and high-quality welds can be explored in future research.

- Researchers have examined the use of shielding gas in FSW of ferrous alloys. Studies incorporating a comparison of the mechanical and metallurgical properties achieved in welds with and without shielding gas may be taken up.

- FSW with some auxiliary heating source can be developed for welding steel. The auxiliary heating sources can also be utilized for controlling the cooling rate after welding.

- Appropriate non-destructive techniques can be employed to assess the residual stresses resulting from welding. Additionally, mechanical testing such as three-point bending and corrosion studies can be conducted.

- Experiments can be conducted using a commercially available FSW machine, enabling a comparison between force-controlled machines and position-controlled machines.

- Another critical area of research in FSW of steels is the improvement of joint strength and toughness. Comparative studies on joints formed with varied welding parameters and post-weld heat-treated specimens reveal the profound impact of these factors. Incorporating PWHT can substantially enhance the joint's toughness by reducing hardness and enhancing the material's ductility in the HAZ.

References

1. Achuthamenon Sylajakumari, P., Ramakrishnasamy, R., & Palaniappan, G. (2018). Taguchi grey relational analysis for multi-response optimization of wear in co-continuous composite. *Materials, 11*(9), 1743.

2. Ahmed, M. M. Z., El-Sayed Seleman, M. M., Touileb, K., Albaijan, I., & Habba, M. I. A. (2022). Microstructure, crystallographic texture, and mechanical properties of friction stir welded mild steel for shipbuilding applications. *Materials, 15*, 2905.

3. Arbegast, W. J. (2008). A flow-partitioned deformation zone model for defect formation during friction stir welding. *Scripta Materialia*, *58*(5), 372–376.

4. Ardalanniya, A., Nourouzi, S., & Jamshidi Aval, H. (2021). Fabrication of a laminated aluminium matrix composite using friction stir processing as a cladding method. *Materials Science and Engineering B: Solid-State Materials for Advanced Technology*, *272*(October 2020), 115326.

5. Arya, P. K., Jain, N. K., Murugesan, J., & Patel, V. K. (2022). Developments in friction stir welding of aluminium to magnesium alloy. *Journal of Adhesion Science and Technology*, *36*(13), 1365-1402.

6. ASTM International. (2016). ASTM E23-16b: Standard test methods for notched bar impact testing of metallic materials. ASTM International, West Conshohocken, PA 19428-2959, United States. 1-26.

7. ASTM International. (2017). ASTM E8-17: Standard test methods for tension testing of metallic materials. ASTM International, West Conshohocken, PA 19428-2959, United States. 1-24.

8. ASTM International. (2018). ASTM E647-18: Standard test methods for measurement of fatigue crack growth rates. ASTM International, West Conshohocken, PA 19428-2959, United States. 1-26.

9. ASTM International. (2017). ASTM E92-17a: Standard test methods for Vickers hardness and Knoop hardness of metallic materials. ASTM International, West Conshohocken, PA 19428-2959, United States. 1-10.

10. Avettand-Fènoël, M. N., Nagaoka, T., Fujii, H., & Taillard, R. (2019). Effect of a Ni interlayer on microstructure and mechanical properties of WC-12Co cermet / SC45 steel friction stir welds. *Journal of Manufacturing Processes*, *40*(December 2018), 1–15.

11. American Welding Society. (1996). *AWS Handbook: Welding processes, Part 1* (8th ed., Vol. 3). Miami, FL: American Welding Society.

12. Aydin, M., & Bulut, R. (2010). The weldability of AZ31 magnesium alloy by friction stir welding. *Kovove Materialy-Metallic Materials, 48*, 97-104.

13. Azevedo, J., Quintino, L., Infante, V., Miranda, R. M., & Santos, J. D. (2016). Friction stir welding of shipbuilding steel with primer. *Soldagem & Inspeção, 21*(1), 16-29.

14. Azizi, A., Barenji, R. V., Barenji, A. Vatankhah, Barenji, M., & Hashemipour, M. (2016). Microstructure and mechanical properties of friction stir welded thick pure copper plates. *International Journal of Advanced Manufacturing Technology, 86*, 1985–1995.

15. Babu, N., Karunakaran, N., & Balasubramanian, V. (2017). A study to estimate the tensile strength of friction stir welded AA 5059 aluminum alloy joints. *International Journal of Advanced Manufacturing Technology, 93*, 1-9.

16. Barnes, S. J., Steuwer, A., Mahawish, S., Johnson, R., & Withers, P. J. (2008). Residual strains and microstructure development in single and sequential double-sided friction stir welds in RQT-701 steel. *Materials Science and Engineering A, 492*(1–2), 35–44.

17. Beygi, R., Carbas, R., Queiros, A., Marques, E. A. S., Shi, R., & da Silva, L. F. M. (2022). Comparative study between stainless steel and carbon steel during dissimilar friction stir welding with aluminum: Kinetics of Al-Fe intermetallic growth. *Metallurgical and Materials Transactions A, 28*, 1948-1959.

18. Bhatia, A., & Wattal, R. (2021). Process parameters optimization for maximizing tensile strength in friction stir-welded carbon steel. *Strojniski Vestnik/Journal of Mechanical Engineering, 67*(6), 311–321.

19. Bilgin, M. B., & Meran, C. (2011). The effect of tool rotational and transverse speed on friction stir weldability of AISI 430 ferrite stainless steels. *Materials & Design, 33*(0), 376-383.

20. Bilici, M. K. (2022). Investigation of the effects of welding variables on the welding defects of the friction stir welded high density polyethylene sheets. *Journal of Elastomers & Plastics, 54*(3), 457-476.

21. Bisadi, H., Rasaee, S., & Fotoohi, Y. (2015). Studying of tool rotation speed on mechanical properties of copper–Al5083 butt joint welded by friction stir welding. *Proceedings of the Institution of Mechanical Engineers, Part B: Journal of Engineering Manufacture, 229*, 1734–1741.

22. Boitsov, A. G., Pleshakov, A. S., Siluyanova, M. V., & Baranov, A. A. (2020). Friction stir welding of M1 copper alloy in the production of power equipment. *Russian Engineering Research, 40*, 249-252.

23. Box, G. E. P., Hunter, W. G., & Hunter, J. S. (2005). *Statistics for experimenters: design, innovation, and discovery*. John Wiley & Sons.

24. Callister, W. D., & Rethwisch, D. G. (2018). *Materials Science and Engineering: An Introduction* (10th ed.). Wiley.

25. Çam, G., Serindag, H., Çakan, A., Mistikoglu, S., & Yavuz, H. (2008). The effect of weld parameters on friction stir welding of brass plates. *Materialwissenschaft und Werkstofftechnik, 39*, 394-399.

26. Cao, X., & Jahazi, M. (2011). Effect of tool rotational speed and probe length on lap joint quality of a friction stir welded magnesium alloy. *Materials & Design, 32*(1), 1-11.

27. Cartigueyen, S., & Mahadevan, K. (2015). Role of Friction Stir Processing on Copper and Copper based Particle Reinforced Composites – A Review. *Journal of Materials Science & Surface Engineering, 2*(2), 133–145.

28. Cederqvist, L., & Öberg, T. (2008). Reliability study of friction stir welded copper canisters containing Sweden's nuclear waste. *Reliability Engineering and System Safety, 93*(10), 1491–1499.

29. Charit, I., Mishra, R.S., & Mahoney, W.M. (2002). Multi-sheet structures in 7475 aluminum by friction stir welding in concert with post-weld superplastic forming. *Scripta Materialia, 47*(9), 631-636.

30. Chen H.B., Yan K., Lin T., Chen S.B., Jiang C.Y., Zhao Y. (2006). The investigation of typical welding defects for 5456 aluminum alloy friction stir welds. *Materials Science and Engineering: A. 433* (1–2).64-69.

31. Chen, C. L., Tatlock, G. J., & Jones, A. R. (2010). Microstructural evolution in friction stir welding of nanostructured ODS alloys. *Journal of Alloys and Compounds, 504*, S460-S466.

32. Chen, H.B., Keng, Y., Tao, L., Chen, S.B., & Z., Y. (2006). The investigation of typical welding defects for 5456 aluminum alloy friction stir welds. *Materials Science and Engineering, 433*, 64-69.

33. Chen, J., Li, X., Lin, Y., Yan, W., & Zhou, X. (2016). Evolution of microstructure during hot deformation of a vanadium microalloyed high strength steel. *Materials Science and Engineering: A, 675*, 45-55.

34. Chen, L., Chen, X., Li, B., Zhang, J., Li, Z., & Liu, Y. (2020). Effect of welding speed on the microstructure and mechanical properties of friction stir welded Al-Cu-Li alloy. *Materials Science and Engineering: A, 792*, 139770.

35. Chen, T. (2009). Process parameters study on FSW joint of dissimilar metals for aluminum-steel. *Journal of Materials Science, 44*, 2573-2580.

36. Chen, Y. C., Komazaki, T., Tsumura, T., & Nakata, K. (2008). Role of zinc coat in friction stir lap welding Al and zinc coated steel. *Materials Science and Technology, 24*(1), 33-39.

37. Chen, Y., Ma, Z. Y., & Guo, W. (2016). Effect of Tool Rotational Speed on Friction Stir Welding of 6082 Aluminum Alloy. *Journal of Materials Engineering and Performance, 25*(11), 4559-4568.

38. Cho, H. H., Han, H. N., Hong, S. T., Park, J. H., Kwon, Y. J., Kim, S. H., & Steel, R. J. (2011). Microstructural analysis of friction stir welded ferritic stainless steel. *Materials Science and Engineering A, 528*(6), 2889–2894.

39. Cho, H., Kang, S.H., Kim, S.-H., Oh, K.H., Kim, H.J., Chang, W.S., & Han, H.N. (2012). Microstructural evolution in friction stir welding of high-strength linepipe steel. *Materials & Design, 34*(0), 258-267.

40. Choudhary, S., Pal, T. K., & Das, G. (2013). Effect of tool rotational speed on microstructure and mechanical properties of friction stir welded high strength low alloy steel. *Journal of Materials Engineering and Performance, 22(*10), 2929-2938.

41. Chowdhury, S.M., Chen, D., Bhole, S.D., & Cao, X. (2010). Tensile properties of a friction stir welded magnesium alloy: Effect of pin tool thread orientation and weld pitch. *Materials Science and Engineering: A*, *527*, 6064-6075.

42. Chowdhury, S.M., Chen, D.L., Bhole, S.D., Cao, X., Powidajko, E., Weckman, D.C., & Zhou, Y. (2010). Tensile properties and strain-hardening behavior of double-sided arc welded and friction stir welded AZ31B magnesium alloy. *Materials Science and Engineering: A, 527*(12), 2951-2961.

43. Chung, Y.D., Fujii, H., Ueji, R., & Nogi, K. (2009). Friction stir welding of hypereutectoid steel (SK5) below the eutectoid temperature. *Science and Technology of Welding and Joining, 14*(3), 233-238.

44. Chung, Y.D., Fujii, H., Ueji, R., & Tsuji, N. (2010). Friction stir welding of high carbon steel with excellent toughness and ductility. *Scripta Materialia, 63*(2), 223-226.

45. Colligan, K. (1999). Material flow behavior during friction stir welding of aluminum. *Supplement to the Welding Journal*, 229-237.

46. Costa, J.D., Ferreira, J.A.M., Borrego, L.P., & Abreu, L.P. (2012). Fatigue behavior of AA6082 friction stir welds under variable loadings. *International Journal of Fatigue, 37*, 8-16.

47. Cui, L., Fujii, H., Tsuji, N., & Nogi, K. (2007). Friction stir welding of high carbon steel with excellent toughness and ductility. *Scripta Materialia, 56*(7), 637-640.

48. Datta, A., Shrivastava, A., Mandal, N., Roy, H., & Chakraborty, S. S. (2023). A comparative investigation of butt friction stir welding of aluminium alloys, AA 1100 and AA 7075, with AISI 304 stainless steel. *Welding in the World, 67*, 1449-1465.

49. Demirel, M. Y., & Karaağaç, İ. (2020). Experimental Investigation of Annealing Parameters Effects on Microstructure and Mechanical Properties of 7075-T6 Alloy. *Journal of Polytechnic-Politeknik Dergisi, 23*(2), 283-289.

50. Deng, Q., et al. (2018). Optimization of bacterial cellulose production by Komagataeibacter hansenii using a response surface methodology. *International Journal of Biological Macromolecules, 112*, 18-24.

51. Dieter, G. E., & Bacon, D. J. (2017). *Mechanical metallurgy*. McGraw-Hill Education.

52. Dinda, G. P., & Ramakrishnan, A. (2019). Friction stir welding of high-strength steel. *International Journal of Advanced Manufacturing Technology, 103*, 4763-4769.

53. Dorbane, A., Harrou, F., & Sun, Y. (2023). Exploring Deep Learning Methods to Forecast Mechanical Behavior of FSW Aluminum Sheets. *Journal of Materials Engineering and Performance, 32*(10), 4047–4063.

54. Dos Santos, J. F., Olea, C. A. W., Coelho, R. S., Kostka, A., Paglia, C. S., Ghidini, T., & Donne Eads, C. D. (2010). *Metallurgy and weld performance in friction stir welding*. In D. Lohwasser & Z. Chen (Eds.), Friction Stir Welding (314-410). Woodhead Publishing.

55. Duan, R. H., Xie, G. M., Luo, Z. A., Xue, P., Wang, C., Misra, R. D. K., & Wang, G. D. (2020). Microstructure, crystallography, and toughness in nugget zone of friction stir welded high-strength pipeline steel. *Materials Science and Engineering A*, 791(March), 139620.

56. E. Tekkaya, A. Brosius, and H. Homberg (2005). Investigation on the influence of pin profile on the quality of friction stir welded aluminum sheets. *CIRP Annals, 54* (1), 187-190.

57. Elangovan, K., & Balasubramanian, V. (2008). Influences of tool pin profile and welding speed on the formation of friction stir processing zone in AA2219 aluminum alloy. *Journal of Materials Processing Technology, 200*(1–3), 163–175.

58. Elangovan, K., Balasubramanian, V., & Valliappan, M. (2008). Influences of tool pin profile and axial force on the formation of friction stir processing zone in AA6061 aluminum alloy. *International Journal of Advanced Manufacturing Technology, 38*, 285-295.

59. Emamian, S., Awang, M., Yusof, F., Hussain, P., Mehrpouya, M., Kakooei, S., Moayedfar, M., & Zafar, A. (2017). *A Review of Friction Stir Welding Pin Profile*. In A. K. M. Nurul Amin, A. Z. H. Rizvi, M. W. Kamaruzaman, & M. S. M. Sani (Eds.), Joining and Assembly of Medical Materials and Devices (1-18). Springer.

60. Esmailzadeh, M., Shamanian, M., Kermanpur, A., & Saeid, T. (2013). Microstructure and mechanical properties of friction stir welded lean duplex stainless steel. *Materials Science and Engineering A*, 561, 486–491.

61. Esparza, J. A., Davis, W. C., Trillo, E. A., & Murr, L. E. (2002). Friction-stir welding of magnesium alloy AZ31B. *Journal of Materials Science Letters, 21*, 917-920.

62. Esparza, J.A., Davis, W.C., & Murr, L.E. (2003). Microstructure-property studies in friction-stir welded, Thixomolded magnesium alloy AM60. *Journal of Materials Science, 38*(5), 941–952.

63. Fahimpour, V., Sadrnezhaad, S.K., & Karimzadeh, F. (2012). Corrosion behavior of aluminum 6061 alloy joined by friction stir welding and gas tungsten arc welding methods. *Materials & Design, 39*, 329-333.

64. Fazel-Najafabadi, M., Kashani-Bozorg, S. F., & Zarei-Hanzaki, A. (2010). Joining of CP-Ti to 304 stainless steel using friction stir welding technique. *Materials & Design, 31*(10), 4800-4807.

65. Feng, A. H., & Ma, Z. Y. (2007). Enhanced mechanical properties of Mg-Al-Zn cast alloy via friction stir processing. *Scripta Materialia, 56*(5), 397–400.

66. Fotouhi, Y., Rasaee, S., Askari, A., & Bisadi, H. (2014). Effect of transverse speed of the tool on microstructure and mechanical properties in dissimilar butt friction stir welding of al5083–copper sheets. *Engineering Solid Mechanics, 2*, 239–246.

67. Fricke, W. (2003). Fatigue analysis of welded joints: State of development. *Marine Structures, 16*(3), 185–200.

68. Fuji, H., Ueji, R., Takada, Y., Kitahara, H., Tsuji, N., Nataka, K., & Nogi, K. (2006). Friction stir welding of ultrafine-grained interstitial-free steels. *Materials Transactions, 47*(1), 239-242.

69. Fujii, H., Cui, L., Tsuji, N., Maeda, M., Nakata, K., & Nogi, K. (2006). Friction stir welding of carbon steels. *Materials Science and Engineering A*, 429(1–2), 50–57.

70. Gaddam, S., Haridas, R. S., Tammana, D., Sanabria, C., Lammi, C. J., Berman, D., & Mishra, R. S. (2023). Double-sided friction stir welding of Nitronic-40 stainless steel for application in tokamak devices. *Journal of Materials Science & Technology, 159*, 170-183.

71. Gan, W., Li, Z. T., & Khurana, S. (2007). Tool materials selection for friction stir welding of L80 steel. *Science and Technology of Welding and Joining, 12*(7), 610–613.

72. Gao, Y., Nakata, K., Nagatsuka, K., Liu, F. C., & Liao, J. (2015). Interface microstructural control by probe length adjustment in friction stir welding of titanium and steel lap joint. *Materials & Design, 65*, 17-23.

73. Geiger, M., Micari, F., Merklein, M., Fratini, L., Contorno, D., Giera, A., & Staud, D. (2008). Friction Stir Knead Welding of steel aluminium butt joints. *International Journal of Machine Tools and Manufacture, 48(*5), 515–521.

74. Ghasemi, A., Saboori, A., & Kokabi, A. H. (2015). Friction stir welding of biomedical titanium alloys: a review. *Journal of Materials Engineering and Performance, 24*(5), 1858-1871.

75. Ghiasvand, A., Yavari, M. M., Tomków, J., Guerrero, J. W. G., Kheradmandan, H., Dorofeev, A., Memon, S., & Derazkola, H. A. (2021). Investigation of Mechanical and Microstructural Properties of Welded Specimens of AA6061-T6 Alloy with Friction Stir Welding and Parallel-Friction Stir Welding Methods. *Materials, 14*(20), 6003.

76. Ghosh, M., Hussain, M., & Gupta, R.K. (2012). Effect of welding parameters on microstructure and mechanical properties of friction stir welded plain carbon steel. *ISIJ International, 52*(3), 477-482.

77. Ghosh, M., Kar, A., Kumar, K., & Kailas, S. V. (2012). Structural characterisation of reaction zone for friction stir welded aluminium-stainless steel joint. *Materials Technology, 27*(2), 169-172.

78. Ghosh, M., Kumar, K., & Mishra, R. S. (2010). Analysis of microstructural evolution during friction stir welding of ultrahigh-strength steel. *Scripta Materialia, 63*(8), 851–854.

79. Ghosh, M., Kumar, R., & Husain, M. (2014). Friction Stir Welding of Stainless Steel to Al Alloy: Effect of Thermal Condition on Weld Nugget Microstructure. *Metallurgical and Materials Transactions A*, 45, 854-863.

80. Gong, Y., Li, Y., Li, Y., & Hu, S. (2018). Wear properties and microstructure evolution of tungsten carbide coatings by a supersonic plasma spraying process. *Materials, 11*(9), 1680.

81. Guo, J.F., Chen, H.C., Sun, C.N., Bi, G., Sun, Z., & Wei, J. (2013). Friction stir welding of dissimilar materials between AA6061 and AA7075 Al alloys: Effects of process parameters. *Materials and Design, 56*, 185-192.

82. H. Azimi, M. F. Najafabadi, and S. H. Seyedein (2010). Effect of pin profile on mechanical properties and microstructure of friction stir welded Al 7075-T6 alloy. *Materials & Design, 31*(1). 81-87,

83. Habibnia, M., Shakeri, M., Nourouzi, S., & Besharati Givi, M. K. (2015). Microstructural and mechanical properties of friction stir welded 5050 Al alloy and 304 stainless steel plates. *International Journal of Advanced Manufacturing Technology, 76*, 819-829.

84. Hammood, A. S., Esmailzadeh, M., Hosseini, S. N., Karimi, S., Calliari, I., Pezzato, L., & Brittain, R. (2023). Effect of friction stir welding parameters on microstructure and corrosion behavior of 2101 duplex stainless steel in simulated body fluid. *International Journal of Precision Engineering and Manufacturing-Green Technology, 10,* 327-337.

85. Han, J., Li, H., Zhu, Z., Barbaro, F., Jiang, L., Xu, H., & Ma, L. (2014). Microstructure and mechanical properties of friction stir welded 18Cr–2Mo ferritic stainless steel thick plate. *Materials & Design, 63*, 238-246.

86. Hoyos, E., Escobar Muñoz, S., De Backer, J., Martin, J., & Palacio, M. (2021). *Case Study: Implementation of FSW in the Colombian Rail Transport Sector*. In A. Milenov (Ed.), Sustainable Development in Rail Transport and Machinery: From Ergonomics to Optimized Production Systems (1-12). Springer.

87. Hu, S. J., et al. (2011) Friction stir spot welding with tool oscillation (FSSW-T) of aluminum alloy 6061-T6 sheets. *Journal of Materials Processing Technology* 211.1 77-83.

88. Huang, X., Huang, M., Zhou, D., Yu, Y., Wei, X., & Yang, M. (2018). Continuous dynamic recrystallization behavior and microstructural evolution of AZ31 magnesium alloy during hot deformation. *Journal of Alloys and Compounds, 749*, 587-597.

89. Husain, M. M., Sarkar, R., Pal, T. K., Ghosh, M., & Prabhu, N. (2017). Quantification of microtexture at weld nugget of friction stir-welded carbon steel. *Journal of Materials Engineering and Performance, 26*(7), 2047-2056.

90. Hwang, Y.M., Kang, Z.W., Chiou, Y.C., & Hsu, H.H. (2008). Experimental study on temperature distributions within the workpiece during friction stir welding of aluminum alloys. *International Journal of Machine Tool and Manufacture, 48*, 778-787.

91. Imam, M., Ueji, R., & Fujii, H. (2016). Effect of online rapid cooling on microstructure and mechanical properties of friction stir welded medium carbon steel. *Journal of Materials Processing Technology, 230*, 62–71.

92. International Steel Statistics Bureau. (2022). *Steel Statistical Yearbook 2022*. https://worldsteel.org/media-centre/press-releases/2022/2022-steel-statistical-yearbook-published/

93. Jata, K.V., Sankaran, K.K., & Ruschau, J.J. (2000). Friction-stir welding effects on microstructure and fatigue of aluminum alloy 7050-T7451. *Metallurgical and Materials Transactions A*, 31(9), 2181-2192.

94. Ji, Y. S., Fujii, H., Sun, Y., Maeda, M., Nakata, K., Kimura, H., Inoue, A., & Nogi, K. (2009). Friction stir welding of Zr55Cu50Ni 5Al10 bulk metallic glass. *Materials Transactions, 50*(6), 1300–1303

95. Johnson, P., & Murugan, N. (2020). Microstructure and mechanical properties of friction stir welded AISI321 stainless steel. *Journal of Materials Research and Technology, 9*(3), 3967-3976.

96. Johnson, R., & Threadgill, P. (2016). *Friction Stir Welding of Magnesium Alloys*. In S.N. Mathaudhu, A.A. Luo, N.R. Neelameggham, E.A. Nyberg, & W.H. Sillekens (Eds.), Essential Readings in Magnesium Technology (pp. 117-125). Springer.

97. Karami, S., Jafarian, H., Eivani, A. R., & Kheirandish, S. (2016). Engineering tensile properties by controlling welding parameters and microstructure in a mild steel processed by friction stir welding. *Materials Science and Engineering A*, 670, 68–74.

98. Karami, V., Dariani, B. M., & Hashemi, R. (2021). Investigation of forming limit curves and mechanical properties of 316 stainless steel/St37 steel tailor-welded blanks produced by tungsten inert gas and friction stir welding method. *CIRP Journal of Manufacturing Science and Technology, 32*, 437–446.

99. Kayode, O., & Akinlabi, E. T. (2019). An overview on joining of aluminium and magnesium alloys using friction stir welding (FSW) for automotive lightweight applications. *Mater. Res. Express, 6*, 112005.

100. Ke, L., Huang, C., Xing, L., & Huang, K. (2010). Al-Ni intermetallic composites produced in situ by Friction Stir Processing. *Journal of Alloys and Compounds, 503*(2), 494–499.

101. Khalaf, H. I., Al-Sabur, R., & Derazkola, H. A. (2023). Effect of number of tool shoulders on the quality of steel to magnesium alloy dissimilar friction stir welds. *Archives of Civil and Mechanical Engineering, 23*, 125.

102. Khodaverdizadeh, H., Mahmoudi, A., Heidarzadeh, A., & Nazari, E. (2012). Effect of friction stir welding (FSW) parameters on strain hardening behaviour of pure copper joints. *Materials and Design, 35*, 330-334.

103. Kim, Y. G., Fujii, H., Tsumura, T., Komazaki, T., & Nakata, K. (2006). Three defect types in friction stir welding of aluminum die casting alloy. *Materials Science and Engineering A,* 415(1–2), 250–254.

104. Kimapong, K., & Watanabe, T. (2004). Friction stir welding of aluminum alloy to steel. *Welding Journal, 83*, 277S-282S.

105. Klingensmith, S., Dupont, J. N., & Marder, A. R. (2005). Microstructural Characterization of a Double-Sided Friction Stir Weld on a Superaustenitic Stainless Steel. *Welding Journal*, 77–86.

106. Kocks, U. F., Tomé, C. N., & Wenk, H. R. (2000). *Texture and Anisotropy: Preferred Orientations in Polycrystals and their Effect on Materials Properties*. Cambridge University Press.

107. Konkal, P.J., & Mruczek, M.F. (2007). Comparison of friction stir weldments and submerged arc weldments in HSLA-65 steel. *Welding Journal, 86*(7), 187s-195s.

108. Korkmaz, E., & Meran, C. (2023). The examination of microstructural and mechanical properties of friction stir welded XPF800 steel. *Proceedings of the Institution of Mechanical Engineers, Part C: Journal of Mechanical Engineering Science*, 0(0).

109. Krasnowski, K., Hamilton, C., & Dymek, S. (2015). Influence of the tool shape and weld configuration on microstructure and mechanical properties of the Al 6082 alloy FSW joints. *Archives of Civil and Mechanical Engineering, 15*, 133-141.

110. Küçükömeroğlu, T., Aktarer, S. M., İpekoğlu, G., & Çam, G. (2018). Microstructure and mechanical properties of friction-stir welded St52 steel joints. *International Journal of Minerals, Metallurgy and Materials, 25*(12), 1457–1464.

111. Küçükömeroğlu, T., Şentürk, E., Kara, L., Çam, G., & Özdemir, N. (2016). Microstructural and Mechanical Properties of Friction Stir Welded Nickel-Aluminum Bronze (NAB) Alloy. *Journal of Materials Engineering and Performance, 25*(1), 320–326.

112. Kumar, A., & Suvarna Raju, L. (2012). Influence of tool pin profiles on friction stir welding of copper. *Materials and Manufacturing Processes, 27*(12), 1414-1418.

113. Kumar, K., & Kailas, S. V. (2008). The role of friction stir welding tool on material flow and weld formation. *Materials Science and Engineering A, 485*(1–2), 367–374.

114. Lakshminarayanan, A. K., Annamalai, V. E., & Elangovan, K. (2015). Identification of optimum friction stir spot welding process parameters controlling the properties of low carbon automotive steel joints. *Journal of Materials Research and Technology, 4*(3), 262–272.

115. Lakshminarayanan, A. K., Balasubramanian, V., & Salahuddin, M. (2010). Microstructure, tensile and impact toughness properties of friction stir welded mild steel. *Journal of Iron and Steel Research International, 17*(10), 68–74.

116. Lautrou, N., & Thevenet, D. (2005). A Fatigue Crack Initiation Approach for Naval Welded Joints Nicolas. Oceans - Europe 2005.

117. Lee, W. B., Schmuecker, M., Alfaro Mercardo, U., Biallas, G., & Jung, S. B. (2006). Interfacial reaction in steel-aluminum joints made by friction stir welding. *Scripta Materialia, 55*(4), 355-358.

118. Lee, W., & Jung, S. B. (2004). The joint properties of copper by friction stir welding. *Materials Letters, 58,* 1041-1046.

119. Lee, W., Kim, J.-W., Yeon, Y.-M., & Jung, S.-B. (2003). The Joint Characteristics of Friction Stir Welded AZ91D Magnesium Alloy. *Materials Transactions, 44*, 917-923.

120. Lee, W., Lee, C.-Y., Chang, W.-S., Yeon, Y.-M., & Jung, S.-B. (2005). Microstructural Investigation of Friction Stir Welded Pure Titanium. *Materials Letters, 59*, 3315-3318.

121. Legendre, F., Poissonnet, S., Bonnaillie, P., Boulanger, L., & Forest, L. (2009). Some microstructural characterizations in a friction stir welded oxide dispersion strengthened ferritic steel alloy. *Journal of Nuclear Materials, 386–388*(C), 537–539.

122. Li, H., Chen, Y., Zhou, X., Kang, J., Huang, Y., & Deng, H. (2019). High-strength titanium alloy/steel butt joint produced via friction stir welding. *Materials Letters, 234*, 155-158.

123. Li, H., Yang, S., Shucai, Z., Zhang, B., Jiang, Z., Feng, H., Han, P., & Li, J. (2017). Microstructure evolution and mechanical properties of friction stir welding super-austenitic stainless steel S32654. *Materials & Design, 118*, 1-50.

124. Li, H., Yang, S., Zhang, S., Zhang, B., Jiang, Z., Feng, H., Han, P., & Li, J. (2017). Microstructure evolution and mechanical properties of friction stir welding super-austenitic stainless steel S32654. *Materials & Design, 118*, 207-217.

125. Li, S., Yang, X., Vajragupta, N., Tang, W., Hartmaier, A., & Li, H. (2021). The influence of post-weld tempering temperatures on microstructure and strength in the stir zone of friction stir welded reduced activation ferritic/martensitic steel. *Materials Science and Engineering A, 814*(March), 141224.

126. Li, W., Wang, J., Zhang, Z., Zhang, H., & Lu, Y. (2019). Influence of Shoulder Diameter on Microstructure and Mechanical Properties of Friction Stir Welded Lap Joints. *Journal of Materials Science & Technology, 35*(5), 788-796.

127. Li, Y., Lu, C., & Deng, Z. (2018). Effect of tool tilt angle on microstructure and mechanical properties of friction stir welded low carbon steel. *Materials Science and Engineering: A, 723*, 99-107.

128. Lienert, T. J., Longhurst, W. L., Szymanski, M. G., & Bingel, W. H. (2012). Friction stir spot welding of aluminum alloys: A review. *Welding Journal, 91*(12), 355s-362s.

129. Lienert, T. J., Stellwag, W. L., Grimmett, B. B., & Warke, R. W. (2003b). Friction stir welding studies on mild steel-process results, microstructures, and mechanical properties are reported. *The Welding Journal*, Supplement(January), 1–9.

130. Lim, S., Kim, S., & Kim, S. (2004). Tensile behavior of friction-stir welded A356-T6/Al 6061-T651 bi-alloy plate. *Metallurgical and Materials Transactions A*, 35, 2829-2835.

131. Lin, W. J., Chang, H. C., & Wu, M. H. (2014). Comparison of mechanical properties of pure copper welded using friction stir welding and tungsten inert gas welding. *Journal of Manufacturing Processes, 16*, 296-304.

132. Linert, T.J., Stellwag, W.L., Grimmett, B.B., & Warke, R.W. (2003). Friction stir welding studies on mild steel- Process results, microstructures, and mechanical properties are reported. *Welding Journal, 82*(1), 1s-9s.

133. Liu, F., Zhang, C., Zhang, Z., & Wang, L. (2017). Microstructural evolution and deformation behavior of ferrite steel during hot deformation. *Materials Science and Engineering: A, 689*, 186-198.

134. Liu, G., Murr, L.E., Niou, C.S., McClure, J.C., & Vega, F.R. (1997). Microstructural aspects of the friction-stir welding of 6061-T6 aluminum. *Scripta Materialia, 37*(3), 355-361.

135. Liu, H. J., Shen, J. J., Huang, Y. X., Kuang, L. Y., Liu, C., & Li, C. (2009). Effect of tool rotation rate on microstructure and mechanical properties of friction stir welded copper. *Science and Technology of Welding and Joining, 14*(6), 577-583.

136. Liu, H., & Zhang, Y. (2014). Statistical analysis of factors influencing fatigue life of friction stir welded joints in aluminum alloys. *Materials Science and Engineering: A, 618*, 437-445.

137. Liu, P., Shi, Q., Wang, W., Wang, X., & Zhang, Z. (2008). Microstructure and XRD analysis of FSW joints for copper T2/aluminium 5A06 dissimilar materials. *Materials Letters, 62*, 4106–4108.

138. Lu, H., Peilin, L., Zhongfeng, X., & Meng, X. (2011). The influence of thread form on refilling friction stir welding of 2219 aluminum alloy sheets. *Transactions of JWRI*, 41-42.

139. Luo, J., Wang, X. J., & Wang, J. X. (2009). New technological methods and designs of stir head in resistance friction stir welding. *Science and Technology of Welding and Joining, 14*(7), 650–654.

140. Majeed, T., Mehta, Y., & Siddiquee, A. N. (2021). Analysis of tool wear and deformation in friction stir welding of unequal thickness dissimilar Al alloys. Proceedings of the Institution of Mechanical Engineers, *Part L: Journal of Materials: Design and Applications, 235*(3), 501-512.

141. Maria Posada, Jennifer P. Nguyen, David R. Forrest, J. J. D. (2003). Friction stir welding Advances and joining Technology. *AMP TIAC Quaterly(Special Issue), 7(*3), 18-.

142. Mathon, M. H., Klosek, V., de Carlan, Y., & Forest, L. (2009). Study of PM2000 microstructure evolution following FSW Process. *Journal of Nuclear Materials*, 368-370, 475-478.

143. McNelley, T. R., Swaminathan, S., & Su, J. Q. (2008). Recrystallization mechanisms during friction stir welding/processing of aluminum alloys. *Scripta Materialia*, *58*(5), 349–354.

144. Meng, Y., Ma, Y., Chen, S., Han, Y., Chen, S., Huang, J., & Yang, J. (2021). Friction stir butt welding of magnesium alloy to steel by truncated cone-shaped stirring pin with threads. *Journal of Materials Processing Technology, 291*, 117038.

145. Meran, C. (2006). The joint properties of brass plates by friction stir welding. *Materials & Design, 27*(9), 719-726.

146. Meran, C., & Kovan, V. (2008). Microstructures and mechanical properties of friction stir welded dissimilar copper/brass joints. *Materialwissenschaft und Werkstofftechnik, 39*, 521-530.

147. Meyers, M. A., Mishra, A., & Benson, D. J. (2006). *Mechanical metallurgy*. Cambridge University Press.

148. Miles, M. P., Nelson, T. W., Steel, R., Olsen, E., & Gallagher, M. (2009). Effect of friction stir welding conditions on properties and microstructures of high strength automotive steel. *Science and Technology of Welding and Joining, 14*(3), 228–232.

149. Miles, M. P., Pew, J., Nelson, T. W., & Li, M. (2006). Comparison of formability of friction stir welded and laser welded dual phase 590 steel sheets. *Science and Technology of Welding and Joining, 11*(4), 384–388.

150. Miles, M. P., Ridges, C. S., Hovanski, Y., Peterson, J., Santella, M. L., & Steel, R. (2011). Impact of tool wear on joint strength in friction stir spot welding of DP 980 steel. *Science and Technology of Welding and Joining, 16*(7), 642–647.

151. Miles, M.P., Nelson, T.W., Steel, R., Olsen, E., & Gaallagher, M. (2009). Effect of friction stir welding conditions on properties and microstructures of high-strength automotive steel. *Science and Technology of Welding and Joining, 14*(3), 228-232.

152. Mironov, S., Sato, Y. S., & Kokawa, H. (2008). Microstructural evolution during friction stir-processing of pure iron. *Acta Materialia, 56*(11), 2602–2614.

153. Mishra, R. S., & Ma, Z. Y. (2005). Friction stir welding and processing. *Materials Science and Engineering R: Reports, 50*(1–2), 1–78.

154. Mishra, R. S., and M. W. Mahoney. (2003) Friction stir blind riveting: a new process for joining dissimilar materials. *Materials Science and Engineering: A* 341.1-2 307-310.

155. Mishra, R. S., Ma, Z. Y., & Charit, I. (2003). Friction stir processing: A novel technique for fabrication of surface composite. *Materials Science and Engineering A*, 341(1–2), 307–310.

156. Miura, T., Ueji, R., Fujii, H., Komine, H., & Yanagimoto, J. (2016). Stabilization of austenite in low carbon Cr-Mo steel by high-speed deformation during friction stir welding. *Materials & Design, 90*, 915–921.

157. Miyano, Y., Fujii, H., Sun, Y. F., Katada, Y., Kuroda, S., & Kamiya, O. (2011). Mechanical properties of friction stir butt welds of high nitrogen-containing austenitic stainless steel. *Materials Science and Engineering A-Structural Materials Properties Microstructure and Processing, 528*(6), 2917-2921.

158. Moghadasi, K., Mohd Isa, M. S., Ariffin, M. A., Mohd Jamil, M. Z., Raja, S., Wu, B., Yamani, M., Muhamad, M. R. B., Yusof, F., Jamaludin, M. F., Ab Karim, M. S., Abdul Razak, B. A., & Yusoff, N. (2022). A review on biomedical implant materials and the effect of friction stir based techniques on their mechanical and tribological properties. *Journal of Materials Research and Technology, 17*, 1054-1121.

159. Montgomery, D. C. (2017). *Design and analysis of experiments*. John Wiley & Sons.

160. Muhammad, N. A., Wu, C., & Padhy, G. K. (2018). Review: Progress and Trends in Ultrasonic Vibration Assisted Friction Stir Welding. *Journal of Harbin Institute of Technology (New Series), 25*(3), 16–42.

161. Müller, C., Elaguine, M., Bellon, C., Ewert, U., Zscherpel, U., Scharmach, M., Redmer, B., Ryden, H., & Ronneteg, U. (2006). Reliability evaluation of NDT techniques for Cu-welds for risk assessment of nuclear waste encapsulation. *Materials Testing, 48*(3), 111-117.

162. Murr, L. E., Liu, G., & McClure, J. C. (1999). Dynamics of material flow and microstructural development during friction stir welding of 6061-T6 aluminum. *Materials Science and Engineering: A*, 271(1-2), 213-223.

163. Muthu, M. F. X., & Jayabalan, V. (2015). Tool travel speed effects on the microstructure of friction stir welded aluminum–copper joints. *Journal of Materials Processing Technology, 217*, 105–113.

164. Myers, R. H., & Montgomery, D. C. (2017). *Response surface methodology: process and product optimization using designed experiments*. John Wiley & Sons.

165. Nagamalleswara Rao, A., Srinivas Naik, L., & Srinivas, C. (2017). Evaluation and Impacts of Tool Profile and Rotational Speed on Mechanical Properties of Friction Stir Welded Copper 2200 Alloy. *Materials Today: Proceedings, 4*(2, Part A), 1225-1229.

166. Nandan, R., Roy, G. G., & DebRoy, T. (2007). Numerical simulation of three-dimensional heat transfer and plastic flow during friction stir welding. *Metallurgical and Materials Transactions A, 38*(5), 1147-1158.

167. Newishy, M., Jaskari, M., Järvenpää, A., Fujii, H., & Abdel-Aleem, H. A. (2023). Friction Stir Welding of Dissimilar Al 6061-T6 to AISI 316 Stainless Steel: Microstructure and Mechanical Properties. *Materials, 16*, 4085.

168. Ouyang, J., Yarrapareddy, E., & Kovacevic, R. (2006). Microstructural evolution in the friction stir welded 6061 aluminum alloy (T6-temper condition) to copper. *Journal of Materials Processing Technology, 172*(1), 110-122.

169. Palanivel, R., Mathews, P.K., Murugan, N., & Dinaharan, I. (2012). Effect of tool rotational speed and pin profile on microstructure and tensile strength of dissimilar friction stir welded AA5083-H111 and AA6351-T6 aluminum alloys. *Materials & Design, 40*, 213-230.

170. Palanivel, R., Murugan, N., & Kumar, M. (2012). Experimental investigation on friction stir welding of Al6061-T6 alloy using square and cylindrical tool pin profiles. *Materials and Manufacturing Processes, 27*(3), 321-327.

171. Panneerselvam, K., & Lenin, K. (2014). Joining of nylon 6 plate by friction stir welding process using threaded pin profile. *Materials & Design, 53*(14), 302-307.

172. Park, H. S., Kimura, T., Murakami, T., Nagano, Y., Nakata, K., & Ushio, M. (2004). Microstructures and mechanical properties of friction stir welds of 60% Cu–40% Zn copper alloy. *Materials Science and Engineering: A*, 371(1-2), 160-169.

173. Park, S. H. C., Sato, Y. S., Kokawa, H., Okamoto, K., Hirano, S., & Inagaki, M. (2003). Rapid formation of the sigma phase in 304 stainless steel during friction stir welding. *Scripta Materialia, 49*(12), 1175–1180.

174. Park, S. H. C., Sato, Y. S., Kokawa, H., Okamoto, K., Hirano, S., & Inagaki, M. (2004). Corrosion resistance of friction stir welded 304 stainless steel. *Scripta Materialia, 51*(2), 101-105.

175. Park, S.H.C., Sato, Y.S., & Kokawa, H. (2003). Microstructural evolution and its effect on Hall-Petch relationship in friction stir welding of thixomolded Mg alloy AZ91D. *Journal of Materials Science, 38*(20), 4379–4383.

176. Payganeh, G. H., Mostafa Arab, N. B., DadgarAsl, Y., Ghasemi, F. A., & Saeidi, M. (2011). Effects of friction stir welding process parameters on appearance and strength of polypropylene composite welds. *International Journal of Physics Sciences, 6*(19), 4595-4600.

177. Podržaj, P., Jerman, B., & Klobčar, D. (2015). Welding defects at friction stir welding. *Metalurgija, 54*(2), 387–389.

178. Pramann, Z., Thompson, B., Chrzanowski, J., & Mennel, D. (2014). Friction stir welding for a nuclear fusion reactor. *Materials Science Forum*, 783–786, 1808–1813.

179. Rafiee, A. M., Zakeri, M., & Heydari, S. (2018). The effect of welding speed on microstructure and mechanical properties of AZ31B magnesium alloy joints produced by friction stir welding. *Journal of Materials Research and Technology, 7*(1), 47-57.

180. Rajasekaran, R., Lakshminarayanan, A. K., Damodaram, R., & Balasubramanian, V. (2021). Stress corrosion cracking failure of friction stir welded nuclear grade austenitic stainless steel. *Engineering Failure Analysis, 120*, 105012.

181. Ramesh, R., Dinaharan, I., Kumar, R., & Akinlabi, E. T. (2017). Microstructure and mechanical characterization of friction stir welded high strength low alloy steels. *Materials Science and Engineering A*, 687, 39–46.

182. Ramesh, R., Dinaharan, I., Kumar, R., Prasad, R. V., Arivazhagan, N., & Roy, A. (2019). Microstructure and mechanical characterization of friction-stir-welded 316L austenitic stainless steels. *Journal of Materials Engineering and Performance, 28*(1), 498-511.

183. Rameshbabu, N., Balusamy, V., & Balasubramanian, V. (2011). Influence of taper angle of tool pin on the formation of friction stir processing zone in AA 6061-T6 aluminum alloy. *Journal of Materials Engineering and Performance, 20*(7), 1171-1177.

184. Ravi Kumar, B., Rao, M. S., & Madhusudhan Reddy, G. (2007). Effect of tool pin profile on temperature distribution in friction stir welding of AA6061-T6. *Materials & Design, 28*(1), 168-175.

185. Reynolds, A. P., & Shercliff, H. R. (2004). Model for the heat generation in friction stir welding. *Science and technology of welding and joining, 9*(5), 416-424.

186. Reynolds, A. P., Tang, W., Gnaupel-Herold, T., & Prask, H. (2003). Structure, properties and residual stress of 304L stainless steel friction stir welds. *Scripta Materialia, 48*(9), 1289-1294.

187. Rhode, C.G., Mahoney, W.M., Bingel, W.H., Spurling, R.A., & Bampton, C. (1997). Effects of friction stir welding on microstructure of 7075 aluminum. *Scripta Materialia 36*(1), 69-75.

188. Roa, J. J., Jiménez-Piqué, E., Tarragó, J. M., Zivcec, M., Broeckmann, C., & Llanes, L. (2015). Berkovich nanoindentation and deformation mechanisms in a hardmetal binder-like cobalt alloy. *Materials Science and Engineering A, 621*, 128-132.

189. Rodrigues, D.M., Loureiro, A., Leitao, C., Leal, R.M., Chaparro, B.M., & Vilaca, P. (2009). Influence of friction stir welding parameters on the microstructural and mechanical properties of AA 6016-T4 thin welds. *Materials & Design, 30*, 920-930.

190. Ross, P. J. (1996). *Taguchi techniques for quality engineering: Loss function, orthogonal experiments, parameter, and tolerance design*. Mcgraw-Hill.

191. Roy, R. K. (2001). *Design of experiments using the Taguchi approach: 16 steps to product and process improvement*. John Wiley & Sons.

192. Rzaev, R., Chularis, A., Smirnov, V., & Semyenova, L. (2019). The influence of the friction stir welding parameters on the formation of welded joint of aluminum and copper alloys. *Materials Today: Proceedings, 11*(1), 534-542.

193. Saeid, T., Abdollah-Zadeh, A., Assadi, H., & Ghaini, F. M. (2008). Effect of friction stir welding speed on the microstructure and mechanical properties of a duplex stainless steel. *Materials Science and Engineering A*, 496(1-2), 262-268.

194. Sakthivel, T., & Mukhopadhyay, J. (2007). Microstructure and mechanical properties of friction stir welded copper. *Journal of Materials Science, 42*(23), 8126–8129.

195. Salari, E., Jahazi, M., Khodabandeh, A., & Nanesa, H.G. (2014). Influence of tool geometry and rotational speed on mechanical properties and defect formation in friction stir lap welded 5456 aluminum alloy sheets. *Materials & Design, 58*, 381-389.

196. Santella, M. L., Engstrom, T., Storjohann, D., & Pan, T. Y. (2005). Effects of friction stir processing on mechanical properties of the cast aluminum alloys A319 and A356. *Scripta Materialia, 53*(2), 201–206.

197. Santos, T.F.A., Hermenegildo, T.F.C., Afonso, C.R.M., Marinho, R.R., Paes, M.T.P., & Ramirez, A.J. (2012). Fracture toughness of ISO 3183 X80 M (API 5L X80) steel friction stir welds. *Engineering Fracture Mechanics, 77*(15), 2937-2945.

198. Sato, Y. S., Nelson, T. W., Sterling, C. J., Steel, R. J., & Pettersson, C.-O. (2005). Microstructure and mechanical properties of friction stir welded SAF 2507 super duplex stainless steel. *Materials Science and Engineering A, 397*, 376–384.

199. Sato, Y.S., Yamanoi, H., Kokawa, H., & Furuhara, T. (2007). Microstructure evolution of ultrahigh carbon steel during friction stir welding. *Scripta Materialia, 57*(6), 557-560.

200. Schmidt, H.N.B., Dickerson, T.L., & Hattel, J.H. (2006). Material flow in butt friction stir welds in AA2024-T3. *Acta Materialia, 54*, 1199-1209.

201. Schneider, C., Weinberger, T., Inoue, J., Koseki, T., & Enzinger, N. (2011). Characterisation of interface of steel/magnesium FSW. *Science and Technology of Welding and Joining, 16*(1), 100-107.

202. Schneider, J. A., Willisto, T. L., Murphy, C., Varne, J., & Walker, H. B. (2015). Solid state joining of nickel-based alloy, Haynes 230. *Journal of Materials Processing Technology Transactions, 225*, 1-55.

203. Scialpi, A., Filippis, L.A., & Cavaliere, P. (2007). Influence of shoulder geometry on microstructure and mechanical properties of friction stir welded 6082 aluminum alloy. *Materials & Design, 28*, 1124-1129.

204. Sharma, S., Handa, A., Singh, S. S., & Verma, D. (2019). Influence of tool rotation speeds on mechanical and morphological properties of friction stir processed nano hybrid composite of MWCNT-Graphene-AZ31 magnesium. *Journal of Magnesium and Alloys, 7*(3), 487-500.

205. Shen, J. J., Liu, H. J., & Cui, F. (2010). Effect of welding speed on microstructure and mechanical properties of friction stir welded copper. *Materials & Design, 31*(8), 3937-3942.

206. Siddiquee, A. N., & Pandey, S. (2014). Experimental investigation on deformation and wear of WC tool during friction stir welding (FSW) of stainless steel. *International Journal of Advanced Manufacturing Technology, 73*(1–4), 479–486.

207. Singh, K., Singh, G., & Singh, H. (2018). Investigation of microstructure and mechanical properties of friction stir welded AZ61 magnesium alloy joint. *Journal of Magnesium and Alloys, 6*(3), 292-298.

208. Singh, V. P., & Kuriachen, B. (2022). Experimental Investigations into the Mechanical and Metallurgical Characteristics of Friction Stir Welded AZ31 Magnesium Alloy. *Journal of Materials Engineering and Performance, 31*, 9812-9828.

209. Singh, V. P., Patel, S. K., Kumar, N., & Kuriachen, B. (2019). Parametric effect on dissimilar friction stir welded steel-magnesium alloys joints: a review. *Science and Technology of Welding and Joining, 24*(8), 653-684.

210. Sinka, V. (2014). The present and future prospects of friction stir welding in aeronautics. *Acta Metallurgica Slovaca, 20*, 287-294.

211. Sittiho, A., Tungala, V., Charit, I., & Mishra, R. S. (2018). Microstructure, mechanical properties and strengthening mechanisms of friction stir welded Kanthal APMTTM steel. *Journal of Nuclear Materials, 509*, 435–444.

212. Skoog, D. A., Holler, F. J., & Crouch, S. R. (2017). *Principles of Instrumental Analysis*. Cengage Learning.

213. Song, K. H., Tsumura, T., & Nakata, K. (2009). Development of microstructure and mechanical properties in laser-FSW hybrid welded inconel 600. *Materials Transactions, 50*(7), 1832–1837.

214. Song, K., Lin, Z., Fa, Y., Zhao, X., Zhu, Z., Ya, W., Sun, Z., & Yu, X. (2023). Microstructure and Mechanical Properties of High-Strength, Low-Alloy Steel Thin-Wall Fabricated with Wire and Arc Additive Manufacturing. *Metals, 13*, 764.

215. Stephens, M.A. EDF statistics for goodness of fit and some comparisons. J. Am. *Stat. Assoc. 1974*, 69, 730–737.

216. Su, J. Q., & Nelson, T. W. (2019). Advances in friction stir welding process optimization. *Metals, 9*(2), 199.

217. Su, J.Q., Nelson, T.W., Mishra, R., & Mohaney, M. (2003). Microstructural investigation of friction stir welded 7050-T651 aluminum. *Acta Materialia, 51*(3), 713-729.

218. Sued, M. K., Pons, D., Lavroff, J., & Wong, E. H. (2014). Design features for bobbin friction stir welding tools: Development of a conceptual model linking the underlying physics to the production process. *Materials and Design, 54*, 632–643.

219. Sun, Y. F., & Fujii, H. (2010). Investigation of the welding parameter dependent microstructure and mechanical properties of friction stir welded pure copper. *Materials Science and Engineering: A*, 527(26), 6879-6886.

220. Sun, Y. F., Konishi, Y., Kamai, M., & Fujii, H. (2013). Microstructure and mechanical properties of S45C steel prepared by laser-assisted friction stir welding. *Materials and Design, 47*, 842–849.

221. Sundar Raju, G., Sivakumar, K., & Ragu Nathan, S. (2020). Influence of tool rotational speed on the mechanical and microstructural properties of AISI 316 Austenitic stainless steel friction stir welded joints. *Materials Research Express, 6*(12), 1265d7.

222. Sunil, B. R., Reddy, G. P. K., Patle, H., & Dumpala, R. (2016). Magnesium based surface metal matrix composites by friction stir processing. *Journal of Magnesium and Alloys, 4*(1), 52–61.

223. Suryanarayanan, R., & Sridhar, V. G. (2020). Process parameter optimisation in pinless friction stir spot welding of dissimilar aluminium alloys using Multi-start algorithm. Proceedings of the Institution of Mechanical Engineers, *Part C: Journal of Mechanical Engineering Science, 234*(20), 4101–4115.

224. Taguchi, G. (1986). *Introduction to quality engineering: designing quality into products and processes*. Asian productivity organization.

225. Taguchi, G., & Wu, Y. (1980). *Introduction to off-line quality control: principles and practice.* Central Japan Quality Control Association.

226. Tanaka, T., Morishige, T., & Hirata, T. (2009). Comprehensive analysis of joint strength for dissimilar friction stir welds of mild steel to aluminum alloys. *Scripta Materialia, 61*(7), 756-759.

227. Teimournezhad, J., & Masoumi, A. (2010). Experimental investigation of onion ring structure formation in friction stir butt welds of copper plates produced by non-threaded tool pin. *Science and Technology of Welding and Joining, 15*(2), 166-170.

228. Thomas, W. M., Nicholas, E. D., Needham, J. C., Murch, M. G., Temple-Smith, P., & Dawes, C. J. (1991). Friction stir butt welding. International patent application No. PCT/GB92/02203.

229. Thomas, W.M., Johnson, K., Threadgill, P.L., & Nicholas, E.D. (1998). *Inching onward-friction stir steels the lead*. In TWI Conect. Cambridge, U.K.

230. Thomas, W.M., Johnson, K., Threadgill, P.L., & Nicholas, E.D. (1999). Feasibility of friction stir welding steel. *Science and Technology of Welding and Joining*, 4(6), 365-372.

231. Thomas, W.M., Nicholas, E.D., Needham, J.C., Murch, M.G., Temple-Smith, P., & Dawes, C.J. (1991). Friction stir butt welding. GB Patent Application, 9125978.8.

232. Tiwari, A., Pankaj, P., Biswas, P., Kore, S. D., & Rao, A. G. (2019). Tool performance evaluation of friction stir welded shipbuilding grade DH36 steel butt joints. *International Journal of Advanced Manufacturing Technology*, 103(5–8), 1989–2005.

233. Ueji, R., Fujii, H., Cui, L., Nishioka, A., Kunishige, K., & Nogi, K. (2006). Friction stir welding of ultrafine grained plain low-carbon steel formed by the martensite process. *Materials Science and Engineering A, 423*(1–2), 324–330.

234. Uzun, H., Dalle Donne, C., Argagnotto, A., Ghidini, T., & Gambaro, C. (2005). Friction stir welding of dissimilar Al 6013-T4 To X5CrNi18-10 stainless steel. *Materials & Design, 26*(1), 41-46.

235. Venkateswaran, P., & Reynolds, A. P. (2012). Factors affecting the properties of Friction Stir Welds between aluminum and magnesium alloys. *Materials Science and Engineering: A*, 545, 26-37.

236. Vijayan, S., & Ravichandran, M. (2016). Friction stir welding of dissimilar materials for medical applications: A review. *Journal of Manufacturing Processes*, 24, 394-410.

237. Wahid, M. A., Siddiquee, A. N., & Khan, Z. A. (2020). Aluminum alloys in marine construction: characteristics, application, and problems from a fabrication viewpoint. *Marine Systems & Ocean Technology*, 15, 70-80.

238. Walley, J. L., Heelan, J. L., Vettraino, L. G., Groza, J. R., & Gibeling, J. C. (2010). The influence of post-processing on creep and microstructure of rolled Cu–8Cr–4Nb. *Materials Science and Engineering: A*, 527(26), 6956-6962.

239. Wang, D. A., Chao, C. W., Lin, P. C., & Uan, J. Y. (2010). Mechanical characterization of friction stir spot microwelds. *Journal of Materials Processing Technology, 210*(14), 1942–1948.

240. Wang, W., Han, P., Peng, P., Zhang, T., Liu, Q., Yuan, S. N., Huang, L. Y., Yu, H. L., Qiao, K., & Wang, K. S. (2020). *Friction Stir Processing of Magnesium Alloys: A Review*. Acta Metallurgica Sinica (English Letters), 33(1), 43–57.

241. Wang, W., Shen, J., Li, Y., Liu, J., & Chen, Y. (2019). Mechanical and microstructural characterization of friction stir welded thin sheets of surgical stainless steel. *Materials Science and Engineering: A*, 758, 17-23.

242. Wang, W., Zhang, S., Qiao, K., Wang, K., Peng, P., Yuan, S., Chen, S., Zhang, T., Wang, Q., Liu, T., & Yang, Q. (2020). Microstructure and mechanical properties of friction stir welded joint of TRIP steel. *Journal of Manufacturing Processes, 56*(13), 623–634.

243. Wang, Y. D., Xue, P., Liu, F. C., Wu, L. H., Zhang, H., Zhang, Z., Ni, D. R., Xiao, B. L., & Ma, Z. Y. (2023). Influence of processing innovations on joint strength improvements

in friction stir welded high strength copper alloys. *Materials Science and Engineering: A*, 872, 144983.

244. Wang, Y., Tsutsumi, S., Kawakubo, T., & Fujii, H. (2021). Microstructure and mechanical properties of weathering mild steel joined by friction stir welding. *Materials Science and Engineering: A*, 823, 141715.

245. Watanabe, T., Takayama, H., & Yanagisawa, A. (2006). Joining of aluminum alloy to steel by friction stir welding. *Journal of Materials Processing Technology, 178*(1-3), 342-349.

246. Weinberger, T., Enzinger, N., & Cerjak, H. (2009). Microstructural and mechanical characterisation of friction stir welded 15-5PH steel. *Science and Technology of Welding a Joining, 14*(3), 210–215.

247. Wong, Y. L., et al. (2019). Optimization of a biodegradable plastic production process using a design of experiments approach. *Journal of Cleaner Production, 233*, 432-442

248. World Steel Association. (2022). World Steel in Figures 2022. https://worldsteel.org/steel-topics/statistics/world-steel-in-figures-2022/

249. Wu, J., Ling, C., Ge, A., Jiang, W., Baghaei, S., & Kolooshani, A. (2022). Investigating the performance of tricalcium phosphate bioceramic reinforced with titanium nanoparticles in friction stir welding for coating of orthopedic prostheses application. *Journal of Materials Research and Technology, 20*, 1685-1698.

250. Wu, X., Shen, J., Jiang, F., Wu, H., & Li, L. (2021). Study on the oxidation of WC-Co cemented carbide under different conditions. *International Journal of Refractory Metals and Hard Materials, 94*, 105381.

251. Xie, G. M., Ma, Z. Y., & Geng, L. (2007). Development of a fine-grained microstructure and the properties of a nugget zone in friction stir welded pure copper. *Scripta Materialia, 57*(2), 73-76.

252. Xie, G. M., Ma, Z. Y., & Geng, L. (2009). Partial recrystallization in the nugget zone of friction stir welded dual-phase Cu–Zn alloy. *Philosophical Magazine, 89*(18), 1505-1516.

253. Xie, G., Ma, Z. Y., & Geng, L. (2008). Effects of Friction Stir Welding Parameters on Microstructures and Mechanical Properties of Brass Joints. *Materials Transactions, 49*, 1698-1701.

254. Xu, W., Liu, J., Luan, G., & Dong, C. (2009). Temperature evolution, microstructure and mechanical properties of friction stir welded 2219-O aluminum alloy joints. *Materials & Design, 30*, 1886-1893.

255. Xu, X., Yang, X., Zhou, G., & Tong, J. (2012). Microstructures and fatigue properties of friction stir lap welds in aluminum alloy AA6061-T6. *Materials & Design, 35*, 175-183.

256. Yabuuchi, K., Tsuda, N., Kimura, A., Morisada, Y., Fujii, H., Serizawa, H., Nogami, S., Hasegawa, A., & Nagasaka, T. (2014). Effects of tool rotation speed on the mechanical properties and microstructure of friction stir welded ODS steel. *Materials Science and Engineering A*, 595, 291–296.

257. Yarlagadda, P. K., Prasad, N. R., & Joshi, A. (2018). *Advances in Friction Stir Welding for Structural Materials*. CRC Press.

258. Yazdipour, A., & Heidarzadeh, A. (2016). Effect of friction stir welding on microstructure and mechanical properties of dissimilar Al 5083-H321 and 316L stainless steel alloy joints. *Journal of Alloys and Compounds, 680*, 595-603.

259. Yu, S., Chen, X., Huang, Z., & Liu, Y. (2010). Microstructure and mechanical properties of friction stir welding of AZ31B magnesium alloy added with cerium. *Journal of Rare Earths, 28*(2), 316-320.

260. Zandsalimi, S., Heidarzadeh, A., & Saeid, T. (2019). Dissimilar friction-stir welding of 430 stainless steel and 6061 aluminum alloy: Microstructure and mechanical properties of the joints. *Proceedings of the Institution of Mechanical Engineers, Part L: Journal of Materials: Design and Applications, 233*(9), 1791-1801.

261. Zhang, C., & Yuan, W. (2019). A review of factors influencing the quality of friction stir welding joints. *Journal of Materials Engineering and Performance, 28*(11), 6733-6749.

262. Zhang, D., Suzuki, M., & Maruyama, K. (2005). Microstructural evolution of a heat-resistant magnesium alloy due to friction stir welding. *Scripta Materialia, 52*(9), 899-903.

263. Zhang, H., Lin, S. B., Wu, L., Feng, J. C., & Ma, S. L. (2006). Defects formation procedure and mathematic model for defect free friction stir welding of magnesium alloy. *Materials and Design, 27*(9), 805–809.

264. Zhang, H., Lin, S., Wu, L., Feng, J.C., & Ma, S.L. (2006). Defects formation procedure and mathematic model for defect free friction stir welding of magnesium alloy. *Materials & Design, 27*, 805-809.

265. Zhang, P., Huang, Y., Chen, J., Li, X., & Cui, J. (2019). Effect of tool tilt angle on microstructure and mechanical properties of friction stir welded high-strength steel. *Journal of Materials Processing Technology, 269*, 222-232.

266. Zhang, Y., et al. (2018). Statistical optimization of medium components for glycerol production by newly isolated Lactobacillus frumenti TD 20 using one-factor-at-a-time

and response surface methodology approaches. *Biocatalysis and Agricultural Biotechnology, 13*, 33-40.

267. Zhang, Y., He, Y., Su, J., Hu, D., & Wu, D. (2018). The Effects of Welding Parameters on the Mechanical Properties of Friction Stir Welded Aluminum Alloy. *Materials Research Express, 5*(1), 016578.

268. Zhang, Y., Sato, Y. S., Kokawa, H., Hwan, S. Park, C., & Hirano, S. (2008). Microstructural characteristics and mechanical properties of Ti-6Al-4V friction stir welds. *Materials Science and Engineering A, 485*, 448-455.

269. Zhang, Y., Sato, Y., Kokawa, H., Park, S., & Hirano, S. (2008). Microstructural characteristics and mechanical properties of Ti-6Al-4V friction stir welds. Materials Science and Engineering A-Structural Materials Properties *Microstructure and Processing, 485,* 448-455.

270. Zhao, Y., Cui, X., Li, J., Yang, G., & Liu, W. (2019). Continuous dynamic recrystallization behavior of an Al-Mg alloy during hot deformation. *Journal of Alloys and Compounds, 805*, 38-45.

271. Zhou, L., Zhou, W. L., Huang, Y. X., & Feng, J. C. (2015). Interface behavior and mechanical properties of 316L stainless steel filling friction stir welded joints. *International Journal of Advanced Manufacturing Technology, 81*, 577-583.

LIST OF PUBLICATIONS

1. Bhatia, A., & Wattal, R. (2022). Fatigue behaviour and impact strength assessment of friction stir welded carbon steel joints. *Proceedings of the Institution of Mechanical Engineers, Part E: Journal of Process Mechanical Engineering*, Advance online publication. https://doi.org/10.1177/09544089221130615 (**SCIE Indexed, Impact Factor: 2.4**) published online on 6th October 2022.

2. Bhatia, A., & Wattal, R. (2021). Process parameters optimization for maximizing tensile strength in friction stir-welded carbon steel. *Strojniški vestnik - Journal of Mechanical Engineering, 67*(6), 311-321. http://dx.doi.org/10.5545/sv-jme.2021.7203 (**SCIE Indexed, Impact Factor: 1.6**)

3. Bhatia, A., & Wattal, R. (2022). *Friction-stir welding: A sustainable procedure for joining steels.* In S. Kaushal, I. Singh, S. Singh, & A. Gupta (Eds.), Sustainable Advanced Manufacturing and Materials Processing (pp. 95-115). New York: Routledge. https://doi.org/10.1201/9781003269298-6 (**Scopus Indexed Book Chapter**).

4. Bhatia, A., & Wattal, R. (2020). Friction-stir welding of carbon steel: Effect on microstructure and tensile strength. In Proceedings of the 10th International Conference on Materials Processing and Characterization (ICMPC-2020) (pp. 1803-1808). Mathura, India: Department of ME, GLA University, in association with Gokaraju Rangaraju Institute of Engineering and Technology (GRIET), Hyderabad, and Indian Institute of Metals (IIM). *Materials Today: Proceedings, 26*(2). https://doi.org/10.1016/j.matpr.2020.02.378. (**Scopus Indexed, Cite Score: 2.3**).

5. Bhatia, A., & Wattal, R. (2016). Paradigm shifts in friction stir welding research: A critical review. Proceedings of the International Conference on Advanced Production and Industrial Engineering (ICAPIE 2016) (pp. 312-320). New Delhi, India: Department of Mechanical, Production, and Industrial Engineering, Delhi Technological University.

CURRICULUM VITAE

ANMOL BHATIA

PROFILE SUMMARY

- Eleven years of work experience, having taught a diverse range of subjects at both the undergraduate and postgraduate levels which has provided a comprehensive understanding of engineering principles and pedagogical techniques.
- The research interests primarily focus on friction stir welding (FSW) of steel, aiming to optimize process parameters, characterize weld properties, and develop advanced FSW techniques to enhance the quality and performance of steel welds.

ACADEMIC QUALIFICATIONS

- Pursuing Ph.D. in the area of friction stir welding of steel; this thesis is submitted to obtain Ph.D. degree from Delhi Technological University, Delhi, India.
- M.Tech (Manufacturing Technology and Automation) from Maharishi Dayanand University, Rohtak, India with 76.68% (2010-2012).
- B.E. (Mechanical Engineering) from Maharishi Dayanand University, Rohtak, India with 75% (2005-2009).
- Higher Secondary education from St. John's School, Faridabad, Haryana, India.

PROFESSIONAL EXPERIENCE

- Assistant Professor (Selection Grade) in the Department of Mechanical Engineering at The NorthCap University, Gurugram, India from August 2020 to till date.
- Assistant Professor (Sr. Scale) in the Department of Mechanical Engineering at The NorthCap University, Gurugram, India from August 2016 to August 2020.
- Assistant Professor in the Department of Mechanical Engineering at The NorthCap University, Gurugram, India from January 2014 to August 2016.
- Assistant Professor in the Department of Mechanical Engineering at Echelon Institute of Technology, Faridabad, Haryana, India from August 2012 to December 2013.

GOOGLE SCHOLAR PROFILE AND ORCID ID

https://tinyurl.com/4dzzzpfb   https://tinyurl.com/2xn9r5xk